Construction and Deconstruction of Carbon–Carbon Bonds using Main Group Reagents

by Richard Yuze Kong

August 2021

Department of Chemistry

Imperial College London

A thesis submitted for a Doctorate of Philosophy

Declaration of Originality

The work discussed in this thesis was conducted in the Department of Chemistry, Imperial College London, between October 2017 and August 2021. Unless stated otherwise, all the work is entirely my own and has not been submitted for a previous degree at this, or any other university.

Copyright Declaration

The copyright of this thesis rests with the author and is made available under a Creative Commons Attribution Non-Commercial No Derivatives licence. Researchers are free to copy, distribute or transmit the thesis on the condition that they attribute it, that they do not use it for commercial purposes and that they do not alter, transform or build upon it. For any reuse or redistribution, researchers must make clear to others the licence terms of this work.

Publications

This thesis has resulted in the following publications at the time of writing:

Kong, R. Y.; Crimmin, M. R. Cooperative Strategies for CO Homologation. *Dalton Trans.* **2020**, *49* (46), 16587–16597. https://doi.org/10.1039/D0DT01564D.

Kong, R. Y.; Crimmin, M. R. Carbon Chain Growth by Sequential Reactions of CO and CO_2 with [$W(CO)_6$] and an Aluminum(I) Reductant. *J. Am. Chem. Soc.* **2018**, *140* (42), 13614–13617. https://doi.org/10.1021/jacs.8b09761.

Kong, R. Y.; Crimmin, M. R. Reversible Insertion of CO into an Aluminium–Carbon Bond. *Chem. Commun.* **2019**, *55* (44), 6181–6184. https://doi.org/10.1039/C9CC02818H.

Kong, R. Y.; Crimmin, M. R. Activation and Functionalization of C–C σ Bonds of Alkylidene Cyclopropanes at Main Group Centers. *J. Am. Chem. Soc.* **2020**, *142* (28), 11967–11971. https://doi.org/10.1021/jacs.0c03383.

Kong, R. Y.; Crimmin, M. R. Chemoselective C–C σ-Bond Activation of the Most Stable Ring in Biphenylene. *Angew. Chem., Int. Ed.* **2021**, *60* (5), 2619–2623. https://doi.org/10.1002/anie.202011594.

Acknowledgments

I would like to express thanks to Xiaoling Yang, Linggen Kong, Natalie Bird, Sean Ding, Anahita Surya, Linda Ma, Lucinda Thurmer, Ellen Cliff, Mark Crimmin, Charles Romain, Anna Barnard, Mark Chadwick, Feriel Rekhroukh, Clare Bakewell, Tom Hooper, Nick Phillips, Maria Batuecas, Nikolaus Gorgas, Andreas Phanopolous, Alex Hicken, Samantha Lau, Wenyi Chen, Marti Garcon, Greg Coates, Greg Baker, Daniel Mulryan, Roland Turnell-Ritson, Yara van Ingen, Joshua Sapsford, Leah Webster, Christian Nielsen, Laura Parsons, Jen Cornwell, Pete Haycock, Andrew White, Corey Fulop, and all my friends in the UK, Australia, or wherever they may be.

Abstract

This is a thesis of two halves.

In the first half of the thesis, the construction of C–C bonds from carbon monoxide units is developed using a mixed transition-metal and main-group metal strategy. In chapter 1, synthetic methods for CO homologation were reviewed. In chapter 2, the formation of carbon–carbon bonds using carbon monoxide as a feedstock was investigated. Reaction of an aluminium(I) reagent with a transition-metal carbonyl resulted in the formation of C–C bonds between CO monomers to form isolable C_2, C_3, and C_4 species. The mechanism was explored using density functional theory calculations and isotope labelling experiments. Control of the chain topology is demonstrated through variation of the transition metal fragment. CO units within the final carbon chain originate from both gaseous CO and transition-metal bound CO units. In chapter 3, the insertion of CO into Al–C bonds was further studied through the reaction of strained aluminacycles with CO gas. The reaction was found to be reversible and was studied using a combination of kinetics and density functional theory calculations. The insertion of CO into Al–C bonds was calculated to proceed *via* an asynchronous but concerted transition state. The synthetic and theoretical work in chapter 2 and 3 are linked through fundamental reactions involving migratory insertion at either transition metal or main group centres.

In the second half of the thesis, the deconstruction of C–C bonds was explored using main-group metals. In chapter 4, the cleavage of C–C bonds in alkylidene cyclopropanes using either an aluminium(I) reagent or magnesium(I) reagent was investigated. The reaction was studied using a combination of density functional theory calculations and kinetics. The reaction of a carbon–carbon double bond in the substrate with the main-group reagent preceded C–C cleavage. The mechanistic insights were used to develop magnesium-based catalysis for C–C bond hydrosilylation. In chapter 5, the reaction of an aluminium(I) reagent with biphenylene was studied. The activation and cleavage of the arene ring was achieved, forming two isomeric products. The integrity of the strained 4-membered ring was observed throughout the course of the reaction. The reaction was studied using density functional theory calculations and a full calculated pathway from the reagents to the products was discovered. The activation strain model was applied to understand the chemoselectivity of the reaction and showed that the position and extension of the frontier molecular orbitals of the aluminium(I) reagent underpin its unique reactivity.

Table of Contents

Contents

Declaration of Originality I

Copyright Declaration I

Publications I

Acknowledgments II

Abstract III

Table of Contents IV

Chapter 1 1

1.1 – Context 2

1.2 – Reduction of CO at a metal or main-group centre 3

1.3 – Reduction of M–CO with an external reductant 9

1.4 – Reduction of CO with M–M, B–Li, Si=Si and B≡B bonds 12

1.5 – Reaction with CO derived carbon chains with H_2 17

1.6 – Conclusion and outlook 19

1.7 – References 20

Chapter 2 23

2.1 – Introduction to reagents 24

2.1.1 – Aluminium(I) compounds 24

2.2 – Results and discussion 25

2.2.1 – Homologation to C^2, C^3 and C^4 chains 25

2.2.2 – Labelling Studies 32

2.2.3 – Electronic structure of **2-2-Mn**, **2-3-Mn** and **2-4-Mn** 32

2.2.4 – Mechanism of the formation **2-2-Mn**, **2-3-Mn**, **2-3-Mn'** and **2-4-Mn** 34

2.2.5 – Homologation to different chain topologies 36

2.2.6 – Insertion of CO_2 into the carbon chain 39

2.3 Conclusion and future work 41

2.4 – Experimental 43

2.4.1 – General experimental 43

2.4.2 Preparation of Compounds 44
2.4.3 – Labelling Experiments 73
2.5 – X-Ray crystal structures 80
2.5.1 – Normalised M=C for **2-3** 104
2.6 – Computational Methods 105
2.6.1 – Calculated pathway to **2-4-W** 106
2.6.2 – Calculated pathway to **2-4-Mn** 108
2.6.3 – Calculated pathway to **2-3-Mn'** 109
2.6.4 – Calculated pathway towards the formation of **2-3-Re'** 110
2.6.5 – ETS-NOCV calculations 112
2.6.6 – NICS calculations on **2-3-Mn** and **2-4-Mn** 113
2.6.7 – Functional testing on key stationary points 114
2.7 – References 115
Chapter 3 117
3.1 – Introduction to migratory insertion 118
3.1.1 – Migratory insertion and reverse elimination 118
3.1.2 – Migratory insertion at main-group centres 118
3.2 – Results and discussion 120
3.2.1 – Synthesis 120
3.2.2 – Kinetics 122
3.2.3 –DFT study of mechanism 123
3.3 – Conclusions and Future Work 125
3.4 – Experimental 126
3.4.1 – General experimental 126
3.4.2 – Preparation of Compounds 127
3.4.3 – Labelling Experiments 132
3.4.4 – Kinetic experiments on the elimination of CO from **3-6** to form **3-5** 135
3.5 – X-ray Structures 137
3.6 – Computational details 139

3.7 – References 140
Chapter 4 141
4.1 – Introduction to C–C activation 142
4.1.1 – Background 142
4.1.2 – Main-group C–C activation 143
4.2 – Results and Discussion 144
4.2.1 – Activation of alkylidene cyclopropanes with an aluminium (I) reagent 144
4.2.2 – Kinetics and DFT investigation into mechanism 146
4.2.3 – Ring opening of alkylidene cyclopropanes with a magnesium(I) reagent 150
4.2.4 – Catalytic hydrosilylation of a C–C σ-bond in alkylidene cyclopropanes 152
4.3 Conclusion and future work 154
4.4 – Experimental 155
4.4.1 – General experimental 155
4.4.2 – Substrate synthesis 157
4.4.3 – Synthesis of compounds 160
4.4.4 – Kinetic experiments on the conversion of **4-6a** to **4-7a** 172
4.4.5 – Magnesium hydride catalysis 176
4.5 – Single crystal X-ray data 180
4.6 – Computational details 189
4.7 – References 190
Chapter 5 192
5.1 – Introduction to Arene Activation 193
5.1.1 – Aromaticity and anti-aromaticity 193
5.1.2 – Arene activation 193
5.1.3 – Biphenylene 197
5.2 – Results and Discussion 198
5.2.1 – Reaction of [Al] with biphenylene 198
5.2.2 – Spectroscopic data and solid state structures 198
5.2.3 – DFT study of the mechanism 199

5.2.4 – DFT study of alternate pathways 202
5.2.5 – Activation strain analysis 205
5.3 Conclusion and future work 206
5.4 – Experimental 208
5.4.1 – General experimental 208
5.4.2 – Synthesis of compounds 209
5.4.3 – Reversibility experiments with **5-15** 214
5.5 – X-ray data 215
5.6 – Computational details 219
5.6.1 – Functional testing 220
5.6.2 – Activation strain analysis 221
5.7 – References 223
Closing Remarks 22325

Chapter 1

Cooperative strategies for CO homologation

1.1 – Context

In response to concerns over anthropogenic CO_2, interest in developing methods to produce liquid hydrocarbons from renewable resources has heightened in recent years. One established technology to achieve this is the Fischer-Tropsch (F-T) process. The F-T process converts syngas mixtures (H_2/CO) into short-to-medium chain hydrocarbons (n = 7-9) using heterogeneous transition metal catalysts (Eq. 1). CO_2 can be incorporated through the water-gas shift reaction (Eq. 2).

$$n\,CO + (2n + 1)\,H_2 \rightarrow C_nH_{2n+2} + n\,H_2O \text{ (Eq. 1)}$$

$$CO_2 + H_2 \rightleftharpoons CO + H_2O \text{ (Eq. 2)}$$

Although syngas is typically produced from coal or natural gas, biomass has also been identified as viable source.[1] F-T catalysis produces hydrocarbons with a range of carbon chain-lengths determined by the Anderson-Schulz-Flory distribution.[2]

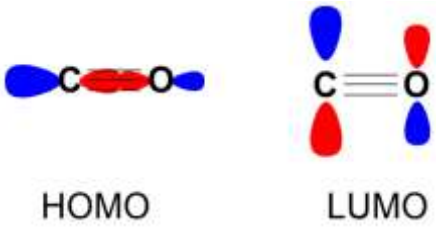


Figure 1.1: Frontier molecular orbitals of CO depicted as combinations of their constituent atomic orbitals. A second degenerate LUMO orthogonal to the plane of the page is not shown for clarity.

Carbon monoxide (CO) is a diatomic molecule with bond order of 3. The HOMO is a σ-orbital with a major contribution from the carbon atom, while the LUMO consists of two degenerate π* orbitals (Figure 1.1). Accordingly, CO is capable of either acting as a Lewis base or Lewis acid through HOMO and LUMO based reactivity respectively. The reduction of CO is also possible through electron transfer to the LUMO from a suitable reductant.

While homogeneous F-T catalysis remains significantly underdeveloped with respect to the heterogeneous commercial process, there is growing interest in this area. Homogeneous models are amenable to study by solution techniques (NMR, IR, UV-vis spectroscopy) and can offer unique insight into fundamental reactivity that may be of relevance to heterogeneous F-T catalysis. In the longer term, using homogeneous catalysis to direct the selectivity of F-T reactions to high-value products is an attractive target.

Herein, contemporary research in CO homologation using cooperative strategies is summarised. That is reactions in which two or more components (typically transition metal or main group complexes) react with CO to form carbon chains by forming new C–C bonds. These reactions

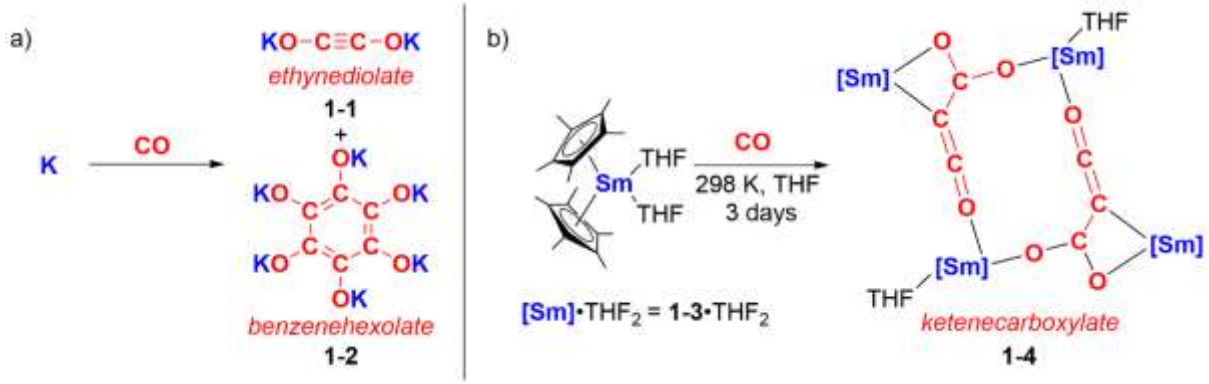
typically involve three stages: initiation, propagation, and termination. Cooperative effects have been observed in each of the separate stages of chain growth.

The initiation step often involves the reduction of CO with electrons from a transition metal or main group complex. Reduction forms a high energy intermediate. The propagation step involves further reaction of this high energy intermediate with CO to form C_2 fragments or less commonly C_3/C_4 chains. Termination involves the sequestration of reactive intermediates into stable, isolable products which do not react with further equivalents of CO. The available mechanisms for CO homologation are diverse, as is the range of compounds used. There are, however, some general themes that emerge. The cooperative approaches to CO homologation have been classified into three categories:

i) Reduction of CO at a metal or main-group centre.
ii) Reduction of transition metal carbonyls (M–CO) with an external reductant
iii) Reduction of CO with M–M, B–Li, Si=Si and B≡B bonds.

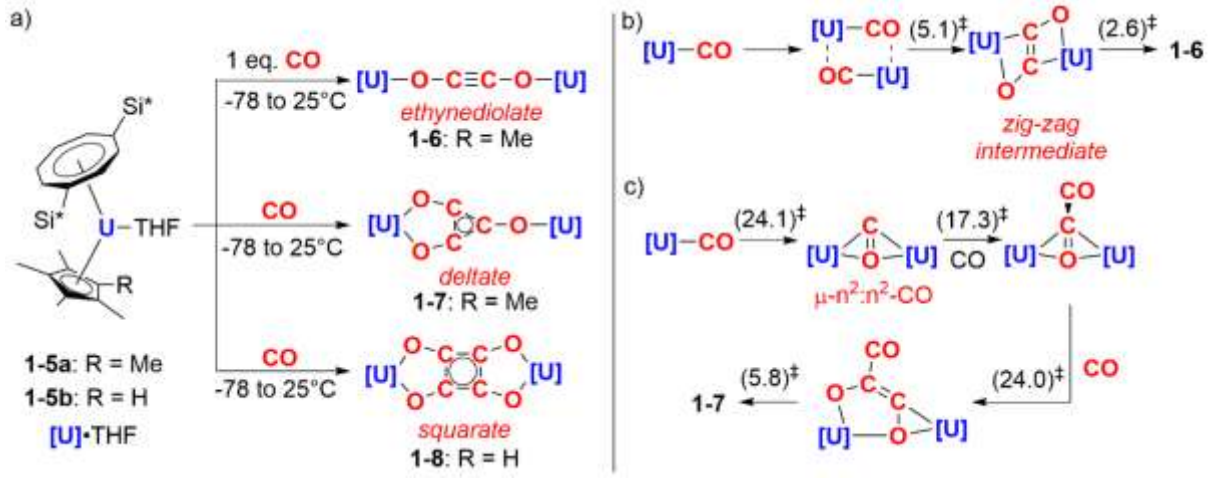
1.2 – Reduction of CO at a metal or main-group centre.

The reductive homologation of CO was first observed by Justus von Liebig in 1834 through reaction with molten potassium to form "potassium carbonyl" (KCO).[3] In 1960, "potassium carbonyl" was shown to be a mixture of potassium ethynediolate (**1-1**) and potassium benzenehexolate (**1-2**) salts (Scheme 1.1a).[4] In 1985 Evans, Atwood and co-workers reported a homogeneous metal complex that could perform a similar reaction with CO to form coupled products (Scheme 1b). Hence, the samarium(II) sandwich complex **1-3**·THF_2 reacted with CO at ambient temperatures and pressures to yield multiple products including **1-4**. **1-4** contains a ketenecarboxylate motif derived from three CO units that bridges two samarium(III) centres.[5] Similar reactivity is accessed through the lanthanum congener of **1-3**, in this case resulting in a diamagnetic product that is amenable to characterisation by multinuclear NMR spectroscopy.[6] Evans noted that the inability of f-block complexes to form stable CO adducts alongside their high oxophilicity affords this unique chain growth reactivity. Both reactions occur with oxidation of Ln(II) to Ln(III) (Ln = Sm, La).



Scheme 1.1: a) Formation of 'potassium carbonyl' reported by Liebig, confirmed by Büchner and Weiss. b) Reductive homologation of CO by decamethyl samarocene to form a ketenecarboxylate.

In 2006, Cloke and co-workers reported the reductive cyclotrimerisation of CO with the uranocene(III) complex **1-5a** to form a deltate anion (**1-7**).[7] The reaction occurred with oxidation of U(III) to U(IV) and required cooperative action of two equiv. of the actinide complex. Remarkably, further studies showed that acyclic and cyclic carbon chains of different lengths and shapes – ethynediolate (**1-6**) and squarate (**1-8**) – could be accessed by controlling either the stoichiometry of the reaction or the steric profile of the ligands on the uranium centre (Scheme 1.2a).[8–10]

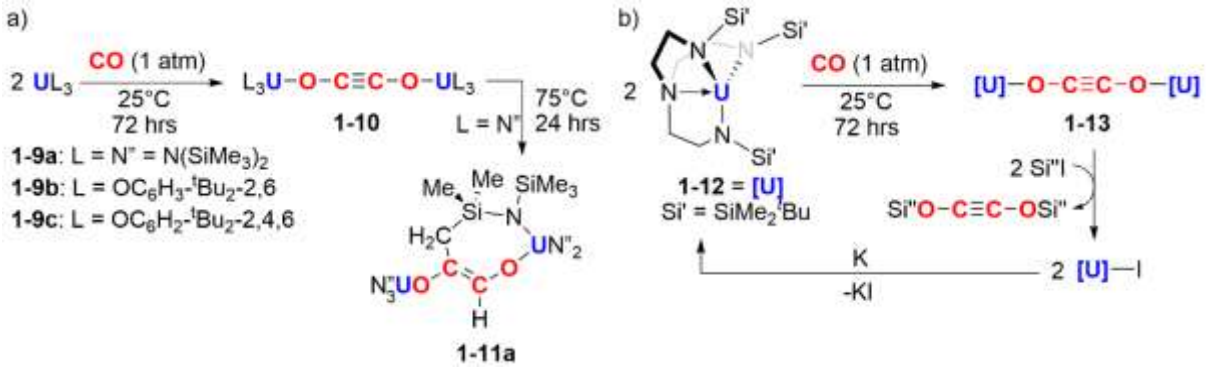


Scheme 1.2: a) Experimental CO homologation. Si*=Si^{i}Pr$_3$ b) Computational pathway towards the formation of ethynediolate. c) Computational pathway towards the formation of deltate. Calculations performed using the B3PW91 functional. (Gibbs free energies in kcal mol^{-1}) l

DFT calculations have been used to study how carbon chain growth occurs with this well-defined system. These calculations suggest that two distinct mechanisms are in operation, one leads to the formation of the ethynediolate and the other the deltate. In the case of ethynediolate, calculations by Green and co-workers suggest that an intermediate uranium(III) (mono)carbonyl is formed which can undergo sequential dimerisation and electron transfer steps, forming a 'zig-zag' intermediate which isomerises to the experimentally-observed linear

ethynediolate (Scheme 1.2b).[9] In the case of the deltate, Maron and co-workers propose that the same uranium(III) (mono)carbonyl is reduced by a second equivalent of the uranium(III) starting material resulting in the formation of a μ-η²:η²-CO ligand bridging two uranocene centres. A second CO equivalent reacts with this bridging CO ligand to directly form a new C–C bond and a $\{\mu\text{-}\eta^2\text{:}\eta^2\text{-}C_2O_2\}^{2-}$ moiety that spans two uranium centres. A third equivalent of CO inserts into the U–C bond of this intermediate which, following a series of isomerisation steps, results in the formation of the deltate product (Scheme 1.2c).[11] While the proposed uranium(III) carbonyl intermediates have not been isolated, closely related structurally characterised uranium(III) carbonyl complexes are known.[12,13]

The potential for f-block reductants to couple CO units together has been further elaborated by other groups, though exclusively towards the formation of ethynediolate products. Arnold and co-workers showed that simple uranium(III) alkoxide and amide complexes (**1-9a-c**) reduce CO under ambient conditions to ethynediolate containing products (**1-10a-c**). In the case of the amide (**1-9a**), further reactivity of the ethynediolate is observed; C–H activation of a methyl group of the ligand occurred by addition across the C≡C bond, forming metallacycle **1-11a** (Scheme 1.3).[14,15] A uranium(III) complex supported by a tripodal (tris)amidoamine ligand (**1-12**) also reacts with CO to form an ethynediolate (**1-13**), as reported by Liddle and co-workers. Notably **1-12** could be regenerated from the ethynediolate uranium(IV) species through further silylation and reduction steps. This creates a closed chemical loop with respect to the uranium fragment (Scheme 4).[16]



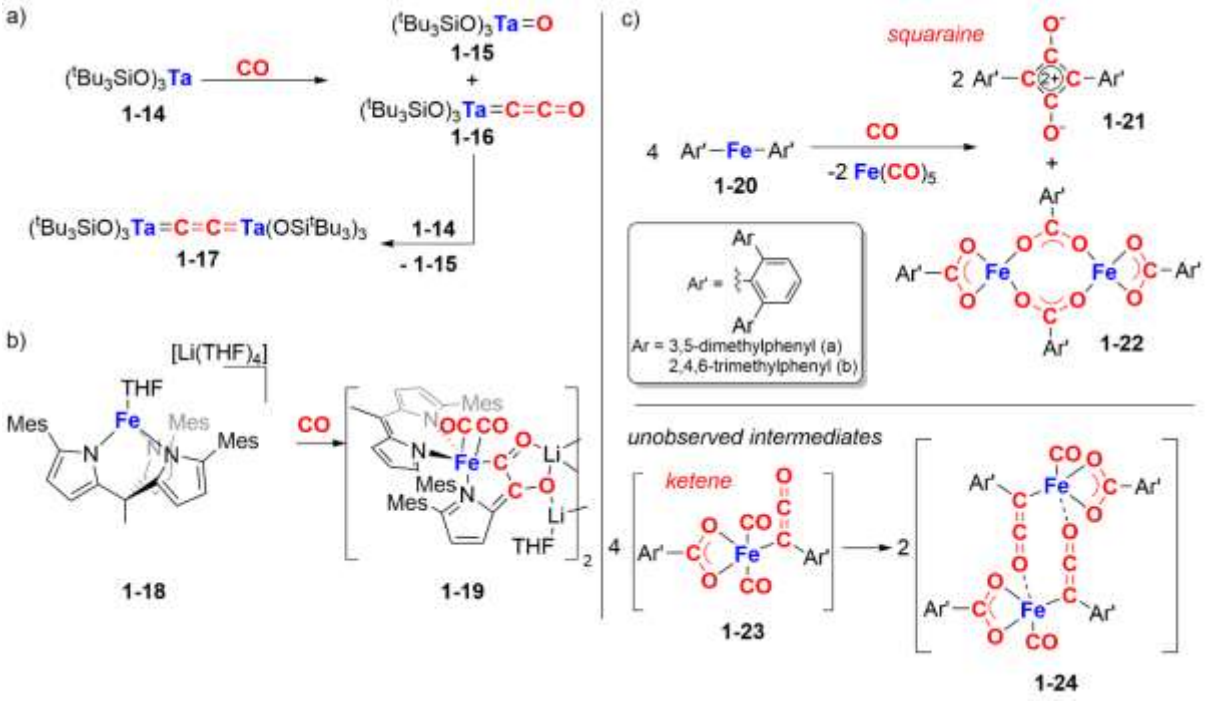
Scheme 1.3: a)Reduction of CO by uranium tris-amide (**1-9a-c**) and tris-aryloxide (**1-9b-c**) complexes to the ethynediolate (**10a-c**). Further reactivity observed for **10a** to **11a**. b) Reductive homologation of CO by a tris(amido)amine uranium(III) complex **1-12**. Si" = SiMe3 or SiMe2Ph.

Transition metal analogues of this type reactivity are far rarer. Wolczanski and coworkers reported the reductive homologation of CO by a tantalum(III) tris(siloxide) complex, **1-14**. Reaction of **1-14** with CO yielded the tantalum(V) oxide complex **1-15** and one equiv. of the tantalum ketenylidene complex **1-16**. Treatment of **1-16** with a further equivalent of **1-14**

resulted in formation of a further equivalent of **1-15**, and formation of the dicarbide complex **1-17** (Scheme 3.5a). [17,18]

Transition metal reactivity often involves direct participation of metal–ligand bonds in the homologation of CO. For example, in 2014 Sazama and Betley reported the homologation of CO at a high-spin iron centre (Scheme 3.5b, **1-18**) along with concomitant fragmentation of the tris(pyrrolide)ethane ligand. The oxidation of the ligand, rather than the metal centre, drives the reductive coupling of CO to form **1-19**.[19]

In 2018, Kays and coworkers reported the deoxygenative coupling of CO using bis(terphenyl) iron(II) complex **1-20** to form squaraine **1-21**, and iron carboxylate complex **1-22** along with concomitant formation of iron pentacarbonyl (Scheme 3.5c).[20] The reaction is proposed to proceed through the ketene intermediate **1-23**, which derives from the formal fragmentation of CO into C and CO_2. Dimerisation of **1-23** forms **1-24**, which reacts with excess CO to yield the products **1-21** and **1-22**, along with concomitant elimination of $[Fe(CO)_5]$. This system is unusual as the organometallic reagent does not reduce CO but facilitates a disproportionation of CO.

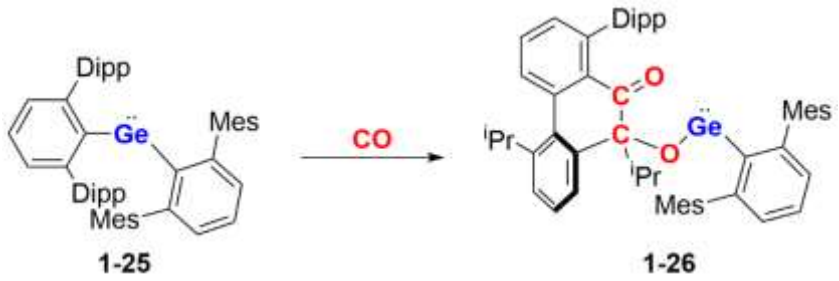


Scheme 1.4: a) Reductive coupling of CO by a tantalum trisiloxide complex **1-14**. b) Reductive coupling of CO at a high-spin iron centre. c) Deoxygenative coupling of CO to form a squaraine using bis(terphenyl) iron complex **1-20**.

While the reaction of low-valent f-block compounds with CO has been studied in detail in the last two decades, analogous chemistry with main-group reagents has only recently come into focus through the study of silylenes. In contrast to the $1e^-$ reduction per metal centre of f-block complexes, silylenes function as $2e^-$ reductants per silicon(II) centre. Early work in this area

demonstrated that the addition of transient silylenes [R_2Si:] (R = alkyl, aryl) to CO resulted in the formation of simple adducts of the form [R_2Si:(CO)], stable only at –196°C.[21–23] The CO adduct of gallium and silicon substituted silylenes have been isolated recently.[24,25] The onward reactivity of these silylene CO complexes did not result in any C–C bond formation to the bound CO ligand.

In 2009, Power and coworkers reported the first example of CO homologation at a main-group centre using a bis(terphenyl) Ge(II) complex **1-25**.[26] The coupled CO unit inserts into the Ge–C bond, and a C–C bond of the ligand, to form the observed product **1-26**. Carbene intermediates are implicated in the mechanism.

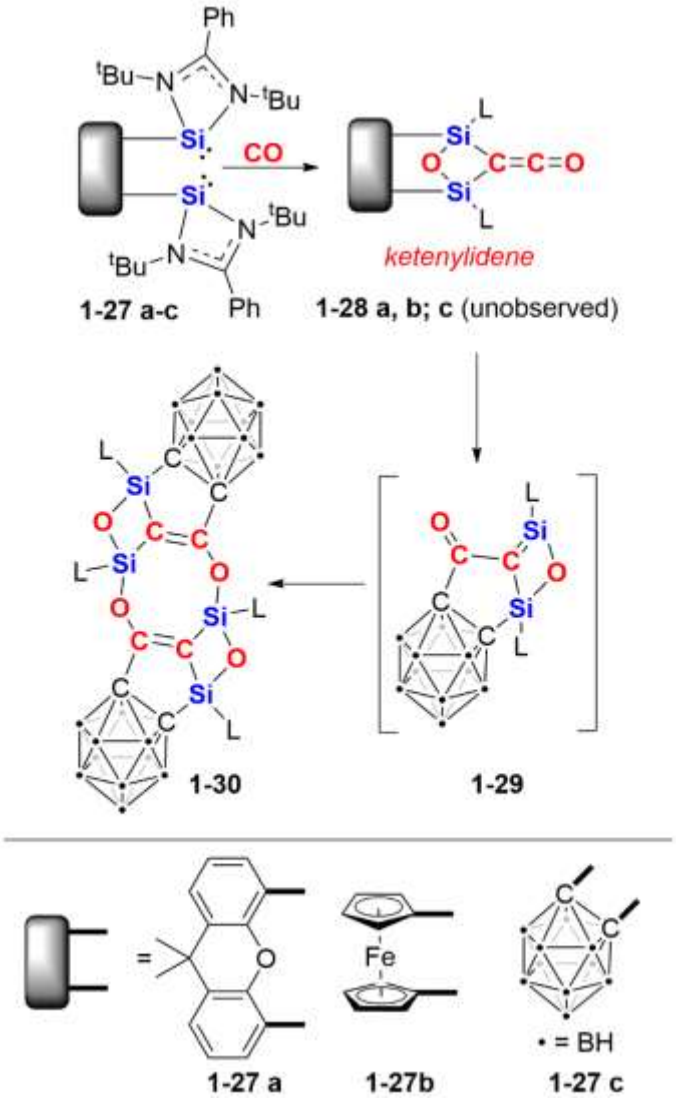


1-25 **1-26**

Scheme 1.5: Coupling of CO at a germylene. Dipp = 2,6-di-iso-propylphenyl.

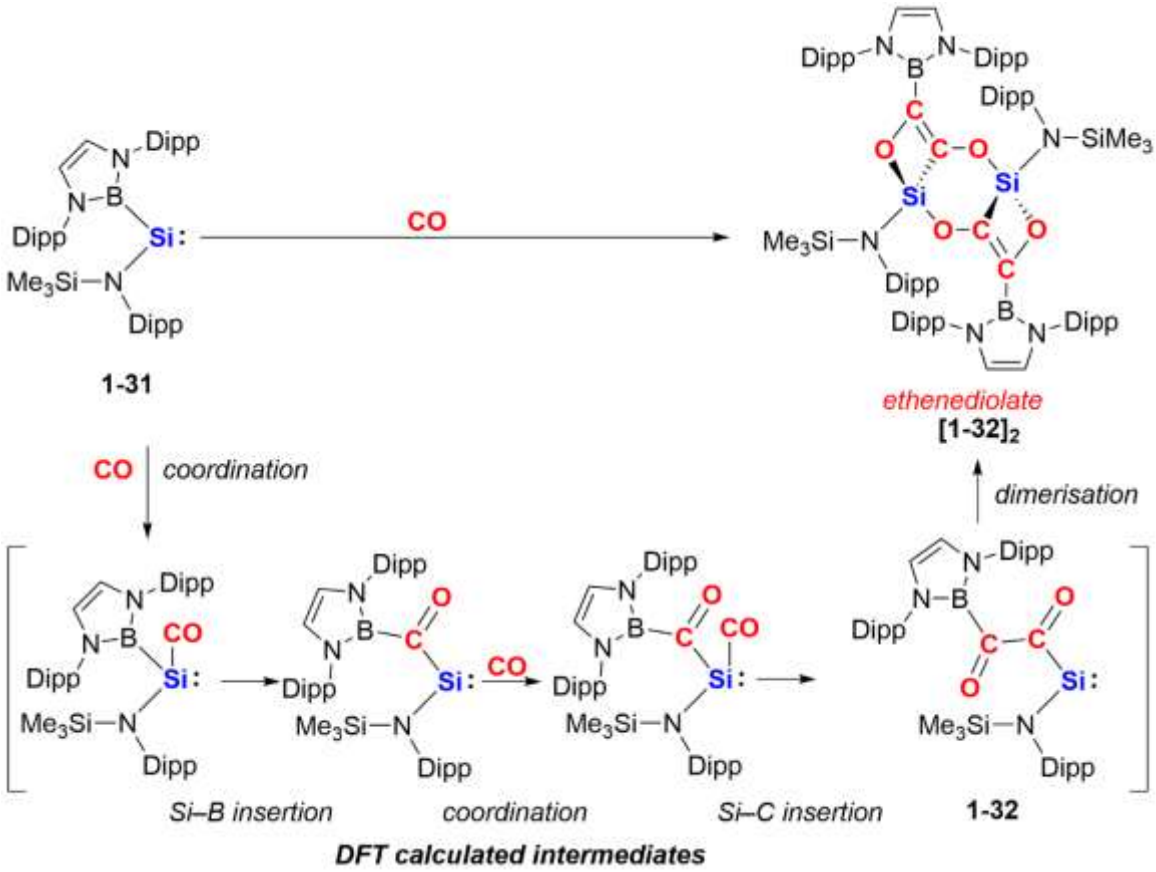
In 2019, Driess and co-workers reported the silicon-mediated coupling of CO with a series of bis(silylene) compounds supported by dinucleating ligands incorporating either a xanthenyl (**1-27a**) or ferrocenyl (**1-27b**) backbone (Scheme 1.6).[27] The resultant products are 1,1-disilyloxetanes (**1-28a-b**) in which two silicon(IV) centres are bridged by a ketenylidene and an oxo ligand. The oxo ligand is derived from complete cleavage of a C≡O bond. A total of four electrons are transferred to two molecules of CO. Crucially, cooperativity between the silylene units is necessary for CO reduction: this type of reactivity is not observed using analogous amidinate or β-diketiminate mono(silylene) reagents or when the silicon sites of the bis(silylene) compound are separated by greater than 6 Å.

Upon modifying the dinucleating ligand to include an *ortho*-carborane backbone, a different outcome was observed.[28] Hence, **1-27c** reacts to form **1-30** via a multistep process (Scheme 1.6). The first step is proposed to form an identical intermediate to those observed with xanthenyl- and ferrocenyl-based ligands. In the case of the carborane-based ligand this intermediate is unstable and reacts further with cleavage of the Si–$C_{carborane}$ bond and concomitant C_{ketene}–$C_{carborane}$ bond formation, resulting in monomer **1-29**. Dimerisation of **1-29** results in the crystallographically and spectroscopically characterised product, **1-30**.



Scheme 1.6: Reductive homologation of CO to a ketenylidene ligand by a (bis)silylene.

More recently, it has been shown that dinuclear systems are not required for CO homologation and that cooperative effects can be achieved through intermolecular rather than intramolecular assistance. Aldridge and co-workers reported the reductive coupling of CO using a boryl-substituted acyclic silylene **1-31** to form an ethenediolate species **[1-32]$_2$** (Scheme 1.7).[29] The acyclic silylene **1-31** has previously been reported to activate H_2; the high reactivity of **1-31** has been ascribed to the strong σ-donating ability of the boryl ligand and the resultant small HOMO–LUMO gap.[30] DFT calculations by Guo and Lin suggested that the reaction proceeds *via* successive coordination of CO to the silylene centre and insertion to form the unobserved monomer **1-32** which dimerises to form the isolated **[1-32]$_2$**.[31]



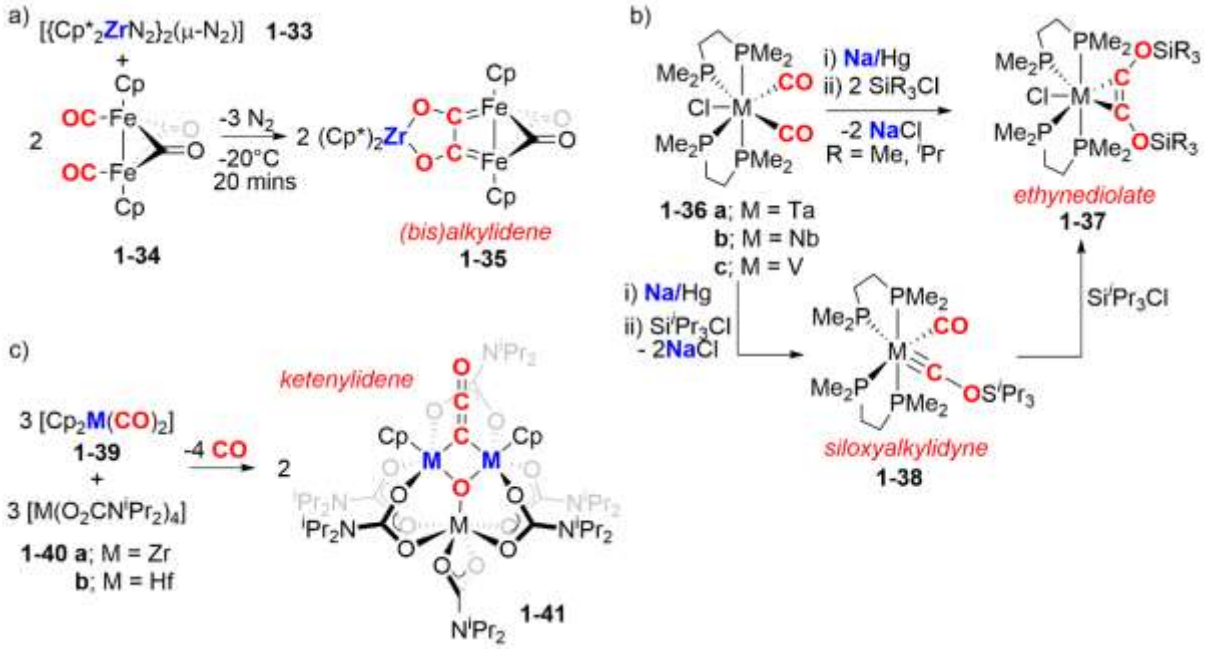
Scheme 1.7: CO homologation by an acyclic silylene. Dipp = 2,6-di-iso-propylphenyl.

1.3 – Reduction of M–CO with an external reductant

The previous section highlighted the capability of some redox-active metal centres to reduce atmospheric CO as a first step for carbon chain growth. An alternative cooperative strategy is to separate the CO binding event from the reduction and chain growth steps. To achieve this, transition metal carbonyls are typically used as the CO source, while a second low-oxidation state reagent is used as a reductant.

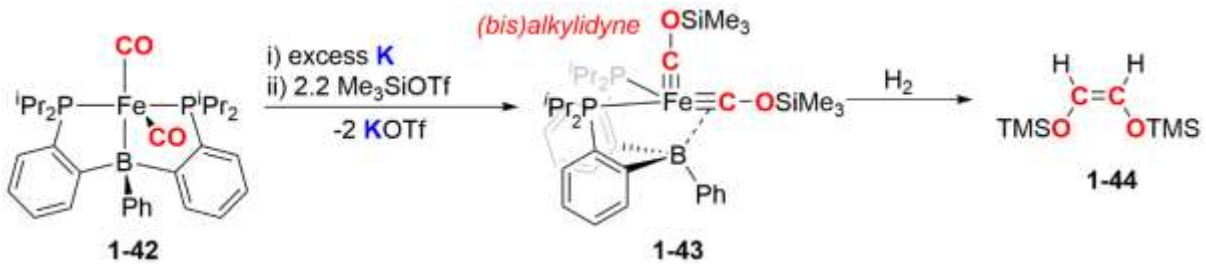
In 1982 Bercaw, Mertes, and co-workers reported the reaction of a zirconocene(II) reductant (**1-33**) with an iron carbonyl dimer (Scheme 1.8a).[32] In this reaction, **1-33** performed the 2e⁻ reduction of two *cis*-oriented CO ligands in **1-34** to form the bis(alkylidene) moiety **1-35**. Interestingly, the coupling of CO is reversible as reaction of **1-35** with CO regenerates **1-34** with concomitant formation of $[(Cp^*)_2Zr(CO)_2]$. In 1986, Lippard and co-workers reported the reductive coupling of two *cis*-disposed carbonyl ligands of a group 5 metal complex (**1-36**) using sodium amalgam as the reducing agent (Scheme 1.8b). Subsequent addition of two equivalents a tri-alkylsilyl chloride (SiR_3Cl, R = Me, ^{i}Pr) resulted in a η^2-coordinated silylated ethynediolate (**1-37**).[33,34] Reduction of **1-36** followed by addition of one equivalent of tri-isopropylsilyl chloride affords the siloxyalkylidyne complex **1-38**. Addition of a further equivalent of tri-iso-

propylsilyl chloride to **1-38** confirmed it to be an intermediate *en route* to **1-37**.[35,36] In the case of the vanadium compound, **1-37c**, reaction with hydrogen yielded an ethenediolate fragment (**1-44**, Scheme 1.19) and unidentified transition-metal fragments.[37] In 1996, Pampaloni and co-workers reported the reductive coupling of CO in which group 4 complexes played the role of both the transition metal carbonyl and the reductant (Scheme 1.8c). Hence, reaction of a group 4 metallocene dicarbonyl (**1-39a-b**) with the respective homoleptic group 4 *N*,*N*-dialkylcarbamate complex (**1-40a-b**) resulted in the formation of trinuclear metal clusters with ketenylidene ligands (**1-41**). The origin of the ketenylidene ligand is likely two *cis*-disposed CO units which are coupled with concomitant reductive cleavage of a CO triple bond to form a μ_1-oxo ligand.[38,39]



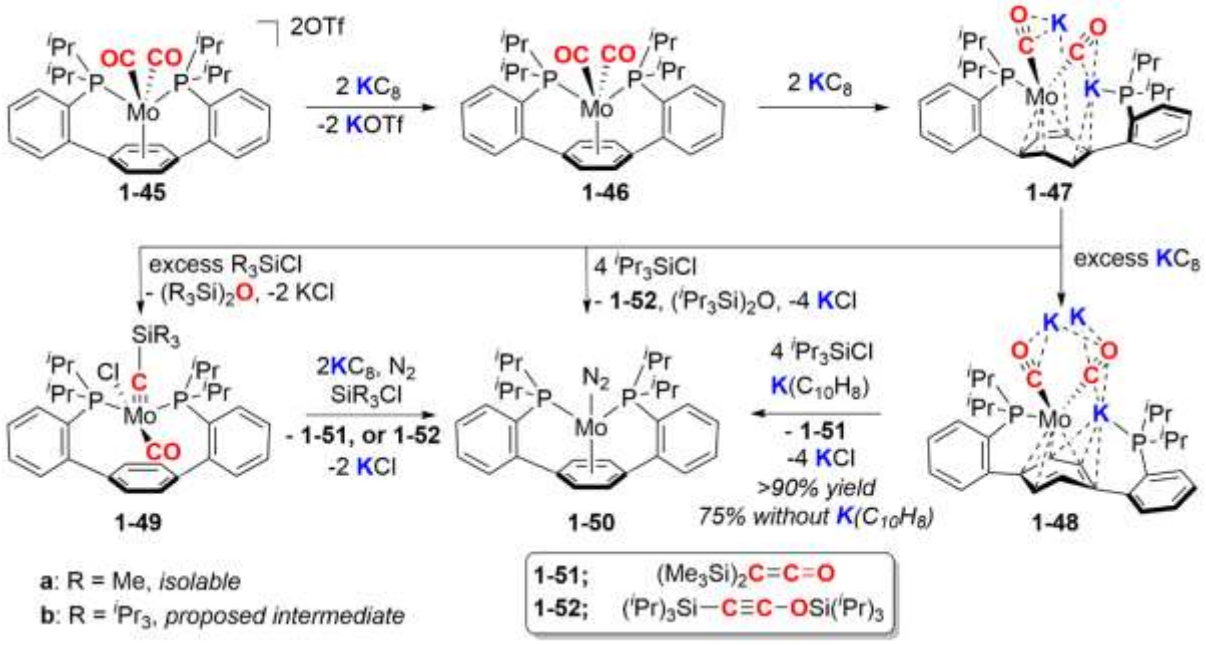
Scheme 1.8: Reductive coupling of transition metal bound CO by a) a zirconocene(II) reductant, b) sodium/mercury amalgam, and c) group 4 metallocenes.

In 2013, Suess and Peters demonstrated that an iron (bis)alkylidyne complex derived from a metal carbonyl releases an alkene upon hydrogenation (Scheme 1.9). The carbon atoms in the alkylidyne ligands originate from CO.[40] Reduction of iron dicarbonyl complex **1-42** using potassium, followed by addition of trimethylsilyl triflate resulted in generation of the (bis)alkylidyne complex **1-43**. Reaction of **1-43** with dihydrogen gas resulted in liberation of the C_2 fragment **1-44**, exclusively as the *Z*-alkene. Paramagnetic iron-containing products from the hydrogenation have eluded characterisation and are yet to be isolated. This example is notable as H_2, a key component of syngas used in F-T catalysis, is used to achieve the dissociation of a CO derived hydrocarbon from the transition metal fragment.



Scheme 1.9: Reduction of CO to form a (bis)alkylidyne complex and reductive coupling of the (bis)alkylidyne to liberate a hydrocarbon fragment.

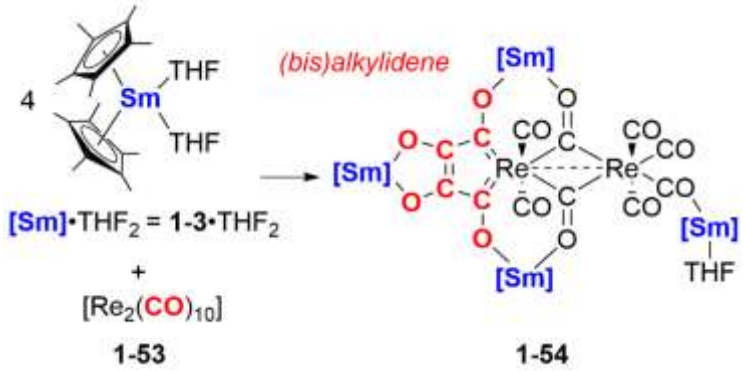
In 2016, Buss and Agapie reported the 4-electron deoxygenative coupling of CO using a molybdenum complex (Scheme 1.10). The Mo(II) dicarbonyl complex **1-45** could be successively reduced to the Mo(0) **1-46**, Mo(-II) **1-47**, and Mo(-III) species with 2, 4, and 7 (excess) equiv. of KC_8 respectively. The deoxygenative coupling of the CO ligands in the reduced complexes to form C_2 fragments is effected by addition of trialkylsilyl chloride and further equivalents of reductant to form either disilaketene (**1-51**, R = Me) or a disilaethynolate (**1-52,** R = ^{i}Pr) products and the molybdenum dinitrogen complex **1-50**.[41]



Scheme 1.10: Four-electron deoxygenative coupling of CO at molybdenum.

During these experiments the silylalkylidyne intermediate **1-49** was isolated. Both the structure and reactivity of **1-49a** parallel the reactivity of siloxyalkylidyne complexes explored by Lippard and co-workers (*vide supra*).[35] The P–Ar–P pincer ligand is a key design motif in this chemistry as the arene functions as a 'reservoir of electrons' capable of stabilising the myriad of oxidation states of molybdenum through a range of coordination (η^6-, η^4-, η^0-) modes.[41] Subsequent computational and synthetic studies on the mechanism suggest the C–C bond formation step proceeds *via* a (bis)alkylidyne-type complex.[42]

In 2019, Roesky and coworkers documented carbon chain growth of the CO ligands of $[Re_2(CO)_{12}]$ using a samarium(II) reductant, **1-3** (Scheme 1.11). While **1-3** has been shown to reductively couple two CO units to the ketenecarboxylate (*vide supra*),[5] altering the source of CO to a rhenium carbonyl cluster **1-53** results in four CO units being coupled together. The coupled CO units form a bis(alkylidene) ligand bound to the rhenium centre in **1-54**. Interestingly, CO coupling is only observed in the case of decamethyl samarocene and the rhenium carbonyl: variation of the CO source to $[Mn_2(CO)_{10}]$ or reductant to a bis(amidinate)-supported lanthanide complex (Ln = Sm, Yb) yielded a suite of isocarbonyl-bridged complexes but provided no evidence for carbon chain growth from CO.[43]



Scheme 1.11: Homologation of rhenium bound CO units using a samarocene reductant.

1.4 – Reduction of CO with M–M, B–Li, Si=Si and B≡B bonds

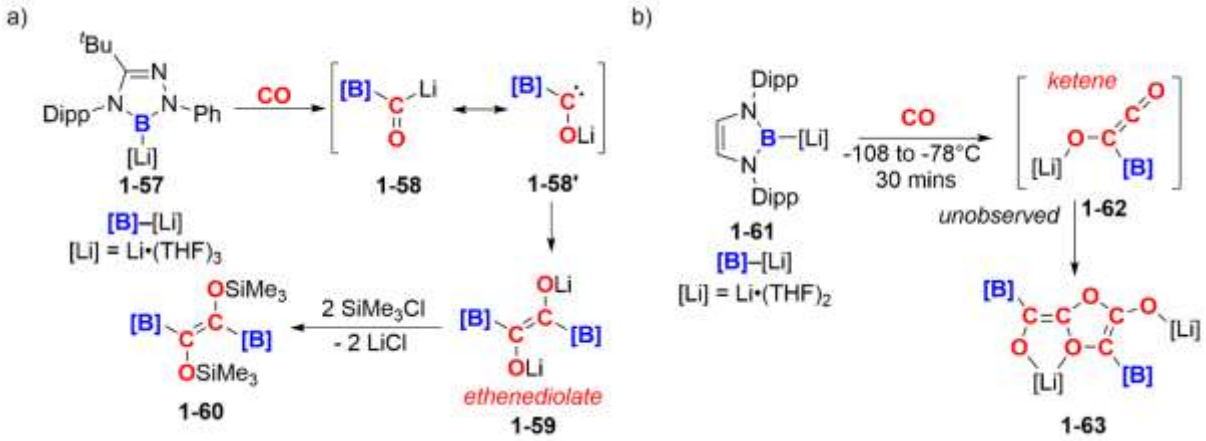
The strategies for carbon chain growth from CO outlined above involve the use of low-valent metal centres which can transfer electrons to CO to initiate a chain growth sequence. An alternative approach to CO homologation involves the use of low-oxidation state compounds that possess a metal–metal or element–element bond. These bonds are potential reactive sites, and reduction of CO can occur by transfer of electrons in the bond to the substrate with concomitant oxidation of the metal centres. The cooperative action of two reactive sites, this time connected directly through a bond in the ground state of the starting material, is a key consideration for the reaction with CO.

Wayland and co-workers first utilised this strategy in 1989. They reported the selective dimerisation of CO using a rhodium porphyrin dimer (**1-55**) containing a Rh–Rh bond (Scheme 1.12). The product of reductive coupling is proposed to be an ethanedionyl complex derived from the double insertion of CO into the Rh–Rh bond. The product (**1-56**) was not amenable to NMR or solid state characterisation and was inferred through IR studies on ^{12}CO and ^{13}CO isotopomers.[44]



Scheme 1. 12: Formation of an ethanedionyl ligand from CO using rhodium porphyrin dimer **1-55**. Ar = 3,5-dimethylphenyl

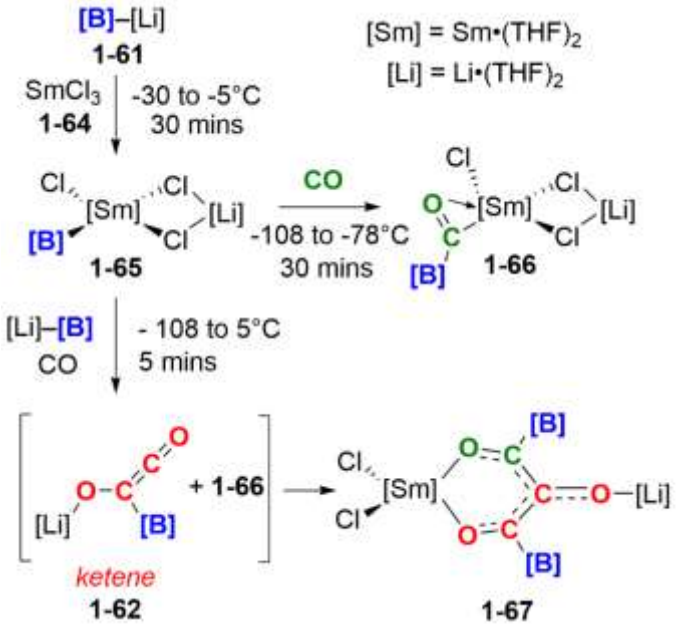
In 2016, Kinjo and co-workers reported the isolation of the boryllithium compound **1-57** (Scheme 1.13a). Insertion of CO into the B–Li bond of this highly reactive species forms the bora-acyllithium **1-58**, with tautomerises to **1-58'**. Dimerisation of **1-58'** results in the lithium ethenediolate **1-59** which has been tentatively assigned using ^{11}B NMR spectroscopy. **1-59** is unstable and can only be observed transiently, however reaction with trimethylsilyl chloride allowed the isolation of **1-60**, which has been structurally characterised. Overall, the reaction resulted in the reductive coupling and functionalisation of two CO molecules. The high polarity of the B–Li bond is thought to be important in determining the reaction of **1-57** with CO; no reaction is observed for analogous [B]–M (M = Mg, Al, Au, Zn, Sb, Bi) complexes.[45] In a similar manner, boryllithium **1-61** reacts with CO to form an unobserved ketene (**1-62**), which dimerises above –78°C to form the isolable product **1-63** (Scheme 1.13b).[46]



Scheme 1.13: a) Formation of an ethenediolate from boryllithium **1-57**. b) Tetramerisation of CO by a boryllithium. Dipp = 2,6-di-iso-propyl-phenyl.

Incorporating $SmCl_3$ into this reaction gave a completely different result (Scheme 1.14). Samarium(III) chloride (**1-64**) and boryllithium **1-61** react to yield samarium(III) boryl complex **1-65**, which in the presence of CO can form the bora-acyl samarium complex, **1-66**. **1-66** is proposed to originate from the insertion of CO into the Sm–B bond of **1-65** and similar reactivity has been observed before.[47] If the reaction with CO occurs in the presence of an excess of **1-61** both **1-62** and **1-66** can be generated *in situ*. These intermediates can combine to form a

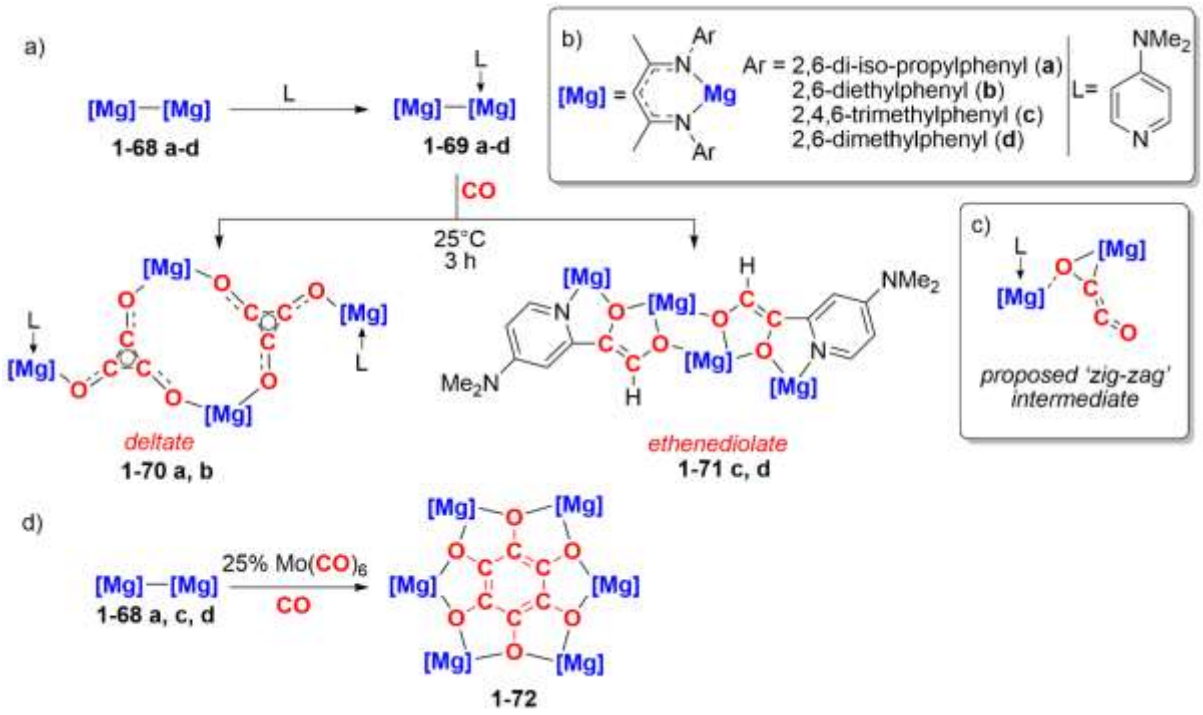
C_3 carbon chain bearing both Sm and Li substituents, **1-67**. Both isotopic labelling experiments and DFT calculations support the proposed mechanism. The tandem cooperative CO homologation strategy employed to access a C_3 product (**1-67**) provides a novel approach towards the construction and elaboration of carbon chains.



Scheme 1.14: Trimerisation of CO by a boryllithium/$SmCl_3$.

The use of well-defined s-block metal complexes to reductively couple CO was first reported in 2019 by Jones, Maron and co-workers (Scheme 1.15a).[48,49] Reaction of a magnesium(I) dimer **1-68 a-d** with one equivalent of a donor ligand (L = DMAP) yielded an asymmetric derivative of the parent dimer **1-69a-d** (Scheme 1.15a-b). Remarkably, while the parent dimer does not react with CO, the ligated dimer reduces CO and forms carbon chains. Sterically bulkier magnesium centres (**1-68a-b**) yield the deltate $\{C_3O_3\}^{2-}$, while comparatively less crowded magnesium centres (**1-68c-d**) yield a bridging ethenediolate $\{C_2O_2\}^{2}$. The steric profile of the magnesium centres controlling the degree of CO homologation parallels observations by Cloke and co-workers when studying uranocene reductants.[7–11]

DFT calculations were employed to investigate the mechanism of chain growth. Insertion of CO into the Mg–Mg bond followed by insertion of a second equivalent of CO into the resultant Mg–C bond yielded a 'zig-zag' intermediate (Scheme 1.15c).[48,49] This 'zig-zag' intermediate bears a striking resemblance to the proposed intermediate in the ethynediolate formation with mixed uranocene complexes reported by Cloke and co-workers (*vide supra*). A barrierless insertion of a third equivalent of CO into the Mg–C bond results in formation of the deltate ion in compounds **1-70a-b**. From the same intermediate, insertion into an *ortho* C–H bond of the DMAP ligand followed by isomerisation results in the ethenediolate products **1-71c-d**.

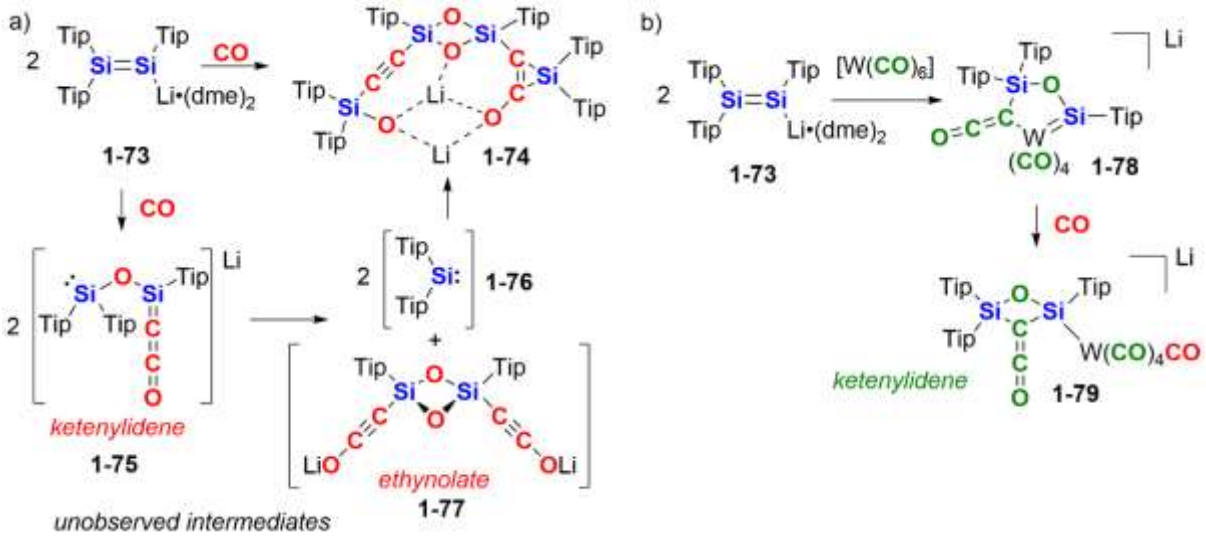


Scheme 1.15: a) Formation of the deltate and ethenediolate products from activated magnesium(I) dimers. b) Structure of Mg–Mg compounds. c) Proposed zig-zag intermediate. d) Catalytic formation of magnesium ligated benzenehexolate compound **1-72**.

Altering the source of CO from gaseous CO to a transition metal carbonyl allowed the less sterically bulky magnesium(I) dimers **1-68 (a, c, d)** to activate CO even in the absence of an external donor ligand (Scheme 1.15d). Reaction of **1-68 (a, c, d)** with a catalytic amount of molybdenum hexacarbonyl (25 mol%) under an atmosphere CO gas at 80°C resulted in the formation of **1-72**, a magnesium-ligated benzenehexolate compound. This is reminiscent of the reduction of CO by K first reported by Justus von Liebig (*vide supra*). Remarkably, the transition metal carbonyl functions as a catalyst that promotes the hexamerisation of CO.[50]

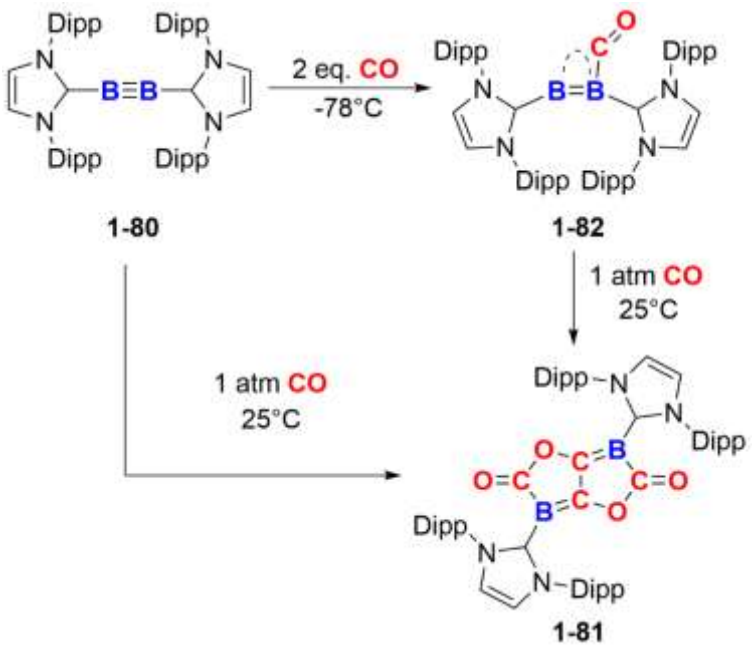
In 2015, Scheschkewitz and co-workers reported the reductive coupling of CO by the disilenide compound **1-73**. **1-73** contains a Si=Si bond and the Si centres act in a cooperative manner in the reduction of CO (Scheme 1.16a).[51] The complete cleavage of the CO triple bond is achieved resulting in the formation of a silanone dimer with pendant alkynylsilyl and silirene groups, **1-74**. Two CO units are coupled per Si=Si unit, with the Si=Si bond providing 4e⁻ in the reaction. The mechanism is proposed to proceed through a key intermediate **1-75** in which two CO units form a ketenylidene moiety along with concomitant cleavage of a CO triple bond to form a bridging oxo ligand. **1-75** is proposed to undergo a ligand metathesis to form two equiv. of silylene **1-76** and ethynolate **1-77**. The extruded silylene units then recombine with **1-77** by (2+1) cycloaddition to the C≡C bond and oxidative addition to the C–OLi bond resulting in formation of the final product **1-74**.

Altering the source of CO to a transition metal carbonyl complex again changed the observed reactivity (Scheme 1.16b).[51] Hence, reaction of **1-73** with [W(CO)$_6$], allowed for the isolation of a ketenylidene-ligated group 6 metal-silylene complex, **1-78**. Reaction of **1-78** with a further equivalent of CO gas liberates the ketenylidene ligand from the transition metal, resulting in the formation of a 2,4-disilaoxetane **1-79**. In these reactions, the carbon units that make up the chain can be derived from both atmospheric CO as well as transition-metal bound CO units.



Scheme 1.16: Disilenide reactivity with a) CO and b) tungsten hexacarbonyl. Tip = 2,4,6-tri-iso-propylphenyl, dme = 1,2-dimethoxyethane.

In 2013, Braunschweig and co-workers documented the reductive coupling of four CO units at B≡B bond through reaction of CO with diboryne **1-80** (Scheme 1.17). The reaction is unusual due to the head-to-tail coupling of two CO units to form an ethenediolate species, **1-81**. Most examples of CO homologation involve head-to-head dimerization and C–C bond formation rather than C–O bond formation. The stoichiometric addition of 1 equiv. of CO to **1-80** affords a coordination compound **1-82** in which CO act as a ligand. The CO ligand is coordinated to the two boron centres in a semi-bridging fashion. The long C=O bond distance (1.249(2) Å) provides structural evidence for back-donation from the B_2 unit to the π* orbital of CO.[52] A number of related examples of this type of interaction of CO with boron sites are known.[53] The N-heterocyclic carbene (NHC) ligands on the diboryne unit play an important role in determining the reactivity toward CO.[54] The stabilisation of the singlet ground state of the B_2 permits back-donation from the triple bond in B_2 into the π* antibonding of CO, allowing both binding and activation of CO akin to transition-metal reactivity.[55] Addition of excess CO to **1-82** affords the homologation product **1-81**.



Scheme 1.17: CO reduction and homologation at a diboryne centre. Dipp = 2,6-di-iso-propyl-phenyl. **1-82** has been drawn as depicted in ref. 52.

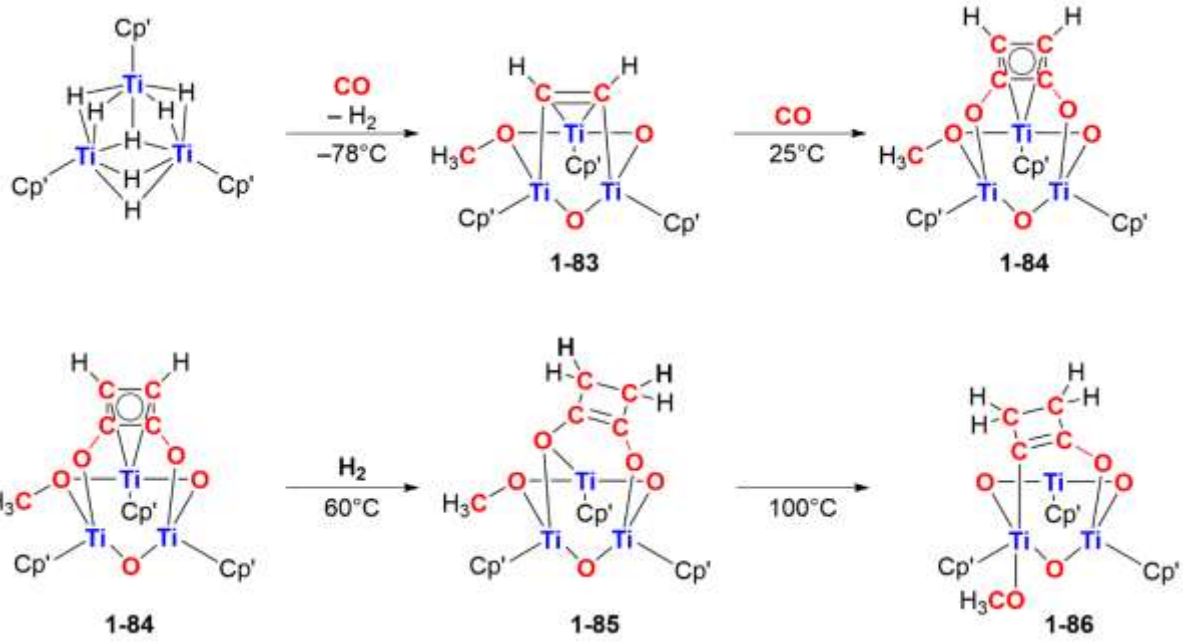
1.5 – Reaction with CO derived carbon chains with H_2

A key aspect of the Fischer-Tropsch reaction is the hydrogenation of carbon chains to form hydrocarbon products. In this reaction, the total deoxygenation of the carbon chain is achieved to liberate alkane chains, along with concomitant formation of water. In the context of Fischer-Tropsch models, however, reactivity of carbon chains directly with dihydrogen is underexplored. Reactive metal hydrides have often used as a surrogate for dihydrogen gas to study the reaction of carbon monoxide with hydrogen under Fischer-Tropsch conditions. This area of research has been reviewed recently and is out of the scope of the introduction to this chapter.[56] Aside from the examples from Peters and Lippard in Section 1.3, only two other examples of the direct reaction of CO derived carbon chains with dihydrogen gas have been reported.

In 2020, Hou and co-workers reported the reductive tetramerisation of CO by a trinuclear titanium heptahydride cluster (Scheme 1.18).[57] While reaction of the cluster with CO resulted in a mixture of products, lowering the temperature to –78°C resulted in the formation of a 1,2-dimetallated ethene moiety **1-83**. The complete deoxygenation of both CO molecules was achieved. **1-83** incorporates a third CO molecule as a bridging methoxy group between two titanium centres.

Stirring **1-83** under an atmosphere of CO at room temperature resulted in the formation of the C_4 complex **1-84**. The C_4 fragment in **1-83** forms a planar four-membered ring. The oxycarbon fragment in **1-84** was assigned as tetranionic fragment in which two negative charges are

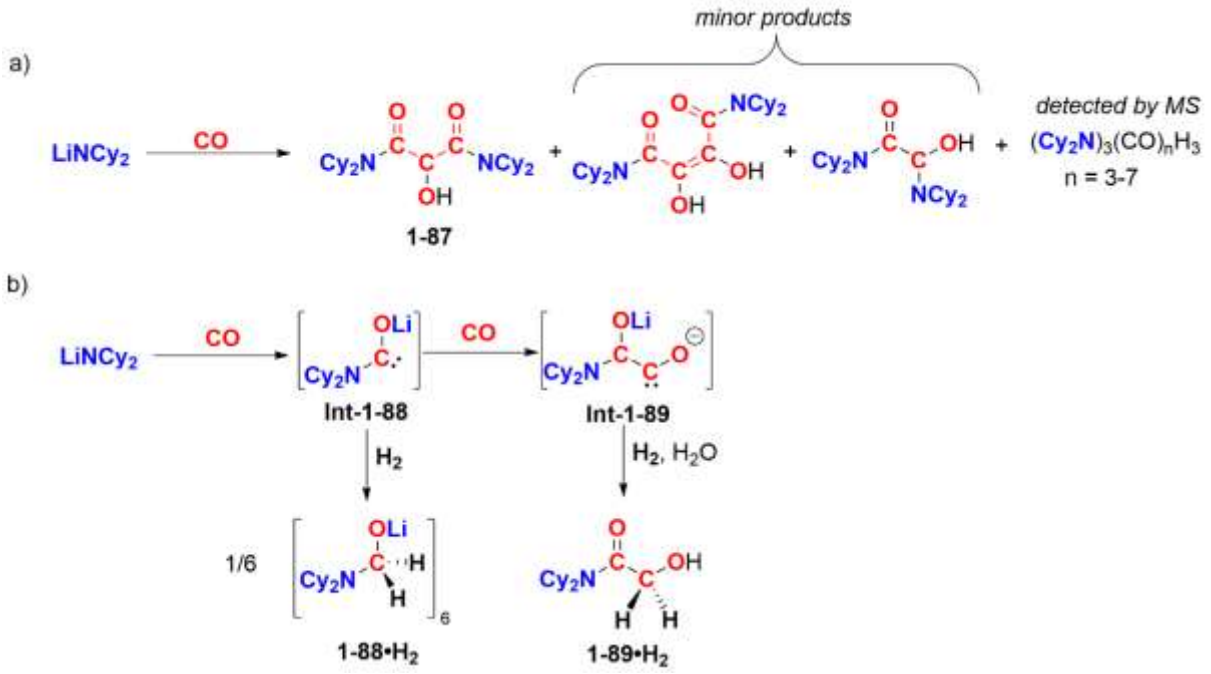
localised on the oxygen atoms, and two negative charges localised onto the C_4 to form a planar, delocalised 6π-electron system. Acidolysis with HCl of **1-84** results in the formation of a γ-butyronlactone and Cp'$TiCl_3$.



Scheme 1.18: Reductive homologation of CO by a trititanium heptahydride complex and subsequent onward reactivity with H_2. Cp' = $C_5Me_4SiMe_3$.

Reaction of **1-84** with dihydrogen at 60°C resulted in the hydrogenation of the C_4 ring to form **1-85**. σ-bond metathesis of the Ti–C bonds in **1-85** and H_2 is proposed as the mechanism of the transformation. The reaction did not liberate the C_4 carbon ring from the titanium centres. Further heating of **1-85** at 100°C resulted in cleavage of one C–O bond to form **1-86**. Acidolysis of **1-86** with HCl afforded cyclobutanone and [(η^5-$C_5Me_4SiMe_3$)$TiCl_3$]

In 2021, Stephan and co-workers reported homologation of CO using lithium dicyclohexylamide.[58] The reaction generated a range of products (Scheme 1.19a), of which **1-87** was formed as the major species in 79% yield. Higher homologues were also isolated as minor products, or detected by mass spectrometry. Performing the reaction under using a mixture of 1:1 CO:H_2 syngas mixture resulted in C_2 homologated products. The reaction was proposed to proceed *via* nucleophilic attack of the amide onto CO which generated a reactive carbene species, **1-88** (Scheme 3.3b). **1-88** can react with an equivalent of H_2 to yield the hexameric alkoxide **1-88•H_2** in <1% yield. Alternatively, **1-88** can react with another equivalent of CO to form C_2 carbene species **1-89•H_2** in 6% yield. Competitive reactions include the direct reaction of [$LiNCy_2$] with CO or H_2 separately. Isotopic labelling showed that both dihydrogen and CO incorporated into the products originate from the gas phase.



Scheme 1.19: Reaction of lithium amides with CO and H_2.

1.6 – Conclusion and outlook

Cooperative strategies have emerged as a key feature in the initiation and propagation events in CO homologation. Using two or more metal centres, the discrete coordination, reduction, and finally C–C bond formation steps can be achieved. In many cases either proposed transition states or intermediates involve the cooperative action of two or more reactive sites with CO. This approach also provides a coordination framework made of multiple sites which can support the growing carbon chain.

The mechanism of any chain growth sequence using CO (or CO_2) as a C_1 building block to form C_n chains can be conceptualised in terms of initiation, propagation, and termination events. In the long term, the detailed understanding of each of these events may allow for the development of methods to convert CO and/or CO_2 to higher-value products with greater selectivity and ultimately pave the way for catalytic methods.

The initial activation of CO often involves the formation of a metal–carbon bond. Formation of the metal–carbon bond occurs most commonly through coordination of CO to a metal-centre. In a number of cases described herein, metal carbonyls have been computationally shown to be key intermediates. Isolable transition metal-carbonyl complexes have also been used as the CO source in homologation strategies. In the latter approach, geometric and electronic restrictions on CO reactivity may provide insight into the C–C bond formation process on heterogeneous F-T catalysts. Geometrically, a cis carbonyl relationship has been observed in numerous systems to be critical in transition-metal mediated chain-growth steps. Electronically, transition-metal

bound CO units are shown to react with low-oxidation state compounds where atmospheric CO is inert.

Following the generation of a reactive organometallic intermediate from CO, the formation of C–C bonds occurs in the propagation stage, resulting in growth of a carbon chain. In almost all studies, this is studied computationally as these reactive intermediates are transient species and only the final chain-growth products are experimentally isolated and characterised.

For the model complexes described herein, the termination of chain-growth usually involves the formation of stable M–O bonds. Comparatively few studies have demonstrated the dissociation of the carbon chain from the metal sites. The onward reaction of the carbon chain and liberation from the metal fragments is essential for the development of catalytic processes. Trialkylsilyl halides have been used as hydrogen surrogates to liberate carbon chains from metal complexes, however only a handful of reactions of CO derived carbon-chains with dihydrogen have been reported to date. A detailed mechanistic understanding of the reactivity of dihydrogen with metal-bound carbon chains is also critical to both developing F-T models, as well as catalytic homogeneous chemistry.

As the field develops, more strategies will arise to couple CO units together at metal centres. The study of these numerous disparate systems will build clearer understanding of CO reactivity. Ultimately this understanding has the potential to culminate in catalytic methodologies where the controlled coupling of CO to value-added products is achieved.

1.7 – References

1 S. S. Ail and S. Dasappa, *Renew. Sust. Energ. Rev.*, 2016, **58**, 267–286.
2 R. B. Anderson, R. A. Friedel and H. H. Storch, *J. Chem. Phys.*, 1951, **19**, 313–319.
3 J. Liebig, *Liebigs Ann.*, 1834, **11**, 182.
4 W. Büchner and E. Weiss, *Helv. Chim. Act.*, 1964, **47**, 1415–1423.
5 W. J. Evans, J. W. Grate, L. A. Hughes, H. Zhang and J. L. Atwood, *J. Am. Chem. Soc.*, 1985, **107**, 3728–3730.
6 W. J. Evans, D. S. Lee, J. W. Ziller and N. Kaltsoyannis, *J. Am. Chem. Soc.*, 2006, **128**, 14176–14184.
7 O. T. Summerscales, F. G. N. Cloke, P. B. Hitchcock, J. C. Green and N. Hazari, *Science*, 2006, **311**, 829–831.
8 O. T. Summerscales, F. G. N. Cloke, P. B. Hitchcock, J. C. Green and N. Hazari, *J. Am. Chem. Soc.*, 2006, **128**, 9602–9603.
9 A. S. Frey, F. G. N. Cloke, P. B. Hitchcock, I. J. Day, J. C. Green and G. Aitken, *J. Am. Chem. Soc.*, 2008, **130**, 13816–13817.
10 N. Tsoureas, O. T. Summerscales, F. G. N. Cloke and S. M. Roe, *Organometallics*, 2013, **32**, 1353–1362.
11 D. McKay, A. S. P. Frey, J. C. Green, F. G. N. Cloke and L. Maron, *Chem. Commun.*, 2012, **48**, 4118–4120.
12 J. Parry, E. Carmona, S. Coles and M. Hursthouse, *J. Am. Chem. Soc.*, 1995, **117**, 2649–2650.

13 W. J. Evans, S. A. Kozimor, G. W. Nyce and J. W. Ziller, *J. Am. Chem. Soc.*, 2003, **125**, 13831–13835.
14 P. L. Arnold, Z. R. Turner, R. M. Bellabarba and R. P. Tooze, *Chem. Sci.*, 2010, **2**, 77–79.
15 S. M. Mansell, N. Kaltsoyannis and P. L. Arnold, *J. Am. Chem. Soc.*, 2011, **133**, 9036–9051.
16 B. M. Gardner, J. C. Stewart, A. L. Davis, J. McMaster, W. Lewis, A. J. Blake and S. T. Liddle, *Proc. Natl. Acad. Sci.*, 2012, **109**, 9265–9270.
17 R. E. LaPointe, P. T. Wolczanski and J. F. Mitchell, *J. Am. Chem. Soc.*, 1986, **108**, 6382–6384.
18 D. R. Neithamer, R. E. LaPointe, R. A. Wheeler, D. S. Richeson, G. D. Van Duyne and P. T. Wolczanski, *J. Am. Chem. Soc.*, 1989, **111**, 9056–9072.
19 G. T. Sazama and T. A. Betley, *Organometallics*, 2011, **30**, 4315–4319.
20 H. R. Sharpe, A. M. Geer, L. J. Taylor, B. M. Gridley, T. J. Blundell, A. J. Blake, E. S. Davies, W. Lewis, J. McMaster, D. Robinson and D. L. Kays, *Nat. Commun.*, 2018, **9**, 3757.
21 M. Ann. Pearsall and Robert. West, *J. Am. Chem. Soc.*, 1988, **110**, 7228–7229.
22 R. Becerra and R. Walsh, *J. Am. Chem. Soc.*, 2000, **122**, 3246–3247.
23 H. Bornemann and W. Sander, *J. Organomet. Chem.*, 2002, **641**, 156–164.
24 C. Ganesamoorthy, J. Schoening, C. Wölper, L. Song, P. R. Schreiner and S. Schulz, *Nat. Chem.*, 2020, **12**, 608–614.
25 D. Reiter, R. Holzner, A. Porzelt, P. Frisch and S. Inoue, *Nat. Chem.*, 2020, **12**, 1131–1135.
26 X. Wang, Z. Zhu, Y. Peng, H. Lei, J. C. Fettinger and P. P. Power, *J. Am. Chem. Soc.*, 2009, **131**, 6912–6913.
27 Y. Wang, A. Kostenko, T. J. Hadlington, M.-P. Luecke, S. Yao and M. Driess, *J. Am. Chem. Soc.*, 2019, **141**, 626–634.
28 Y. Xiong, S. Yao, T. Szilvási, A. Ruzicka and M. Driess, *Chem. Commun.*, 2020, **56**, 747–750.
29 A. V. Protchenko, P. Vasko, D. C. H. Do, J. Hicks, M. Á. Fuentes, C. Jones and S. Aldridge, *Angew. Chem., Int. Ed.*, 2019, **58**, 1808–1812.
30 A. V. Protchenko, K. H. Birjkumar, D. Dange, A. D. Schwarz, D. Vidovic, C. Jones, N. Kaltsoyannis, P. Mountford and S. Aldridge, *J. Am. Chem. Soc.*, 2012, **134**, 6500–6503.
31 X. Guo and Z. Lin, *Inorg. Chem.*, 2021, **60**, 8998–9007.
32 D. H. Berry, J. E. Bercaw, A. J. Jircitano and K. B. Mertes, *J. Am. Chem. Soc.*, 1982, **104**, 4712–4715.
33 P. A. Bianconi, I. D. Williams, M. P. Engeler and S. J. Lippard, *J. Am. Chem. Soc.*, 1986, **108**, 311–313.
34 P. A. Bianconi, R. N. Vrtis, C. Pulla. Rao, I. D. Williams, M. P. Engeler and S. J. Lippard, *Organometallics*, 1987, **6**, 1968–1977.
35 R. N. Vrtis and S. J. Lippard, *Isr. J. Chem.*, 1990, **30**, 331–341.
36 R. N. Vrtis, C. Pulla. Rao, Steve. Warner and S. J. Lippard, *J. Am. Chem. Soc.*, 1988, **110**, 2669–2670.
37 J. D. Protasiewicz and S. J. Lippard, *J. Am. Chem. Soc.*, 1991, **113**, 6564–6570.
38 F. Calderazzo, U. Englert, A. Guarini, F. Marchetti, G. Pampaloni and A. Segre, *Angew. Chem., Int. Ed.*, 1994, **33**, 1188–1189.
39 F. Calderazzo, U. Englert, A. Guarini, F. Marchetti, G. Pampaloni, A. Segre and G. Tripepi, *Chem. Eur. J.*, 1996, **2**, 412–419.
40 D. L. M. Suess and J. C. Peters, *J. Am. Chem. Soc.*, 2013, **135**, 12580–12583.
41 J. A. Buss and T. Agapie, *Nature*, 2016, **529**, 72–75.
42 J. A. Buss and T. Agapie, *J. Am. Chem. Soc.*, 2016, **138**, 16466–16477.
43 R. Yadav, T. Simler, M. T. Gamer, R. Köppe and P. W. Roesky, *Chem. Commun.*, 2019, **55**, 5765–5768.
44 B. B. Wayland, A. E. Sherry and V. L. Coffin, *J. Chem. Soc., Chem. Commun.*, 1989, 662–663.
45 W. Lu, H. Hu, Y. Li, R. Ganguly and R. Kinjo, *J. Am. Chem. Soc.*, 2016, **138**, 6650–6661.
46 B. Wang, G. Luo, M. Nishiura, Y. Luo and Z. Hou, *J. Am. Chem. Soc.*, 2017, **139**, 16967–16973.
47 B. Wang, X. Kang, M. Nishiura, Y. Luo and Z. Hou, *Chem. Sci.*, 2015, **7**, 803–809.
48 K. Yuvaraj, I. Douair, A. Paparo, L. Maron and C. Jones, *J. Am. Chem. Soc.*, 2019, **141**, 8764–8768.
49 K. Yuvaraj, I. Douair, D. D. L. Jones, L. Maron and C. Jones, *Chem. Sci.*, 2020, **11**, 3516–3522.

50 A. Paparo, K. Yuvaraj, A. J. R. Matthews, I. Douair, L. Maron and C. Jones, *Angew. Chem., Int. Ed.*, 2021, **60**, 630–634.
51 M. Majumdar, I. Omlor, C. B. Yildiz, A. Azizoglu, V. Huch and D. Scheschkewitz, *Angew. Chem., Int. Ed.*, 2015, **54**, 8746–8750.
52 H. Braunschweig, T. Dellermann, R. D. Dewhurst, W. C. Ewing, K. Hammond, J. O. C. Jimenez-Halla, T. Kramer, I. Krummenacher, J. Mies, A. K. Phukan and A. Vargas, *Nat. Chem.*, 2013, **5**, 1025–1028.
53 H. Braunschweig, R. D. Dewhurst, F. Hupp, M. Nutz, K. Radacki, C. W. Tate, A. Vargas and Q. Ye, *Nature*, 2015, **522**, 327–330.
54 N. Holzmann, M. Hermann and G. Frenking, *Chem. Sci.*, 2015, **6**, 4089–4094.
55 H. Zhang, Z. Cao, W. Wu and Y. Mo, *Angew. Chem., Int. Ed.*, 2018, **57**, 13076–13081.
56 N. M. West, A. J. M. Miller, J. A. Labinger and J. E. Bercaw, *Coord. Chem. Rev.*, 2011, **255**, 881–898.
57 S. Hu, T. Shima and Z. Hou, *J. Am. Chem. Soc.*, 2020, **142**, 19889–19894.
58 M. Xu, Z. Qu, S. Grimme and D. W. Stephan, *J. Am. Chem. Soc.*, 2021, **143**, 634–638.

Chapter 2

CO Homologation with an Aluminium(I) Reductant: from C_1 to C_4 Chains

2.1 – Introduction to reagents

2.1.1 – Aluminium(I) compounds

Aluminium is the third most abundant element in the Earth's crust. It is typically found in the +3 oxidation state both in minerals and molecular compounds. In the latter case, aluminium(III) compounds are well known as potent Lewis acids and are frequently used as additives in catalysis.

Molecular aluminium compounds in the +1 oxidation state which are stable at room temperature have been known since Schnöckel's seminal synthesis of $[Cp^*Al]_4$ (Figure 2.1).[1] Schnöckel and co-workers synthesised $[Cp^*Al]_4$ from a metastable solution of the aluminium(I) chloride AlCl *via* salt metathesis with KCp^*.[2] Since this discovery, several other aluminium(I) species have been reported. The synthesis of anionic aluminium(I) compounds has also been pioneered within the last decade.[3–7] In addition, a cAAC-stabilised aluminium(I) hydride[8] and dimeric aluminium (I) species have been reported recently.[37,38] The synthesis and reactivity of these compounds has been reviewed extensively in recent years.[9–12]

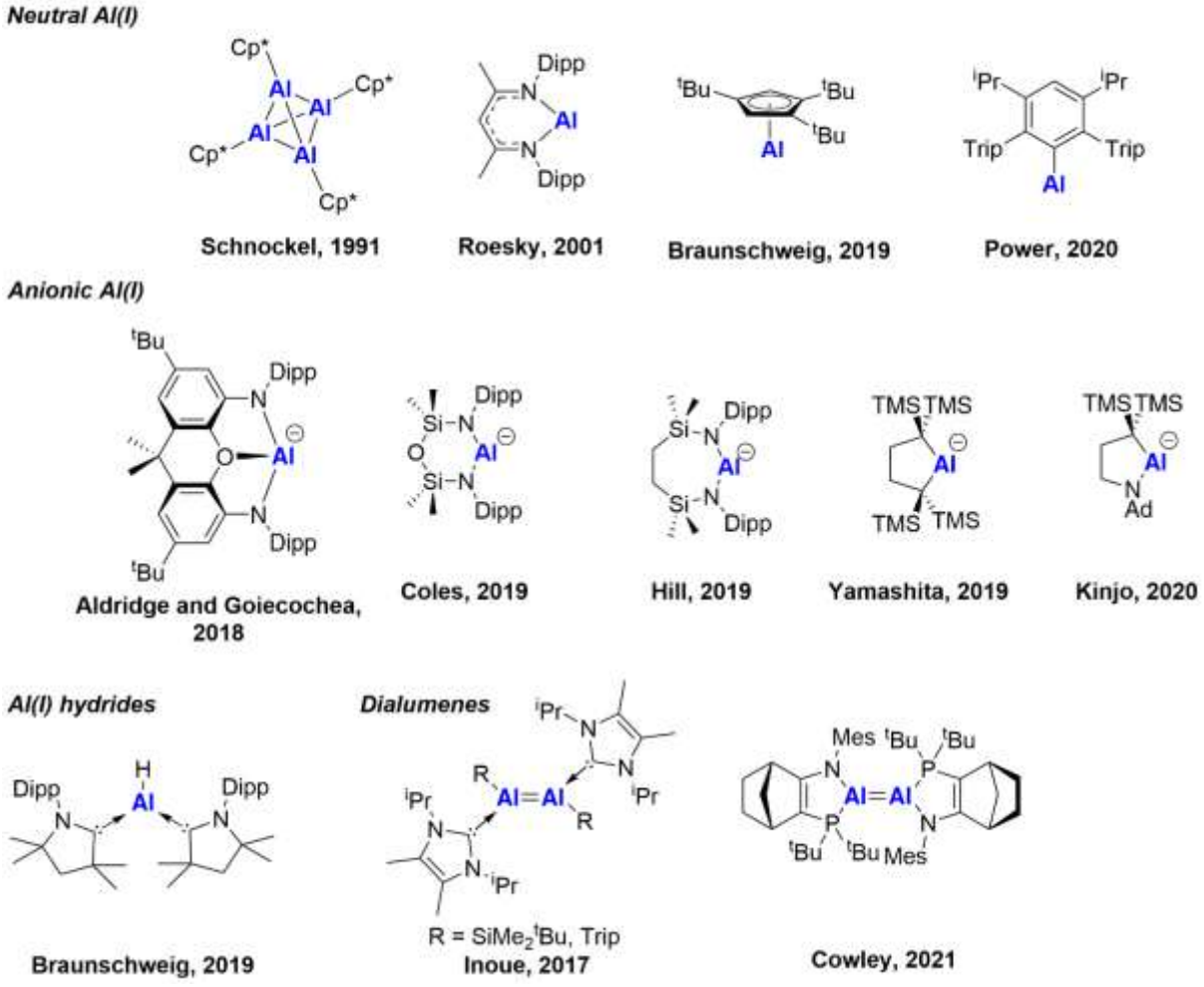
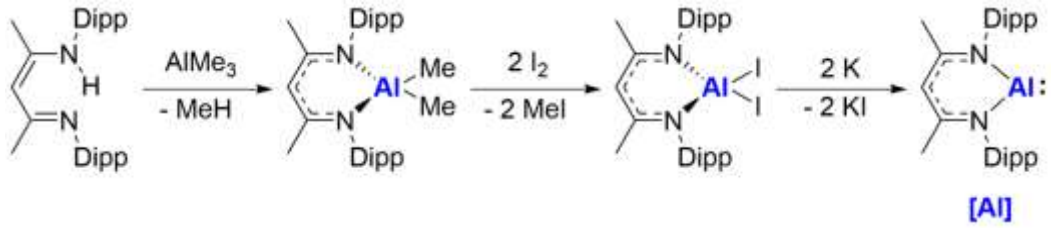


Figure 2.1: Isolated aluminium(I) compounds. Dipp = 2,6-di-iso-propylphenyl. Trip = 2,4,6-tri-iso-propylphenyl.

The reactivity of aluminium(I) reagents is dominated by their reducing power. Reactions of aluminium(I) compounds typically proceed *via* the transfer of two electrons from the aluminium(I) complex to the substrate. Accordingly, the oxidative addition of a range of σ-bonds has been observed at aluminium(I) centres.[9-12, 17] Aluminium(I) has further been shown to react with π-bonds in a pericyclic manner to furnish metallacycles.[4,13–15]

The aluminium(I) reagent used in this thesis was originally synthesised by Roesky and co-workers in 2001 (**[Al]**, Scheme 2.1).[16] It is a monomeric aluminium(I) reagent which is isolable as a crystalline solid. The high reactivity of this compound is associated with its ambiphilicity: a highly reducing lone-pair is complemented by a vacant p-orbital on the aluminium centre. An isoelectronic and isolobal analogy can be drawn between **[Al]** and the well-known class of N-heterocyclic carbene compounds. Oxidative cleavage of a series of σ-bonds has been demonstrated using **[Al]** and this reactivity has been reviewed in depth in the last five years.[10,17]



Scheme 2.1: Synthesis of **[Al]**.

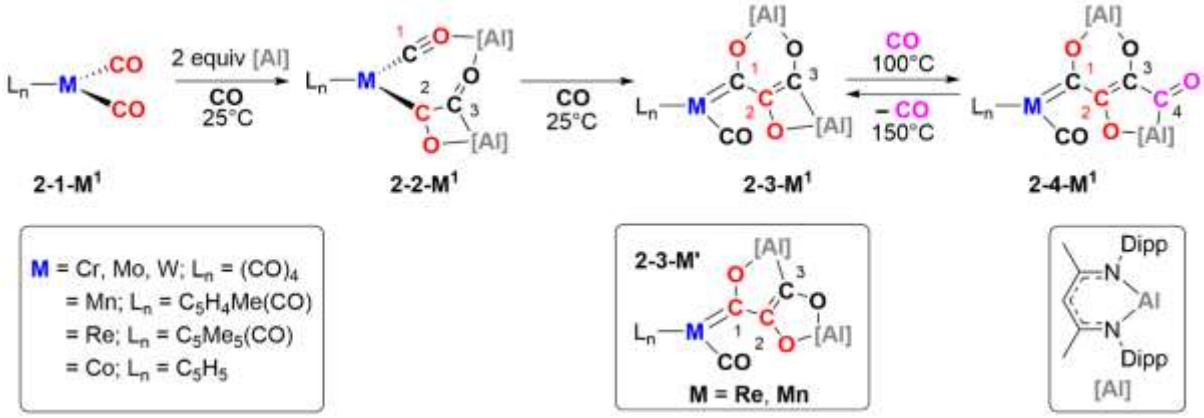
Despite the high reducing power of **[Al]**, its reactivity with carbon monoxide has not been reported. This chapter examines the reactivity of **[Al]** with CO gas, in the presence of a transition metal carbonyl. A cooperative strategy in which **[Al]** reacts exclusively with a transition-metal bound CO fragment unlocks previously unobserved CO homologation chemistry. Variation of the transition metal identity allowed some degree of control of the reaction rate, and products. Isolation of 2-,3- and 4-carbon chains provided a complete picture of C_1 metal carbonyl to C_4 carbon chain growth. The mechanism was investigated using a combination of DFT and isotopic ^{13}CO labelling experiments.

2.2 – Results and discussion

2.2.1 – Homologation to C^2, C^3 and C^4 chains

Reaction of **[Al]** with a series of group 6-9 metal carbonyl complexes in the presence of CO was investigated (Scheme 2.2). The transition metal complexes were selected based on an 18-electron configuration and low-spin electronic structure. In addition, a *cis*-dicarbonyl motif was considered an essential reactive component for chain growth.

These reactions allowed the isolation of a series of heterometallic products incorporating C_2, C_3 or C_4 chains derived from a 2:1 stoichiometry of **[Al]** : **2-1-M**. The aluminium(I) complex **[Al]** acts as a formal 2-electron reductant in these reactions transferring a total of 4-electrons to the CO derived ligand in the chain growth process. Most notably modification of the electronics at the transition metal appears, qualitatively, to influence the reaction rate of each chain growth step, allowing isolation of an unusual C_2 intermediate. Hence while reaction of **2-1-Cr**, **2-1-Mo**, **2-1-W**, or **2-1-Co** with **[Al]** under CO (1 atm.) led directly to the C_3 products **2-3-Cr**, **2-3-Mo**, **2-3-W**, and **2-3-Co** at 25 °C, in the case of **2-1-Mn** conversion to the C_2 homologue **2-2-Mn** was achieved. **2-2-Mn** could be isolated and shown to convert to **2-3-Mn** under an atmosphere of CO at 25 °C. A minor isomeric product tentatively assigned as **2-3-Mn'** was observed alongside **2-3-Mn** in crude reactions mixtures. **2-3-Mn** and **2-3-Mn'** formed in a 9:1 ratio and likely co-crystallise based on disorder within the crystallographic data. Reaction of **[Al]** with $[Co_2(CO)_8]$ or $[Fe(CO)_5]$ did not result in any isolable products which contained carbon-chains derived from CO. Similarly, reaction of **2-1-M** with an isoelectronic gallium(I) β-diketiminate[18] or silicon(II) β-diketiminate[19] did not result in any products which contained carbon-chains derived from CO.



Scheme 2.2: Synthesis of C_2 to C_4 carbon chains from C_1 metal carbonyls. Dipp = 2,6-di-isopropylphenyl.

The reaction of **2-1-Re** with CO formed a 3 : 1 mixture of two products from CO homologation, the expected product **2-3-Re** which contained a [6,4]-fused ring system, alongside **2-3-Re'** an isomer with a [5,5]-fused ring system (Scheme 2.2). The ratio of **2-3-Re** : **2-3-Re'** was unaffected by heating for 18 h at 100 °C and current evidence suggests that these species do not interconvert.

Under more forcing conditions (1 atm., 100 °C), **2-3-Cr**, **2-3-Mo**, **2-3-W**, **2-3-Mn**, **2-3-Re**, and **2-3-Co** could all be converted to the C_4 products **2-4-Cr**, **2-4-Mo**, **2-4-W**, **2-4-Mn**, **2-4-Re**, and **2-4-Co** respectively. These reactions were found to be reversible and at elevated temperatures (100 – 150 °C) under a nitrogen atmosphere the de-insertion of CO was observed by ^{1} spectroscopy. Mixtures of **2-3-Re : 2-3-Re'** reacted selectively to form **2-4-Re**. Only **2-3-Re** was consumed in

this reaction suggesting that the strained [4,6] fused ring system is more labile than the [5,5] isomer. **2-4-Re** could be selectively crystallised allowing separation from **2-3-Re'**. Subsequent heating of **2-4-Re** under a N_2 atmosphere to effect CO de-insertion allowed the synthesis of a pure sample of **2-3-Re**.

	2-3-Cr	**2-3-Mo**	**2-3-W**	**2-3-Mn**	**2-3-Re**	**2-3-Re'**	**2-3-Co**
C^1 (ppm)	314.6	305.7	288.6[a]	311.7	265.0	273.0	-
C^2 (ppm)	169.2	170.6	172.4[a]	166.7	170.5	178.5	-
C^3 (ppm)	-	-	176.5[a]	-	-	-	-

Table 2.1: Key ^{13}C NMR resonances of chain positions in **2-3**. [a] Attained from a ^{13}C labelled sample.

In C_6D_6 solution, **2-2-Mn** displays ^{13}C NMR resonances for the carbonyl and isocarbonyl ligands at δ = 236.8 and 189.5 ppm respectively, along with diagnostic resonances for the C_2 ligand fragment at δ = 249.2 and 167.2 ppm. In the solid-state, the IR spectrum of **2-2-Mn** shows an absorption at 1921 cm^{-1} assigned to CO vibration of the carbonyl. The C_3 homologation products, **2-3-Cr, 2-3-W, 2-3-Mn, 2-3-Re** and **2-3-Co** are characterised by diagnostic ^{13}C resonances ranging from δ = 265 – 315 ppm and 169 – 172 ppm for the C^1 and C^2 positions respectively (Table 2.1). The largest variation in these data across the series is seen for the C^1 position as it is connected directly to the transition metal fragment and influenced by the nature of the M–C^1 bond. Chemical shifts of the C^2 position are insulated from the transition metal fragment and vary little across the series. In nearly all cases the quadrupolar broadening associated with the ^{27}Al nucleus prevents identification of the C^3 resonance. Despite the different topologies chemical shifts of the C^1 and C^2 position of **2-3-Re** and **2-3-Re'** are similar. The synthesis of ^{13}C enriched isotopomers of **2-3-W** was also achieved and these compounds allowed aspects of the J coupling in the carbon chain to be resolved and the C^3 resonance to be unambiguously identified. Hence, ^{13}CO enriched **2-3-W** in which all 3 positions are labelled shows the C^3 resonance at δ = 176.5 ppm. The coupling constants in the chain were determined as $^1J_{C2-C3}$ = 41.8 Hz, $^1J_{C1-C2}$ = 37.1 Hz, along with $^1J_{W-C1}$ = 102 Hz determined from natural abundance satellites of ^{183}W (Figure 2.2, see Section 2.4.2 for further details).

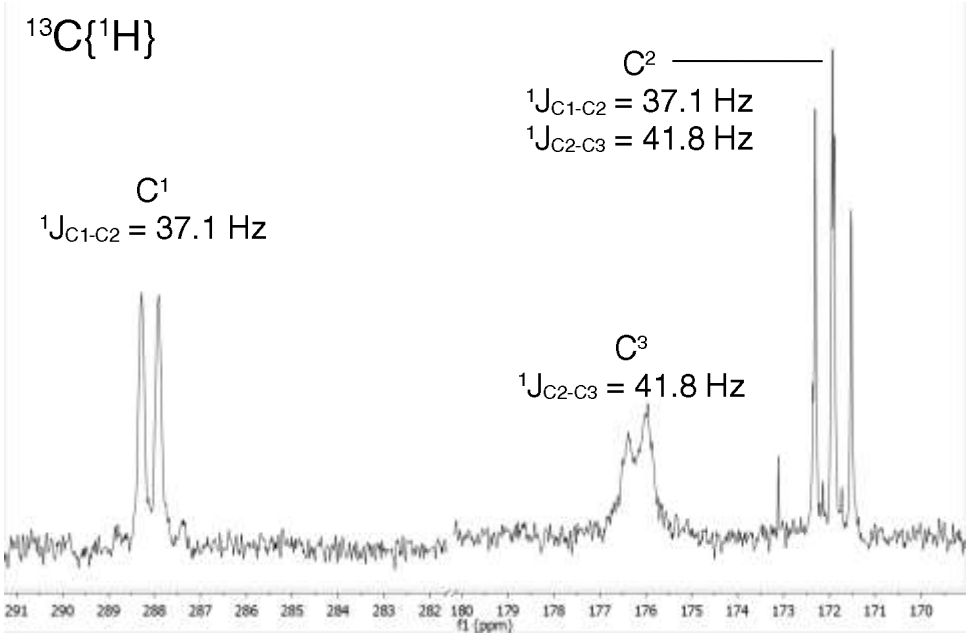


Figure 2.2: $^{13}C\{^{1}H\}$ NMR of ^{13}C labelled **2-3-W**.

The C_4 homologation products, **2-4-W, 2-4-Mn** and **2-4-Re** are characterised by diagnostic ^{13}C resonances for the C^1, C^2, and C^3 positions which range from δ = 281 – 349 ppm, 161 – 169 ppm, and 135 – 145 ppm respectively (Table 2.2). The ^{13}C NMR of ^{13}C enriched samples of **2-4-W** provide ^{13}C–^{13}C coupling constants of the carbon chain with $^{1}J_{C1\text{-}C2}$ = 35.8 Hz, $^{1}J_{C3\text{-}C4}$ = 27.4 Hz, and $^{2}J_{C2\text{-}C4}$ = 9.1 Hz. The coupling from W to the C^1 position of **2-4-W** is $^{1}J_{W\text{–}C1}$ = 109 Hz and is similar to the value observed in **2-3-W**, suggesting little change in the nature of the carbene ligand on elongation of the carbon chain from C_3 to C_4.

	2-4-Cr	**2-4-Mo[a]**	**2-4-W**	**2-4-Mn**	**2-4-Re**	**2-4-Co**
C^1 (ppm)	348.4	348.8	329.2[a]	332.3	280.6	-
C^2 (ppm)	160.8	161.7	164.6[a]	160.7	169.1	163.5
C^3 (ppm)	140.1	144.7	135.3[a]	135.7	144.5	137.3
C^4 (ppm)	-	-	260.6[a]	-	-	-

Table 2.2: Key ^{13}C NMR resonances of chain positions in **2-4**. [a] Attained from a ^{13}C labelled sample.

The X-ray structure of **2-2-Mn** incorporates a [7,4] ortho-fused ring system (Figure 2.3). Bond lengths and angles at the main group fragments support the assignment of an aluminium +3 oxidation state.[16] The 7-membered ring system incorporates both Mn and Al centres along with the C_2 fragment and iso-carbonyl ligand. The C^1---C^2 distance is 2.633(7) Å and the system is pre-organised for carbon–carbon bond formation through ring contraction. The C^1–O^1 bond length of 1.209(6) Å of the iso-carbonyl ligand is ~0.1 Å longer than the terminal carbonyl of 1.097(8) Å. The C_2 fragment is bound to Mn through a short Mn–C^2 bond of 1.971(5) Å. The C^2–

C^3 distance of 1.481(7) Å is beyond that expected for a C=C bond. Similarly, the C^2–O^2 bond of 1.500(6) Å is long. Both these bond lengths shorten on forming the ring contraction product **2-3-Mn**. While the C^3–O^3 bond length remains near constant in **2-2-Mn** and **2-3-Mn** taking values of 1.365(5) and 1.364(4) Å, the Al–C^3 length is ~0.1 Å shorter in **2-2-Mn** than **2-3-Mn** and the O^2–Al–C^2 angle is more obtuse. Both the lengthening of the C≡O bond and the unusual bonding features of the C_2 fragment are consistent with electron transfer from Al to CO on reaction of **2-1-Mn**. For comparison, $\{C_2O_2\}^{2-}$ 'zig-zag' intermediates have been proposed in the formation $\{C_2O_2\}^{2-}$ ethynediolate and $\{C_3O_3\}^{2-}$ deltate complexes from reaction of CO with uranium(III) and magnesium(I) compounds (see Chapter 1).[20] While neither isolated nor spectroscopically characterised, these species have been inferred by DFT studies. The C_2 fragment of **2-2-Mn** is distinct from these proposed zig-zag intermediates; the C_2 ligand in **2-2-Mn** shows considerable asymmetry and a unique elongated C–O bond that strongly suggests a distinct electronic structure.

	2-Mn	**2-3-Cr**	**2-3-Mo[a]**	**2-3-W**	**2-3-Mn**	**2-3-Re**	**2-3-Re'**	**2-3-Co**
M–C^1	1.742(6)	2.055(3)	2.250(4)	2.195(3)	1.922(3)	2.019(6)	2.015(4)	1.810(2)
M=C^2	1.971(5)	–	–	–	–	–	–	–
C^1---C_2	2.633(7)	1.445(4)	1.428(6)	1.437(4)	1.454(5)	1.482(9)	1.485(6)	1.447(3)
C^2=C^3	1.481(7)	1.375(4)	1.399(6)	1.379(4)	1.386(5)	1.382(10)	1.372(7)	1.380(3)
C^1–O^1	1.209(6)	1.335(3)	1.337(5)	1.337(3)	1.353(4)	1.366(8)	1.344(6)	1.353(3)
C^2–O^2	1.500(6)	1.412(3)	1.403(5)	1.409(3)	1.418(4)	1.410(9)	1.375(5)	1.409(3)
C^3–O^3	1.365(5)	1.362(3)	1.328(5)	1.360(3)	1.364(4)	1.321(9)	1.383(6)	1.371(3)
Al–C	1.843(4)	1.979(3)	1.977(4)	1.982(3)	1.942(3)	1.993(8)	1.953(5)	1.946(2)
O–Al–C	82.25(19)	73.89(10)	74.82(16)	74.13(11)	75.37(13)	73.4(3)	90.02(19)	75.50(9)

Table 2.3: Structural metrics of **2-2**, and **2-3**. All distances are in Å and angles are in °. [a] two molecules are in the asymmetric unit of the crystal structure, data listed here provided for the molecule suffixed "B".

With the exception of the transition metal fragment, the solid-state structures of **2-3** and **2-4** vary only slightly within their series. Key bonding metrics for both the C_3 and C_4 carbon chains are consistent, within error, across every single crystal X-ray diffraction study reported herein. **2-3** possesses an *ortho*-fused [6,4] ring system derived from contraction of the [7,4] system in **2-2**, while **2-4** contains a [6,5] ring system. The side product **2-3-Re'** contains a [5,5] *ortho*-fused ring system. In all cases, the carbon atoms of both the C_3 and C_4 carbon chains are close to idealised sp^2 hybridised. The C^1–C^2 and C^2–C^3 bond lengths of **2-3** range from 1.427(6) – 1.482(9) and 1.375(4) – 1.399(6) Å respectively, those for **2-4** are similar. In combination with the C^3–C^4 lengths of **2-4** which vary from 1.486(7) – 1.510(5) Å, the data are consistent with an alternating array of C–C and C=C bonds in the carbon chains.

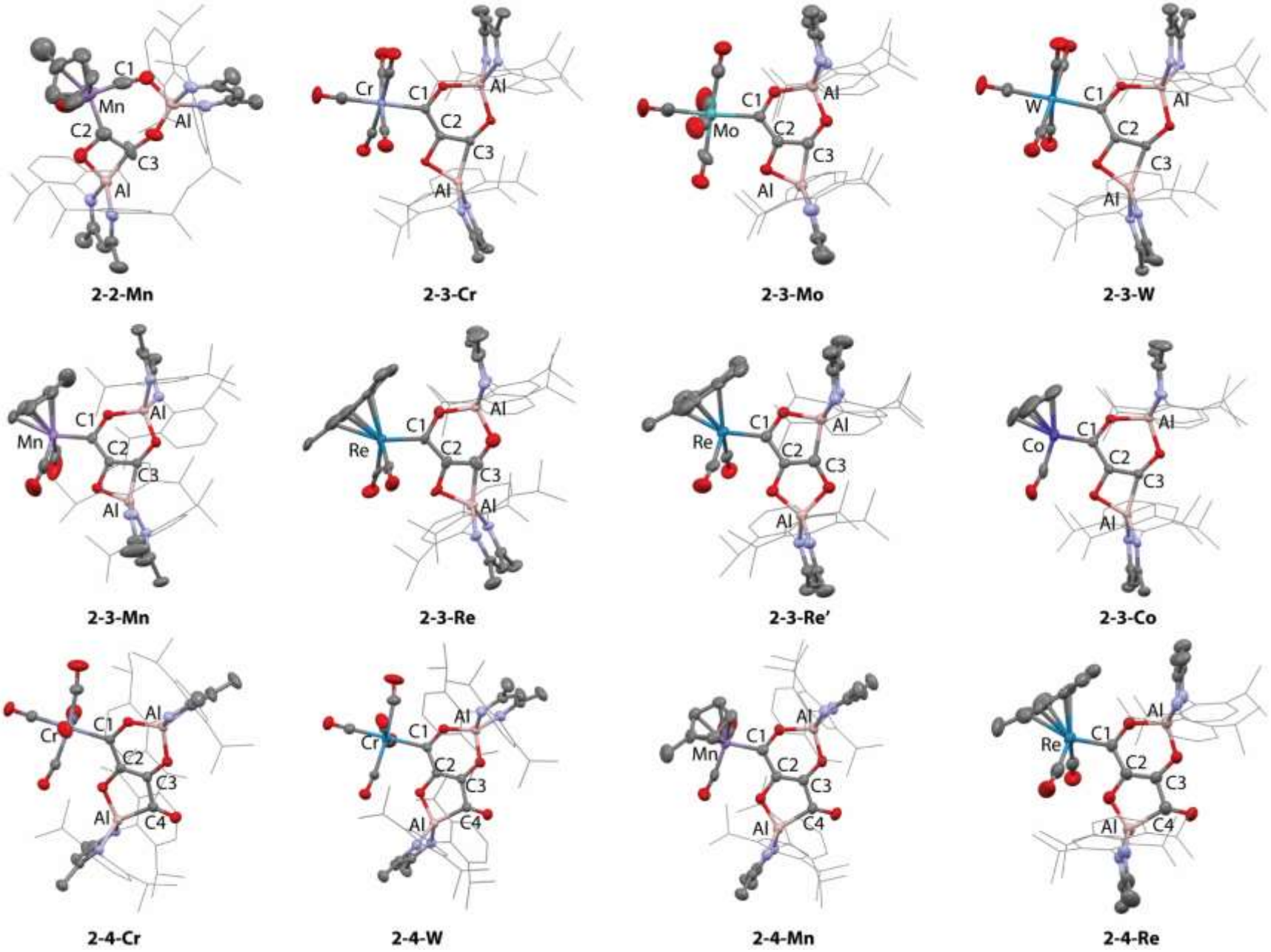


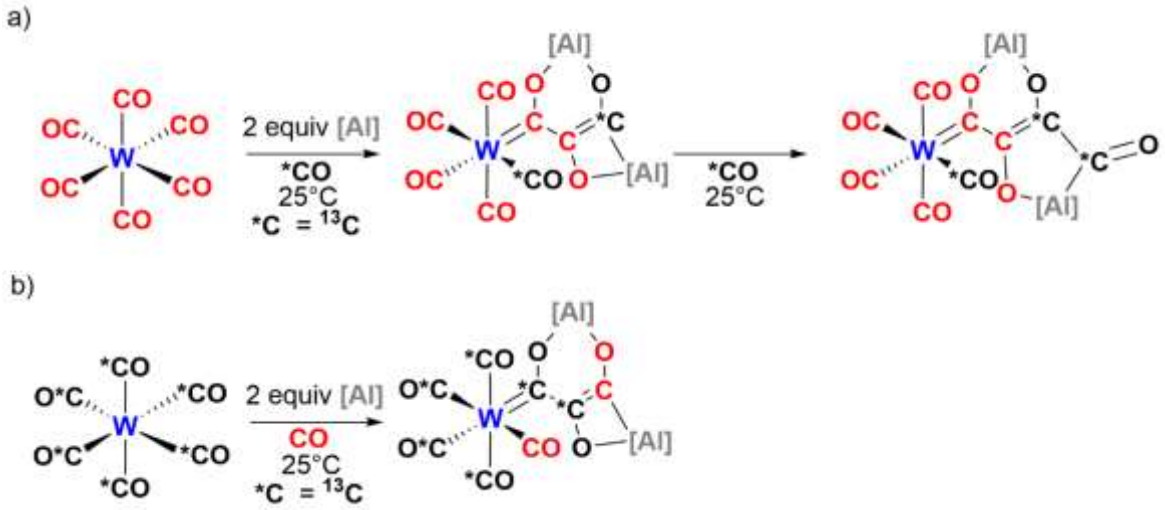
Figure 2.3: X-ray crystal structures of **2-2**, **2-3**, and **2-4**.

The C^1–O^1, C^2–O^2 and C^3–O^3 bond lengths of **2-3** and **2-4** range from approximately 1.3 to 1.4 Å and are consistent their assignment as C–O bonds, while the C^4–O^4 distances of **2-4** are shorter at 1.228(5) – 1.246(6) Å and assigned as C=O bonds. The bond lengths in **2-3-Re** and **2-3-Re'** are remarkably similar, despite the isomerisation of the [6,4] to a [5,5] ring system, the major difference is expansion of the O–Al–C angle from 73.4(3) to 90.02(19) °. It should be noted, that despite these metrics, the localised resonance structures are an imperfect description as there is the potential for delocalisation of electrons within the $\{C_3O_3\}^{4-}$ and $\{C_4O_4\}^{4-}$ units. Of the data considered only the M–C^1 distance shows any real variation across the series. Nevertheless, comparison of **2-3-W** with **2-4-W**, **2-3-Re** with **2-4-Re**, and **2-3-Mn** with **2-4-Mn** shows that there is no change in this bond length, within error, on elongation of the carbon chain from C_3 to C_4. This observation is consistent with NMR data and the insensitivity of the $^1J_{W-C1}$ coupling constants to chain length. Moreover, when considering **2-3-Cr**, **2-3-W**, **2-3-Mo, 2-3-Mn**, **2-3-Re**, and **2-3-Co** if the covalent radii of the transition metal are factored in, the normalised M–C^1 bond lengths are remarkably similar with a slight contraction occurring across the period (group 8 < group 7 < group 6, see Section 2.5.1 for further detail).

	2-4-Cr	**2-4-Mo**	**2-4-W**	**2-4-Mn**	**2-4-Re**
M=C^1	2.084(4)	2.231(2)	2.233(4)	1.902(4)	2.030(4)
C^1–C^2	1.474(5)	1.466(4)	1.457(5)	1.499(6)	1.497(6)
C^2=C^3	1.374(5)	1.396(3)	1.396(5)	1.391(6)	1.407(7)
C^3–C^4	1.510(5)	1.499(4)	1.507(5)	1.486(7)	1.494(7)
C^1–O^1	1.322(4)	1.322(3)	1.322(5)	1.334(6)	1.330(6)
C^2–O^2	1.370(4)	1.375(3)	1.373(5)	1.368(6)	1.372(6)
C^3–O^3	1.335(4)	1.337(3)	1.334(5)	1.348(6)	1.353(6)
C^4–O^4	1.246(5)	1.229(3)	1.233(5)	1.228(5)	1.246(6)
Al–C	1.990(4)	2.002(3)	1.996(4)	2.010(5)	1.990(5)
O–Al–C	90.19(14)	90.83(10)	90.37(15)	89.81(17)	91.16(18)

Table 2.4: Structural metrics for **2-4**.

2.2.2 – Labelling Studies



Scheme 2.3: ^{13}C labelling studies on the reaction between [Al], CO, and $[W(CO)_6]$

A series of isotopic labelling experiments were conducted with ^{13}CO gas and ^{13}C labelled $[W(CO)_6]$ (Scheme 2.3). These reactions showed that the first two carbon units of the chain, C^1 and C^2, are derived from the transition metal carbonyl fragment, while the second two units, C^3 and C^4, originate from gaseous CO. Hence, reaction of **[Al]** with $[W(^{12}CO)_6]$ in the presence of ^{13}CO forms labelled samples of **2-3-W** in which isotopic enrichment at the chain terminus (C^3) and the *cis*-position of the transition metal complex is observed, as evidenced by ^{13}C NMR spectroscopy. Isotopic enrichment of the transition metal carbonyl fragment is consistent with a mechanism in which following initiation of chain growth, any coordination sites which ^{12}CO vacates are occupied by external ^{13}CO. Reaction of a sample of **2-3-W** labelled at the C^3 position with ^{13}C with ^{13}CO forms **2-4-W** with ^{13}C enrichment at the C^4 position. The source of each carbon atom in the chain was unambiguously confirmed by performing a series of reactions with $[W(^{13}CO)_6]$ and **[Al]** in the presence of ^{12}CO (See Section 2.4.3 for further details).

2.2.3 – Electronic structure of 2-2-Mn, 2-3-Mn and 2-4-Mn

Members of the manganese series (**2-2-Mn**, **2-3-Mn**, and **2-4-Mn**) were interrogated by DFT calculations. Geometries were optimised in the gas-phase using the ωB97x functional with a split 6-31G**(C, H, N, O)/SDDAll (Al, Mn) basis set. These calculations provide insight into the electronic structure of the carbon-chain, how this responds to the number of carbon atoms, and how the carbon chain interacts with the transition metal and main group centres.

NBO calculations (version 6.0) show that the primary interaction between the carbon chains and aluminium atoms is ionic. The natural population analysis (NPA) charges across all Al sites in **2-2-Mn**, **2-3-Mn**, and **2-4-Mn** range from +2.02 to +2.25. The ionic component to the bonding

is further reflected in the large charge localisation on oxygen (–0.86 to –1.05) and carbon (–0.48 to –0.04) atoms directly connected to Al in these complexes. These data are consistent with assignment of a formal +3 oxidation state to aluminium and consideration of the chain as a $\{C_nO_n\}^{4-}$ fragment. For **2-3-Mn** and **2-4-Mn**, the Wiberg Bond Indices (WBI) between the C–C (C^1–C^2 = 1.07, 1.09; C^2–C^3 = 1.55, 1.57; C^3–C^4 = 1.03) and C–O (C^1–O^1 = 1.14, 1.18; C^2–O^2 = 0.96, 1.02; C^3–O^3 = 1.03, 1.04; C^4–O^4 = 1.76) atoms of the $\{C_nO_n\}^{4-}$ chain reflect the alternating array of single and double bonds suggested by the solid-state structures. While these data hint at a degree of delocalisation of electron density across the 4-, 5- and 6-membered rings of **2-3-Mn** and **2-4-Mn**, NICS(0) calculations show that these ring systems are non-aromatic (See Section 2.6.6).

The relatively large WBI for the C^1–C^2 and C^1–O^1 units of **2-3-Mn** and **2-4-Mn** warrants further comment but requires consideration of the nature of M=C^1 bond to explain. The manganese centre of these complexes bears a slight negative charge (–0.34) while the adjacent carbon atom C^1 is electropositive (+0.40,+0.42). The calculated WBI for the bond between Mn and C^1 (0.83) is slightly smaller than that to the carbon atom of the terminal carbonyl ligand (0.95–0.99). The data vary little between **2-3-Mn** and **2-4-Mn** and along with the nominal changes in M=C^1 bond length and $^1J_{W-1C}$ coupling constant strongly suggest that the metal-ligand interaction in these complexes is very similar. ETS-NOCV calculations reveal two primary components to the M=C^1 interaction of **2-3-Mn** comprised of σ-donation from a filled C^1-based orbital to the metal (ρ_1, along with π-backdonation from a metal d-orbital to C^1 (Figure 3a) In combination the data allow the assignment of the carbon-chain of **2-3-Mn** and **2-4-Mn** as a metallocarbene ligand.

Charge localisation on Mn, along with the large C^1–O^1 and C^1–C^2 WBIs can be rationalised by a series of zwitterionic resonance structures, reminiscent of those commonly invoked for Fischer carbenes (Figure 2.4b). The electronic structure of **2-2-Mn** is more complex. While variable temperature NMR data suggests that **2-2-Mn** may undergo a fluxional rearrangement in solution (*vide infra*), there is no evidence this species is paramagnetic. The calculated singlet-triplet gap for **2-2-Mn** is 38.0 kcal mol^{-1} – while such values are known to be functional dependent, the data strongly suggest a singlet ground state. The Mn–C^2 WBI in **2-2-Mn** (0.58) is notably lower than the Mn–C^1 values in **2-3-Mn** and **2-4-Mn**. In combination with the large C^2–C^3 WBI (1.79) and increased charge accumulation on C^2 (+0.15) and C^3 (–0.48) in this complex relative to **2-3-Mn** and **2-4-Mn**, these calculations suggest a unique electronic structure of **2-2-Mn** with the C_2 ligand adopting some vinyl character. ETS-NOCV calculations support this assertion and capture only a σ-component to the bonding with no clear π-backdonation from the metal to C^2 (supporting information). The WBIs calculated for the isocarbonyl fragment

suggest a lengthened C=O bond (1.38) and compressed M=C bond (1.52) relative to the terminal CO ligand as is typical of bridging isocarbonyl fragments.

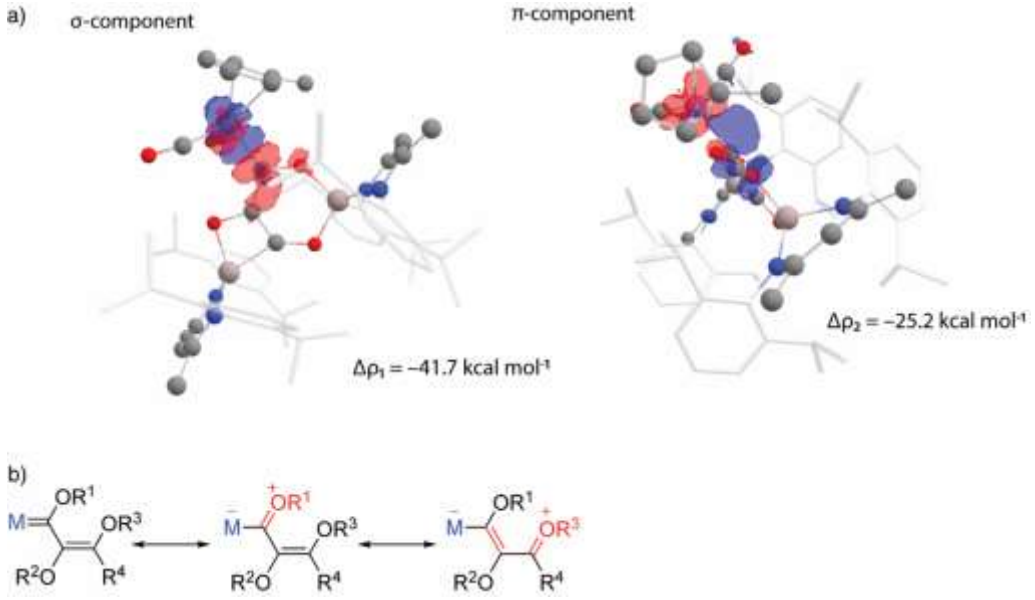


Figure 2.4: a) ETS-NOCV calculations on **2-3-Mn** showing principle components $\Delta\rho_1$ and $\Delta\rho_1$ of ΔE_{orb}. (b) Simplified resonance structures for neutral and zwitterionic bonding components of **2-3-M**.

2.2.4 – Mechanism of the formation 2-2-Mn, 2-3-Mn, 2-3-Mn' and 2-4-Mn

Experiments using ^{13}C labelled materials [$W(^{13}CO)_6$] and ^{13}CO showed that the first two carbon atoms of **2-4** (C^1 and C^2) derive from the transition metal carbonyl, while the second two carbon atoms (C^3 and C^4) derive from atmospheric CO. Further, these labelling experiments reveal that an additional equivalent of atmospheric CO is incorporated into the *cis*-position of the transition metal complex during the reaction sequence. Any plausible mechanism for chain formation must account for these isotopic labelling experiments.

The DFT calculations were employed to consider the formation of the key intermediate **2-2-Mn** along with the interconversion of **2-2-Mn → 2-3-Mn → 2-4-Mn** (Figure 2.5). The C_1 to C_4 chain-growth mechanism involves alternating reduction and oxidation events at the growing carbon, by **[Al]** and CO respectively. Stationary points were optimised using the ωB97x functional and single point energies were calculated using the M06l functional with dispersion (D3) and solvent (PCM, benzene) corrections. The M06l functional has been previously benchmarked to provide the good agreement with experimentally derived thermodynamic parameters on closely related systems.[21]

The calculated pathway begins with nucleophilic attack of **[Al]** onto a $C^2{\equiv}O^2$ unit bound to the transition-metal centre, forming **Int-1**. A single transition state connects the starting materials, [Cp'$Mn(CO)_3$] and **[Al]**, with **Int-1**. The aluminium centre is bound to both the C^2 and O^2 atoms in

Int-1 to form a three-membered ring. NBO analysis of **Int-1** shows that 2e⁻ have been transferred from **[Al]** to the CO unit; both the natural charges on C^2 (–0.11) and O^2 (–0.85) are lower than that of terminal Mn bound CO (+0.69 and –0.52 respectively). Donation of the lone-pair of **[Al]** into the CO π* orbital is a key interaction in **TS-1**.

Alternative chain-initiation reactions were also considered. Attempts were made to model the nucleophilic attack of **[Al]** onto CO, however no stationary point could be located. This finding supports experimental data as **[Al]** does not react with CO at 25°C, nor could a reversible adduct be observed to form at –80°C in VT NMR experiments. Experimentally, isolated heterometallic species containing M–[Al] bonds including [Cp'Mn(CO)$_2$**[Al]**] do not react with additional equivalents of **[Al]** and CO to form the chain-growth products.[22] The data support the hypothesis that the attack of a transition-metal bound CO is the first step in chain-growth.

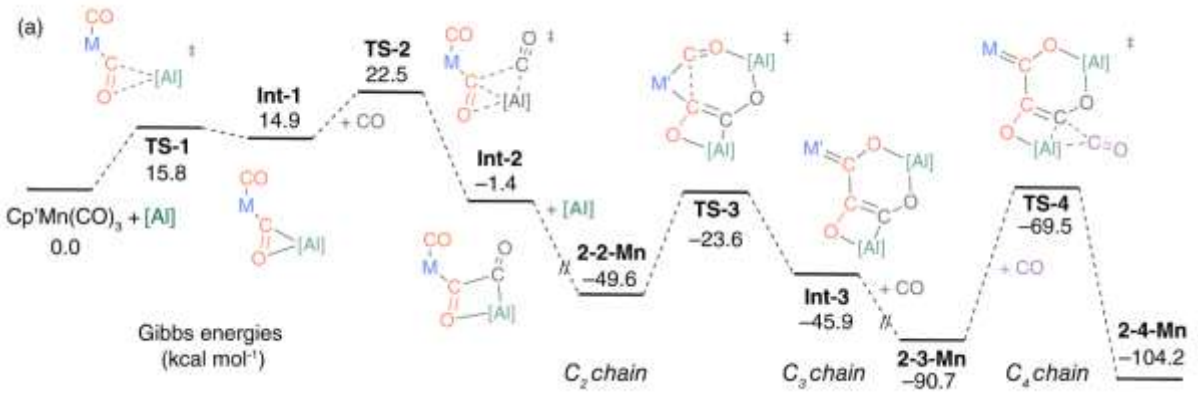


Figure 2.5: Pathway towards the formation of **2-4-Mn** from the starting materials [Cp'Mn(CO)$_3$] and [Al]. M = {Cp'Mn(CO)}, M' = {Cp'Mn(CO)$_2$}

Subsequent insertion of exogeneous CO into the Al–C bond of **Int-1** is calculated to be facile. This occurs *via* a single transition state, **TS-2**, to form the acyl intermediate **Int-2**. This step of the mechanism is the first carbon–carbon bond forming event but constructs the C^2–C^3 bond. The NPA charge analysis shows that insertion of $C^3{\equiv}O^3$ into the Al–C^2 bond of **Int-1** is accompanied by partial oxidation of the carbon chain; both carbon atoms of **Int-2** have positive NPA charges (C^2 +0.31; C^3 +0.02). There is literature precedent for the insertion of CO into three-membered aluminacyclopropanes[14] and aluminacyclopropenes (see Chapter 3).[23] Calculations have shown that these reactions are reminiscent of migratory insertion of CO at transition metal centres but have a propensity to occur in a concerted manner (see Chapter 3 for more detail).[14] The reaction of a second equivalent of **[Al]** with **Int-2** is calculated to be thermodynamically downhill ($\Delta G°_{298K}$ = –48.2 kcal mol^{-1}). The NPA charge of the C^2 and C^3 carbon in **2-2-Mn** (+0.15, –0.48) are lower than those in **Int-2** (+0.31, +0.02) reflecting the reduction of the carbon chain in this step. Although a transition state could not be located for

this intermolecular process, the step is entirely feasible and leads directly to the key intermediate **2-2-Mn**, which has been isolated and crystallographically characterised.

The structure of **2-2-Mn** is preorganised for the migratory insertion of the C_2 carbon chain into the Mn–C^1≡O^1 isocarbonyl bond. The C^1–C^2 bond along with the [6,4] fused ring system of **2-3-Mn** is formed in this reaction step. A single transition state, **TS-3**, connects **2-2-Mn** with **Int-3**. The reaction barrier from **2-2-Mn** to **TS-3** ($\Delta G^{\ddagger}_{298K}$ = 26.0 kcal $mol^{-1,}$) is consistent with this being a slow step, and combined with the relative thermodynamic stability of **2-2-Mn**, predicts this intermediate to be an isolable species. For comparison, the equivalent step in the pathway from **2-1-W** is calculated to occur via a lower in energy transition state (see Section 2.6.1) and all attempts to detect **2-2-W**, similar to **2-2-Mn**, failed. Migratory insertion reactions at transition metal centres are commonly reversible, with trapping of the products by an exogeneous ligand providing a thermodynamic driving force for the forward reaction. In line with this statement, the formation of **Int-3** from **2-2-Mn** is calculated to mildly endergonic ($\Delta G°_{298K}$ = 6.4 kcal mol^{-1}) and likely reversible. Coordination of CO to **Int-3** results in the formation of **2-3-Mn** and is downhill from **2-2-Mn** ($\Delta G°_{298K}$ = –41.1 kcal mol^{-1}). This coordination event explains the incorporation of exogenous CO into the *cis*-position of the transition metal fragment observed in isotopic labelling studies.

Insertion of a further equivalent of exogeneous C^4≡O^4 into the Mn–C^3 bond of **2-3-Mn** is calculated to occur by **TS-4** and results in the construction of the C^3–C^4 bond and formation of **2-4-Mn**. The activation barrier and thermodynamics for this step ($\Delta G^{\ddagger}_{298K}$ = 21.2 kcal mol^{-1}; $\Delta G°_{298K}$ = –13.5 kcal mol^{-1}) again suggest that **2-3-Mn** should be isolable. The calculations are also consistent with the reverse reaction, deinsertion of C^4≡O^4 from **2-4-Mn** to form **2-3-Mn**, being feasible under forcing conditions ($\Delta G^{\ddagger}_{298K}$ = 34.7 kcal mol^{-1}) as observed experimentally.

2.2.5 – Homologation to different chain topologies

In the preceding sections, the synthesis of **2-3-M** and **2-3-M'** (M = Mn, Re) was reported, and calculations reveal that the transition metal identity plays a key role in determining the products of the CO homologation reaction. The control of carbon chain topology through systematic variation of transition metal fragment is of immense contemporary interest in CO homologation chemistry. As a result, there was considerable interest in exploring other side products of the CO homologation reaction.

Successive recrystallisation of the reaction mixture of **2-3-Mn** furnished a single crystal suitable for X-ray diffraction (Figure 2.6). The X-ray crystal structure of compound **2-5-Mn** compound differs to the characterised complexes, and features a benzenehexolate ligated by a manganese centre and 3 equivalents of [Al]. **2-5-Mn** could only be isolated as single crystals, and its

formation is not clearly identified by ^{1}H NMR spectroscopy. The benzenehexolate $[C_6O_6]^{6-}$ ligand is similar to the products reported by Jones and co-workers using a magnesium (I) reductant.[24]

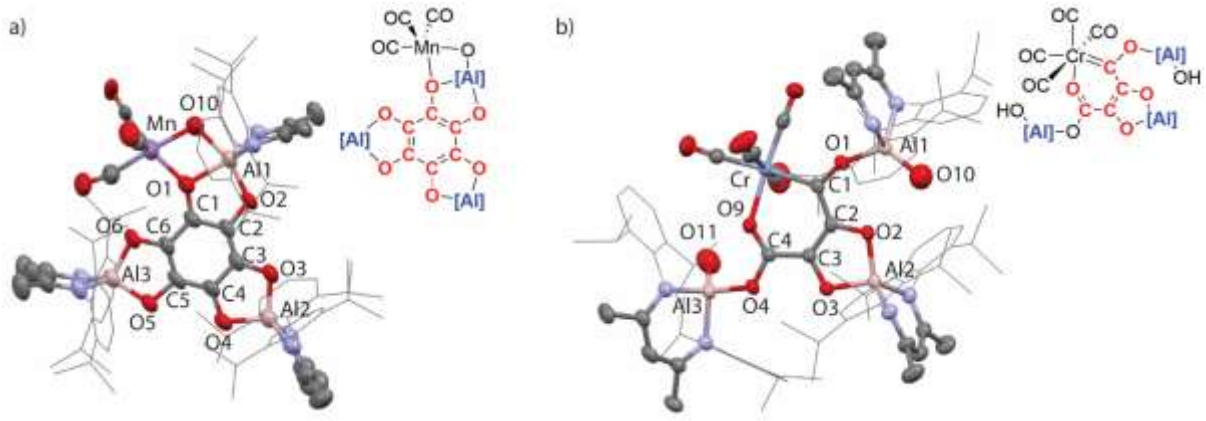


Figure 2.6: The X-ray crystal structure of a) **2-5-Mn**, and b) **2-6-Cr**.

The Al–N bond metrics suggest that all aluminium centres are best described in the +3 oxidation state. Each aluminium centre is further bound to the benzenehexolate ligand through two oxygen centres, forming 5-membered rings. In the case of Al^1, an oxo ligand bridges the Al^1 metal centre to a Mn carbonyl. The number of CO ligands on the Mn centre is somewhat ambiguous as two CO molecules were found to be at 50% occupancy within the crystal structure. The Mn centre is further bound to the hexolate ligand through the oxygen atom O^1. The Mn–O^1 and Mn–O^{10} distance are 1.939(5) and 1.956(6) Å respectively and statistically identical. The carbon–carbon bond lengths in the benzenehexolate ligand range from 1.346(8) to 1.428(9) Å and are consistent with the assignment of the C^1---C^6 ring system as an aromatic ring. While this product is likely the result of oxidation of a species formed from CO homologation, the benzenehexolate system has not been previously observed to form in our systems, and suggests that precise control of the transition metal fragment may allow control of products of CO homologation.

In a similar manner, repeated recrystallisation of the reaction mixture of **2-3-Cr** afforded single crystals suitable for X-ray diffraction. The resultant compound **2-6-Cr** contains a C_4 carbon chain formed from four CO units, and ligated by three Al centres and bound to the Cr centre through C1 and O9. As above, **2-6-Cr** is a minor product and not clearly identifiable in the ^{1}H NMR spectrum of crude reaction mixtures. The Al–N bond metrics suggest that each aluminium centre is in the +3 oxidation state and hence, the formulation of this carbon chain as the 6 e$^-$ reduced species $\{C_4O_4\}^{6-}$. The chain is most reminiscent of the reaction of decamethyl samarocene and $[Re_3(CO)_{12}]$ (See Chapter 1). While the formation of **2-4-Cr** is known to occur after heating **2-3-Cr**, formation of a C_4 chain has not been observed at room temperature in this system. As with **2-5-Mn**, **2-6-Cr** is likely the result of oxidation of a chain growth product.

The C^1–C^2, C^2–C^3, and C^3–C^4 bond lengths (1.463(6), 1.380(5), 1.462(5) Å respectively) indicate that the carbon chain has an alternating single, double, single bond structure. The Cr–C^1 bond length of 2.035(4) Å is statistically identical to that of **2-3-Cr** and **2-4-Cr**, indicating that the carbon chain is bound to Cr as a Fischer carbene. The C4 carbon is best described as a carboxylate group – the compressed C^4–O^9 bond length of 1.235(5) Å suggests assignment as a double bond, whereas the longer C^4–O^4 1.313(5) is best assigned as a single bond.

The aluminium centres are bound to the carbon chain through an oxygen atom. Hydroxide ligands (O^{10} and O^{11}) are also observed on the aluminium centres. In the case of Al^3, the O^{11} atom was found to be in only 35% occupancy. This partial occupancy hydroxide ligand is likely a consequence of only partial hydrolysis of the aluminium centre. At present it is unclear what the major component of the disorder is.

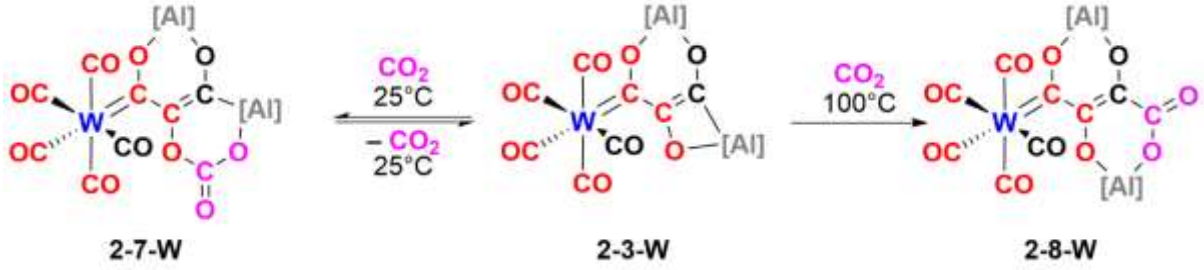
Bond	**2-5-Mn**	**2-6-Cr**
C^1–C^2	1.42(1)	1.463(6)
C^2–C^3	1.390(9)	1.380(5)
C^3–C^4	1.39(1)	1.462(5)
C^4–C^5	1.428(9)	-
C^5–C^6	1.346(8)	-
C^6–C^1	1.40(1)	-
M–C^1	-	2.035(4)
Al^1–N	1.922(5) 1.947(5)	1.883(3) 1.886(4)
Al^2–N	1.885(7) 1.868(6)	1.862(3) 1.862(4)
Al^3–N	1.872(6) 1.865(5)	1.898(4) 1.894(3)
C^4–O^4	1.377(7)	1.313(5)
C^4–O^9	-	1.235(5)

Table 2.5: Bond lengths in compounds **2-5-Mn** and **2-6-Cr**. All distances are provided in Å.

While the two products reported in this section are likely decomposition products through oxidation, the chain topology observed in each is unique to the previously established syntheses of **2-3-Cr** and **2-3-Mn**. The results suggest that it is possible to control chain topology and length through judicious selection of transition metal identity and associated ligand set.

2.2.6 – Insertion of CO_2 into the carbon chain

CO_2 is often present in Fischer-Tropsch feedstocks. Curious as to whether an alternate C_1 feedstock may be incorporated into the carbon chain, the reaction of **2-3-W** with CO_2 was explored. Placing a C_6D_6 solution of **2-3-W** under 1 bar of CO_2 resulted in the formation of the kinetic product **2-7-W** in which CO_2 has inserted into the Al–O bond of the 4-membered ring (Scheme 2.4). The isolation of **2-7-W** is amenable through its low solubility in benzene solution and the compound crystallised directly from the reaction mixture. **2-7-W** is not stable, however, and readily de-inserts CO_2 under an atmosphere of N_2 to reform **2-3-W** both in solution and as a solid.



Scheme 2.4: Reaction of **2-3-W** with CO_2

Heating solutions of **2-7-W** under an atmosphere of CO_2 resulted in the formation of the thermodynamic product **2-8-W**. **2-8-W** is an isomer of **2-7-W**, and is the product of CO_2 insertion into the Al–C bond of **2-3-W**. **2-8-W** is the thermodynamic product of the reaction and the de-insertion CO_2 is not observed after 18 h at 100°C.

Both **2-7-W** and **2-8-W** have been characterised by X-ray crystallography (Figure 2.7). The W–C^1 bond lengths are statistically identical within the two structures suggesting little variation within the nature of the metal carbene. Similarly, the C^1–C^2, and C^2–C^3 bond lengths are statistically identical within the two structures, suggesting that the single and double bond motif remains intact after the reaction. The C^3–C^4 bond length (1.51(1) Å) is consistent with a C–C single bond in **2-8-W** (Table 2.6).

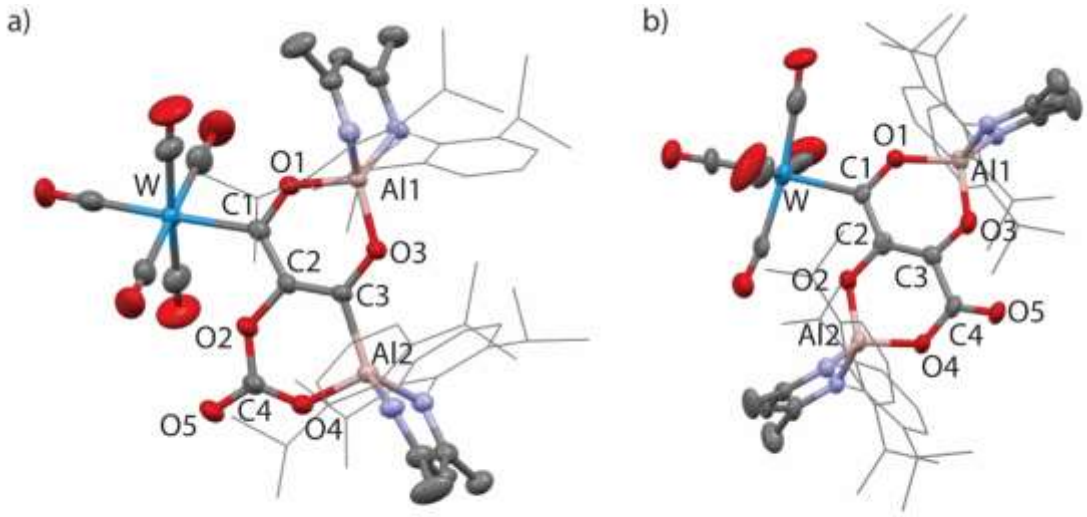


Figure 2.7: X-ray crystal structures of **2-7-W** and **2-8-W**.

	2-7-W	**2-8-W**
W–C1	2.217(6)	2.24(1)
C1–C2	1.453(7)	1.48(1)
C2–C3	1.371(8)	1.38(2)
C3–C4	-	1.51(1)

Table 2.6: Key bond metrics from structures in Figure 2.7.

DFT calculations were used to explore the transformation (Figure 2.8). The insertion of CO_2 into the Al–O bond of **2-3-W** was found to proceed through a single, low-energy, transition state **TS-8** ($\Delta G^{\ddagger}_{298K}$ = 14.3 kcal mol^{-1}) which is consistent with the observed reaction at room temperature. The product, **2-8-W** was calculated to be only 4.4 kcal mol^{-1} more stable than the reagents. Hence, the barrier for the de-insertion of CO_2 from **2-8-W** ($\Delta G^{\ddagger}_{298K}$ = 18.7 kcal mol^{-1}) is consistent with the observation of de-insertion at 25°C.

The reaction of **2-3-W** with CO_2 at the Al–C bond was found to be proceed through a single transition state, **TS-9**. The activation energy for **TS-9** is notably higher ($\Delta G^{\ddagger}_{298K}$ = 24.4 kcal mol^{-1}) and the product, **2-8-W** is calculated to be more stable than the starting materials (ΔG_{298K} = –29.8 kcal mol^{-1}), confirming the assignment of **2-8-W** as the thermodynamic product. The de-insertion of CO_2 is calculated to be inaccessible under the reaction conditions for **2-8-W** ($\Delta G^{\ddagger}_{298K}$ = 54.2 kcal mol^{-1}). Coordination of an oxygen atom in CO_2 is a key interaction in both transition states (Figure 2.8 b,c).

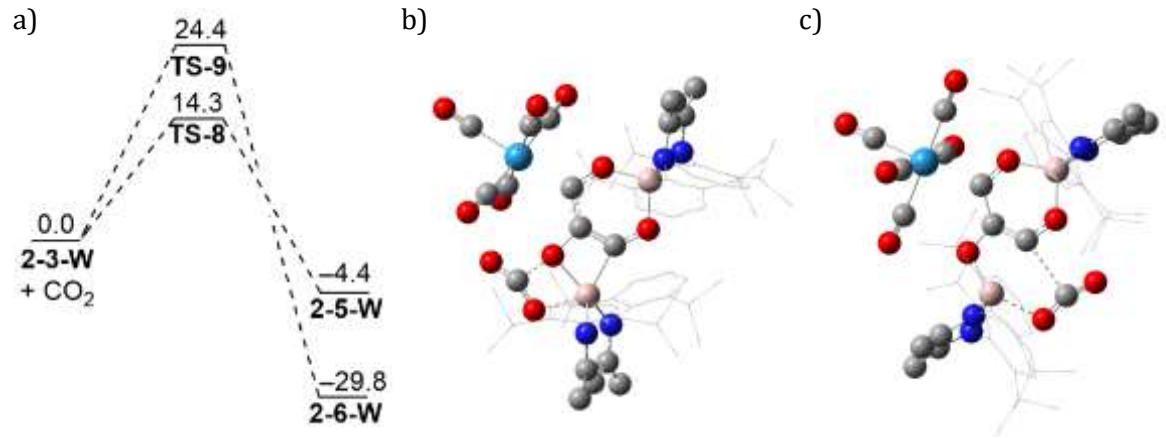


Figure 2.8: a) Calculated pathways towards the formation of **2-7-W** and **2-8-W**.* Structures of b) **TS-8** and c) **TS-9**.

2.3 Conclusion and future work

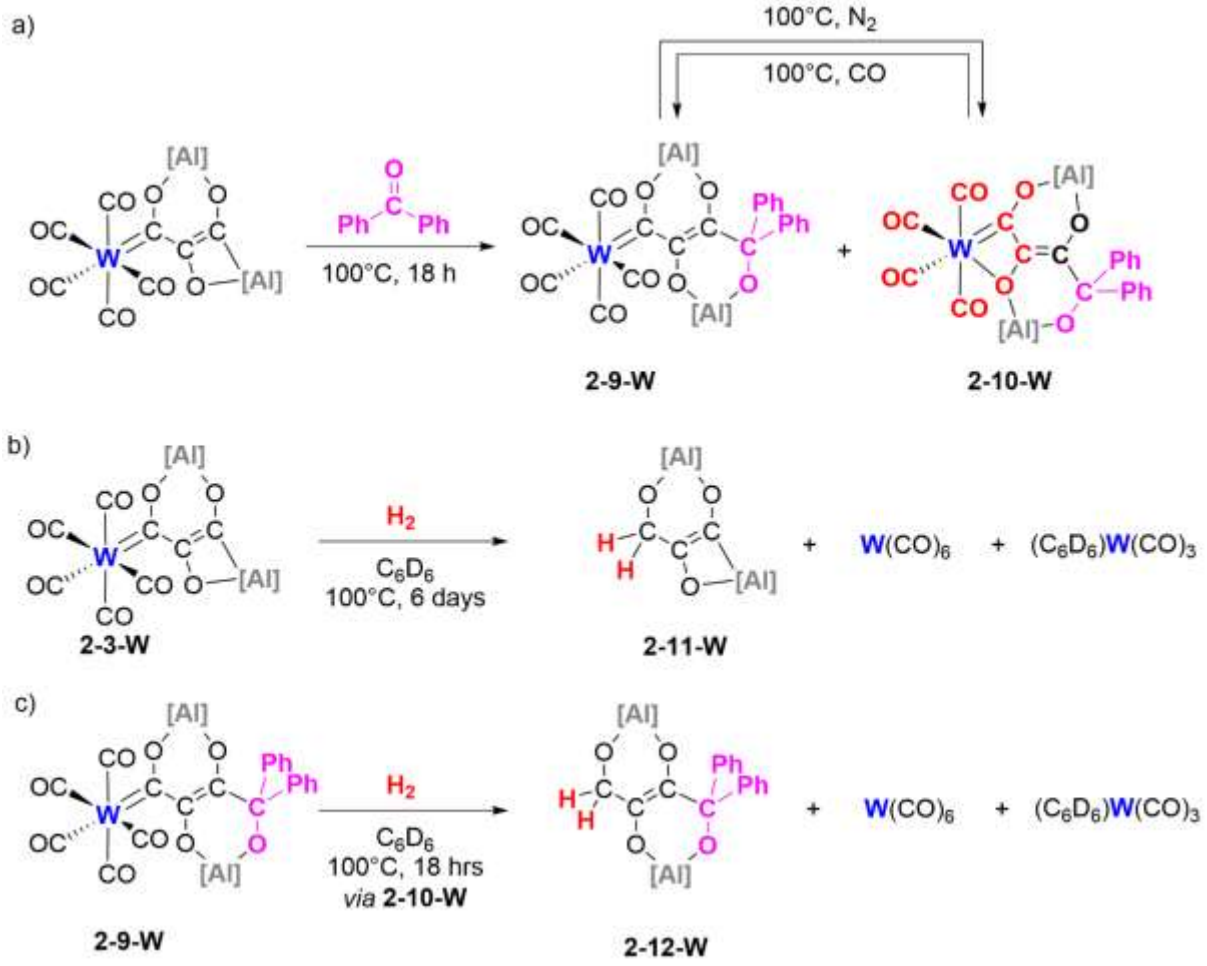
In this chapter, the homologation of CO to C_4 carbon chains was achieved using CO gas, a transition-metal CO complex, and a main-group reductant. A complete picture of chain-growth from C_1 metal carbonyls to C_4 chains was developed through the isolation of intermediates, and DFT calculations. Variation of the transition-metal fragment resulted in kinetic control of the observed products, and allowed for the isolation of a C_2 intermediate.

These results show that a rich chemical space exists in which an external reductant is coupled with a transition-metal carbonyl. In particular, the system explored in this chapter particularly has been demonstrated to result in different products depending on the transition-metal identity. Further alteration of the transition-metal fragment may allow a structure-activity relationship to be built, and ultimately provide insight into what factors govern chain growth to C_3 units and beyond. The structural characterisation of **2-3-Re'**, and implied formation of **2-3-Mn'**, demonstrate that judicious choice of transition-metal fragment influences the observed products. Further work on variation of transition-metal fragment may result in other coupling products, and a deeper understanding of chain-growth processes.

The reaction of these carbon chains with alternate electrophiles may also illuminate the role of the transition-metal in chain-growth reactions. Insertion of benzophenone into the Al–C bond of **2-3-W** results in the formation of two products, the expected insertion product **2-9-W** and a chelated structure **2-10-W** in which the transition-metal has lost one CO ligand, and the carbon chain chelates to the transition-metal centre. Both **2-9-W** and **2-10-W** have been characterised by single crystal X-ray diffraction. Preliminary experiments suggest that **2-9-W** can be

* The calculated energies differ slightly to the published figures[25] as they have been calculated using the M06l functional with Grimme's D3 dispersion correction and a PCM solvent model using the ωB97x geometries.

converted to **2-10-W** through heating under an atmosphere of N_2, and vice versa through heating under an atmosphere of CO gas.



Scheme 2.5: a) Reaction of 2-3-W with benzophenone. b) Reaction of **2-3-W** with dihydrogen gas. c) Reaction of **2-9-W** with dihydrogen gas.

The reaction of these transition-metal bound carbon chains is also of interest. Preliminary experiments show that reaction of **2-3-W** with dihydrogen gas results in hydrogenolysis of the metal carbene bond, to yield **2-11-W**. By products of the reaction include $[W(CO)_6]$ and $[(\eta^6\text{-}C_6D_6)W(CO)_3]$. Reaction of hydrogen with **2-9-W** similarly affords **2-12-W**. Interestingly, **2-10-W** is observed to form during the course of the reaction implicating a transition-metal mediated process. The hexacarbonyl product is notably similar to that reported by Jones and co-workers The mechanism and detail of this reaction is a current topic of investigation.

2.4 – Experimental

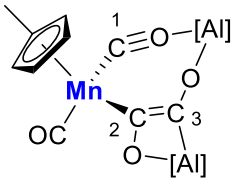
2.4.1 – General experimental

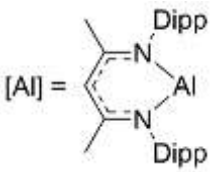
All manipulations were carried out using standard Schlenk-line and glovebox techniques under an inert atmosphere of argon or dinitrogen. A MBraun Labmaster glovebox was employed, operating at <0.1 ppm O_2 and <0.1 ppm H_2O. A Polar Bear Cub reactor located inside this MBraun Labmaster glovebox operating was used as the low-temperature reactor. A Grant XUBA1 ultrasonic bath was used to sonicate samples. Solvents were dried over activated alumina from a SPS (solvent purification system) based upon the Grubbs design and degassed before use. Glassware was dried for 12 h at 120°C prior to use. C_6D_6 was dried over 3 Å molecular sieves and freeze-pump-thaw degassed thrice before use.

NMR Spectra were recorded on Bruker 400 MHz or 500 MHz at 298 K unless otherwise stated and values recorded in ppm. Data were processed in MestReNova software. Where needed, chemical shifts were assigned with the assistance of 2D NMR (HSQC, HMBC, COSY) spectra. **[Al]**[16] and **1-Re**[26] were synthesized according to literature procedures. IR spectra were recorded on an Agilent Cary630 ATR FTIR spectrometer located inside an MBraun glovebox operating at <0.1 ppm H_2O and <0.1 ppm O_2. Chemicals were purchased from Sigma Aldrich, Fluorochem, Alfa Aesar, or VWR and used as received. CO was purchased from BOC Ltd and used as received. Elemental analyses were performed by London Metropolitan University and Elemental Labs (https://www.elementallab.co.uk/). Primary data (NMR, IR, .xyz coordinates) can be downloaded from https://dx.doi.org/10.14469/hpc/8698.

2.4.2 Preparation of Compounds

*Preparation of **2-2-Mn***





In a glovebox, to a solution of **[Al]** (36 mg, 0.08 mmol. 2 equiv) in C_6D_6 (1.2 mL) was added [(η^5-C_5H_4Me)$Mn(CO)_3$](8 µL, 11 mg, 0.050 mmol, 1.3 equiv.). The reaction mixture was distributed equally (2x 0.6 mL) into two separate NMR tubes. and the headspace of each NMR tube was evacuated *in vacuo*. The NMR tubes were removed from the glovebox, and CO gas (~ 1 bar) was introduced into the tubes. The resultant solutions were sonicated for 15 minutes to ensure the complete dissolution of **[Al]**. At this point, the tubes were shaken several times and allowed to stand for 2.5 h at 25°C. Both reactions were monitored by ^{1}H NMR spectroscopy and deemed complete upon total consumption of **[Al]**. At this point, the NMR tubes were returned to the glovebox, the headspace was evacuated to remove any remaining CO gas, and the solutions from both NMR tubes were diluted with toluene (~2x 1 mL) and decanted into in a 20 mL scintillation vial. The resultant dark purple solution was concentrated *in vacuo* until approximately 0.5 mL of solvent remained, at which point the solution was filtered into a 4 mL vial. The filtrate was further concentrated until only ~0.1 mL of solvent remained. n-Pentane (~2 mL) was layered on top of this solution, and the vial was placed in the glovebox freezer (–35°C) and **2-2-Mn** was allowed to crystallise as black-purple blocks. The supernatant was decanted, and the crystals were washed with cold n-pentane thrice (3x 1mL) before being dried briefly *in vacuo* (~2 minutes). Yield: 12 mg, 0.012 mmol, 31%.

^{1}H NMR (400 MHz, C_6D_6, 298 K) δ 0.49 (s br, 6H, 2x (C***H*₃**)CH(CH_3)), 0.98 (d, $^3J_{HH}$ = 7.0 Hz, 3H, (C***H*₃**)CH(CH_3)), 1.02 (d, $^3J_{HH}$ = 6.8 Hz, 3H, (C***H*₃**)CH(CH_3)), 1.05 (d, $^3J_{HH}$ = 6.8 Hz, 3H, (C***H*₃**)CH(CH_3)), 1.14 (d, $^3J_{HH}$ = 6.9 Hz, 3H, (C***H*₃**)CH(CH_3)), 1.19 (d, $^3J_{HH}$ = 6.9 Hz, 3H, (C***H*₃**)CH(CH_3)), 1.23 (d, $^3J_{HH}$ = 6.7 Hz, 3H, (C***H*₃**)CH(CH_3)), 1.27 (d, $^3J_{HH}$ = 6.1 Hz, 3H, (C***H*₃**)CH(CH_3)), 1.32 (d, $^3J_{HH}$ = 7.0 Hz, 3H, (C***H*₃**)CH(CH_3)), 1.35 (s, 3H, (C***H*₃**)CH(CH_3)), 1.40 (s, 3H, (C***H*₃**)C(CH)C(CH_3)), 1.47 (d, $^3J_{HH}$ = 6.7 Hz, 3H, (C***H*₃**)CH(CH_3)), 1.53 (s, 3H, (C***H*₃**)C(CH)C(CH_3)), 1.54 (s, 3H, (C***H*₃**)C(CH)C(CH_3)), 1.59 (s, 3H, (C***H*₃**)C(CH)C(CH_3)), 1.66 (d, $^3J_{HH}$ = 6.5 Hz, 3H, (C***H*₃**)CH(CH_3)), 1.72 (s, 3H, Cp'C***H*₃**), 2.84 (hept, $^3J_{HH}$ = 6.7 Hz, 1H, (CH_3)C***H***(CH_3)), 2.91-3.26 (m overlapping, 5H, 5x (CH_3)C***H***(CH_3)), 3.33 (s br, 1H, (CH_3)C***H***(CH_3)), 3.60 (s br, 1H, (CH_3)C***H***(CH_3)), 3.79 (s br, 1H, Cp'C***H***), 3.93 (s br, 1H, Cp'C***H***), 4.25 (s br, 1H, Cp'C***H***), 4.68 (s br, 1H, Cp'C***H***), 4.79 (s, 1H, (CH_3)C(C***H***)C(CH_3)), 4.93 (s, 1H, (CH_3)C(C***H***)C(CH_3)), 6.74 – 7.50 (m, 12H, Ar-***H***).

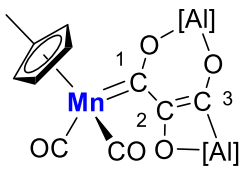
^{13}C NMR (101 MHz, C_6D_6, 298 K) δ 14.6 (Cp'$\boldsymbol{C}$H$_3$), 23.5 ($\boldsymbol{C}$H$_3$), 23.6 ($\boldsymbol{C}$H$_3$), 24.0 ($\boldsymbol{C}$H$_3$), 24.2 ($\boldsymbol{C}$H$_3$), 24.2 ($\boldsymbol{C}$H$_3$), 24.5 ($\boldsymbol{C}$H$_3$), 24.7 ($\boldsymbol{C}$H$_3$), 24.9 ($\boldsymbol{C}$H$_3$), 25.1 ($\boldsymbol{C}$H$_3$), 25.3 ($\boldsymbol{C}$H$_3$), 26.2 ($\boldsymbol{C}$H$_3$), 26.3 ($\boldsymbol{C}$H$_3$), 28.3 ((CH$_3$)$\boldsymbol{C}$H(CH$_3$)), 28.7 ((CH$_3$)$\boldsymbol{C}$H(CH$_3$)), 28.8 ((CH$_3$)$\boldsymbol{C}$H(CH$_3$)), 28.9 ((CH$_3$)$\boldsymbol{C}$H(CH$_3$)), 29.0 ((CH$_3$)$\boldsymbol{C}$H(CH$_3$)), 29.0 ((CH$_3$)$\boldsymbol{C}$H(CH$_3$)), 29.2 ((CH$_3$)$\boldsymbol{C}$H(CH$_3$)), 29.3 ((CH$_3$)$\boldsymbol{C}$H(CH$_3$)), 84.0 (Cp'$\boldsymbol{C}$H), 86.6 (Cp'$\boldsymbol{C}$H), 89.1 (Cp'$\boldsymbol{C}$H), 91.7 (Cp'$\boldsymbol{C}$H), 98.0 ((CH$_3$)C($\boldsymbol{C}$H)C(CH$_3$)), 98.3 ((CH$_3$)C($\boldsymbol{C}$H)C(CH$_3$)), 102.7 (Cp'$\boldsymbol{C}$CH$_3$), 123.5 (Ar$\boldsymbol{C}$), 124.2 (Ar$\boldsymbol{C}$), 124.4 (Ar$\boldsymbol{C}$), 124.6 (Ar$\boldsymbol{C}$), 124.7 (Ar$\boldsymbol{C}$), 124.9 (Ar$\boldsymbol{C}$), 125.2 (Ar$\boldsymbol{C}$), 125.3 (Ar$\boldsymbol{C}$), 125.6 (Ar$\boldsymbol{C}$), 126.9 (Ar$\boldsymbol{C}$), 127.2 (Ar$\boldsymbol{C}$), 139.3 (Ar$\boldsymbol{C}$), 139.6 (Ar$\boldsymbol{C}$), 140.9 (Ar$\boldsymbol{C}$), 141.6 (Ar$\boldsymbol{C}$), 143.7 (Ar$\boldsymbol{C}$), 143.9 (Ar$\boldsymbol{C}$), 144.0 (Ar$\boldsymbol{C}$), 144.3 (Ar$\boldsymbol{C}$), 144.6 (Ar$\boldsymbol{C}$), 145.2 (Ar$\boldsymbol{C}$), 145.8 (Ar$\boldsymbol{C}$), 146.5 (Ar$\boldsymbol{C}$), 167.2 ($\boldsymbol{C^3}$), 169.2 ((CH$_3$)C($\boldsymbol{C}$H)C(CH$_3$)), 171.8 ((CH$_3$)C($\boldsymbol{C}$H)C(CH$_3$)), 172.7 ((CH$_3$)C($\boldsymbol{C}$H)C(CH$_3$)), 172.9 ((CH$_3$)C($\boldsymbol{C}$H)C(CH$_3$)), 189.5 ($\boldsymbol{C^1}$), 236.8 (Mn$\boldsymbol{C}$O), 249.2 ($\boldsymbol{C^2}$).

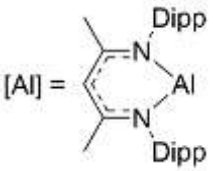
Many methyl and aromatic carbon resonances are broad and overlapping, and could not be observed or identified. $\boldsymbol{C^3}$ is a tentative assignment as it is uncharacteristically sharp for a nucleus bound to quadrupolar ^{29}Al (I = 5/2) nucleus.

IR (ATR), ν_{CO} (cm^{-1}): 1921 (s).

Anal. Calc. ($C_{68}H_{89}Al_2MnN_4O_4$): C, 71.94; H, 7.90; N, 4.93. Found: C, 71.30; H, 7.90; N, 4.76.

*Preparation of **2-3-Mn***





In a glovebox, to a solution of **[Al]** (36 mg, 0.08 mmol. 2 equiv) in C_6D_6 (1.2 mL) was added [η^5-(η^5-C_5H_4Me)$Mn(CO)_3$] (8 µL, 11 mg, 0.050 mmol, 1.3 equiv.). The reaction mixture was distributed equally (2x 0.6 mL) into two separate NMR tubes and the headspace of each NMR tube was evacuated *in vacuo*. The NMR tubes were removed from the glovebox, and CO gas (~ 1 bar) was introduced into the tubes. The resultant solutions were sonicated for 15 minutes to ensure the complete dissolution of **[Al]**. At this point, the tubes were shaken several times and allowed to stand for 48 h at 25°C. The reaction was monitored by ^{1}H NMR spectroscopy and was complete upon total consumption of **2-2-Mn** and **[Al]**. At this point, the NMR tubes were returned to the glovebox, the headspace evacuated to remove any remaining CO gas, and the solutions from both NMR tubes were decanted into a 20 mL scintillation vial containing ~5 mL of n-heptane. The resultant dark red solution was concentrated *in vacuo* until a precipitate began to form, at which point the solution was filtered and the residue was redissolved in the minimum amount of toluene, and recombined with the filtrate. The resultant solution was placed in the glovebox freezer and **2-3-Mn** was allowed to recrystallise at –35°C as orange-red blocks. The supernatant was decanted, and the resultant crystals were washed with cold n-pentane thrice (3x 1mL) before being dried briefly *in vacuo* (~2 minutes). A second crop can be collected from the filtrate by concentrating and crystallizing under identical conditions as above. Yield: 20 mg, 0.017 mmol, 43%. A minor component of **2-3-Mn'** (9%) could be observed in the ^{1}H NMR spectrum on dissolution of single crystals obtained this preparation which could not be removed by fractional crystallisation.

^{1}H NMR (400 MHz, C_6D_6, 298 K) δ 0.64 (d, $^3J_{HH}$ = 6.8 Hz, 6H, (C***H***$_3$)$_2$CH), 0.70 (d, $^3J_{HH}$ = 6.6 Hz, 6H, (C***H***$_3$)$_2$CH), 0.94 (d, $^3J_{HH}$ = 6.8 Hz, 6H, (C***H***$_3$)$_2$CH), 1.03 (d, $^3J_{HH}$ = 6.7 Hz, 6H, (C***H***$_3$)$_2$CH), 1.07 (d, $^3J_{HH}$ = 6.8 Hz, 6H, (C***H***$_3$)$_2$CH), 1.33 (d, $^3J_{HH}$ = 6.8 Hz, 6H, (C***H***$_3$)$_2$CH), 1.38 (d, $^3J_{HH}$ = 6.7 Hz, 6H, (C***H***$_3$)$_2$CH), 1.41 (s, 6H, {(C***H***$_3$)C}$_2$CH), 1.44 (s, 6H, {(C***H***$_3$)C}$_2$CH), 1.64 (d, $^3J_{HH}$ = 6.8 Hz, 6H, (C***H***$_3$)$_2$CH), 2.02 (s, 3H, Cp'-C***H***$_3$), 2.93 (hept, $^3J_{HH}$ = 6.6 Hz, 2H, 2x $(CH_3)_2$C***H***), 2.96 (hept, $^3J_{HH}$ = 6.8 Hz, 2H, 2x $(CH_3)_2$C***H***), 3.27 (hept, $^3J_{HH}$ = 6.8 Hz, 2H, 2x $(CH_3)_2$C***H***), 3.40 (hept, $^3J_{HH}$ = 6.7 Hz, 2H, 2x $(CH_3)_2$C***H***), 4.75 (virtual t, $^3J_{HH}$ = 2.3 Hz, 2H, Cp'-C***H***), 4.87 (s, 1H, {$(CH_3)C$}$_2$C***H***), 4.94 (s, 1H, {$(CH_3)C$}$_2$C***H***), 5.33 (t, $^3J_{HH}$ = 2.2 Hz, 2H, Cp'-C***H***), 6.78 (dd, $^3J_{HH}$ = 5.1, 4.2 Hz, 2H, Ar-***H***), 6.98 – 7.30 (m, 10H, Ar-***H***).

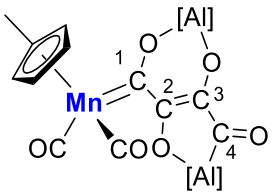
^{13}C NMR (101 MHz, C_6D_6, 298 K) δ 14.5 (Cp'–***C***H_3), 23.6 ({(***C***H_3)C}$_2$CH), 23.6 ({(***C***H_3)C}$_2$CH), 23.8 ((***C***H_3)$_2$CH), 24.2 ((***C***H_3)$_2$CH), 24.6 ((***C***H_3)$_2$CH), 24.8 ((***C***H_3)$_2$CH), 25.1 ((***C***H_3)$_2$CH), 25.1 ((***C***H_3)$_2$CH), 25.7 ((***C***H_3)$_2$CH), 26.4 ((***C***H_3)$_2$CH), 28.2 (2x (CH$_3$)$_2$***C***H), 28.7 (2x (CH$_3$)$_2$***C***H), 28.9 (2x (CH$_3$)$_2$***C***H), 29.1 (2x (CH$_3$)$_2$***C***H), 84.8 (2x Cp'–***C***H), 87.6 (2x Cp'***C***–H), 98.4 ({(CH$_3$)$_2$C}$_2$***C***H), 99.8 ({(CH$_3$)$_2$C}$_2$***C***H), 102.1 (Cp'***C***–CH$_3$), 123.7 (Ar***C***), 124.5 (Ar***C***), 125.0 (Ar***C***), 126.1 (Ar***C***), 127.2 (Ar***C***), 129.3 (Ar***C***), 139.1 (Ar***C***), 139.7 (Ar***C***), 142.7 (Ar***C***), 143.1 (Ar***C***), 144.4 (Ar***C***), 146.3 (Ar***C***), 166.7 (***C***^{2}), 172.3 ({(CH$_3$)$_2$***C***}$_2$CH), 172.7 ({(CH$_3$)$_2$***C***}$_2$CH), 236.5 (Mn(***C***O)$_2$, 311.7 (***C***^{1}).

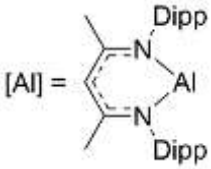
The Al–***C***^{3} resonance could not be observed in the ^{13}C NMR spectrum due to coupling to the quadrupolar ^{27}Al (I = 5/2) nucleus.

IR (ATR), ν_{CO} (cm^{-1}): 1916 (s), 1847 (s).

Anal. Calc. ($C_{69}H_{89}Al_2MnN_4O_5$): C, 71.24; H, 7.71; N, 4.82. Found: C, 71.98; H, 7.45; N, 4.75.

*Preparation of **2-4-Mn***





In a glovebox, to an NMR tube charged with **[Al]** (36 mg, 0.08 mmol, 2 equiv) in C_6D_6 (0.6 mL) was added [(η^5-C_5H_4Me)$Mn(CO)_3$] (8 µL, 11 mg, 0.050 mmol, 1.3 equiv.). The reaction mixture was distributed equally into two separate NMR tubes. The headspace of each NMR tube was evacuated *in vacuo*. The NMR tubes were removed from the glovebox, and CO gas (~ 1 bar) was introduced into the tubes. The resultant solutions were sonicated for 15 minutes to ensure the complete dissolution of **[Al]**. Upon complete dissolution of **[Al]**, the tubes were shaken several times and allowed to stand for 6 h at 25°C. After 6 h, the tubes were heated at 80°C for 48 h. The CO atmosphere of the tubes was refreshed at the 24 h time interval. The reaction was monitored by ^{1}H NMR spectroscopy and was complete upon consumption of **2-3-Mn**. The NMR tubes were returned to the glovebox, the headspace evacuated to remove any remaining CO gas, and the solutions from both NMR tubes were decanted into neat n-heptane (~5 mL) in a 20 mL scintillation vial. The resultant dark red solution was concentrated *in vacuo* until a precipitate began to form, at which point the solution was filtered and **2-4-Mn** was allowed to crystallise at –35°C in the glovebox freezer as dark red blocks. The supernatant was decanted, and the resultant crystals were washed with cold n-pentane thrice (3x 1mL) before the crystals were dried briefly *in vacuo* (~2 minutes). Yield: 24 mg, 0.020 mmol, 50%.

^{1}H NMR (400 MHz, C_6D_6, 298 K) δ 0.57 (d, $^3J_{HH}$ = 6.6 Hz, 6H, (C***H***$_3$)$_2$CH), 0.93 (d, $^3J_{HH}$ = 6.7 Hz, 6H, (C***H***$_3$)$_2$CH), 1.05 (d, $^3J_{HH}$ = 6.9 Hz, 6H, (C***H***$_3$)$_2$CH), 1.08 (d, $^3J_{HH}$ = 6.8 Hz, 6H, (C***H***$_3$)$_2$CH), 1.25 (d, $^3J_{HH}$ = 6.8 Hz, 6H, (C***H***$_3$)$_2$CH), 1.29 (d, $^3J_{HH}$ = 6.6 Hz, 6H, (C***H***$_3$)$_2$CH), 1.41 (s, 6H, {(C***H***$_3$)C}$_2$CH), 1.43 (s, 6H, {(C***H***$_3$)C}$_2$CH), 1.43 (d overlapping, $^3J_{HH}$ = 6.7 Hz, 6H, (C***H***$_3$)$_2$CH), 1.48 (d, $^3J_{HH}$ = 6.7 Hz, 6H, (C***H***$_3$)$_2$CH), 1.80 (s, 3H, Cp'-C***H***), 3.07 (hept, $^3J_{HH}$ = 6.7 Hz, 2H, 2x (CH$_3$)$_2$C***H***), 3.24 (hept overlapping, $^3J_{HH}$ = 6.7 Hz, 2H, 2x (CH$_3$)$_2$C***H***), 3.25 (hept overlapping, $^3J_{HH}$ = 6.7 Hz, 2H, 2x (CH$_3$)$_2$C***H***), 3.54 (hept, $^3J_{HH}$ = 6.7 Hz, 2H, 2x (CH$_3$)$_2$C***H***), 4.39 (virtual t, $^3J_{HH}$ = 2.1 Hz, 2H, 2x Cp'-***H***), 4.44 (virtual t, $^3J_{HH}$ = 2.1 Hz, 2H, 2x Cp'-***H***), 4.77 (s, 1H, {(CH$_3$)$_2$C}$_2$C***H***), 4.87 (s, 1H, {(CH$_3$)$_2$C}$_2$C***H***), 7.03 – 7.30 (m, 12H, Ar-***H***).

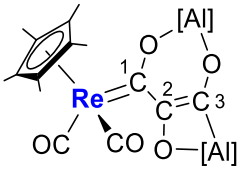
^{13}C NMR (101 MHz, C_6D_6, 298 K) δ 13.9 (Cp'$\boldsymbol{C}$H$_3$), 23.4 ({($\boldsymbol{C}$H$_3$)C}$_2$CH), 23.5 ({($\boldsymbol{C}$H$_3$)C}$_2$CH), 24.3 (($\boldsymbol{C}$H$_3$)$_2$CH), 24.3 (($\boldsymbol{C}$H$_3$)$_2$CH), 24.5 (($\boldsymbol{C}$H$_3$)$_2$CH), 24.8 (($\boldsymbol{C}$H$_3$)$_2$CH), 24.9 (($\boldsymbol{C}$H$_3$)$_2$CH), 24.9 (($\boldsymbol{C}$H$_3$)$_2$CH), 25.3 (($\boldsymbol{C}$H$_3$)$_2$CH), 27.0 (($\boldsymbol{C}$H$_3$)$_2$CH), 28.2 (2x (CH$_3$)$_2\boldsymbol{C}$H), 28.4 (2x (CH$_3$)$_2\boldsymbol{C}$H), 29.1 (2x (CH$_3$)$_2\boldsymbol{C}$H), 29.3 (2x (CH$_3$)$_2\boldsymbol{C}$H), 85.1 (2x Cp'$\boldsymbol{C}$H), 88.5 (2x Cp'$\boldsymbol{C}$H), 98.7 ({(CH$_3$)$_2$C}$_2\boldsymbol{C}$H), 99.4 ({(CH$_3$)$_2$C}$_2\boldsymbol{C}$H), 102.8 (Cp'$\boldsymbol{C}$CH$_3$), 124.3 (2x Ar$\boldsymbol{C}$), 124.8 (Ar$\boldsymbol{C}$), 125.1 (Ar$\boldsymbol{C}$), 127.7 (Ar$\boldsymbol{C}$), 127.9 (Ar$\boldsymbol{C}$), 135.7 ($\boldsymbol{C^3}$), 138.5 (Ar$\boldsymbol{C}$), 139.6 (Ar$\boldsymbol{C}$), 143.2 (Ar$\boldsymbol{C}$), 143.9 (Ar$\boldsymbol{C}$), 145.4 (Ar$\boldsymbol{C}$), 145.4 (Ar$\boldsymbol{C}$), 160.7 ($\boldsymbol{C^2}$), 172.6 ({(CH$_3$)$_2\boldsymbol{C}$}$_2$CH), 172.6 ({(CH$_3$)$_2\boldsymbol{C}$}$_2$CH), 235.6 (Mn($\boldsymbol{C}$O)$_2$), 332.3 ($\boldsymbol{C^1}$).

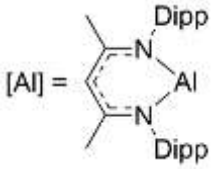
The Al–$\boldsymbol{C^4}$ resonance could not be observed in the ^{13}C NMR spectrum due to coupling to the quadrupolar ^{27}Al (I = 5/2) nucleus.

IR (ATR), ν_{CO} (cm^{-1}): 1920 (s), 1860(s), 1585 (m).

Anal. Calc. ($C_{70}H_{89}Al_2MnN_4O_6$): C, 70.57; H, 7.53; N, 4.70. Found: C, 72.04; H, 7.56; N, 4.26.

*Preparation of **2-3-Re***





In a glovebox, **2-4-Re** (24 mg, 0.017 mmol) was suspended in C_6D_6 (0.6 mL) and transferred to a J-Young NMR tube. The tube was heated at 100°C for 4 days. At 24 h intervals, the headspace of the tube was evacuated *in vacuo* and refilled with N_2. The reaction was monitored by ^{1}H NMR spectroscopy. On complete consumption of **2-4-Re**, the J-Young NMR tube was returned to the glovebox, the reaction mixture was then diluted with n-heptane (~1 mL), decanted into a 20 mL scintillation vial and concentrated *in vacuo* until precipitation of the product was observed. The reaction mixture was filtered, and any solid residue was dissolved in the minimum amount of C_6H_6 and combined with the filtrate before the resultant solution was placed in the glovebox freezer. **2-3-Re** crystallised at –35°C as orange-red blocks. The supernatant was decanted, and the resultant crystals were washed with cold n-pentane thrice (3x 1mL) before the crystals were dried briefly *in vacuo* (~2 minutes). Yield: 8 mg, 0.0059 mmol, 35%,

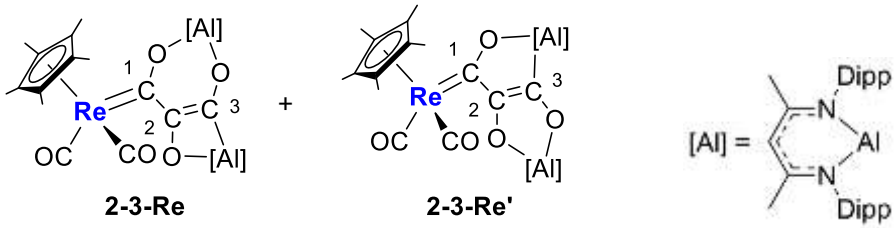
^{1}H NMR (400 MHz, C_6D_6, 298 K) δ 0.59 (d, $^3J_{HH}$ = 6.8 Hz, 6H, (C***H***$_3$)$_2$CH), 0.71 (d, $^3J_{HH}$ = 6.7 Hz, 6H, (C***H***$_3$)$_2$CH), 0.94 (d, $^3J_{HH}$ = 6.9 Hz, 6H, (C***H***$_3$)$_2$CH), 1.07 (d, $^3J_{HH}$ = 6.8 Hz, 6H, (C***H***$_3$)$_2$CH), 1.11 (d, $^3J_{HH}$ = 6.9 Hz, 6H, (C***H***$_3$)$_2$CH), 1.25 (d, $^3J_{HH}$ = 6.7 Hz, 6H, (C***H***$_3$)$_2$CH), 1.37 (d, $^3J_{HH}$ = 6.8 Hz, 6H, (C***H***$_3$)$_2$CH), 1.45 (s, 6H, {(C***H***$_3$)C}$_2$CH), 1.45 (s, 6H, {(C***H***$_3$)C}$_2$CH), 1.85 (d, $^3J_{HH}$ = 6.8 Hz, 6H, (C***H***$_3$)$_2$CH), 2.12 (s, 15H, Cp*(C***H***$_3$)$_5$), 3.00 (hept, $^3J_{HH}$ = 6.8 Hz, 2H, 2x (CH$_3$)$_2$C***H***), 3.02 (hept, $^3J_{HH}$ = 6.7 Hz, 2H, 2x (CH$_3$)$_2$C***H***), 3.09 (hept, $^3J_{HH}$ = 6.7 Hz, 2H, 2x (CH$_3$)$_2$C***H***), 3.28 (hept, $^3J_{HH}$ = 6.8 Hz, 2H, 2x (CH$_3$)$_2$C***H***), 4.96 (s, 1H, {(CH$_3$)C}$_2$C***H***), 5.04 (s, 1H, {(CH$_3$)C}$_2$C***H***), 6.83 (m, 2H, Ar-***H***), 7.05 – 7.38 (m, 10H, Ar-***H***).

^{13}C NMR (101 MHz, C_6D_6, 298 K) δ 11.2 (Cp*(***C***H$_3$)$_5$), 23.4 ({(***C***H$_3$)C}$_2$CH), 23.5 ({(***C***H$_3$)C}$_2$CH), 23.8 ((***C***H$_3$)$_2$CH), 24.4 ((***C***H$_3$)$_2$CH), 24.8 ((***C***H$_3$)$_2$CH), 24.9 ((***C***H$_3$)$_2$CH), 25.2 ((***C***H$_3$)$_2$CH), 25.8 ((***C***H$_3$)$_2$CH), 25.8 ((***C***H$_3$)$_2$CH), 26.0 ((***C***H$_3$)$_2$CH), 28.0 (2x (CH$_3$)$_2$***C***H), 28.8 (2x (CH$_3$)$_2$***C***H), 28.9 (2x (CH$_3$)$_2$***C***H), 29.2 (2x (CH$_3$)$_2$***C***H), 98.4 ({(CH$_3$)$_2$C}$_2$***C***H), 98.9 (5x Cp****C***CH$_3$), 99.3 ({(CH$_3$)$_2$C}$_2$***C***H), 124.1 (Ar-***C***), 124.3 (Ar-***C***), 125.3 (Ar-***C***), 126.2 (Ar-***C***), 127.4 (Ar-***C***), 127.5 (Ar-***C***), 139.7 (2x Ar-***C***), 142.8 (Ar-***C***), 142.9 (Ar-***C***), 144.9 (Ar-***C***), 146.0 (Ar-***C***), 170.5 (***C***^{2}), 172.3 ({(CH$_3$)$_2$***C***}$_2$CH), 172.6 ({(CH$_3$)$_2$***C***}$_2$CH), 210.3 (Re(***C***O)$_2$), 265.0 (***C***^{1}).

The Al–C^3 resonance could not be observed in the ^{13}C NMR spectrum due to coupling to the quadrupolar ^{27}Al (I = 5/2) nucleus.

IR (ATR), ν_{CO} (cm^{-1}): 1917 (s), 1848 (s).

Preparation of a mixture of ***2-3-Re/2-3-Re'***



2-3-Re **2-3-Re'**

In a glovebox, to a solution of **[Al]** (36 mg, 0.08 mmol, 2 equiv) in C_6D_6 (0.6 mL) was added a solution of [(η^5-C_5Me_5)Re(CO)$_3$] (18 mg, 0.044 mmol, 1.1 equiv) in C_6D_6 (0.6 mL). The reaction mixture was equally divided (2x 0.6 mL) into two J-Young NMR tubes and the headspace of each NMR tube was evacuated *in vacuo*. The NMR tubes were removed from the glovebox, and CO gas (~ 1 bar) was introduced into the tubes. The resultant solutions were sonicated for 15 minutes to ensure the complete dissolution of **[Al]**. At this point, the tubes were shaken several times and allowed to stand for 48 h at 25°C. The reaction was monitored by ^{1}H NMR spectroscopy and was complete upon complete consumption of **[Al]**. **2-3-Re** and **2-3-Re'** were observed to form in ca. 3 : 1 ratio at this timepoint using ^{1}H NMR spectroscopy. At this point, the NMR tubes were returned to the glovebox, the headspace evacuated to remove any remaining CO gas, and the solutions from both NMR tubes were decanted into neat n-heptane (~5 mL) in a 20 mL scintillation vial. The resultant dark red solution was concentrated *in vacuo* until approximately 2 mL of solvent remains, at which point the solution was filtered into a 4 mL vial. The resultant solution was placed in the glovebox freezer and **2-3-Re/2-3-Re'** was allowed to recrystallise at –35°C as orange-red blocks. **2-3-Re** and **2-3-Re'** co-crystallise and cannot be separated by fractional crystallization. ^{1}H NMR spectroscopy of single crystals show that the products co-crystallise in a virtually identical ratio to their formation (**2-3-Re** : **2-3-Re'** = 3 : 1). The supernatant was decanted, and the resultant crystals were washed with cold n-pentane thrice (3x 1mL) before being dried briefly *in vacuo* (~2 minutes). Yield: 33 mg, 0.024 mmol, 61%.

Data for **2-3-Re** match the data reported above.

Data for **2-3-Re'**

^{1}H NMR (400 MHz, C_6D_6, 298 K) δ 0.42 (d, $^3J_{HH}$ = 6.7 Hz, 6H, (C***H***$_3$)$_2$CH), 0.96 (d, $^3J_{HH}$ = 6.8 Hz, 6H, (C***H***$_3$)$_2$CH), 1.13 (d, $^3J_{HH}$ = 6.8 Hz, 6H, (C***H***$_3$)$_2$CH), 1.14 (d, $^3J_{HH}$ = 6.9 Hz, 6H, (C***H***$_3$)$_2$CH), 1.24 (d, $^3J_{HH}$ = 6.5 Hz, 6H, (C***H***$_3$)$_2$CH), 1.39 (d, $^3J_{HH}$ = 6.7 Hz, 6H, (C***H***$_3$)$_2$CH), 1.41 (d, $^3J_{HH}$ = 6.7 Hz, 6H, (C***H***$_3$)$_2$CH), 1.44 (s, 6H, {(C***H***$_3$)C}$_2$CH), 1.44 (s, 6H, {(C***H***$_3$)C}$_2$CH), 1.89 (d, $^3J_{HH}$ = 6.8 Hz, 6H, (C***H***$_3$)$_2$CH), 2.12 (s,

15H, Cp*(C***H₃***)$_5$), (2.84 – 3.33, m overlapping, 8H, 8x $(CH_3)_2C$***H***), 4.92 (s, 1H, {$(CH_3)C$}$_2$C***H***), 5.10 (s, 1H, {$(CH_3)C$}$_2$C***H***), 6.92 (m, 2H, Ar-***H***), 7.02 – 7.35 (m, 10H, Ar-***H***).

^{13}C NMR (101 MHz, C_6D_6, 298 K) 14.4 (Cp*(***C***H_3)$_5$, 23.1 ({(***C***H_3)C}$_2$CH), 23.7 ({(***C***H_3)C}$_2$CH), 24.2 ($(***C***H_3)_2$CH), 24.4 ($(***C***H_3)_2$CH), 24.5 ($(***C***H_3)_2$CH), 25.1 ($(***C***H_3)_2$CH), 25.5 ($(***C***H_3)_2$CH), 25.6 ($(***C***H_3)_2$CH), 25.8 ($(***C***H_3)_2$CH), 29.5 (2x $(CH_3)_2$***C***H), 29.7 (2x $(CH_3)_2$***C***H), 32.3 (2x $(CH_3)_2$***C***H), 98.3 ({$(CH_3)_2C$}$_2$***C***H), 99.1 (5x Cp****C***CH_3), 99.8 ({$(CH_3)_2C$}$_2$***C***H), 124.1 (Ar***C***), 124.7 (Ar***C***), 125.5 (Ar***C***), 126.1 (Ar***C***), 127.4 (Ar***C***), 139.6 (Ar***C***), 140.7 (Ar***C***), 143.0 (Ar***C***), 143.4 (Ar***C***), 143.5 (Ar***C***), 145.9 (Ar***C***), 172.1 ({$(CH_3)_2$***C***}$_2$CH), 172.3 ({$(CH_3)_2$***C***}$_2$CH), 178.5 (***C²***), 210.2 (Re(***C***O)$_2$), 273.0 (***C¹***).

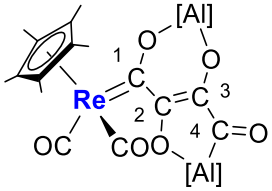
The spectra for **2-3-Re'** were measured from a mixture of **2-3-Re'** and **2-3-Re**. The $(CH_3)_2C$***H*** resonances for **2-3-Re'** in the ^{1}H spectrum overlap with $(CH_3)_2C$***H*** resonances for **2-3-Re** and cannot be assigned. Some Ar-***C***, ***C***H_3, and ***C***H resonances overlap with ^{13}C **2-3-Re** resonances and cannot be identified. The Al–***C³*** resonance could not be observed in the ^{13}C NMR spectrum due to coupling to the quadrupolar ^{27}Al (I = 5/2) nucleus.

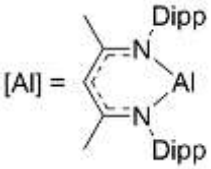
IR (ATR), ν_{CO} (cm^{-1}): 1904 (sh), 1809 (m).

Anal. Calc. ($C_{73}H_{97}Al_2N_4O_5Re$): C, 64.91; H, 7.24; N, 4.15. Found: C, 66.14; H, 7.91; N, 3.97. †

† The high C and H content measured by elemental analysis likely suggests the presence of solvent. A molecule of benzene per molecule of **3-Re/3-Re'** would result in the following elemental analysis: C, 66.41; H, 7.27; N, 3.92.

*Preparation of **2-4-Re***





In a glovebox, to an NMR tube charged with **[Al]** (40 mg, 0.090 mmol, 2 equiv) in C_6D_6 (0.6 mL) was added a solution of [(η^5-C_5Me_5)Re(CO)$_3$] (21 mg, 0.052 mmol, 1.2 equiv) in C_6D_6 (0.6 mL). The reaction mixture was equally divided (2x 0.6 mL) into two J-Young NMR tubes and the headspace of each NMR tube was evacuated *in vacuo*. The NMR tubes were removed from the glovebox, and CO gas (~ 1 bar) was introduced into the tubes. The tubes were heated at 80°C for 6 h. At this point, the CO atmosphere was refreshed and the tubes heated for a further 48 h at 80°C. The reaction was monitored by ^{1}H NMR spectroscopy. Upon complete consumption of **[Al]** and **2-3-Re** the NMR tubes were returned to the glovebox, the headspace evacuated to remove any remaining CO gas, and the solutions from both NMR tubes were decanted into neat n-heptane (~5 mL) in a 20 mL scintillation vial. The resultant dark red solution was concentrated *in vacuo* until approximately 2 mL of solution remains, at which point the solution was filtered into a 4 mL vial. The resultant solution was placed in the glovebox freezer and **2-4-Re** was allowed to recrystallise at –35°C as dark red/black blocks. The supernatant was decanted, and the resultant crystals were washed with cold n-pentane thrice (3x 1mL) before the crystals were dried briefly *in vacuo* (~2 minutes). Yield: 25 mg, 0.018 mmol, 37%.

The mother liquor was concentrated *in vacuo* to ca. 0.2 mL, layered with pentane (~0.4 mL), and placed in the freezer (–35°C). Single crystals of **2-3-Re'** suitable for X-ray diffraction formed as pale yellow crystals under these conditions, however **2-4-Re** was found to additionally precipitate as a dark red/black solid which could be separated manually on a glass slide from **2-3-Re'**.

^{1}H NMR (400 MHz, C_6D_6, 298 K) δ 0.76 (d, $^3J_{HH}$ = 6.6 Hz, 6H, (C***H***$_3$)$_2$CH), 0.98 (d, $^3J_{HH}$ = 6.7 Hz, 6H, (C***H***$_3$)$_2$CH), 1.05 (d, $^3J_{HH}$ = 6.7 Hz, 6H, (C***H***$_3$)$_2$CH), 1.06 (d, $^3J_{HH}$ = 6.8 Hz, 6H, (C***H***$_3$)$_2$CH), 1.15 (d, $^3J_{HH}$ = 6.8 Hz, 6H, (C***H***$_3$)$_2$CH), 1.17 (d, $^3J_{HH}$ = 6.7Hz, 6H, (C***H***$_3$)$_2$CH), 1.19 (d, $^3J_{HH}$ = 6.6 Hz, 6H, (C***H***$_3$)$_2$CH), 1.39 (s, 6H, {(C***H***$_3$)C}$_2$CH), 1.40 (s, 6H, {(C***H***$_3$)C}$_2$CH), 1.74 (d, $^3J_{HH}$ = 6.7 Hz, 6H, (C***H***$_3$)$_2$CH), 2.00 (s, 15H, Cp*(***C***H$_3$)$_5$), 3.05 (hept, $^3J_{HH}$ = 6.7 Hz, 2H, 2x (CH$_3$)$_2$C***H***), 3.13 (hept, $^3J_{HH}$ = 6.9 Hz, 2H, 2x (CH$_3$)$_2$C***H***), 3.15 (hept, $^3J_{HH}$ = 6.7 Hz, 2H, 2x (CH$_3$)$_2$C***H***), 3.48 (hept, $^3J_{HH}$ = 6.7 Hz, 2H, 2x (CH$_3$)$_2$C***H***), 4.70 (s, 1H, {(CH$_3$)C}$_2$C***H***), 4.87 (s, 1H, {(CH$_3$)C}$_2$C***H***), 7.08 – 7.28 (m, 12H, Ar-***H***)

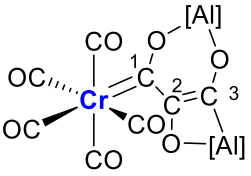
^{13}C NMR (101 MHz, C_6D_6, 298 K) δ 11.1 (Cp*(***C***H_3)$_5$), 23.5 ({(***C***H_3)$_2$C}$_2$CH), 23.8 ({(***C***H_3)$_2$C}$_2$CH), 24.5 ((***C***H_3)$_2$CH), 24.6 ((***C***H_3)$_2$CH), 25.0 ((***C***H_3)$_2$CH), 25.5 ((***C***H_3)$_2$CH), 25.7 ((***C***H_3)$_2$CH), 25.8 ((***C***H_3)$_2$CH), 26.4 ((***C***H_3)$_2$CH), 28.1 (2x (CH$_3$)$_2$***C***H), 28.4 (2x (CH$_3$)$_2$***C***H), 28.9 (2x (CH$_3$)$_2$***C***H), 29.5 (2x (CH$_3$)$_2$***C***H), 98.8 ({(CH$_3$)$_2$C}$_2$***C***H), 99.2 ({(CH$_3$)$_2$C}$_2$***C***H), 99.7 (5x Cp****C***CH$_3$), 124.6 (Ar***C***), 124.7 (Ar***C***), 124.8 (Ar***C***), 124.9 (Ar***C***), 127.5 (Ar***C***), 128.7 (Ar***C***), 138.9 (Ar***C***), 139.8 (Ar***C***), 144.0 (Ar***C***), 144.5 (Ar***C***), 144.5 (***C³***), 144.6 (Ar***C***), 144.7 (Ar***C***), 169.1 (***C²***), 172.8 ({(CH$_3$)$_2$***C***}$_2$CH), 173.0 ({(CH$_3$)$_2$***C***}$_2$CH), 209.6 (Re(***C***O)$_2$), 280.6 (***C¹***).

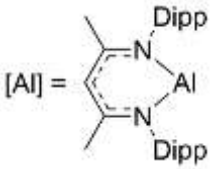
The Al–***C⁴*** resonance could not be observed in the ^{13}C NMR spectrum due to coupling to the quadrupolar ^{27}Al (I = 5/2) nucleus.

IR (ATR), ν_{CO} (cm^{-1}): 1929 (s), 1861 (s), 1584 (m).

Anal. Calc. ($C_{74}H_{97}Al_2N_4O_6Re$): C, 64.46;H, 7.09; N, 4.06. Found: C, 65.63; H, 6.78; N, 3.96.

*Preparation of **2-3-Cr***





In a glovebox, to an NMR tube charged with a frozen suspension of **[Al]** (18 mg, 0.04 mmol, 2 equiv) in C_6D_6 (0.3 mL) cooled to –35°C using a low temperature reactor was added [$Cr(CO)_6$] (5 mg, 0.023 mmol, 1.2 equiv) slowly as a slurry in C_6D_6 (0.3 mL) *via* Pasteur pipette. Care was taken to ensure that the mixture remains frozen. The headspace of the NMR tube was evacuated, and the NMR tube was removed from the glovebox quickly and placed into a liquid-nitrogen bath (–196°C) to keep the suspension frozen. The NMR tube was removed from the liquid nitrogen bath and CO gas (~1 bar) was quickly introduced into the headspace of the cold NMR tube before the frozen mixture began to thaw. The mixture was allowed to thaw, and during this process the tube was shaken vigorously to ensure incorporation of CO gas into solution. The reaction was assumed to be complete once the mixture had completely thawed. At this point, **[Al]** was completely dissolved, and the solution darkened to an orange-brown colour. A precipitate formed. The NMR tube was returned to the glovebox, the headspace of the NMR tube was evacuated to remove the remaining CO gas, and the suspension was diluted with ~0.5 mL of toluene and decanted into a 20 mL scintillation vial. The reaction mixture was concentrated *in vacuo* until approximately ~0.5 mL remained at which point THF was added until all solids were dissolved. The resultant solution was filtered, and concentrated *in vacuo* until approximately ~0.6 mL of solution remained. The reaction mixture was placed in the freezer (–35°C) and **2-3-Cr** crystallised as bright orange blocks. The crystals were washed thrice with pentane (3 x 1mL) and dried briefly *in vacuo* (~2 minutes). Yield: 11 mg, 0.0094 mmol, 24% yield.

^{1}H NMR (400 MHz, C_6D_6, 298 K) δ 0.51 (d, $^3J_{HH}$ = 6.8 Hz, 6H, (C***H***$_3$)$_2$CH), 0.69 (d, $^3J_{HH}$ = 6.7 Hz, 6H, (C***H***$_3$)$_2$CH), 0.89 (d, $^3J_{HH}$ = 6.8 Hz, 6H, (C***H***$_3$)$_2$CH), 0.99 (d, $^3J_{HH}$ = 6.8 Hz, 6H, (C***H***$_3$)$_2$CH), 1.08 (d, $^3J_{HH}$ = 6.8 Hz, 6H, (C***H***$_3$)$_2$CH), 1.30 (d, $^3J_{HH}$ = 6.8 Hz, 6H, (C***H***$_3$)$_2$CH), 1.33 (d overlapping, $^3J_{HH}$ = 6.7 Hz, (C***H***$_3$)$_2$CH), 1.33 (s, 6H, {(C***H***$_3$)C}$_2$CH), 1.42 (s, 6H, {(C***H***$_3$)C}$_2$CH), 1.70 (d, $^3J_{HH}$ = 6.8 Hz, 6H, (C***H***$_3$)$_2$CH), 2.85 (hept, $^3J_{HH}$ = 6.8 Hz, 2H, 2x (CH$_3$)$_2$C***H***), 2.95 (hept, $^3J_{HH}$ = 6.8 Hz, 2H, 2x (CH$_3$)$_2$C***H***), 3.15 (hept, $^3J_{HH}$ = 6.8 Hz, 2H, 2x (CH$_3$)$_2$C***H***), 3.20 (hept, $^3J_{HH}$ = 6.7 Hz, 2H, 2x (CH$_3$)$_2$C***H***), 4.83 (s, 1H, {(CH$_3$)C}$_2$C***H***), 4.93 (s, 1H, {(CH$_3$)C}$_2$C***H***), 6.77 (m, 2H, Ar-***H***), 6.96 – 7.35 (m, 10H, Ar-***H***).

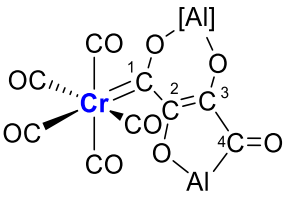
^{13}C NMR (101 MHz, C_6D_6, 298 K) δ 23.4 ({(***C***H_3)C}$_2$CH), 23.5 ({(***C***H_3)C}$_2$CH), 23.7 ((***C***H_3)$_2$CH), 24.2 ((***C***H_3)$_2$CH), 24.7 (2x (***C***H_3)$_2$CH), 24.8 ((***C***H_3)$_2$CH), 25.0 ((***C***H_3)$_2$CH), 25.3 ((***C***H_3)$_2$CH), 26.6 ((***C***H_3)$_2$CH), 28.1 (2x (CH$_3$)$_2$***C***H), 28.8 (2x (CH$_3$)$_2$***C***H), 28.9 (2x (CH$_3$)$_2$***C***H), 29.0 (2x (CH$_3$)$_2$***C***H), 98.6 ({(CH$_3$)$_2$C}$_2$***C***H), 100.4 ({(CH$_3$)$_2$C}$_2$***C***H), 124.0 (Ar***C***), 124.4 (Ar***C***), 125.4 (Ar***C***), 125.7 (2x Ar***C***), 126.2 (Ar***C***), 138.5 (Ar***C***), 139.1 (Ar***C***), 142.7 (Ar***C***), 142.8 (Ar***C***), 144.4 (Ar***C***), 146.3 (Ar***C***), 169.2 (***C^2***), 172.8 ({(CH$_3$)$_2$***C***}$_2$CH), 173.4 ({(CH$_3$)$_2$***C***}$_2$CH), 219.9 (Cr(***C***O)$_4$), 226.2 (Cr***C***O), 314.6 (***C^1***).

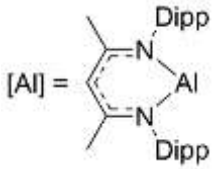
The Al–***C^3*** resonance could not be observed in the ^{13}C NMR spectrum due to coupling to the quadrupolar ^{27}Al (I = 5/2) nucleus.

IR (ATR), ν_{CO} (cm^{-1}): 2042 (m), 1922 (s), 1904 (s), 1886 (s), 1872 (s).

Anal. Calc. ($C_{66}H_{82}Al_2CrN_4O_8$): C, 68.02; H, 7.09; N, 4.81. Found: C, 62.04; H, 6.68; N, 4.62. The low C content, but accurate H and N content likely reflect limitations of the technique (e.g. incomplete C combustion).

*Preparation of **2-4-Cr***





In a glovebox, an NMR tube charged with a frozen suspension of **[Al]** (8.9 mg, 0.02 mmol, 2 equiv) in C_6D_6 (0.3 mL) was cooled to –35°C using a low temperature reactor. [$Cr(CO)_6$] (2.2 mg, 0.01 mmol, 1 equiv) was added slowly as a slurry in C_6D_6 (0.3 mL) *via* Pasteur pipette. Care was taken to ensure that the reaction mixture remained frozen. The headspace of the NMR tube was evacuated, and the NMR tube was removed from the glovebox quickly and placed into a liquid-nitrogen bath (–196°C). The tube was removed from the liquid nitrogen bath, and CO gas (~1 bar) was introduced into the headspace of the NMR tube while the mixture was still frozen. The mixture was allowed to thaw, and during this process the tube was shaken vigorously to ensure incorporation of CO gas into solution. The resultant mixture was heated at 100°C and conversion to **2-4-Cr** was complete after 18 h, as monitored by ^{1}H NMR spectroscopy. The NMR tube was returned to the glovebox, the headspace of the NMR tube was evacuated to remove the remaining CO gas, and the dark purple reaction mixture was diluted with ~0.5 mL of toluene and decanted into a 20 mL scintillation vial. The resultant solution was concentrated *in vacuo* to ~0.2 mL and placed in the glovebox freezer (–35°C). **2-4-Cr** crystallised as purple needles. The supernatant was decanted, and the resultant crystals were washed with cold n-pentane thrice (3x 0.5mL) before being dried briefly *in vacuo* (~ 2 minutes). Yield: 6.2 mg, 0.0052 mmol, 52%.

^{1}H NMR (400 MHz, C_6D_6, 298 K) δ 0.36 (d, $^3J_{HH}$ = 6.6 Hz, 6H, (C***H***$_3$)$_2$CH), 0.84 (d, $^3J_{HH}$ = 6.7 Hz, 6H, (C***H***$_3$)$_2$CH), 1.01 (d, $^3J_{HH}$ = 6.7 Hz, 6H, (C***H***$_3$)$_2$CH), 1.07 (d, $^3J_{HH}$ = 6.8 Hz, 6H, (C***H***$_3$)$_2$CH), 1.13 (d, $^3J_{HH}$ = 6.7 Hz, 6H, (C***H***$_3$)$_2$CH), 1.23 (d, $^3J_{HH}$ = 6.7 Hz, 6H, (C***H***$_3$)$_2$CH), 1.38 (s, 6H, {(C***H***$_3$)C}$_2$CH), 1.39 (s, 6H, {(C***H***$_3$)C}$_2$CH), 1.54 (d, $^3J_{HH}$ = 6.6 Hz, 6H, (C***H***$_3$)$_2$CH), 1.64 (d, $^3J_{HH}$ = 6.8 Hz, 6H, (C***H***$_3$)$_2$CH), 2.96 (hept, $^3J_{HH}$ = 6.7 Hz, 2H, (CH$_3$)$_2$C***H***), 3.17 (hept, $^3J_{HH}$ = 6.7 Hz, 2H, (CH$_3$)$_2$C***H***), 3.33 (hept, $^3J_{HH}$ = 6.8 Hz, 2H, (CH$_3$)$_2$C***H***), 3.48 (hept, $^3J_{HH}$ = 6.7 Hz, 2H, (CH$_3$)$_2$C***H***), 4.79 (s, 1H, {(CH$_3$)C}$_2$C***H***), 4.89 (s, 1H, {(CH$_3$)C}$_2$C***H***), 6.94 - 7.27 (m overlapping signals, 12H, Ar-***H***).

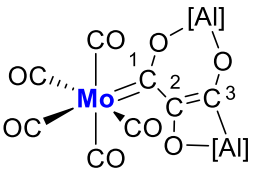
$^{13}C\{^{1}H\}$ NMR (101 MHz, C_6D_6, 298 K) δ 23.4 ({(***C***H$_3$)C}$_2$CH), 23.5 ({(***C***H$_3$)$_2$C}CH), 23.7 ((***C***H$_3$)$_2$CH), 24.2 ((***C***H$_3$)$_2$CH), 24.7 (2x (***C***H$_3$)$_2$CH), 24.8 ((***C***H$_3$)$_2$CH), 25.0 ((***C***H$_3$)$_2$CH), 25.3 ((***C***H$_3$)$_2$CH), 26.6 ((***C***H$_3$)$_2$CH), 28.1 (2x (CH$_3$)$_2$***C***H), 28.8 (2x (CH$_3$)$_2$***C***H), 28.9 (2x (CH$_3$)$_2$***C***H), 29.0 (2x (CH$_3$)$_2$***C***H), 98.6 ({(CH$_3$)$_2$C}$_2$***C***H), 100.4 ({(CH$_3$)$_2$C}$_2$***C***H), 124.0 (Ar***C***), 124.4 (Ar***C***), 125.4 (Ar***C***), 125.7 (2x Ar***C***), 126.2 (Ar***C***), 138.5 (Ar***C***), 139.1 (Ar***C***), 142.7 (Ar***C***), 142.8 (Ar***C***), 144.4 (Ar***C***), 146.3 (Ar***C***), 169.2 (***C***^{2}), 172.8 ({(CH$_3$)$_2$***C***}$_2$CH), 173.4 ({(CH$_3$)$_2$***C***}$_2$CH), 219.9 (Cr(***C***O)$_4$), 226.2 (Cr***C***O), 314.6 (***C***^{1}).

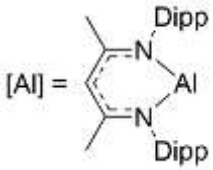
The Al–***C***^{4} resonance could not be observed in the ^{13}C NMR spectrum due to coupling to the quadrupolar ^{27}Al (I = 5/2) nucleus.

IR (ATR), ν_{CO} (cm^{-1}): 2042 (m), 1922 (s), 1904 (s), 1886 (s), 1872 (s).

Anal. Calc. ($C_{67}H_{82}Al_2CrN_4O_9$): C, 67.43; H, 6.93; N, 4.69. Found: C, 60.64; H, 6.29; N, 4.28. The low C content, but accurate H and N content likely reflect limitations of the technique (e.g. incomplete C combustion).

*Preparation of **2-3-Mo***





In a glovebox, an NMR tube was charged with a suspension of **[Al]** (18 mg, 0.04 mmol, 2 equiv) in C_6D_6 (0.3 mL), cooled to –35°C using a low temperature reactor and [$Mo(CO)_6$] (6 mg, 0.023 mmol, 1.2 equiv) was added slowly as a slurry in C_6D_6 (0.3 mL) *via* Pasteur pipette. Care was taken to ensure that the reaction mixture remained frozen and that the reagents do not mix. The headspace of the NMR tube was evacuated, and the NMR tube was removed from the glovebox quickly and placed into a liquid-nitrogen bath (–196°C). The tube was removed from the liquid nitrogen bath, and CO gas (~1 bar) was introduced into the headspace of the cold NMR tube while the mixture was still frozen. The mixture was allowed to thaw, and during this process the tube was shaken vigorously to ensure incorporation of CO gas into solution. The reaction was assumed to be complete once the mixture had completely thawed, **[Al]** was completely dissolved, and the solution darkened to an orange-brown colour. The NMR tube was returned to the glovebox, the headspace of the NMR tube was evacuated to remove the remaining CO gas, and the solution was diluted with ~0.5 mL of toluene. The resultant solution was concentrated *in vacuo* to ~0.2 mL, filtered, and carefully layered with n-pentane (~1 mL). The vial was placed in the freezer (– 35°C) and **2-3-Mo** crystallised as bright orange blocks. Yield: 10 mg, 0.0083 mmol, 41% yield.

^{1}H NMR (400 MHz, C_6D_6, 298 K) δ 0.57 (d, $^3J_{HH}$ = 6.7 Hz, 6H, (C***H***$_3$)$_2$CH), 0.61 (d, $^3J_{HH}$ = 6.8 Hz, 6H, (C***H***$_3$)$_2$CH), 0.89 (d, $^3J_{HH}$ = 6.8 Hz, 6H, (C***H***$_3$)$_2$CH), 0.98 (d, $^3J_{HH}$ = 6.8 Hz, 6H, (C***H***$_3$)$_2$CH), 1.07 (d, $^3J_{HH}$ = 6.8 Hz, 6H, (C***H***$_3$)$_2$CH), 1.28 (d, $^3J_{HH}$ = 6.8 Hz, 6H, (C***H***$_3$)$_2$CH), 1.31 (d, $^3J_{HH}$ = 6.7 Hz, 6H, (C***H***$_3$)$_2$CH), 1.34 (s, 6H, {(C***H***$_3$)C}$_2$CH), 1.40 (s, 6H, {(C***H***$_3$)C}$_2$CH), 1.69 (d, $^3J_{HH}$ = 6.7 Hz, 6H, (C***H***$_3$)$_2$CH), 2.87 (hept overlapping, $^3J_{HH}$ = 6.7 Hz, 2H, 2x (CH$_3$)$_2$C***H***), 2.91 (hept overlapping, $^3J_{HH}$ = 6.8 Hz, 2H, 2x (CH$_3$)$_2$C***H***), 3.09 (hept overlapping, $^3J_{HH}$ = 6.8 Hz, 2H, 2x (CH$_3$)$_2$C***H***), 3.12 (hept overlapping, $^3J_{HH}$ = 6.7 Hz, 2H, 2x (CH$_3$)$_2$C***H***), 4.91 (s, 1H, {(CH$_3$)C}$_2$C***H***), 4.93 (s, 1H, {(CH$_3$)C}$_2$C***H***), 6.68 (m, 2H, Ar-***H***), 7.00 – 7.24 (m, 10 H, Ar-***H***).

^{13}C NMR (101 MHz, C_6D_6, 298 K) δ 23.4 ({(***C***H$_3$)C}$_2$CH), 23.4 ({(***C***H$_3$)C}$_2$CH), 23.5 ((***C***H$_3$)$_2$CH), 24.1 ((***C***H$_3$)$_2$CH), 24.4 ((***C***H$_3$)$_2$CH), 24.7 ((***C***H$_3$)$_2$CH), 24.8 ((***C***H$_3$)$_2$CH), 25.0 ((***C***H$_3$)$_2$CH), 26.3 ((***C***H$_3$)$_2$CH), 26.7 ((***C***H$_3$)$_2$CH), 28.1 (2x (CH$_3$)$_2$***C***H), 28.8 (2x (CH$_3$)$_2$***C***H), 28.9 (2x (CH$_3$)$_2$***C***H), 29.2

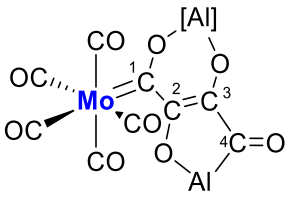
(2x $(CH_3)_2\boldsymbol{C}H$), 98.7 ($\{(CH_3)_2C\}_2\boldsymbol{C}H$), 100.2 ($\{(CH_3)_2C\}_2\boldsymbol{C}H$), 123.9 (Ar$\boldsymbol{C}$), 124.3 (Ar$\boldsymbol{C}$), 125.4 (Ar$\boldsymbol{C}$), 126.0 (Ar$\boldsymbol{C}$), 127.5 (Ar$\boldsymbol{C}$), 127.8 (Ar$\boldsymbol{C}$), 138.4 (Ar$\boldsymbol{C}$), 138.9 (Ar$\boldsymbol{C}$), 142.6 (Ar$\boldsymbol{C}$), 142.6 (Ar$\boldsymbol{C}$), 145.0 (Ar$\boldsymbol{C}$), 146.3 (Ar$\boldsymbol{C}$), 170.6 ($\boldsymbol{C^2}$), 172.7 ($\{(CH_3)_2\boldsymbol{C}\}_2CH$), 173.5 ($\{(CH_3)_2\boldsymbol{C}\}_2CH$), 209.7 (Mo($\boldsymbol{C}O)_4$), 216.1 (Mo($\boldsymbol{C}$O)), 305.7 ($\boldsymbol{C^1}$).

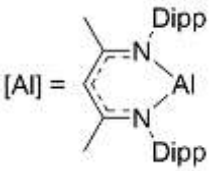
The Al–$\boldsymbol{C^3}$ resonance could not be observed in the ^{13}C NMR spectrum due to coupling to the quadrupolar ^{27}Al (I = 5/2) nucleus.

IR (ATR), ν_{CO} (cm^{-1}): 2052 (m), 1935 (s), 1905 (s), 1871 (s).

Anal. Calc. ($C_{66}H_{82}Al_2MoN_4O_8$): C, 65.55;H, 6.83; N, 4.63. Found: C, 65.83; H, 7.09; N, 5.05.

*Preparation of **2-4-Mo***





In a glovebox, a NMR tube was charged with a suspension of **[Al]** (8.9 mg, 0.02 mmol, 2 equiv) in C_6D_6 (0.3 mL) was cooled to –35°C using a low temperature reactor. [$Mo(CO)_6$] (2.5 mg, 0.01 mmol, 1 equiv) was added slowly as a slurry in C_6D_6 (0.3 mL) *via* Pasteur pipette. Care was taken to ensure that the reaction mixture remains frozen. The headspace of the NMR tube was evacuated, and the NMR tube was removed from the glovebox quickly and placed into a liquid-nitrogen bath (–196°C). The tube was removed from the liquid nitrogen bath, and CO gas (~1 bar) was introduced into the headspace of the NMR tube while the mixture was still frozen. Upon addition of CO gas, the mixture was allowed to thaw, and during this process the tube was shaken vigorously to ensure incorporation of CO gas into solution. The resultant mixture was heated at 100°C and conversion to **2-4-Mo** was complete after 18 h, as monitored by ^{1}H NMR spectroscopy. The NMR tube was returned to the glovebox, the headspace of the NMR tube was evacuated to remove the remaining CO gas, and the dark purple reaction mixture was diluted with ~0.5 mL of toluene and decanted into a 20 mL scintillation vial. The resultant solution was concentrated *in vacuo* to ~0.2 mL, filtered into a 4 mL vial, and carefully layered with n-pentane (~2 mL). The vial was placed in the glovebox freezer (–35°C) and **2-4-Mo** crystallised as red blocks. The supernatant was decanted, and the resultant crystals were washed with cold n-pentane thrice (3x 0.5mL) before being dried briefly *in vacuo* (~ 2 minutes). Yield: 5.6 mg, 0.0045 mmol, 45%.

^{1}H NMR (400 MHz, C_6D_6, 298 K) δ 0.35 (d, $^3J_{HH}$ = 6.6 Hz, 6H, (C***H***$_3$)$_2$CH), 0.79 (d, $^3J_{HH}$ = 6.7 Hz, 6H, (C***H***$_3$)$_2$CH), 1.01 (d, $^3J_{HH}$ = 6.7 Hz, 12H, (C***H***$_3$)$_2$CH), 1.08 (d, $^3J_{HH}$ = 6.8 Hz, 6H, (C***H***$_3$)$_2$CH), 1.25 (d, $^3J_{HH}$ = 6.7 Hz, 6H, (C***H***$_3$)$_2$CH), 1.40 (s, 6H, {(C***H***$_3$)C}$_2$CH), 1.41 (s, 6H, {(C***H***$_3$)C}$_2$CH), 1.57 (d, $^3J_{HH}$ = 6.7 Hz, 6H, (C***H***$_3$)$_2$CH), 1.70 (d, $^3J_{HH}$ = 6.8 Hz, 6H, (C***H***$_3$)$_2$CH), 2.97 (hept, $^3J_{HH}$ = 6.7 Hz, 2H, (CH$_3$)$_2$C***H***), 3.12 (hept, $^3J_{HH}$ = 6.8 Hz, 2H, (CH$_3$)$_2$C***H***), 3.24 (hept, $^3J_{HH}$ = 6.7 Hz, 2H, (CH$_3$)$_2$C***H***), 3.53 (hept, $^3J_{HH}$ = 6.7 Hz, 2H, (CH$_3$)$_2$C***H***), 4.86 (s, 1H, {(CH$_3$)C}$_2$C***H***), 4.92 (s, 1H, {(CH$_3$)C}$_2$C***H***), 6.94 - 7.23 (m overlapping signals, 12H, Ar-***H***).

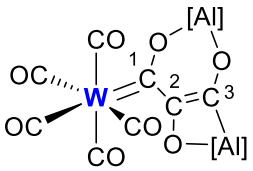
$^{13}C\{^{1}H\}$ NMR (101 MHz, C_6D_6, 353 K) δ 23.3 ({(***C***H_3)C}$_2$CH), 23.5 ({(***C***H_3)C}$_2$CH), 24.1 (***C***H_3)$_2$CH), 24.3 (***C***H_3)$_2$CH), 24.4 (***C***H_3)$_2$CH), 24.7 (***C***H_3)$_2$CH), 24.8 (***C***H_3)$_2$CH), 24.9 (***C***H_3)$_2$CH), 25.8 (***C***H_3)$_2$CH), 27.0 (***C***H_3)$_2$CH), 28.0 ((CH$_3$)$_2$***C***H), 28.1 ((CH$_3$)$_2$***C***H), 29.4 ((CH$_3$)$_2$***C***H), 29.4 ((CH$_3$)$_2$***C***H), 98.7 ({(CH$_3$)$_2$C}$_2$***C***H), 99.7 ({(CH$_3$)$_2$C}$_2$***C***H), 124.3 (Ar***C***), 124.8 (Ar***C***), 125.1 (Ar***C***), 125.2 (Ar***C***), 137.8, 139.2 (Ar***C***), 143.9 (Ar***C***), 144.0 (Ar***C***), 144.7 (***C***^{3}), 145.3 (Ar***C***), 146.3 (Ar***C***), 161.7 (***C***^{2}), 173.2 ({(CH$_3$)$_2$***C***}$_2$CH), 173.2 ({(CH$_3$)$_2$***C***}$_2$CH), 173.8 ({(CH$_3$)$_2$***C***}$_2$CH), 173.8 ({(CH$_3$)$_2$***C***}$_2$CH), 209.3 (Mo(***C***O)$_4$), 216.6 (Mo(***C***O)), 348.8 (***C***^{1}).

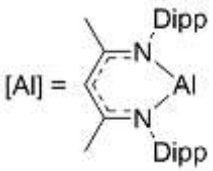
The Al–***C***^{4} resonance could not be observed in the ^{13}C NMR spectrum due to coupling to the quadrupolar ^{27}Al (I = 5/2) nucleus.

IR (ATR), ν_{CO} (cm^{-1}): 2050 (m),1916 (s), 1895 (s).

Anal. Calc. ($C_{67}H_{82}Al_2MoN_4O_9$): C, 65.04; H, 6.68; N, 4.53. Found: C, 65.03; H, 6.20; N, 4.10.

*Preparation of **2-3-W***





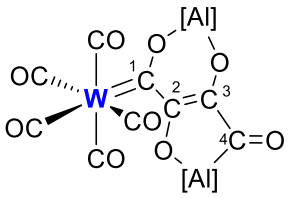
In a glovebox, a suspension of $[W(CO)_6]$ (7.0 mg, 0.20 mmol) in 0.3 mL of C_6D_6 was transferred to a J-Young NMR tube and frozen by cooling to –35°C. A suspension of **[Al]** (18 mg, 0.040 mmol) in 0.3 mL of benzene-d_6 was added to the frozen mixture. The J-Young NMR tube was quickly removed from the glovebox and placed into a –78°C dry ice/acetone bath. While the suspension was frozen, the headspace of the J-Young NMR tube was evacuated and refilled with CO (~1 bar) gas. The reaction was deemed complete once the reaction mixture had completely thawed, and the solution was a dark orange-brown colour. The J-Young NMR tube was returned to the glovebox and the reaction mixture was diluted with ca. 2 mL of toluene, transferred to a 20 mL scintillation vial, and **2-3-W** was recrystallised from toluene/*n*-hexane at –35°C. The mother liquor was removed by decantation, the solid washed with *n*-pentane (3 x 0.5 mL) and dried briefly under vacuum to afford **2-3-W** as bright orange crystals (15 mg, 12 mmol, 58% yield). X-ray quality crystals were obtained by recrystallisation from a concentrated toluene solution at –35°C.

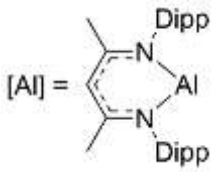
^{1}H NMR (400 MHz, C_6D_6, 298 K) δ 0.57 (d, $^3J_{HH}$ = 6.7 Hz, 6H, (C***H***$_3$)$_2$CH), 0.61 (d, $^3J_{HH}$ = 6.8 Hz, 6H, (C***H***$_3$)$_2$CH), 0.89 (d, $^3J_{HH}$ = 6.8 Hz, 6H, (C***H***$_3$)$_2$CH), 0.98 (d, $^3J_{HH}$ = 6.8 Hz, 6H, (C***H***$_3$)$_2$CH), 1.07 (d, $^3J_{HH}$ = 6.9 Hz, 6H, (C***H***$_3$)$_2$CH), 1.28 (d, $^3J_{HH}$ = 6.9 Hz, 6H, (C***H***$_3$)$_2$CH), 1.31 (d, $^3J_{HH}$ = 6.7 Hz, 6H, (C***H***$_3$)$_2$CH), 1.34 (s, 6H, {(C***H***$_3$)C}$_2$CH), 1.40 (s, 6H, {(C***H***$_3$)C}$_2$CH), 1.68 (d, $^3J_{HH}$ = 6.8 Hz, 6H, (C***H***$_3$)$_2$CH), 2.86 (hept, $^3J_{HH}$ = 6.8 Hz, 2H, 2x (CH$_3$)$_2$C***H***), 2.91 (hept, $^3J_{HH}$ = 6.8 Hz ,2H, 2x (CH$_3$)$_2$C***H***), 3.09 (hept, $^3J_{HH}$ = 6.7 Hz, 2H, 2x (CH$_3$)$_2$C***H***), 3.11 (hept, $^3J_{HH}$ = 6.7 Hz, 2H, 2x (CH$_3$)$_2$C***H***), 4.91 (s, 1H, {(CH$_3$)C}$_2$C***H***), 4.93 (s, 1H, {(CH$_3$)C}$_2$C***H***), 6.67 (m, 2H, Ar-***H***), 7.00 – 7.27 (m, 8H, Ar-***H***).

^{13}C NMR (101 MHz, C_6D_6, 298 K) δ 23.4 ({(***C***H$_3$)$_2$C}CH), 23.4 ({(***C***H$_3$)C}$_2$CH), 23.5 ((***C***H$_3$)$_2$CH), 24.0 ((***C***H$_3$)$_2$CH), 24.4 ((***C***H$_3$)$_2$CH), 24.6 ((***C***H$_3$)$_2$CH), 24.8 ((***C***H$_3$)$_2$CH), 25.0 ((***C***H$_3$)$_2$CH), 26.3 ((***C***H$_3$)$_2$CH), 26.7 ((***C***H$_3$)$_2$CH), 28.1 (2x (CH$_3$)$_2$***C***H), 28.8 (2x (CH$_3$)$_2$***C***H), 28.9 (2x (CH$_3$)$_2$***C***H), 29.2 (2x (CH$_3$)$_2$***C***H), 98.7 ({(CH$_3$)$_2$C}$_2$***C***H), 100.2 ({(CH$_3$)$_2$C}$_2$***C***H), 123.9 (Ar***C***), 124.3 (Ar***C***), 125.4 (Ar***C***), 126.0 (Ar***C***), 138.3 (Ar***C***), 138.9 (Ar***C***), 142.6 (Ar***C***), 142.7 (Ar***C***), 145.1 (Ar***C***), 146.3 (Ar***C***), 172.4 (***C***^{2}), 172.8 ({(CH$_3$)$_2$***C***}$_2$CH), 173.5 ({(CH$_3$)$_2$***C***}$_2$CH), 201.7 (W(***C***O)), 205.5 (W(***C***O)$_4$).

Anal. Calc. ($C_{66}H_{82}Al_2N_4O_8W$): C 61.11, H 6.37, N 4.32. Found: C 60.96, H 6.52, N 4.31.

*Preparation of **2-4-W***





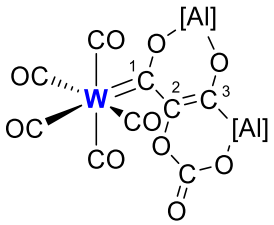
In a glovebox, a suspension of $[W(CO)_6]$ (7.0 mg, 0.20 mmol) in 0.3 mL of C_6D_6 was transferred to a J-Young NMR tube and frozen by cooling to –35°C. A suspension of **[Al]** (17.8 mg, 0.040 mmol) in 0.3 mL of benzene-d_6 was added. The J-Young NMR tube was quickly removed from the glovebox and placed into a -78°C dry ice/acetone bath. While the reaction mixture was frozen, the headspace of the J-Young NMR tube was evacuated and refilled with CO (~ 1 bar) gas. The resultant mixture was heated at 100°C and conversion to **2-4-W** was complete after 18 h, as monitored by ^{1}H NMR spectroscopy. The dark purple reaction mixture was diluted with ca. 2 mL of toluene, transferred to a 20 mL scintillation vial, concentrated and left to recrystallise in the freezer (–35°C). The mother liquor was removed by decantation and the resultant dark purple crystals washed with THF (1 x 0.3mL) and n-hexane (3 x 0.5 mL) to afford **2-4-W** (11 mg, 42% yield).

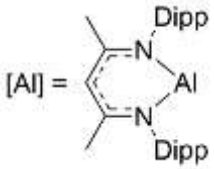
^{1}H NMR (400 MHz, C_6D_6, 298 K) δ 0.37 (d, $^3J_{HH}$ = 6.7 Hz, 6H, (C***H***$_3$)$_2$CH), 0.80 (d, $^3J_{HH}$ = 6.8 Hz, 6H, (C***H***$_3$)$_2$CH), 1.00 (d, $^3J_{HH}$ = 6.7 Hz, 6H, (C***H***$_3$)$_2$CH), 1.02 (d, $^3J_{HH}$ = 6.7 Hz, 6H, (C***H***$_3$)$_2$CH), 1.08 (d, $^3J_{HH}$ = 6.8 Hz, 6H, (C***H***$_3$)$_2$CH), 1.25 (d, $^3J_{HH}$ = 6.8 Hz, 6H, (C***H***$_3$)$_2$CH), 1.41 (s, 6H, {(C***H***$_3$)C}$_2$CH), 1.41 (s, 6H, {(C***H***$_3$)C}$_2$CH), 1.56 (d, $^3J_{HH}$ = 6.7 Hz, 6H, (C***H***$_3$)$_2$CH), 1.69 (d, $^3J_{HH}$ = 6.8 Hz, 6H, (C***H***$_3$)$_2$CH), 2.97 (hept, $^3J_{HH}$ = 6.7 Hz, 2H, 2x (CH$_3$)$_2$C***H***), 3.12 (hept, $^3J_{HH}$ = 6.8 Hz, 2H, 2x (CH$_3$)$_2$C***H***), 3.25 (hept, $^3J_{HH}$ = 7.0 Hz, 2H, 2x (CH$_3$)$_2$C***H***), 3.52 (hept, $^3J_{HH}$ = 6.7 Hz, 2H, 2x (CH$_3$)$_2$C***H***), 4.87 (s, 1H, {(CH$_3$)C}$_2$C***H***), 4.92 (s, 1H, {(CH$_3$)C}$_2$C***H***), 6.97 (m, 2H, Ar-***H***), 7.07 – 7.24 (m, 10H, Ar-***H***).

^{13}C NMR (101 MHz, C_6D_6, 298 K) δ 23.3 ({(***C***H$_3$)C}$_2$CH), 23.5 ({(***C***H$_3$)C}$_2$CH), 24.1 (2x (***C***H$_3$)$_2$CH), 24.3 ((***C***H$_3$)$_2$CH), 24.7 (2x (***C***H$_3$)$_2$CH), 24.9 ((***C***H$_3$)$_2$CH), 25.7 ((***C***H$_3$)$_2$CH), 27.0 ((***C***H$_3$)$_2$CH), 27.9 (2x (CH$_3$)$_2$***C***H), 28.0 (2x (CH$_3$)$_2$***C***H), 29.3 (2x (CH$_3$)$_2$***C***H), 29.4 (2x (CH$_3$)$_2$***C***H), 98.7 ({(CH$_3$)$_2$C}$_2$***C***H), 99.7 ({(CH$_3$)$_2$C}$_2$***C***H), 124.2 (Ar***C***), 124.7 (Ar***C***), 125.1 (Ar***C***), 125.1 (Ar***C***), 137.5 (Ar***C***), 138.8 (Ar***C***), 143.5 (Ar***C***), 143.7 (Ar***C***), 145.0 (Ar***C***), 145.9 (Ar***C***), 173.0 ({(CH$_3$)$_2$***C***}$_2$CH), 173.7 ({(CH$_3$)$_2$***C***}$_2$CH), 201.2 (W(***C***O)$_4$). Some quarternary ***C*** resonances cannot be observed due to the low solubility of **2-4-W**.

Anal calc'd ($C_{67}H_{82}Al_2N_4O_9W$): C 60.73, H 6.24, N 4.23. Found: C 60.64, H 6.29, N 4.28.

*Preparation of **2-7-W***



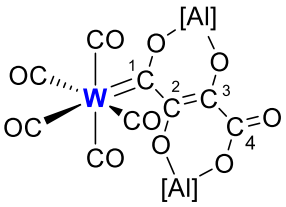


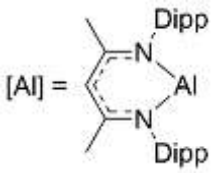
In a glovebox, a suspension of $[W(CO)_6]$ (3.5 mg, 0.10 mmol) in 0.3 mL of C_6D_6 was transferred to a J-Young NMR tube and frozen by cooling to –35°C. A suspension of **[Al]** (8.9 mg, 0.020 mmol) in 0.3 mL of C_6D_6 was added to the frozen mixture. The J-Young NMR tube was quickly removed from the glovebox and placed into a -78°C dry ice/acetone bath. While the suspension was frozen, the headspace of the J-Young NMR tube was evacuated and refilled with CO (~ 1 bar) gas. Upon warming, the formation of **2-3-W** was complete as observed by the complete consumption of **[Al]** in the ^{1}H NMR spectrum. The resultant mixture was degassed *via* the freeze-pump-thaw procedure thrice before an atmosphere of CO_2 gas (ca. 1 bar) introduced. The solution was set aside to allow for the recrystallization of **2-7-W** over a period of 7 days. The mother liquor was removed by decantation and the crystals washed with n-pentane (3 x 0.5 mL) and briefly dried under vacuum to afford **2-7-W** as red crystals (7.2 mg, 5.5 mmol, 55% yield).

^{1}H NMR (400 MHz, THF-d_8, 298 K) δ 0.15 (d, $^3J_{HH}$ = 6.8 Hz, 6H, (C***H***$_3$)$_2$CH), 0.55 (d, $^3J_{HH}$ = 6.8 Hz, 6H, (C***H***$_3$)$_2$CH), 0.85 (d, $^3J_{HH}$ = 6.8 Hz, 6H, (C***H***$_3$)$_2$CH), 1.02 (d, $^3J_{HH}$ = 6.6 Hz, 6H, (C***H***$_3$)$_2$CH), 1.09 (d, $^3J_{HH}$ = 6.7 Hz, 12H, 2x (C***H***$_3$)$_2$CH), 1.19 (d, $^3J_{HH}$ = 6.8 Hz, 6H, (C***H***$_3$)$_2$CH), 1.36 (d, $^3J_{HH}$ = 6.8 Hz, 6H, (C***H***$_3$)$_2$CH), 1.70 (s, 6H, {(C***H***$_3$)$_2$C}$_2$CH), 1.82 (s, 6H, {(C***H***$_3$)$_2$C}$_2$CH), 2.68 (hept overlapping, $^3J_{HH}$ = 6.8 Hz, 4H, 4x (CH$_3$)$_2$C***H***), 2.93 (hept, $^3J_{HH}$ = 6.8 Hz, 2H, 2x (CH$_3$)$_2$C***H***), 3.14 (hept, $^3J_{HH}$ = 6.8 Hz, 2H, 2x (CH$_3$)$_2$C***H***), 5.55 (s, 1H, {(CH$_3$)C}$_2$C***H***), 5.97 (s, 1H, {(CH$_3$)C}$_2$C***H***), 6.46 (m, 2H, Ar-***H***), 7.02 – 7.53 (m, 10H, Ar-***H***).

The reversible formation of **2-7-W** in combination with its low solubility in common solvents (benzene, toluene, THF) precluded the acquisition of spectroscopic data beyond ^{1}H NMR spectroscopic and single-crystal X-ray diffraction data.

*Preparation of **2-8-W***





In a glovebox, a suspension of [$W(CO)_6$] (7.0 mg, 0.20 mmol) in 0.300 mL of benzene-d_6 was transferred to a J-Young NMR tube and frozen by cooling to –35°C. A suspension of **[Al]** (18 mg, 0.040 mmol) in 0.300 mL of benzene-d_6 was added to the frozen mixture. The J-Young NMR tube was quickly removed from the glovebox and placed into a -78°C dry ice/acetone bath. While the reaction mixture was frozen, the headspace of the J-Young NMR tube was evacuated and refilled with ca. 1 bar of CO gas. Upon warming, the formation of **2-3-W** was complete as observed by the complete consumption of **[Al]** in the ^{1}H NMR spectrum. Upon warming, the formation of **2-3-W** was complete as observed by the complete consumption of **[Al]** in the ^{1}H NMR spectrum. The mixture was degassed *via* the freeze-pump-thaw method thrice and an atmosphere of CO_2 (ca. 1 bar) was introduced. The reaction mixture was heated at 100°C and conversion to **2-8-W** was complete after 48 h as monitored by ^{1}H NMR spectroscopy. The J-Young NMR tube was returned to the glovebox and the reaction mixture was diluted with ca. 2 mL of toluene, concentrated, and transferred to a 20 mL scintillation vial and **2-8-W** was crystallised from toluene/hexane (1:4) at -35°C. The mother liquor was removed by decantation and the crystals washed with pentane (3 x 0.5 mL) and dried under vacuum to afford **2-8-W** as red crystals (14 mg, 11 mmol, 53% yield).

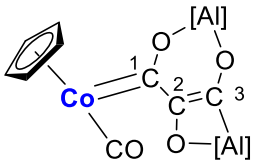
^{1}H NMR (400 MHz, C_6D_6, 298 K) δ 0.78 (d, $^3J_{HH}$ = 6.6 Hz, 6H, (C***H***$_3$)$_2$CH), 0.81 (d, $^3J_{HH}$ = 6.7 Hz, 6H, (C***H***$_3$)$_2$CH), 0.84 (d, $^3J_{HH}$ = 6.7 Hz, 6H, (C***H***$_3$)$_2$CH), 1.03 (d, $^3J_{HH}$ = 6.8 Hz, 6H, (C***H***$_3$)$_2$CH), 1.07 (d, $^3J_{HH}$ = 6.8 Hz, 6H, (C***H***$_3$)$_2$CH), 1.28 (d, $^3J_{HH}$ = 6.8 Hz, 6H, (C***H***$_3$)$_2$CH), 1.37 (s, 6H, {(C***H***$_3$)C}$_2$CH), 1.42 (d, $^3J_{HH}$ = 7.1 Hz, 6H, (C***H***$_3$)$_2$CH), 1.43 (s, 6H, {(C***H***$_3$)C}$_2$CH), 1.65 (d, $^3J_{HH}$ = 6.8 Hz, 6H, (C***H***$_3$)$_2$CH), 3.09 (hept, $^3J_{HH}$ = 6.7 Hz, 2H, 2x (CH$_3$)$_2$C***H***), 3.15 (hept, $^3J_{HH}$ = 6.8 Hz, 2H, 2x (CH$_3$)$_2$C***H***), 3.28 (hept, $^3J_{HH}$ = 6.7 Hz, 2H, 2x (CH$_3$)$_2$C***H***), 3.50 (hept, $^3J_{HH}$ = 6.7 Hz, 2H, 2x (CH$_3$)$_2$C***H***), 4.90 (s, 1H, {(CH$_3$)C}$_2$C***H***), 4.96 (s, 1H, {(CH$_3$)C}$_2$C***H***), 7.05 (m, 12H, Ar-***H***).

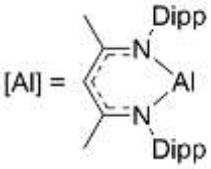
13C NMR (101 MHz, C_6D_6) δ 23.4 ({(***C***H$_3$)C}$_2$CH), 23.7 ({(***C***H$_3$)C}$_2$CH), 24.1 ((***C***H$_3$)$_2$CH), 24.4 ((***C***H$_3$)$_2$CH), 24.6 ((***C***H$_3$)$_2$CH), 24.8 ((***C***H$_3$)$_2$CH), 25.1 ((***C***H$_3$)$_2$CH), 25.1 ((***C***H$_3$)$_2$CH), 25.6 ((***C***H$_3$)$_2$CH), 26.3 ((***C***H$_3$)$_2$CH), 28.0 (2x (CH$_3$)$_2$***C***H), 28.1 (2x (CH$_3$)$_2$***C***H), 29.0 (2x (CH$_3$)$_2$***C***H), 29.4 (2x (CH$_3$)$_2$***C***H), 99.2 ({(CH$_3$)$_2$C}$_2$***C***H), 100.2 ({(CH$_3$)$_2$C}$_2$***C***H), 124.7 (Ar***C***), 124.8 (Ar***C***), 125.1 (Ar***C***), 125.5 (Ar***C***), 131.2 (***C***^{2}) 137.8 (Ar***C***), 138.3 (Ar***C***), 143.5 (Ar***C***), 144.3 (Ar***C***), 145.2 (Ar***C***), 145.8 (Ar***C***), 155.1 (***C***^{3}) 173.4 ({(CH$_3$)$_2$***C***}$_2$CH), 174.1 ({(CH$_3$)$_2$***C***}$_2$CH), 201.3 ($W(CO)_4$), 326.3 (***C***^{1}). Some

Ar***C*** are not observed due to overlap with the benzene ^{13}C resonance. C^{1-4} resonances have been assigned from the ^{13}C labelled isotoplogues (See Section 2.4.2 for details).

Anal calc'd ($C_{67}H_{82}Al_2N_4O_9W$): C 60.00, H 6.16, N 4.18. Found C 60.43 H 7.02, N 4.15.

*Preparation of **2-3-Co***





In a glovebox, a solution of **[Al]** (36 mg, 0.08 mmol, 2 equiv) in C_6D_6 (0.6 mL) was equally divided into two separate J-Young NMR tubes. The solutions were frozen using a low-temperature reactor cooled to –35°C. A solution of [(η^5-C_5H_5)Co(CO)$_2$] (6.0 µL, 8.2 mg, 0.044 mmol, 1.1 equiv) in C_6D_6 (0.6 mL) was divided into two portions (2x 0.3 mL) and one portion was added to each NMR tube. Care was taken to ensure that the reaction mixture in each NMR tube remained frozen. The headspace of each NMR tube was evacuated, and the NMR tubes were removed from the glovebox quickly and placed into a liquid-nitrogen bath (–196°C). The NMR tubes were removed from the liquid nitrogen bath and CO gas (~ 1 bar) was introduced into the tubes while the mixture was still frozen. Upon addition of CO gas, the mixture was allowed to thaw, and during this process the tube was shaken vigorously to ensure incorporation of CO gas into solution. The reaction was assumed complete upon the formation of a dark homogeneous solution. The NMR tubes were returned to the glovebox, and the solutions from both NMR tubes were combined and decanted into neat n-heptane (~5 mL) in a 20 mL scintillation vial. The resultant solution was concentrated *in vacuo* until a precipitate began to form, at which point the solution was filtered. The residue was redissolved in the minimum amount of toluene (< 0.1 mL) and filtered. All organic fractions were combined. The resultant solution was placed in the glovebox freezer and **2-3-Co** was allowed to crystallise at –35°C as dark purple-red crystals. The supernatant was decanted, and the resultant crystals were washed with cold n-pentane thrice (3x 1mL) before the crystals were dried briefly *in vacuo* (~2 minutes). Yield: 21 mg, 0.019 mmol, 48%.

^{1}H NMR (400 MHz, C_6D_6, 298 K) δ 0.80 (d, $^3J_{HH}$ = 6.8 Hz, 6H, (C***H***$_3$)$_2$CH), 0.84 (s br, 6H, (C***H***$_3$)$_2$CH), 1.00 (d, $^3J_{HH}$ = 6.9 Hz, 6H, (C***H***$_3$)$_2$CH), 1.03 (d, $^3J_{HH}$ = 6.8 Hz, 6H, (C***H***$_3$)$_2$CH), 1.06 (d, $^3J_{HH}$ = 6.8 Hz, 6H, (C***H***$_3$)$_2$CH), 1.27 (s br, 6H, (C***H***$_3$)$_2$CH), 1.31 (d, $^3J_{HH}$ = 6.8 Hz, 6H, (C***H***$_3$)$_2$CH), 1.41 (s, 6H, {(C***H***$_3$)C}$_2$CH), 1.47 (s, 6H, {(C***H***$_3$)C}$_2$CH), 1.76 (s br, 6H, (C***H***$_3$)$_2$CH), 2.86 (hept, $^3J_{HH}$ = 6.7 Hz, 2H, 2x (CH$_3$)$_2$C***H***), 2.89 (hept, $^3J_{HH}$ = 6.8 Hz, 2H, 2x (CH$_3$)$_2$C***H***), 3.28 (hept, $^3J_{HH}$ = 6.7 Hz, 2H, 2x (CH$_3$)$_2$C***H***), 3.41 (hept, $^3J_{HH}$ = 6.7 Hz, 2H, 2x (CH$_3$)$_2$C***H***), 4.87 (s, 1H, {(CH$_3$)C}$_2$C***H***), 4.94 (s, 1H, {(CH$_3$)C}$_2$C***H***), 5.02 (s, 5H, Cp-***H***), 6.59 – 6.78 (m, 2H, Ar-***H***), 7.00-7.25 (m, 10H, Ar-***H***).

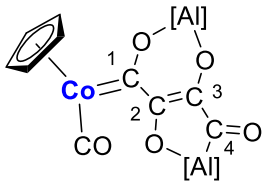
^{13}C NMR (101 MHz, C_6D_6, 298 K) δ 23.2 ({(***C***H_3)C}$_2$CH), 23.4 ({(***C***H_3)C}$_2$CH), 24.4 ((***C***H_3)$_2$CH), 24.6 ((***C***H_3)$_2$CH), 24.6 ((***C***H_3)$_2$CH), 24.9 (2x (***C***H_3)$_2$CH), 24.9 ((***C***H_3)$_2$CH), 26.5 ((***C***H_3)$_2$CH), 27.4 ((***C***H_3)$_2$CH), 28.6 (2x (CH_3)$_2$***C***H), 28.2 (2x (CH_3)$_2$***C***H), 28.8 (2x (CH_3)$_2$***C***H), 29.3 (2x (CH_3)$_2$***C***H), 85.1 (5x Cp'***C***H), 98.0 ({(CH_3)$_2$C}$_2$***C***H), 98.7 ({(CH_3)$_2$C}$_2$***C***H), 123.6 (Ar***C***), 124.0 (Ar***C***), 125.0 (Ar***C***), 125.9 (Ar***C***), 127.1 (Ar***C***), 128.6 (Ar***C***), 138.5 (Ar***C***), 139.4 (Ar***C***), 142.4 (Ar***C***), 142.9 (Ar***C***), 145.2 (Ar***C***), 145.8 (Ar***C***), 171.7 ({(CH_3)$_2$***C***}$_2$CH), 172.1 ({(CH_3)$_2$***C***}$_2$CH).

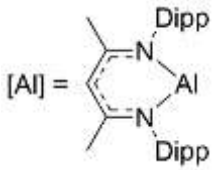
The Al–***C³*** and Co–***C¹*** resonance could not be observed in the ^{13}C NMR spectrum due to coupling to the quadrupolar ^{27}Al (I = 5/2) and ^{59}Co (I = 7/2) nuclei respectively. The low solubility of **2-3-Co** in C_6D_6 precluded observation of the ***C²*** resonance.

IR (ATR), ν_{CO} (cm^{-1}): 1938 (s).

Anal. Calc. ($C_{67}H_{87}Al_2CoN_4O_4$): C, 71.51; H, 7.79; N, 4.98. Found: C, 68.63; H, 7.44; N, 5.07. The low C content, but accurate H and N content likely reflect limitations of the technique (e.g. incomplete C combustion).

*Preparation of **2-4-Co***





In a glovebox, to an NMR tube charged with a frozen suspension of **[Al]** (26 mg, 0.058 mmol, 2 equiv) in C_6D_6 (0.3 mL) was added a solution of [(η^5-C_5H_5)Co(CO)$_2$] (4.0 µL, 5.5 mg, 0.029 mmol, 1 equiv) in C_6D_6 (0.3 mL). Care was taken to ensure that the reaction mixture remained frozen and that the reagents do not mix. The headspace of the NMR tube was evacuated, and the NMR tube was removed from the glovebox quickly and placed into a liquid-nitrogen bath (–196°C) to keep the suspension frozen. The NMR tube was removed from the liquid nitrogen bath and CO gas (~ 1 bar) was introduced while the mixture was still frozen. Upon addition of CO gas, the mixture was allowed to thaw, and during this process the tube was shaken vigorously to ensure incorporation of CO gas into solution. The CO atmosphere of the J-Young NMR tube was refreshed at this timepoint. The NMR tube was then heated at 100°C for 18 h. The NMR tube was returned to the glovebox, diluted with toluene (~0.6 mL). The reaction mixture was concentrated *in vacuo* until ~0.3 mL of the solution remains, at which point the solution was filtered and n-pentane (~2 mL) was layered on top of the filtrate. The resultant solution was placed in the glovebox freezer and **2-4-Co** was allowed to crystallize at –35 °C as black needles. The supernatant was decanted, and the resultant crystals were washed with cold n-pentane thrice (3 x 1mL) before the crystals were dried briefly *in vacuo* (~2 min). Yield: 18 mg, 0.016 mmol, 54%.

^{1}H NMR (400 MHz, C_6D_6, 298 K) δ 0.37 (d, $^3J_{HH}$ = 6.6 Hz, 6H, (C***H***$_3$)$_2$CH), 0.87 (d, $^3J_{HH}$ = 6.7 Hz, 6H, (C***H***$_3$)$_2$CH), 1.07 (d, $^3J_{HH}$ = 6.5 Hz, 6H, (C***H***$_3$)$_2$CH), 1.08 (d, $^3J_{HH}$ = 6.8 Hz, 6H, (C***H***$_3$)$_2$CH), 1.08 (d, $^3J_{HH}$ = 6.7 Hz, 6H, (C***H***$_3$)$_2$CH), 1.35 (d, $^3J_{HH}$ = 6.8 Hz, 6H, (C***H***$_3$)$_2$CH), 1.45 (s, 6H, {(C***H***$_3$)C}$_2$CH), 1.46 (s, 6H, {(C***H***$_3$)C}$_2$CH), 1.61 (d, $^3J_{HH}$ = 6.8 Hz, 6H, (C***H***$_3$)$_2$CH), 1.66 (d, $^3J_{HH}$ = 6.7 Hz, 6H, (C***H***$_3$)$_2$CH), 3.08 (hept, $^3J_{HH}$ = 6.6 Hz, 2H, (CH$_3$)$_2$C***H***), 3.18 (hept, $^3J_{HH}$ = 6.8 Hz, 2H, (CH$_3$)$_2$C***H***), 3.22 (hept, $^3J_{HH}$ = 6.6 Hz, 2H, (CH$_3$)$_2$C***H***), 3.65 (hept, $^3J_{HH}$ = 6.6 Hz, 2H, (CH$_3$)$_2$C***H***), 4.64 (s, 5H, 5x **Cp-H**), 4.78 (s, 1H, {(CH$_3$)C}$_2$C***H***), 4.93 (s, 1H, {(CH$_3$)C}$_2$C***H***), 7.00 – 7.31 (m, 12H, Ar-***H***).

^{13}C NMR (101 MHz, C_6D_6, 298 K) δ 23.2 ({(***C***H$_3$)C}$_2$CH), 23.3 ({(***C***H$_3$)C}$_2$CH), 24.3 (2x (***C***H$_3$)$_2$CH), 24.6 ((***C***H$_3$)$_2$CH), 24.7 ((***C***H$_3$)$_2$CH), 24.9 ((***C***H$_3$)$_2$CH), 25.0 (2x (***C***H$_3$)$_2$CH), 27.0 ((***C***H$_3$)$_2$CH), 28.1 (2x (CH$_3$)$_2$***C***H), 28.1 (2x (CH$_3$)$_2$***C***H), 29.1 (2x (CH$_3$)$_2$***C***H), 29.6 (2x (CH$_3$)$_2$***C***H), 84.9 (Cp-***C***H), 98.6

({{CH_3)$_2$C}$_2$***C***H), 98.8 ({{CH_3)$_2$C}$_2$***C***H), 124.0 (Ar***C***), 124.2 (Ar***C***), 125.0 (Ar***C***), 125.3 (Ar***C***), 127.6 (Ar***C***), 127.7 (Ar***C***), 137.3 (***C***^{2}), 138.6 (Ar***C***), 139.2 (Ar***C***), 143.2 (Ar***C***), 143.6 (Ar***C***), 145.6 (Ar***C***), 145.9 (Ar***C***), 163.5 (***C***^{3}), 172.0 ({{CH_3)$_2$***C***}$_2$CH), 172.4 ({{CH_3)$_2$***C***}$_2$CH).

The Al–***C***^{4} and Co–***C***^{1} resonance could not be observed in the ^{13}C NMR spectrum due to coupling to the quadrupolar ^{27}Al (I = 5/2) and ^{59}Co (I = 7/2) nuclei respectively.

IR (ATR), ν_{CO} (cm^{-1}): 1941 (s), 1569 (m).

2.4.3 – Labelling Experiments

In order to unequivocally assign chemical shifts for the carbon environments in the chain, ^{13}C labelled samples of **2-3-W, 2-4-W**, and **2-8-W** were synthesized. ^{13}C NMR spectra of the crude reaction mixtures are provided below.

*Labelling studies of **2-3-W***



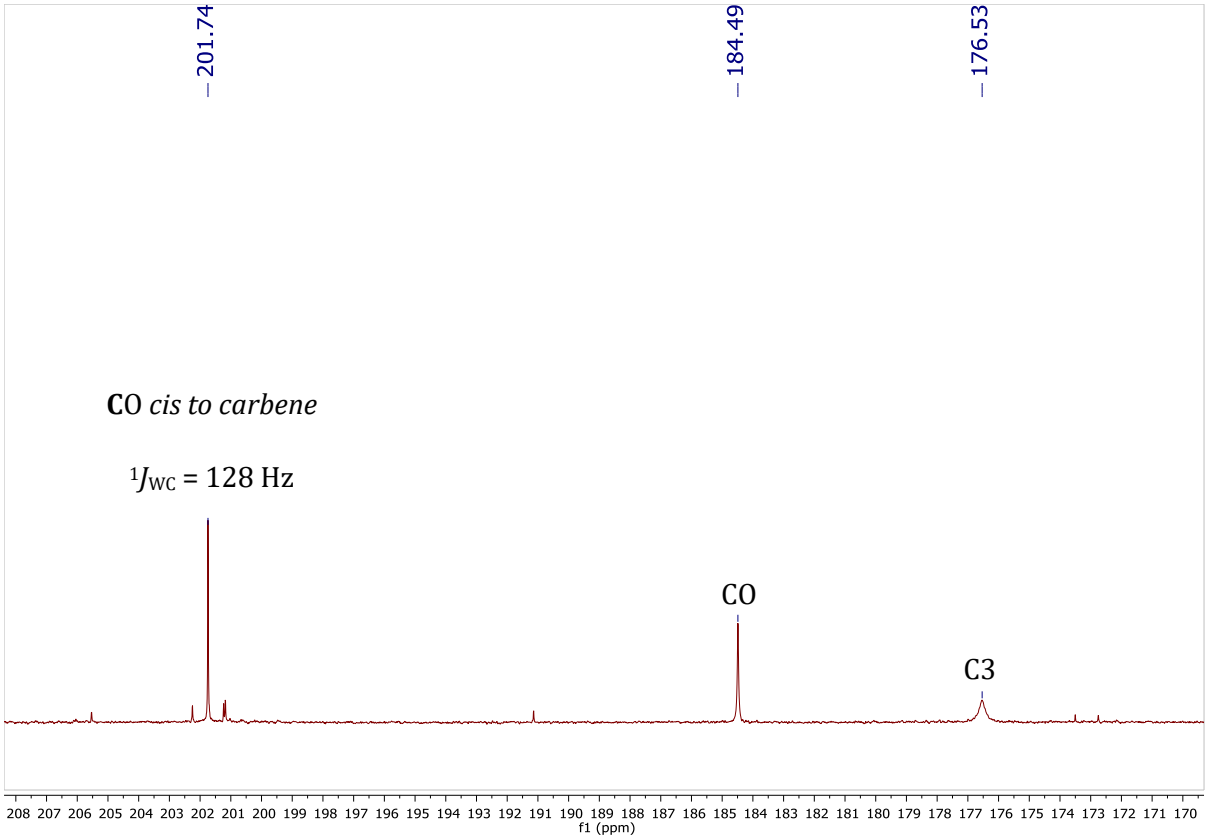


Figure 2.9: ^{13}C NMR spectrum of C^3 ^{13}C labelled **2-3-W.**

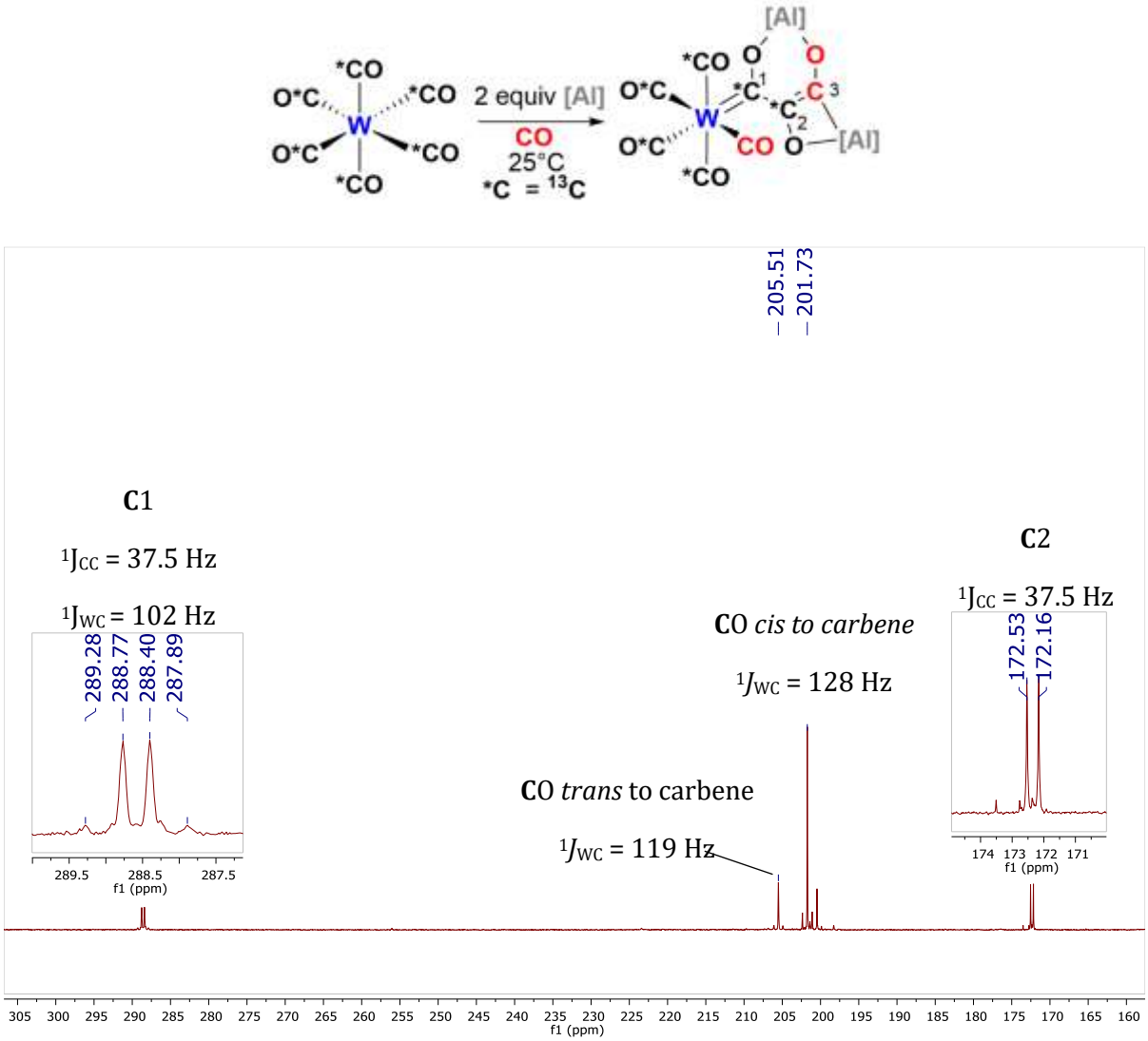


Figure 2.10: ^{13}C NMR spectrum of C^1 and C^2 ^{13}C labelled **2-3-W**.

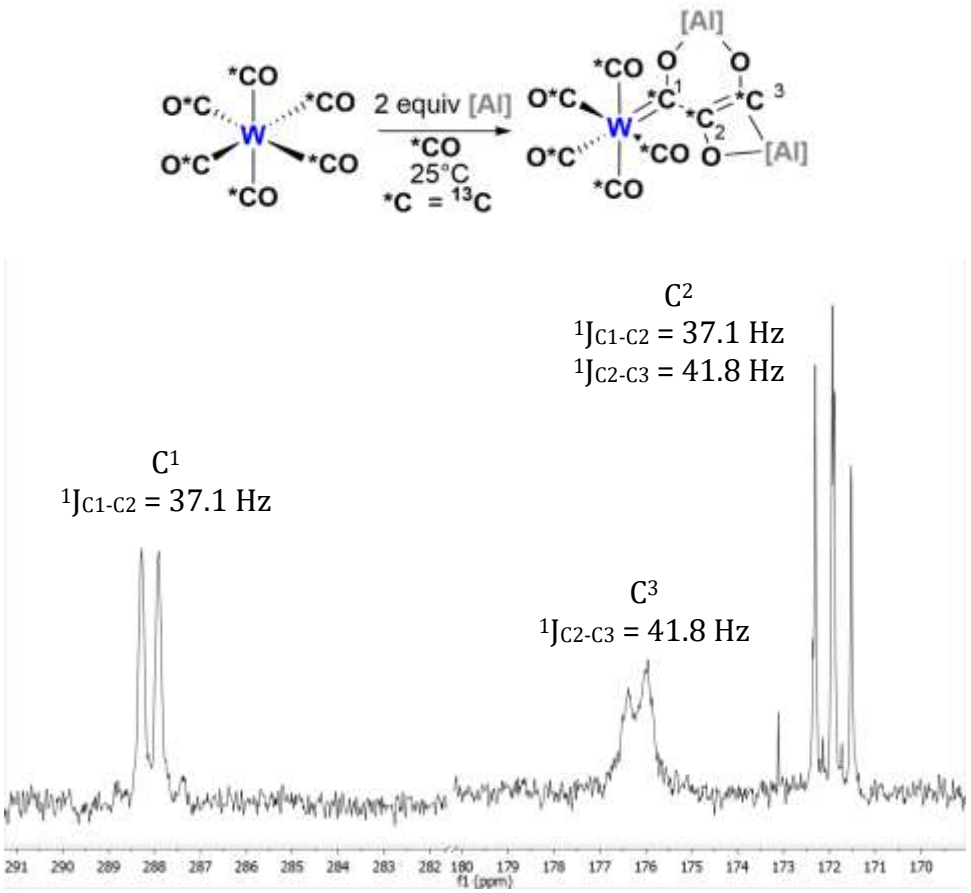


Figure 2.11: Expanded region of ^{13}C NMR spectrum depicting C^1, C^3, and C^3 resonances of ^{13}C labelled **2-3-W**.

Labelling studies of **2-8-W**

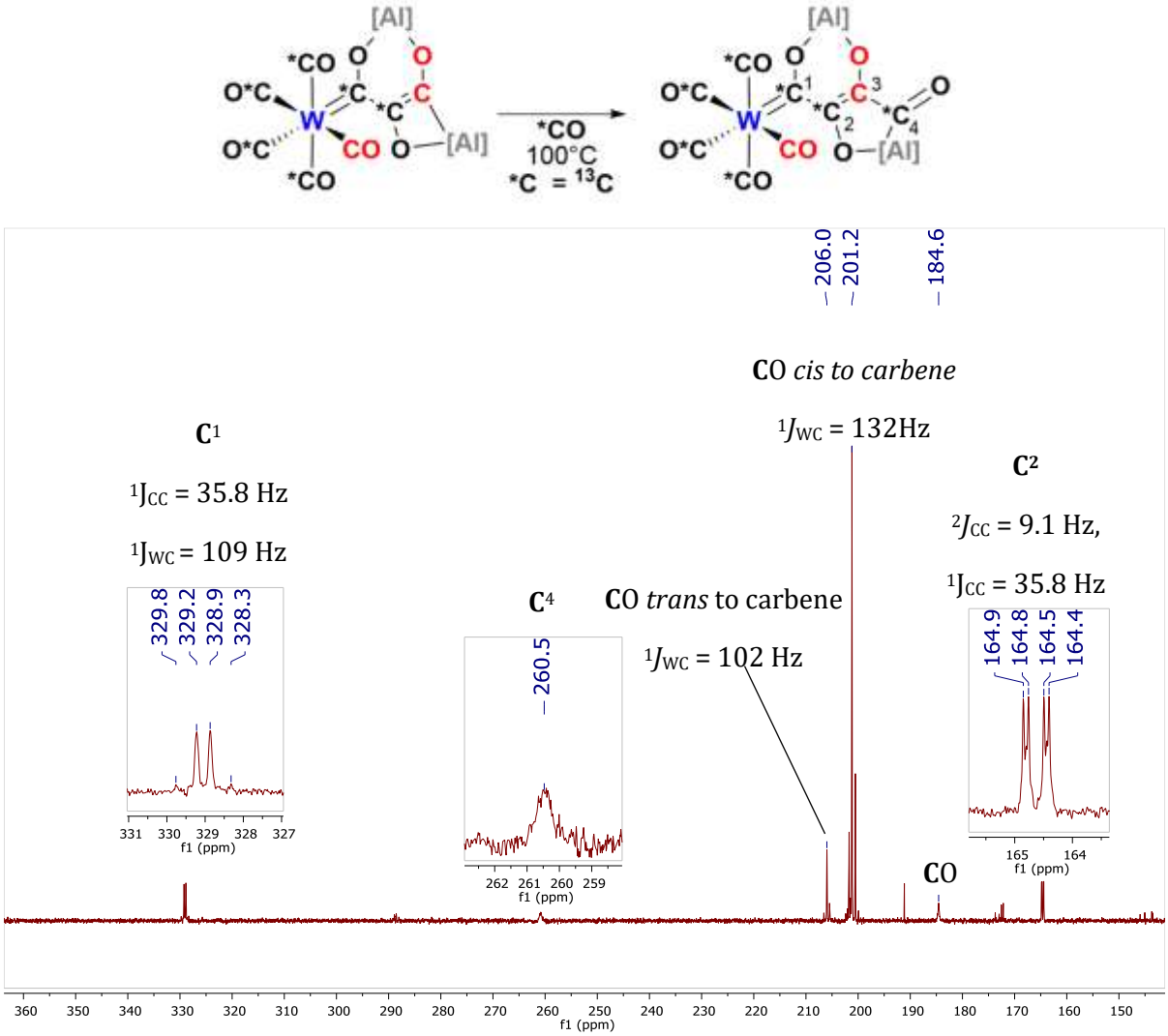


Figure 2.12: ^{13}C NMR spectrum of C^1, C^2, and C^4 ^{13}C labelled **2-8-W**.

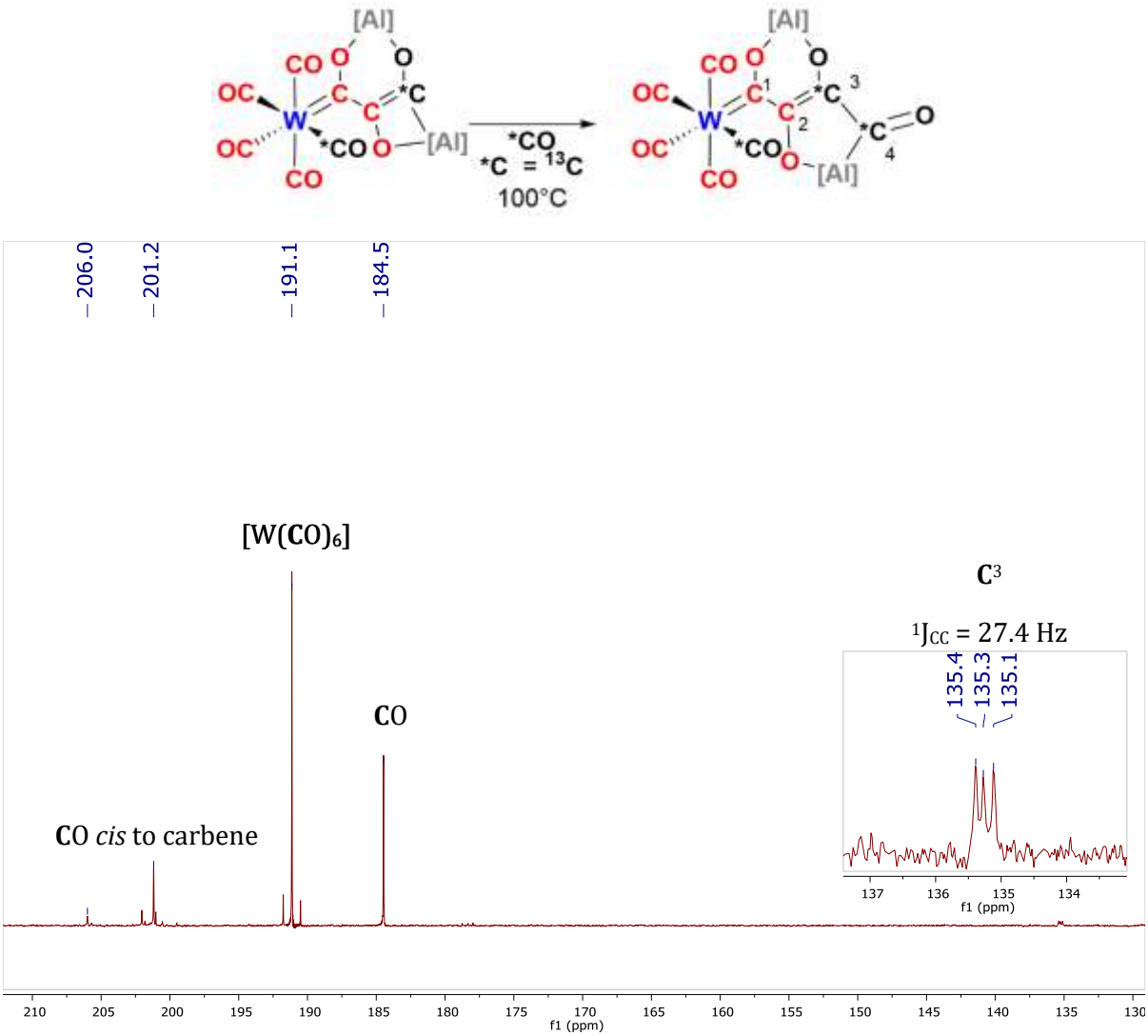


Figure 2.13: *^{13}C NMR spectrum of C^3 and C^4 labelled* **2-4-W**.

The multiplicity of C^3 is due to the ^{12}CO and ^{13}CO scrambling within the sample; leading to approximately a 1:2 ^{12}CO:^{13}CO labelling at C^4. The source appears to be exchange of atmospheric ^{13}CO with the compound at the *cis* and *trans* locations of the carbene as well as with $[W(CO)_6]$. Furthermore, in this sample, concentration limitations precluded the observation of C^4 due to quadrupolar broadening.

Labelling studies of **2-8-W**

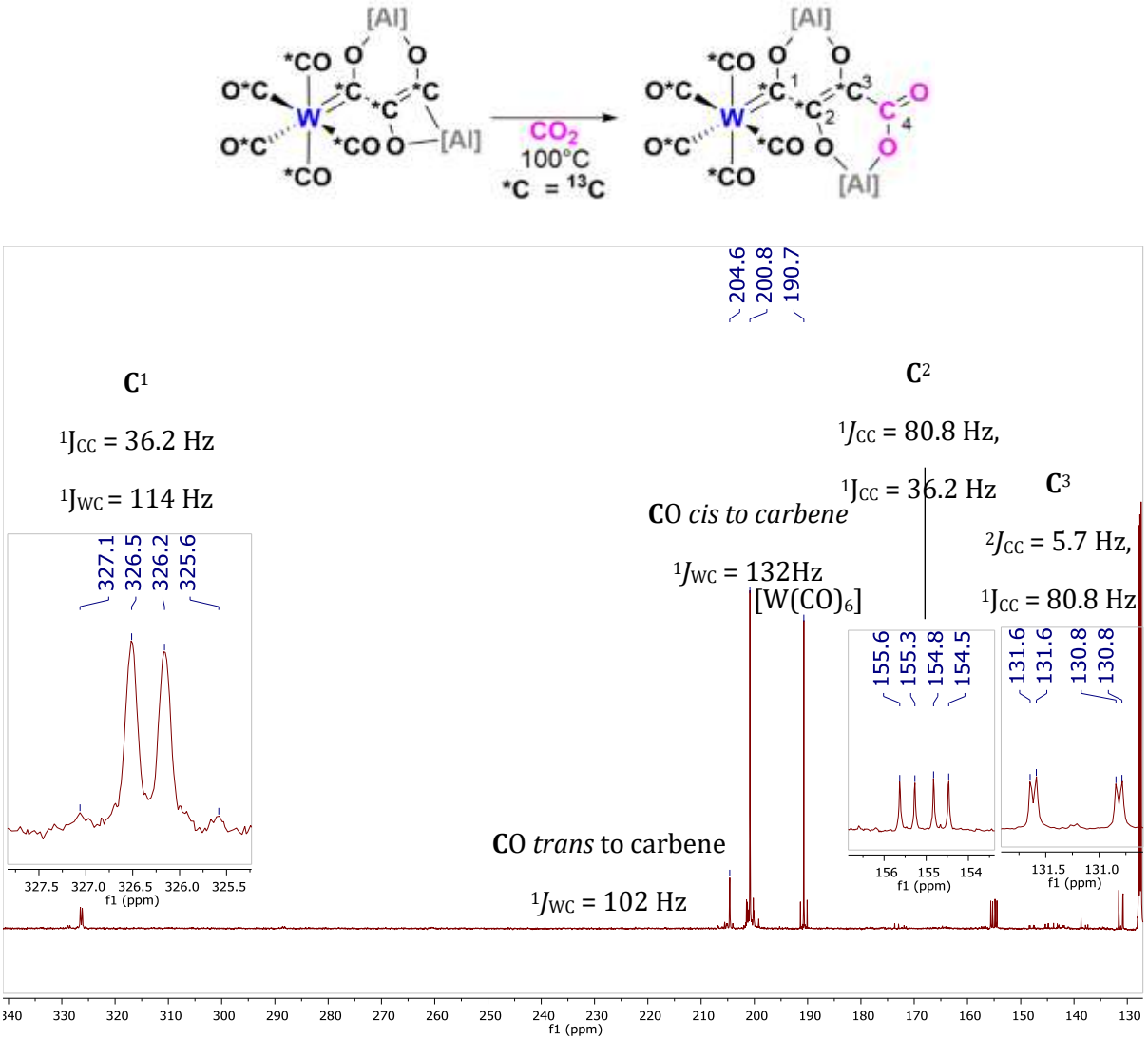


Figure 2.14: ^{13}C NMR spectrum of C^1, C^2, and C^3 ^{13}C labelled **2-8-W**.

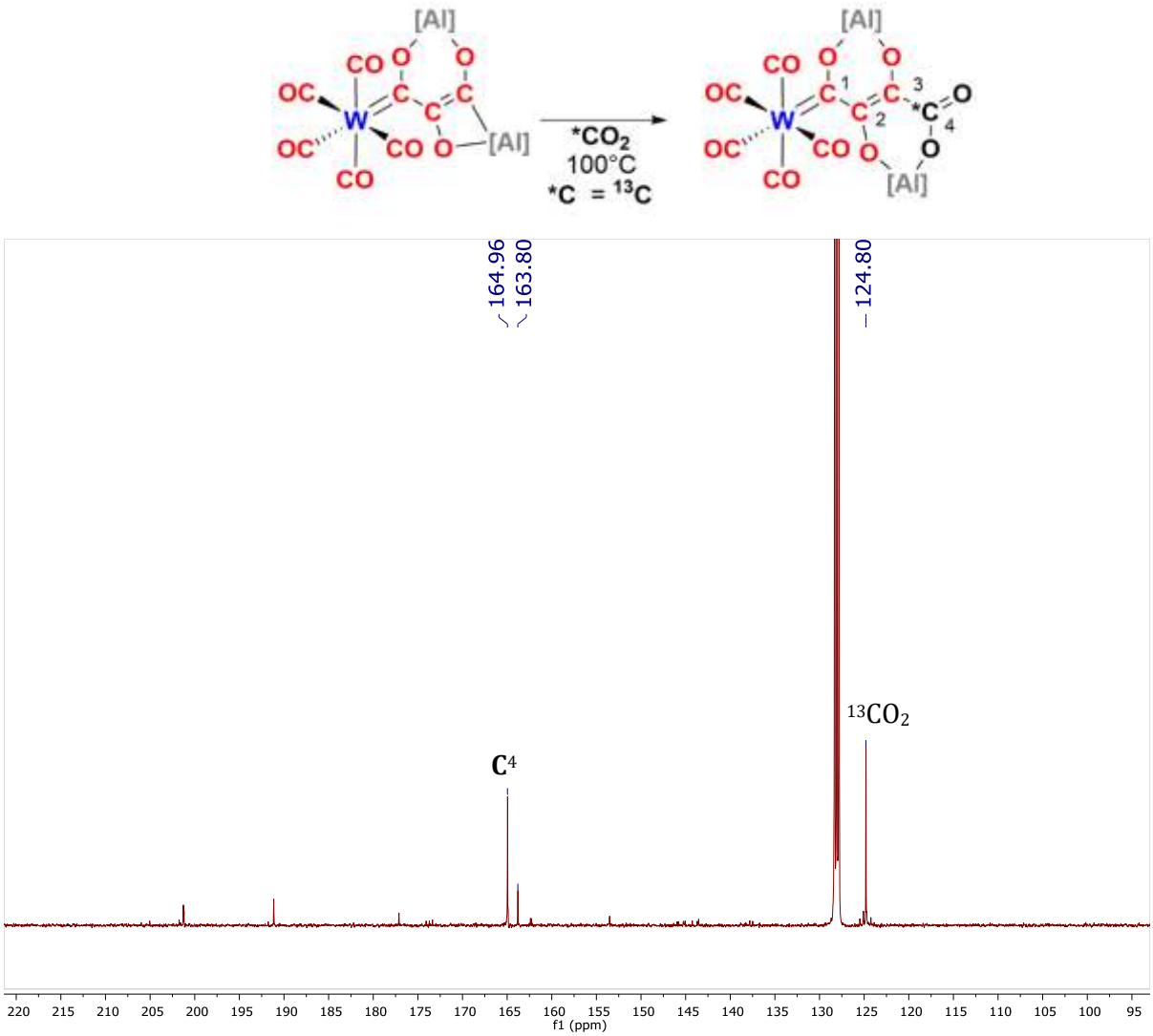


Figure 2.15: ^{13}C NMR spectrum of C^4 ^{13}C labelled **2-8-W**.

2.5 – X-Ray crystal structures

The X-ray structure of **2-2-Mn**

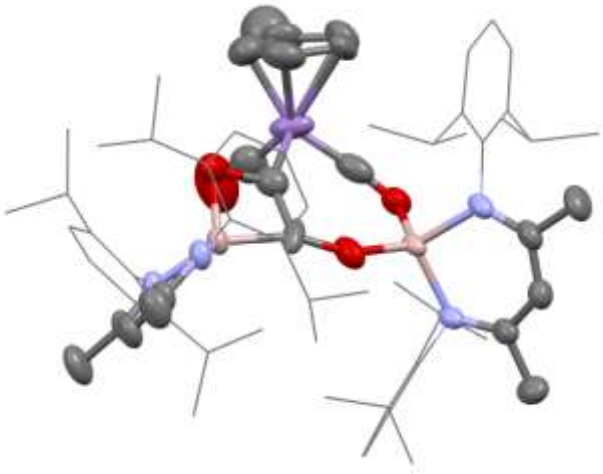


Figure 2.16: The X-ray structure of **2-2-Mn**.

2-2-Mn was found to crystallise in the $P2_1/n$ space group with one included hexane molecule in the asymmetric unit for a total of four within the unit cell.

The methylcyclopentadienyl ligand on manganese was found to be disordered. The carbon atoms C5>C10 were modelled as disordered over two sites in *ca.* 55:45 occupancies for the major and minor orientations respectively. The thermal parameters of adjacent atoms in the major and minor components were restrained to be similar, and only the non-hydrogen atoms in the major orientation were refined anisotropically (those in the minor orientation were refined isotropically).

The included hexane molecule was found to be disordered. The carbon atoms C69>C74 were modelled as disordered over two sites in *ca.* 74:26 occupancies for the major and minor orientations respectively. The thermal parameters of adjacent atoms in the major and minor components were restrained to be similar, their geometries optimized, and only the non-hydrogen atoms in the major orientation were refined anisotropically (those in the minor orientation were refined isotropically).

Crystal Data for $C_{74}H_{103}Al_2MnN_4O_4$, M =1221.50, monoclinic, space group $P2_1/n$ (no. 14), a = 12.8408(5) Å, b = 27.5925(9) Å, c = 19.8503(6) Å, β = 92.256(3)°, V = 7027.7(4) Å^3, Z = 4, ρ_{calc}g/cm^3 = 1.154, μ(MoKα) = 0.262 mm^{-1}, T = 173.00(14), black blocks, F^2 refinement, R_1(obs) = 0.0843, wR_2(all) = 0.2668, 14077 independent observed reflections (R_{int} = 0.0309), 8735 independent measured reflections [$|F_o| > 4\sigma(|F_o|)$, $2\theta_{full}$ = 56.704], 820 parameters. CCDC 2095244.

The X-ray structure of **2-3-Mn**

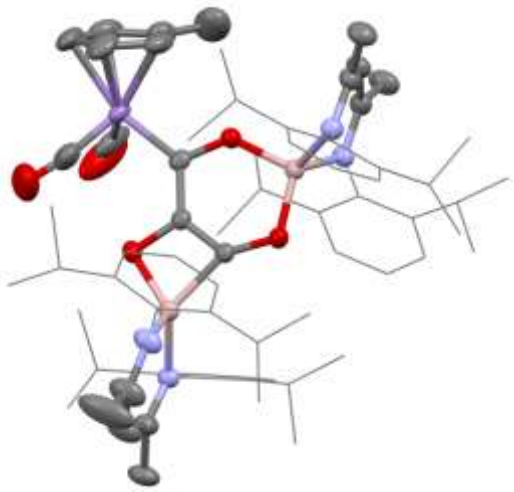


Figure 2.17: The X-ray structure of **2-3-Mn**.

2-3-Mn was found to crystallise in the $P2_1/n$ space group with one included toluene molecule for a total of four within the unit cell.

The included benzene molecule (C70>C76) was found to be disordered. As a result the molecule was modelled as disordered over two sites in *ca.* 63:37 occupancies for the major and minor orientations respectively. The thermal parameters of adjacent atoms in the major and minor components were restrained to be similar, and only the non-hydrogen atoms in the major orientation were refined anisotropically (those in the minor orientation were refined isotropically).

The iso-propyl group C52>C54 was found to be disordered. C53 and C54 were modelled as disordered over two sites in *ca.* 81:19 occupancies for the major and minor orientations respectively. The thermal parameters of adjacent atoms in the major and minor components were restrained to be similar, and only the non-hydrogen atoms in the major orientation were refined anisotropically (those in the minor orientation were refined isotropically).

Crystal Data for $C_{76}H_{96}Al_2MnN_4O_5$, M =1254.46, monoclinic, space group $P2_1/n$ (no. 14), a = 16.8912(5) Å, b = 20.7695(8) Å, c = 19.8211(8) Å, β = 90.526(3)°, V = 6953.4(4) Å^3, Z = 4, ρ_{calc}g/cm^3 = 1.198, μ(MoKα) = 0.268 mm^{-1}, T = 173.00(14), red blocks, F^2 refinement, R_1(obs) = 0.0765, wR_2(all) = 0.2194, 14003 independent observed reflections (R_{int} = 0.0484), 9373 independent measured reflections [$|F_o| > 4\sigma(|F_o|)$, $2\theta_{full}$ = 56.614], 844 parameters. CCDC 2095245.

The X-ray structure of **2-4-Mn**

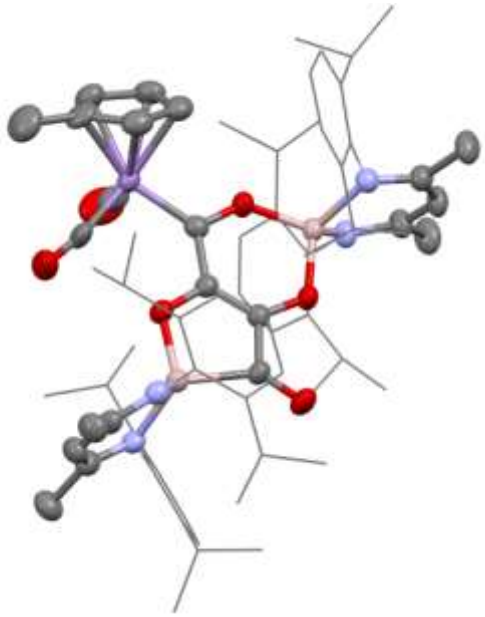


Figure 2.18: The X-ray crystal structure of **2-4-Mn**.

2-4-Mn was found to crystallise in the $P2_1/n$ space group with two included toluene molecules in the asymmetric unit, for a total of eight toluene molecules in the unit cell. The crystal was modelled as a two component twin in ca. 75:25 ratio. The two twin lattices are related by the approximate twin law [-1.0 0.0 0.0 0.0 -1.0 0.0 0.0 0.0 1.0].

The included toluene (C70>C77) was found to be disordered. As a result the molecule was modelled as disordered over two sites in *ca.* 65:35 occupancies for the major and minor orientations respectively. The thermal parameters of adjacent atoms in the major and minor components were restrained to be similar, and only the non-hydrogen atoms in the major orientation were refined anisotropically (those in the minor orientation were refined isotropically).

The included toluene (C78>C83) was found to be disordered. As a result the molecule was modelled as disordered over two sites in *ca.* 58:42 occupancies for the major and minor orientations respectively. The thermal parameters of adjacent atoms in the major and minor components were restrained to be similar, and only the non-hydrogen atoms in the major orientation were refined anisotropically (those in the minor orientation were refined isotropically).

Crystal Data for $C_{84}H_{105}Al_2MnN_4O_6$, M =1375.61, monoclinic, space group $P2_1/n$ (no. 14), a = 16.8869(7) Å, b = 22.7289(9) Å, c = 19.8568(9) Å, β = 91.256(4)°, V = 7619.7(6) Å^3, Z = 4, ρ_{calc}g/cm^3 = 1.199, μ(CuKα) = 2.057 mm^{-1}, T = 173.1(2), red blocks, F^2 refinement, R_1(obs) = 0.0752, wR_2(all) = 0.2248, 24570 independent observed reflections (R_{int} = 0.0737), 11769 independent measured reflections [$|F_o| > 4\sigma(|F_o|)$, $2\theta_{full}$ = 147.336], 909 parameters. CCDC 2095246.

The X-ray structure of **2-5-Mn**

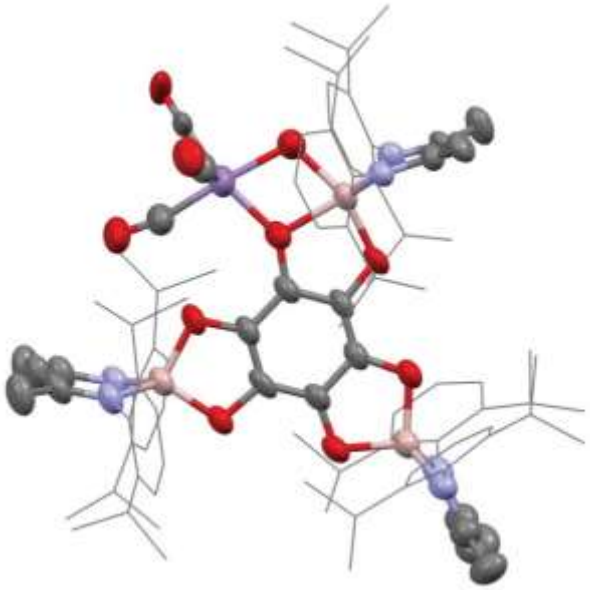


Figure 2.19: The X-ray crystal structure of **2-5-Mn**.

2-5-Mn crystallises in the P-1 space group with one molecule in the asymmetric unit. The carbonyl ligands including carbon atoms C7 and C8 were found to be in 50% occupancy on inspection of thermal ellipsoids. A convincing model of disorder could not be generated.

Crystal Data for $C_{95}H_{122}Al_3MnN_6O_9$, M =1627.86, triclinic, space group P-1 (no. 2), a = 15.5143(11) Å, b = 15.8666(9) Å, c = 23.7731(15) Å, α = 76.980(5)°, β = 85.364(5)°, γ = 72.188(6)°, V = 5427.8(6) Å^3, Z = 2, ρ_{calc}g/cm^3 = 0.996, μ(CuKα) = 1.609 mm^{-1}, T = 173.0(3), yellow plates, F^2 refinement, R_1(obs) = 0.1107, wR_2(all) = 0.3879, 20652 independent observed reflections (R_{int} = 0.1023), 8778 independent measured reflections [$|F_o| > 4\sigma(|F_o|)$, $2\theta_{full}$ = 146.898], 1075 parameters.

The X-ray structure of **2-3-Re**

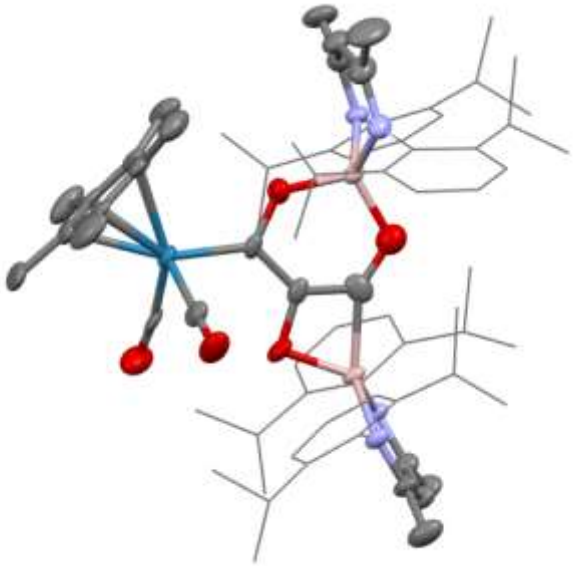


Figure 2.20: The solid-state structure of **2-3-Re**.

2-3-Re was found to crystallise in the Pbca space group. **2-3-Re** is isomorphous to **2-3-Re'** (*vide infra*) and as a result, both **2-3-Re** and **2-3-Re'** co-crystallise from the solution. ^{1}H NMR spectroscopy of the single crystals suggests that the **2-3-Re** and **2-3-Re'** compounds are present in the measured crystal in a ca. 75:25 ratio. As a result disorder of the two isomeric forms of the C1>C3 carbon chain (in **2-3-Re** and **2-3-Re'** respectively) were present. The high degree of overlap (Figure 2.21) between the two isomeric fragments precluded a reasonable model of the minor-component of the disorder. A single Q-peak ca. 1.0 Å away from C3 and corresponding to 2.0 e^{-} A^{-3} was observed and is consistent with a ca. 25% occupancy oxygen atom.

The iso-propyl group C30>C32 was found to be disordered. C31 and C32 were modelled as disordered over two sites in *ca.* 69:31 occupancies for the major and minor orientations respectively. The thermal parameters of adjacent atoms in the major and minor components were restrained to be similar, and their geometries were optimized.

The iso-propyl group C59>C61 was found to be disordered. C59>C61 were modelled as disordered over two sites in *ca.* 57:43 occupancies for the major and minor orientations respectively. The thermal parameters of adjacent atoms in the major and minor components were restrained to be similar, their geometries were optimized, and only the non-hydrogen atoms in the major orientation were refined anisotropically (those in the minor orientation were refined isotropically).

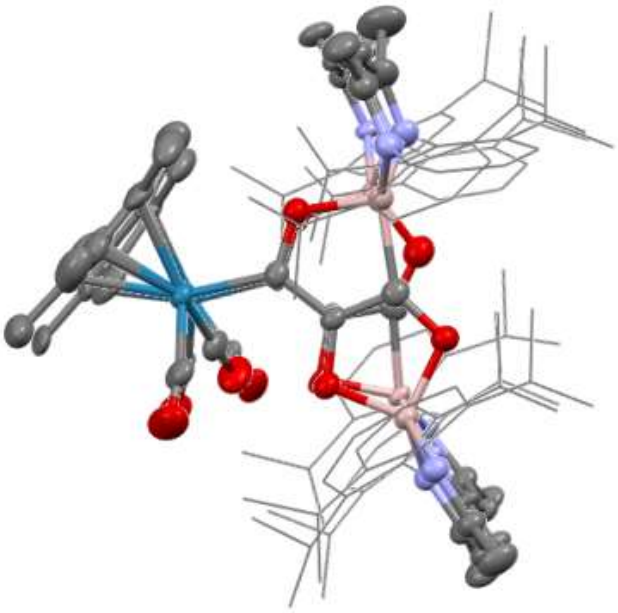


Figure 2.21: Overlay of **2-3-Re'** (front) and **2-3-Re** (behind).

2-3-Re crystallises with 1.5 pentane equivalents in the asymmetric unit, for a total of 12 pentane molecules within the unit cell. The included pentane molecule spanning carbon atoms C79>C83 was found to be in 50% occupancy and disordered over two positions in *ca*. 26:24 ratio for the major and minor orientations respectively. The thermal parameters of adjacent atoms in the major and minor components were restrained to be similar, their geometries were optimized, and only the non-hydrogen atoms in the major orientation were refined anisotropically (those in the minor orientation were refined isotropically).

The included pentane molecule spanning carbon atoms C74>C78 was found to be disordered over three positions in *ca.* 40:34:26 ratio for the three orientations. The thermal parameters of the entire disordered pentane component were restrained to be similar, their geometries were optimized, and all atoms were refined isotropically.

Crystal Data for $C_{80.5}H_{115}Al_2N_4O_5Re$, M =1458.92, orthorhombic, space group Pbca (no. 61), a = 45.706(2) Å, b = 17.2177(17) Å, c = 20.3938(17) Å, V = 16049(2) Å^3, Z = 8, ρ_{calc}g/cm^3 = 1.208, μ(MoKα) = 1.585 mm^{-1}, T = 173.00(14), red plates, F^2 refinement, R_1(obs) = 0.0766, wR_2(all) = 0.1662, 16110 independent observed reflections (R_{int} = 0.0589), 11818 independent measured reflections [$|F_o| > 4\sigma(|F_o|)$, $2\theta_{full}$ = 56.75], 956 parameters. CCDC 2095247.

The X-ray structure of **2-3-Re'**

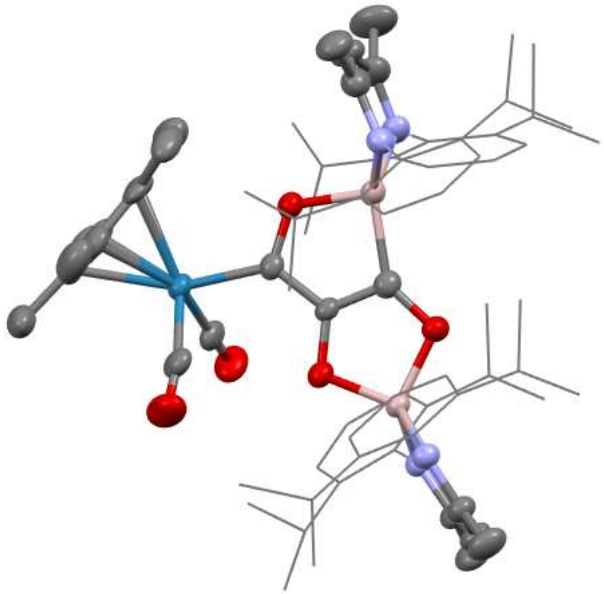


Figure S8: The X-ray structure of **2-3-Re'**.

2-3-Re' was found to crystallise in the Pbca space group with 0.25 of a toluene molecule and 0.25 of a pentane molecule included in the asymmetric unit for a total of four toluene molecules and four pentane molecules within the unit cell. The included toluene molecule was (C74>C79) was fixed at 25% occupancy on the basis of inspection of thermal parameters at various occupancies.

The included pentane (C81>C85) molecule was fixed at 25% occupancy on the basis of inspection of thermal parameters at various occupancies. The geometry of the molecule was optimized, and the thermal parameters of carbon atoms were restrained to be similar.

The iso-propyl group C27>C29 was found to be disordered. C28 and C29 were modelled as disordered over two sites in *ca.* 56:44 occupancies for the major and minor orientations respectively. The thermal parameters of adjacent atoms in the major and minor components were restrained to be similar, their geometries were optimized, and only the non-hydrogen atoms in the major orientation were refined anisotropically (those in the minor orientation were refined isotropically).

The iso-propyl group C68>C70 was found to be disordered. C69 and C70 were modelled as disordered over two sites in *ca.* 58:42 occupancies for the major and minor orientations respectively. The thermal parameters of adjacent atoms in the major and minor components were restrained to be similar, their geometries were optimized, and only the non-hydrogen

atoms in the major orientation were refined anisotropically (those in the minor orientation were refined isotropically).

Crystal Data for $C_{76}H_{102}Al_2N_4O_5Re$, M =1391.77, orthorhombic, space group Pbca (no. 61), a = 17.3541(4) Å, b = 20.3340(5) Å, c = 45.6601(19) Å, V = 16112.5(9) Å^3, Z = 8, ρ_{calc}g/cm^3 = 1.147, μ(CuKα) = 3.513 mm^{-1}, T = 173.00(14), yellow plates, F^2 refinement, R_1(obs) = 0.0535, wR_2(all) = 0.1669, 15643 independent observed reflections (R_{int} = 0.0447), 11650 independent measured reflections [$|F_o| > 4\sigma(|F_o|)$, $2\theta_{full}$ = 146.892], 849 parameters. CCDC 2095248.

The X-ray structure of **2-4-Re**

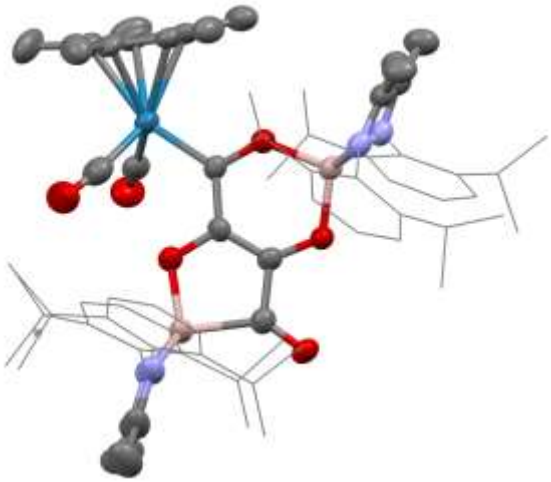


Figure 2.22: The X-ray crystal structure of **2-4-Re**.

2-4-Re was found to crystallise in the $P2_1/n$ space group with 1.5 benzene molecules in the asymmetric unit for a total of six within the unit cell.

The included benzene molecule (C80, C81, C83, C84, C86, C89) was modelled was modelled as disordered over two sites in *ca.* 75:25 occupancies for the major and minor orientations respectively. The thermal parameters of adjacent atoms in the major and minor components were restrained to be similar, and only the non-hydrogen atoms in the major orientation were refined anisotropically (those in the minor orientation were refined isotropically).

The included benzene molecule (C90, C92, C93, C96, C97, C100) was found to be disordered over a special position in two separate orientations. As a result the molecule was modelled as disordered over two sites in *ca.* 37:13 occupancies for the major and minor orientations respectively, to generate one 50% occupancy molecule of benzene (with the symmetry element generating the other 50%.). The thermal parameters of adjacent atoms in the major and minor components were restrained to be similar, and only the non-hydrogen atoms in the major orientation were refined anisotropically (those in the minor orientation were refined isotropically).

The iso-propyl group C55>C57 was found to be disordered. C55>C57 were modelled as disordered over two sites in *ca.* 75:25 occupancies for the major and minor orientations respectively. The thermal parameters of adjacent atoms in the major and minor components were restrained to be similar, and only the non-hydrogen atoms in the major orientation were refined anisotropically (those in the minor orientation were refined isotropically).

The iso-propyl group C70>C72 was found to be disordered. C55>C57 were modelled as disordered over two sites in *ca.* 62:38 occupancies for the major and minor orientations respectively. The thermal parameters of adjacent atoms in the major and minor components were restrained to be similar, and only the non-hydrogen atoms in the major orientation were refined anisotropically (those in the minor orientation were refined isotropically).

Crystal Data for $C_{83}H_{106}Al_2N_4O_6Re$, M =1495.87, monoclinic, space group $P2_1/n$ (no. 14), a = 13.5551(2) Å, b = 15.5294(3) Å, c = 36.6963(10) Å, β = 95.819(2)°, V = 7684.9(3) Å^3, Z = 4, ρ_{calc}g/cm^3 = 1.293, μ(CuKα) = 3.731 mm^{-1}, T = 173.1(2), red plates, F^2 refinement, R_1(obs) = 0.0491, wR_2(all) = 0.1287, 14739 independent observed reflections (R_{int} = 0.0461), 10643 independent measured reflections [$|F_o| > 4\sigma(|F_o|)$, $2\theta_{full}$ = 146.804], 918 parameters. CCDC 2095249.

The X-ray structure of **2-3-Cr**

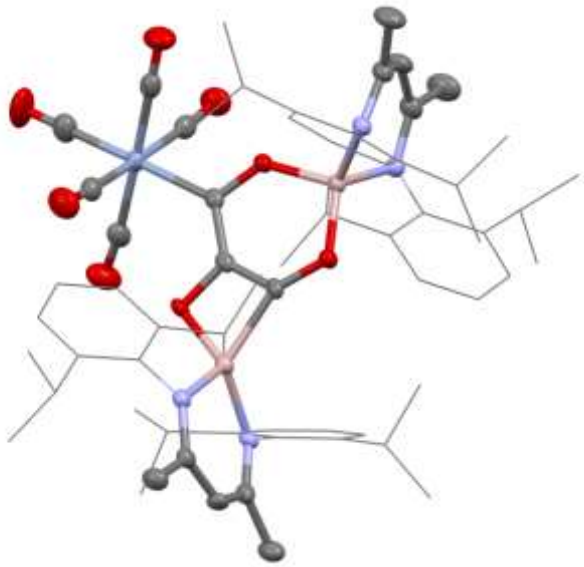


Figure S10: The X-ray crystal structure of **2-3-Cr**.

2-3-Cr was found to crystallise in the $P2_1/c$ space group, with 3.5 molecules of benzene in the asymmetric unit for a total of 14 benzene molecules in the unit cell.

The iso-propyl group C20>C22 was found to be disordered. C21 and C22 were modelled as disordered over two sites in *ca.* 69:31 occupancies for the major and minor orientations respectively. The thermal parameters of adjacent atoms in the major and minor components were restrained to be similar, and only the non-hydrogen atoms in the major orientation were refined anisotropically (those in the minor orientation were refined isotropically).

The included benzene molecule (C66>C71) was found to be disordered. As a result the molecule was modelled as disordered over two sites in *ca.* 80:20 occupancies for the major and minor orientations respectively. The thermal parameters of adjacent atoms in the major and minor components were restrained to be similar, their geometries optimised and only the non-hydrogen atoms in the major orientation were refined anisotropically (those in the minor orientation were refined isotropically).

The included benzene molecule (C73>C78) was found to be disordered. As a result the molecule was modelled as disordered over two sites in *ca.* 75:25 occupancies for the major and minor orientations respectively. The thermal parameters of adjacent atoms in the major and minor components were restrained to be similar, their geometries optimised and only the non-hydrogen atoms in the major orientation were refined anisotropically (those in the minor orientation were refined isotropically).

The included benzene molecule (C73>C78) was found to be disordered over a special position in two different orientations. As a result the molecule was modelled as disordered over two sites in *ca.* 31:19 occupancies for the major and minor orientations respectively to yield one 50% occupancy molecule (with the symmetry element generating the other 50%). The thermal parameters of adjacent atoms in the major and minor components were restrained to be similar, their geometries optimised and only the non-hydrogen atoms in the major orientation were refined anisotropically (those in the minor orientation were refined isotropically).

Crystal Data for $C_{87}H_{100}Al_2CrN_4O_8$, M =1435.66, monoclinic, space group $P2_1/c$ (no. 14), a = 27.4194(8) Å, b = 12.1333(4) Å, c = 24.9290(9) Å, β = 102.408(3)°, V = 8099.9(5) Å^3, Z = 4, ρ_{calc}g/cm^3 = 1.177, μ(MoKα) = 0.219 mm^{-1}, T = 173.00(14), orange plates, F^2 refinement, R_1(obs) = 0.0584, wR_2(all) = 0.1390, 16211 independent observed reflections (R_{int} = 0.0435), 9491 independent measured reflections [$|F_o| > 4\sigma(|F_o|)$, $2\theta_{full}$ = 56.598], 951 parameters. CCDC 2095250.

The X-ray structure of **2-4-Cr**

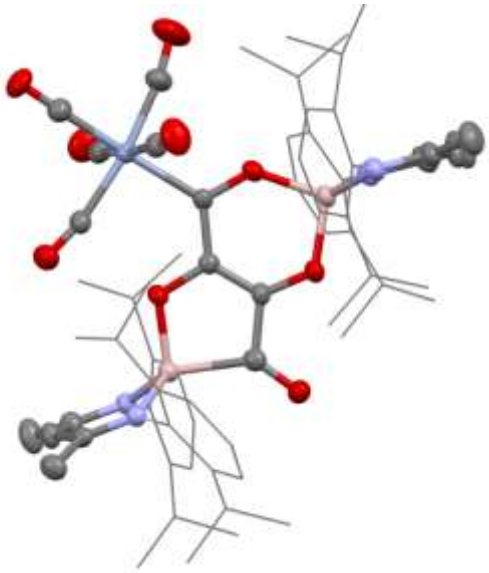


Figure 2.23: The X-ray crystal structure of **2-4-Cr**.

2-4-Cr was found to crystallise in the $P2_1/c$ space group, with one full toluene molecule in the asymmetric unit for a total of four toluene molecules in the unit cell.

Crystal Data for $C_{74}H_{90}Al_2CrN_4O_9$, M =1285.45, monoclinic, space group $P2_1/c$ (no. 14), a = 15.2826(5) Å, b = 21.3743(9) Å, c = 21.5531(8) Å, β = 92.741(3)°, V = 7032.4(5) Å^3, Z = 4, ρ_{calc}g/cm^3 = 1.214, μ(CuKα) = 2.041 mm^{-1}, T = 173.0(3), dull dark violet needles, F^2 refinement, R_1(obs) = 0.0635, wR_2(all) = 0.1480, 13489 independent observed reflections (R_{int} = 0.0806), 8280 independent measured reflections [$|F_o| > 4\sigma(|F_o|)$, $2\theta_{full}$ = 147.074], 832 parameters. CCDC 2095251.

The X-ray structure of **2-6-Cr**

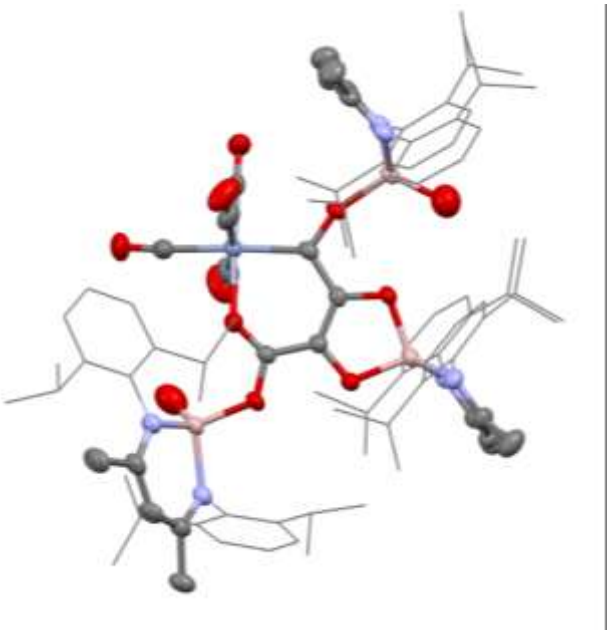


Figure 2.24: The X-ray crystal structure of **2-6-Cr**.

2-6-Cr was found to crystallise in the P-1 space group.

The included toluene molecule (C96>C102) was found to be at half occupancy by inspection of the thermal ellipsoids. The molecule was modelled as disordered over two sites in ca. 25.5:24.5 occupancies for the major and minor orientations respectively. The thermal parameters of adjacent atoms in the major and minor components were restrained to be similar, the geometries optimised, and the atoms were refined isotropically.

The included pentane (C103>C107) molecule was found to be at half occupancy by inspection of the thermal ellipsoids. The molecule was modelled as disordered over two sites in ca. 30:20 occupancies for the major and minor orientations respectively. The thermal parameters of adjacent atoms in the major and minor components were restrained to be similar, their geometries optimised, and the atoms were refined isotropically.

The included toluene molecule (C108>C104) was found to be disordered with a pentane molecule (C18'>C22'). The total occupancy for both molecules was found to be 50% by inspection of thermal ellipsoids. The occupancies were refined to *ca.* 36:14 ratio for the major and minor components respectively, and fixed at those ratios following free-variable refinement. The thermal parameters of adjacent atoms in the major and minor components were restrained to be similar, the geometries optimised, and the atoms were refined isotropically.

Crystal Data for $C_{104.22}H_{138.165}Al_3CrN_6O_{10.35}$, M =1773.54, triclinic, space group P-1 (no. 2), a = 13.1699(6) Å, b = 17.3154(9) Å, c = 26.4131(9) Å, α = 93.107(3)°, β = 104.004(3)°, γ = 108.488(4)°, V = 5486.2(4) Å^3, Z = 2, ρ_{calc}g/cm^3 = 1.074, μ(MoKα) = 0.182 mm^{-1}, T = 173.00(14), ? ?s, F^2 refinement, R_1(obs) = 0.0912, wR_2(all) = 0.3070, 21541 independent observed reflections (R_{int} = 0.0339), 13836 independent measured reflections [$|F_o| > 4\sigma(|F_o|)$, $2\theta_{full}$ = 56.562], 1186 parameters.

The X-ray structure of **2-3-Mo**

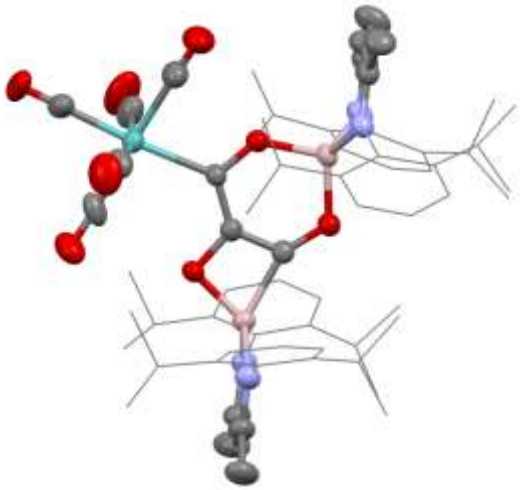


Figure S12: The X-ray crystal structure of **2-3-Mo**. One of two independent molecules shown for clarity.

2-3-Mo was found to crystallise in the $P2_1/c$ space group with two indendent molecules, one quarter of an included toluene molecule, and one quarter of an included hexane molecule in the asymmetric unit for a total of eight whole molecules of **2-3-Mo**, one molecule of toluene and one molecule of hexane in the unit cell.. The crystal was modelled as a two component twin in ca. 63:37 ratio. The two twin lattices are related by the approximate twin law [-1.0 0.0 -0.0 -0.0 1.0 0.0 0.0 0.0 -1.0]

The included toluene (C73>C80) was found to be approximately 0.25 occupancy by inspection of thermal ellipsoids. The thermal parameters of the atoms were restrained to be similar, and the molecule was refined isotropically.

The included hexane (C67>C72) was found to be approximately 0.25 occupancy by inspection of thermal ellipsoids. The thermal parameters of the atoms were restrained to be similar, and the molecule was refined isotropically.

Crystal Data for $C_{67.625}H_{84.75}Al_2MoN_4O_8$, M =1231.54, monoclinic, space group $P2_1/c$ (no. 14), a = 28.5349(5) Å, b = 20.7875(3) Å, c = 26.1992(5) Å, β = 112.641(2)°, V = 14342.9(4) Å^3, Z = 8, ρ_{calc}g/cm^3 = 1.141, μ(CuKα) = 2.136 mm^{-1}, T = 173.0(3), orange blocks, F^2 refinement, R_1(obs) = 0.0702, wR_2(all) = 0.2193, 27591 independent observed reflections (R_{int} = 0.0509), 16366 independent measured reflections [$|F_o| > 4\sigma(|F_o|)$, $2\theta_{full}$ = 147.312], 1540 parameters. CCDC 2095252.

The X-ray structure of **2-4-Mo**

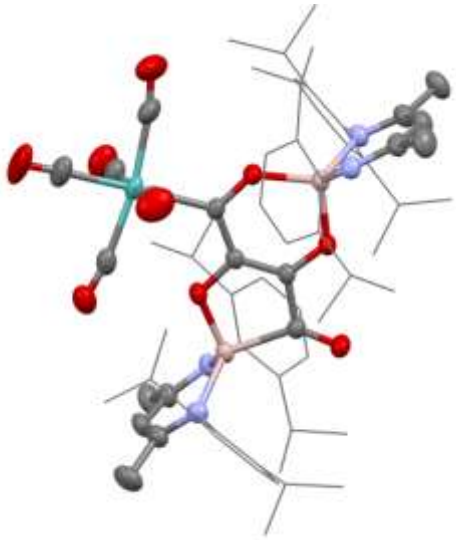


Figure 2.25: The X-ray crystal structure of **2-4-Mo**.

2-4-Mo was found to crystallise in the $P2_1/n$ space group, with one full toluene molecule in the asymmetric unit for a total of four toluene molecules in the unit cell.

Crystal Data for $C_{74}H_{90}Al_2MoN_4O_9$, M =1329.39, monoclinic, space group $P2_1/n$ (no. 14), a = 15.5122(5) Å, b = 12.6927(3) Å, c = 36.0314(9) Å, β = 96.194(3)°, V = 7052.9(3) Å^3, Z = 4, ρ_{calc}g/cm^3 = 1.252, μ(CuKα) = 2.222 mm^{-1}, T = 173.05(10), clear reddish red blocks, F^2 refinement, R_1(obs) = 0.0440, wR_2(all) = 0.1248, 13474 independent observed reflections (R_{int} = 0.0351), 10739 independent measured reflections [$|F_o| > 4\sigma(|F_o|)$, $2\theta_{full}$ = 147.13], 832 parameters. CCDC 2095253.

The X-ray crystal structure of **2-3-W**

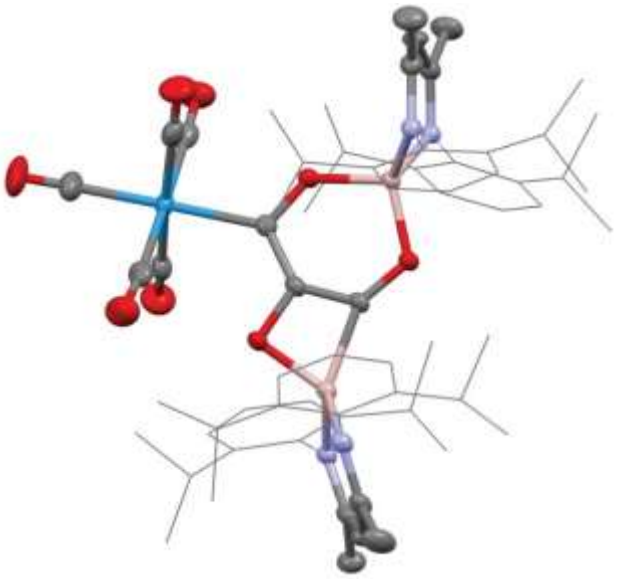


Figure 2.26: The X-ray crystal structure of **2-3-W**.

2-3-W was found to crystalise in the $P2_1/c$ space group. 3.5 toluene molecules were found within the asymmetric unit cell corresponding to 14 within the unit cell. They were modelled as follows: a) disordered over two positions with major and minor occupancies ca. 68% and 32% respectively b) disordered over two positions with major and minor ca. occupancies 69% and 31% respectively c) as a half occupancy molecule disordered over symmetry and d) a full occupancy toluene. The thermal parameters of adjacent atoms were restrained to be similar, and only the non-hydrogen atoms of the major occupancy orientation were refined anisotropically (those of the minor occupancy orientation were refined isotropically). Distance restraints were used on solvent atoms where appropriate in order to produce a reasonable model for disorder.

Crystal data for **2-3-W**: $C_{90.5}H_{110}Al_2N_4O_8W$, M = 1619.63, monoclinic, $P2_1/c$, a = 27.7428(6), b = 12.2385(2), c = 25.2788(5) Å, α = 90, β = 102.219(2), γ = 90 °, V = 8388.5(3) Å^3, Z = 4, D_c = 1.282 g cm^{-3}, μ(Mo-Kα) = 1.455 mm^{-1}, T = 173 K, orange blocks, Agilent Xcalibur 3 E; 16764 independent measured reflections (R_{int} = 0.0231), F^2 refinement,[2] R_1(obs) = 0.0376, wR_2(all) = 0.0791, 12954 independent observed reflections [$|F_o| > 4\sigma(|F_o|)$, $2\theta_{full}$ = 56.6°], 1017 parameters. CCDC 1860655.

The X-ray crystal structure of **2-4-W**

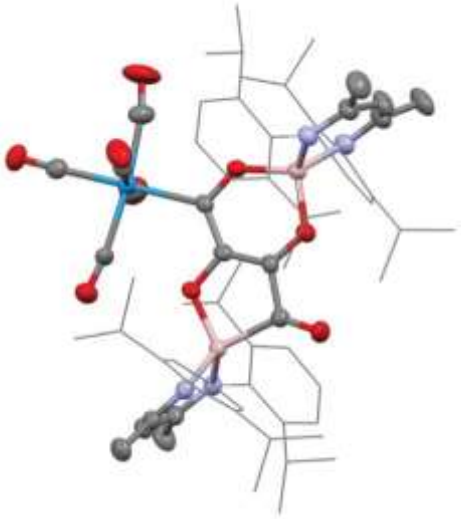


Figure 2.27: The X-ray crystal structure of **2-4-W**.

The included toluene molecule within the structure of **2-4-W** was found to be disordered. Two orientations were identified to ca. 62% and 38% occupancy, their geometries were optimised, the thermal parameters of adjacent atoms were restrained to be similar, and only the non-hydrogen atoms of the major occupancy orientation were refined anisotropically (those of the minor occupancy orientation were refined isotropically).

Crystal data for **2-4-W**: $C_{74}H_{90}Al_2N_4O_9W$, M = 1417.30, monoclinic, $P2_1/c$, a = 15.3318(3), b = 21.4894(3), c = 21.5498(3) Å, α = 90, β = 92.4806(14), γ = 90 °, V = 7093.40(18) Å^3, Z = 4, D_c = 1.327 g cm^{-3}, μ(Cu-Kα) = 3.715 mm^{-1}, T = 173 K, purple plates, Agilent Xcalibur PX Ultra A diffractometer; 13687 independent measured reflections (R_{int} = 0. 0418), F^2 refinement,[2] R_1(obs) = 0.0422, wR_2(all) = 0.1149, 10456 independent measured reflections [$|F_o| > 4\sigma(|F_o|)$, $2\theta_{full}$ = 147.414°], 838 parameters. CCDC 1860656.

The X-ray crystal structure of **2-7-W**

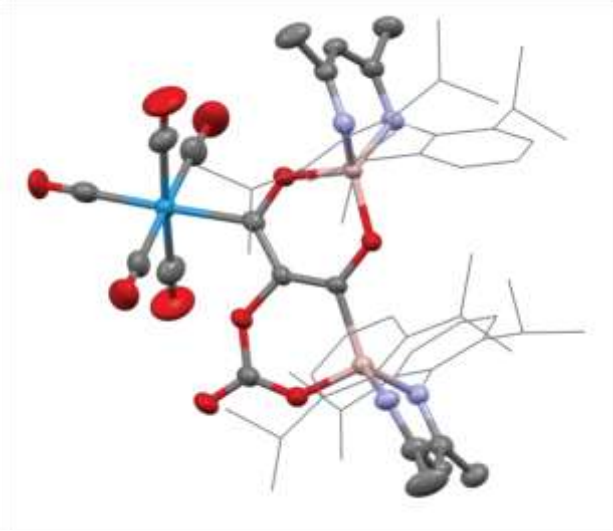


Figure 2.28: The X-ray crystal structure of **2-7-W**.

The crystal was found to be a two component twin in a *ca.* 60:40 ratio, with the two lattices related by the approximate twin law [-1.00 0.00 0.00 0.00 -1.00 -0.00 0.12 0.00 1.00]

Two benzene molecules were found within the asymmetric unit. They were modelled as follows a) two orientations identified to ca. 71% and 21% occupancies and b) three orientations identified to ca. 43%, 21% and 35% occupancies. Their geometries were optimised, the thermal parameters of adjacent atoms were restrained to be similar, and only the non-hydrogen atoms of the major occupancy orientation were refined anisotropically (those of the minor occupancy orientation were refined isotropically). Distance restraints were used were used on solvent atoms where appropriate in order to produce a reasonable model for disorder.

Crystal data for **2-7-W:** $C_{79}H_{94}Al_2N_4O_{10}W$, M = 1497.39, monoclinic, $P2_1/c$, a = 17.8441(9), b = 19.0576(5), c = 22.2871(8) Å, α = 90, β = 92.815(4), γ = 90 °, V = 7569.9(5) Å^3, Z = 4, D_c = 1.314 g cm^{-3}, μ(Cu-Kα) = 3.521 mm^{-1}, T = 173 K, red blocks, Agilent Xcalibur PX Ultra A diffractometer; 19606 independent measured reflections (R_{int} = 0.0559), F^2 refinement,[2] R_1(obs) = 0.0525, wR_2(all) = 0.1463, 15819 independent measured reflections [$|F_o| > 4\sigma(|F_o|)$, $2\theta_{full}$ = 147.58°], 872 parameters. CCDC 1860657.

The X-ray crystal structure of **2-8-W**

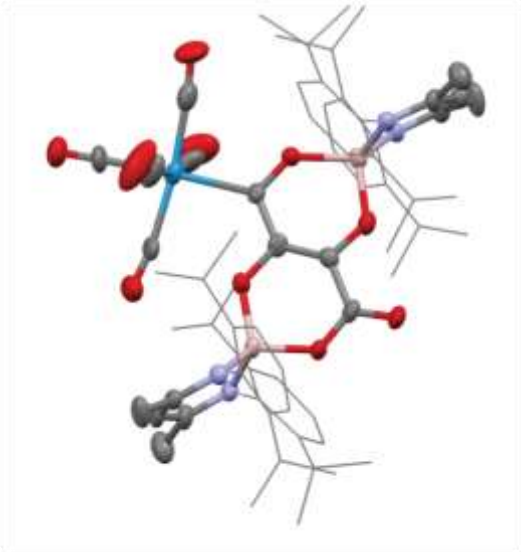


Figure 2.29: The X-ray crystal structure of **2-8-W**.

The crystal was found to be a two component twin in a *ca.* 71:29 ratio, with the two lattices related by the approximate twin law [1.00 0.00 0.00 0.00 1.00 0.00 -0.92 0.00 -1.00].

A total of two crystallographically independent molecules of **2-8-W** were found within the asymmetric unit. One isopropyl group was found to be positionally disordered in each of the independent molecules (C65-C66-C67 and C133-C134-C135). They were modelled accordingly: a) disordered over two sites with major and minor components in ca. 52% and 48% occupancies b) disordered over two sites with major and minor components 50.3% and 49.7% occupancies respectively. Distance restraints were used where appropriate in order to produce a reasonable order for isopropyl disorder. Attempts to refine the minor component isotropically resulted in an unstable structure and so both major and minor components were refined anisotropically.

A total of three toluene molecules were included within the asymmetric unit, two of which are disordered over planar symmetry. They were modelled accordingly as two full occupancy toluene molecules and two half-occupancy toluene molecules disordered over symmetry. Their geometries were optimised, the thermal parameters of adjacent atoms were restrained to be similar, and all non-hydrogen atoms were refined anisotropically. Distance and angle restraints were used were used on solvent atoms where appropriate in order to produce a reasonable model for disorder.

Crystal data for **2-8-W**: $C_{77.5}H_{94}Al_2N_4O_{10}W$, M = 1479.37, monoclinic, $P2_1/c$, a = 36.7014(9), b = 15.0966(4), c = 28.7796(9) Å, α = 90, β = 111.273 (3), γ = 90 °, V = 14859.2(8) Å^3, Z = 8 (two crystallographically independent molecules), D_c = 1.323 g cm^{-3}, μ(Cu-Kα) = 3.580 mm^{-1}, T = 173

K, red plates, Agilent Xcalibur PX Ultra A diffractometer; 33683 independent measured reflections (R_{int} = 0.0982) F^2 refinement,[2] R_1(obs) = 0.0710, wR_2(all) = 0.1966, 23300 independent observed reflections [$|F_o| > 4\sigma(|F_o|)$, $2\theta_{full}$ = 147.8°], 1825 parameters. CCDC 1860658.

The X-ray structure of **2-3-Co**

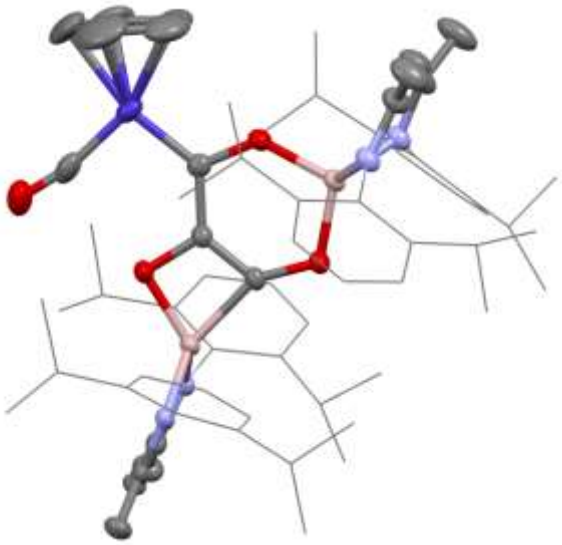


Figure S14: The X-ray crystal structure of **3-Co**.

2-3-Co was found to crystallise in the $P2_1/n$ space group, with 1.5 toluene molecules and 0.5 pentane molecules in the asymmetric unit for a total of six toluene molecules and two pentane molecules in the unit cell.

The included toluene molecule (C75>C81) was found to be disordered over a special position in two different orientations. As a result the molecule was modelled as disordered over two sites in *ca.* 41:9 occupancies for the major and minor orientations respectively to yield one 50% occupancy molecule (with the symmetry element generating the other 50%). The thermal parameters of adjacent atoms in the major and minor components were restrained to be similar, their geometries optimised and only the non-hydrogen atoms in the major orientation were refined anisotropically (those in the minor orientation were refined isotropically).

The included pentane molecule (C82>C86) was found to be disordered over a special position in two different orientations. As a result the molecule was modelled as disordered over two sites in *ca.* 32:18 occupancies for the major and minor orientations respectively to yield one 50% occupancy molecule (with the symmetry element generating the other 50%). The thermal parameters of adjacent atoms in the major and minor components were restrained to be similar, their geometries optimised and only the non-hydrogen atoms in the major orientation were refined anisotropically (those in the minor orientation were refined isotropically).

The iso-propyl group C21>C23 was found to be disordered. C22 and C23 were modelled as disordered over two sites in *ca.* 71:29 occupancies for the major and minor orientations respectively. The thermal parameters of adjacent atoms in the major and minor components

were restrained to be similar, and only the non-hydrogen atoms in the major orientation were refined anisotropically (those in the minor orientation were refined isotropically).

Crystal Data for $C_{80}H_{105}Al_2CoN_4O_4$, M =1299.56, monoclinic, space group $P2_1/n$ (no. 14), a = 13.0460(2) Å, b = 25.0267(5) Å, c = 22.6264(5) Å, β = 96.9581(19)°, V = 7333.1(3) Å^3, Z = 4, ρ_{calc}g/cm^3 = 1.177, μ(MoKα) = 0.309 mm^{-1}, T = 173.00(14), red blocks, F^2 refinement, R_1(obs) = 0.0527, wR_2(all) = 0.1386, 14683 independent observed reflections (R_{int} = 0.0263), 10344 independent measured reflections [$|F_o| > 4\sigma(|F_o|)$, $2\theta_{full}$ = 56.698], 893 parameters. CCDC 2095254.

2.5.1 – Normalised M=C for 2-3

	2-3-Cr	**2-3-Mo**	**2-3-W**	**2-3-Mn**	**2-3-Re**	**2-3-Re'**	**2-3-Co**
M=C (Å)	2.055(3)	2.250(4)	2.195(3)	1.922(3)	2.019(6)	2.015(4)	1.810(2)
FSR	1.04	1.06	1.04	0.99	0.98	0.98	0.97

Table 2.7: Calculated formal shortness ratios for **2-3-M** using the Pyykko definition for covalent radii.[27] FSR is defined as the value obtained by dividing the bond length between two elements and the sum of their covalent radii.

2.6 – Computational Methods

DFT calculations were performed using Gaussian 09 (Revision D.01) using an ultrafine integration grid (int=ultrafine).[28] A hybrid basis set in which Al and transition metal centres were described with Stuttgart SDDAll pseudopotential and associated basis sets and the 6-31G** basis set were used for all other atoms was used in all calculations.[14,21]

Geometry optimisations and frequency calculations were performed using the ωB97X[29] functional. Frequency analyses for all stationary points were performed using the enhanced criteria to confirm the nature of the structures as either minima (no imaginary frequency) or transition states (only one imaginary frequency).

The electronic energies of the optimised geometries were calculated using the M06l functional with the same basis set with solvent corrections (PCM, benzene, ε = 2.2706) and an empirical dispersion correction (Grimme, D3).[30–32] The Gibbs free energy correction from the frequency calculation was added to this electronic energy to generate Gibbs free energy values for the calculated stationary points. Functional testing was performed with the B3LYP,[33] M062X,[34] and B3PW91[35] in addition to the M06L functional and ωB97X functional.

Intrinsic reaction coordinate (IRC) calculations were used to connect transition states and minima located on the potential energy surface allowing a full energy profile (calculated at 298.15 K, 1 atm) of the reaction to be constructed.[36] Natural Bond Orbital analysis was carried out using NBO 6.0 with the ωB97x functional.[37]

ETS-NOCV calculations were performed using Orca 4.2.1. The def2-tzvpp basis set was used in combination with the ωB97X basis set. The RIJCOSX approximation was used with the def2/j auxiliary. Tight SCF settings and an ultrafine integration grid (grid6) were used.

2.6.1 – Calculated pathway to 2-4-W

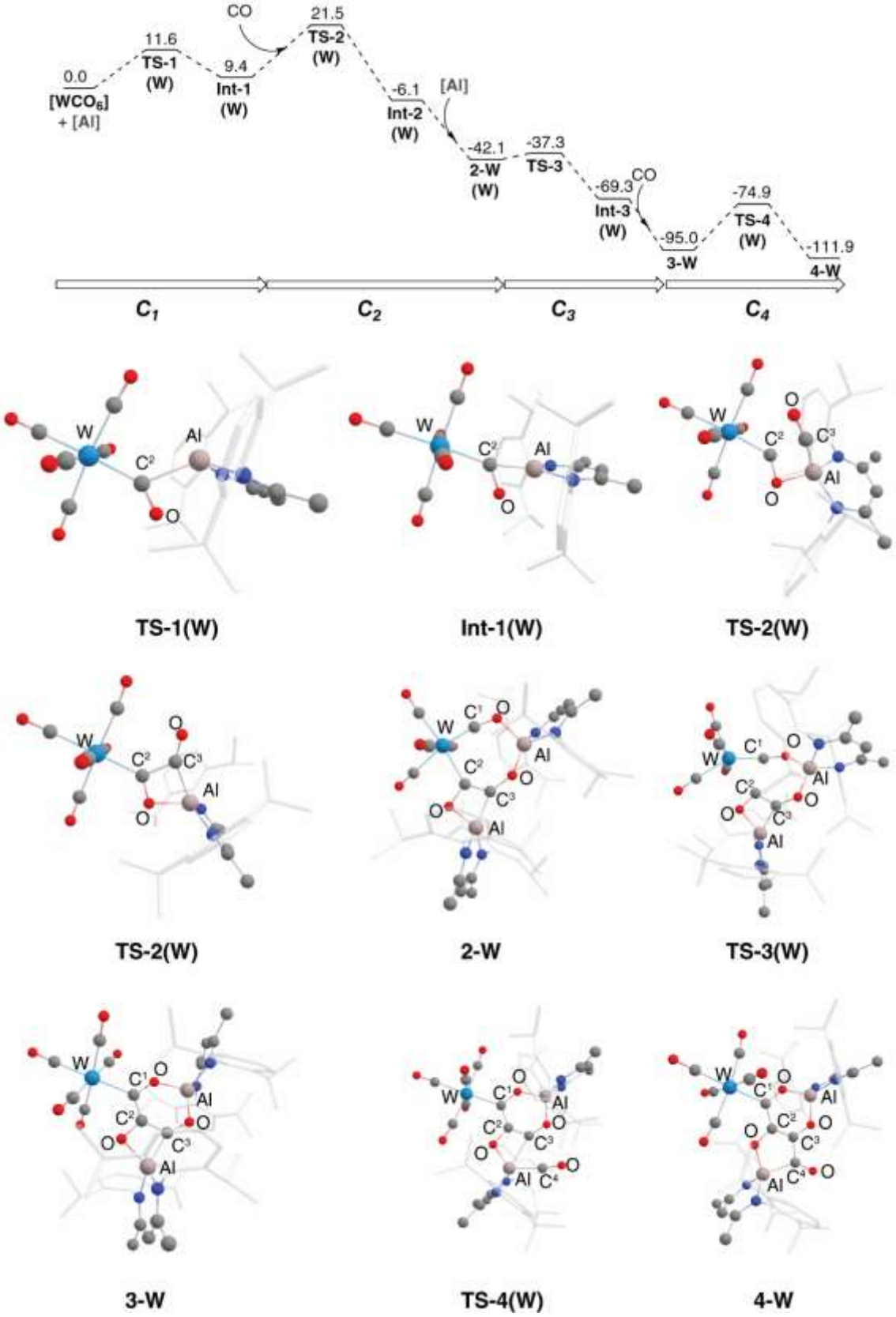


Figure 2.30: Calculated pathway to **2-4-W** formation from $[W(CO)_6]$ and [Al]. All energies in kcal mol^{-1}

The calculated pathway towards the formation of observed products **2-3-W** and **2-4-W** is similar to the calculated pathway for Mn. **TS-1-W** and **TS-2-W** have a similar activation barrier to the analogous transition states for the Mn pathway. The key difference in the W pathway to the Mn pathway is the activation energy to form the C_3 to convert **2-2-W** to **2-3-W**: **TS-3-W** is lower in energy ($\Delta G^{\ddagger}_{298K}$ = 4.8 kcal mol^{-1} from **2-2-W**) than the analogous activation barrier for Mn ($\Delta G^{\ddagger}_{298K}$ = 26.0 kcal mol^{-1} from **2-2-Mn**). The formation of **Int-3-W** (ΔG_{298K} = −27.2 kcal mol^{-1}) from **2-2-W** is also more exergonic than the analogous reaction for Mn (ΔG_{298K} = +3.7 kcal mol^{-1} from **2-2-Mn)**. The data are consistent with the formation of **2-3-W** in 5 minutes at 25°C, compared to the slower reaction times required for the formation **2-3-Mn** and reflects the isolable nature of **2-2-Mn**.

2.6.2 – Calculated pathway to 2-4-Mn

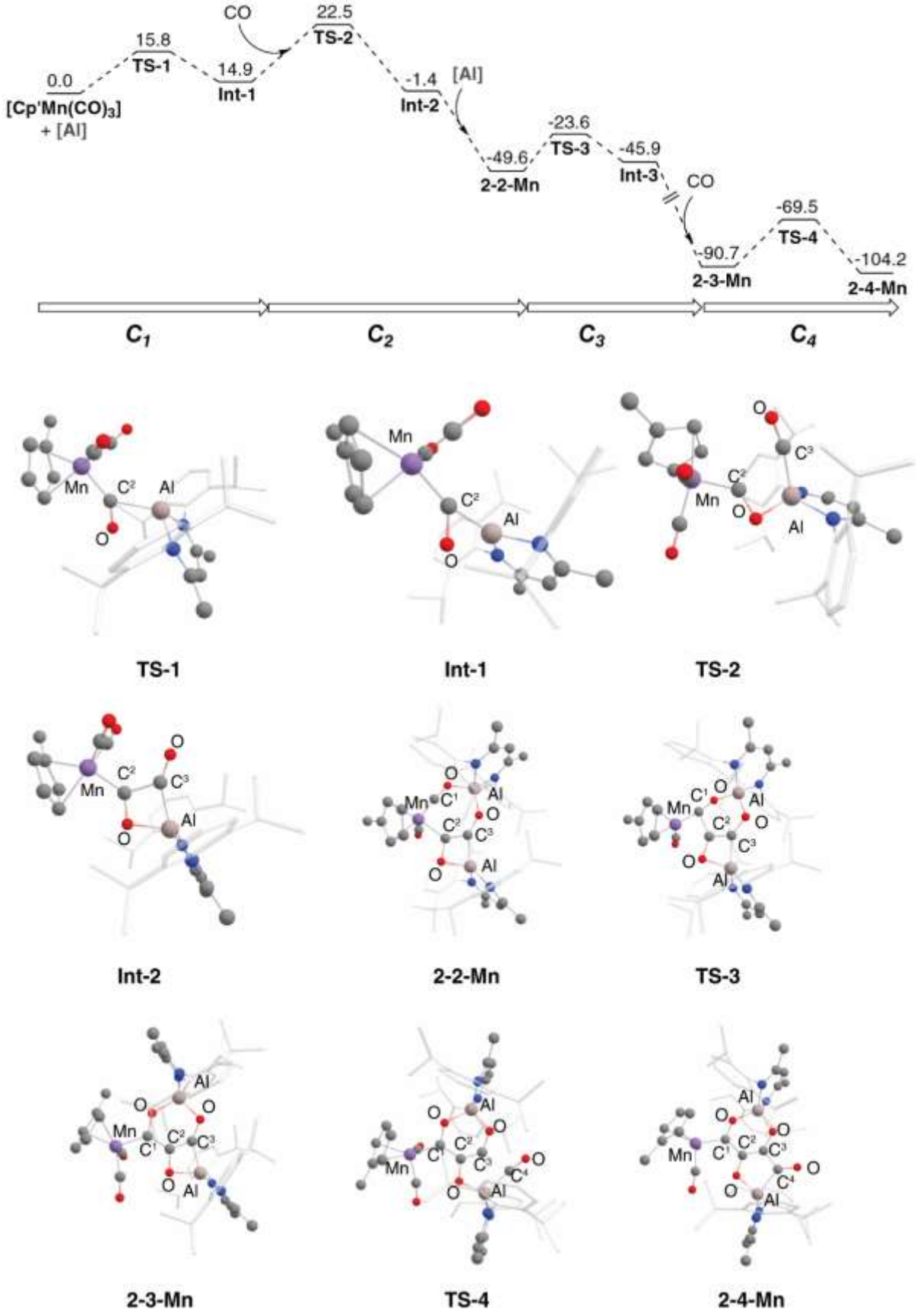


Figure 2.31: Calculated pathway towards the formation of **2-4-Mn.** All energies in kcal mol^{-1}

2.6.3 – Calculated pathway to 2-3-Mn'

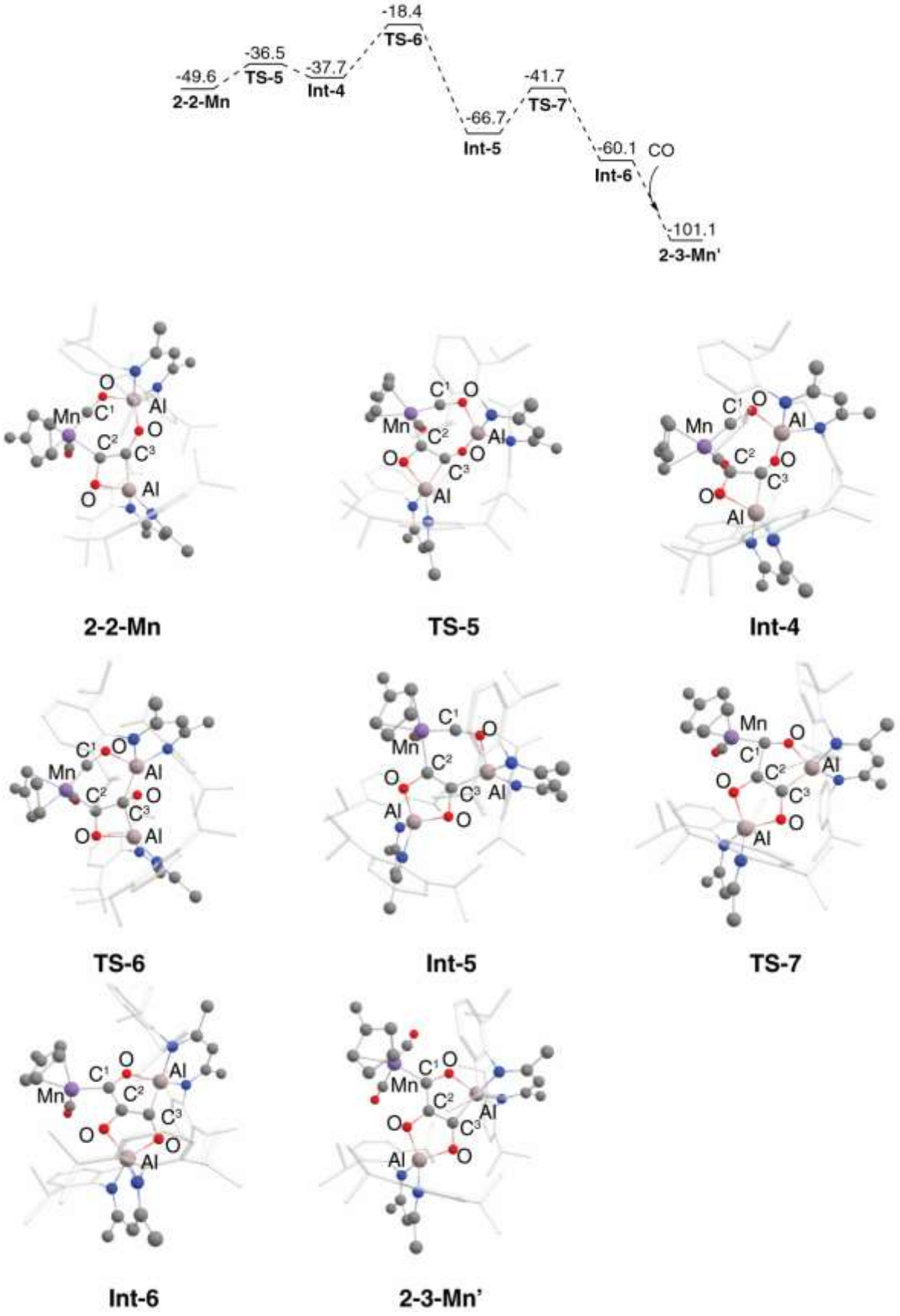


Figure 2.32: Pathway calculated towards the formation of **2-3-Mn'** from **2-2-Mn**. All energies in kcal mol^{-1}

2.6.4 – Calculated pathway towards the formation of 2-3-Re'

The formation of **2-3-Re** and **2-3-Re'** was calculated from **2-2-Re**. Two pathways are available from **2-2-Re**, either **TS-3-Re** which leads to the formation of **2-3-Re** or **TS-6-Re**, which leads to the formation of **2-3-Re'**.

A single transition state, **TS-6-Re** connects **2-2-Re** with **Int-5-Re**. This is in contrast with the pathway involving Mn: in the Mn pathway, **Int-5** was calculated to proceed *via* **Int-4**. Efforts to locate an identical stationary point in the Re pathway, **Int-4-Re**, were unsuccessful.‡ As with the formation of **Int-5** in the Mn pathway, the formation of **Int-5-Re** is likely non-reversible. From **Int-5-Re**, a single transition state, **TS-7-Re** connects I**nt-5-Re** to I**nt-6-Re**, the latter of which forms the observed product **2-3-Re'** upon coordination of another CO molecule. **TS-7-Re** has a similar activation barrier to **TS-3-Re** – both are migratory insertion reactions involving an isocarbonyl CO and C_2 carbon chain.

The selectivity of **2-3-Re** and **2-3-Re'** depends on the relative energies of **TS-3-Re** ($\Delta G^{\ddagger}_{298K}$ = 41.5 kcal mol^{-1} from **2-2-Re**) and **TS-6-Re** ($\Delta G^{\ddagger}_{298K}$ = 34.6 kcal mol^{-1} from **2-2-Re**). The calculated energies incorrectly predict that **2-3-Re'** to be the major product. Nevertheless, comparing the relative barrier heights for **TS-3-Re** ($\Delta G^{\ddagger}_{298K}$ = 41.5 kcal mol^{-1} from **2-2-Re**) compared and **TS-3** ($\Delta G^{\ddagger}_{298K}$ = 26.0 kcal mol^{-1} from **2-2-Mn**) suggests that the migratory insertion is slower at Re than Mn. The activation barriers towards the formation of the isomeric **2-3-Re'** (**TS-6-Re**, $\Delta G^{\ddagger}_{298K}$ = 34.6 kcal mol^{-1} from **2-2-Re**)and **2-3-Mn'** (**TS-6**, $\Delta G^{\ddagger}_{298K}$ = 31.2 kcal mol^{-1} from **2-2-Mn**) are closer in energy than the calculated barriers for the migratory insertion step. Hence, the slower migratory insertion calculated for Re may influence the greater ratio of **2-3-Re'** (75 : 25, **2-3-Re** : **2-3-Re'**) than **2-3-Mn'** (91 : 9, **2-3-Mn**:**2-3-Mn'**) observed to form under their respective reaction conditions.

The analysis can be extended to the W system. The extremely rapid migratory insertion step (**TS-3-W**, $\Delta G^{\ddagger}_{298K}$ = 4.8 kcal mol^{-1}) results in the rapid formation of **2-3-W** under ambient conditions. While the corresponding pathway towards the unobserved **2-3-W'** has not been calculated, precluding a direct comparison, the calculated facile migratory insertion appears to be the origin of the divergent reactivity from Mn and Re centres.

‡ This is not entirely unexpected due to the flat potential energy surface: **Int-4** is only 1.2 kcal mol^{-1} lower in energy than the preceding transition state in the case of Mn – in the case of Re, the structure is not calculated to be a local minimum.

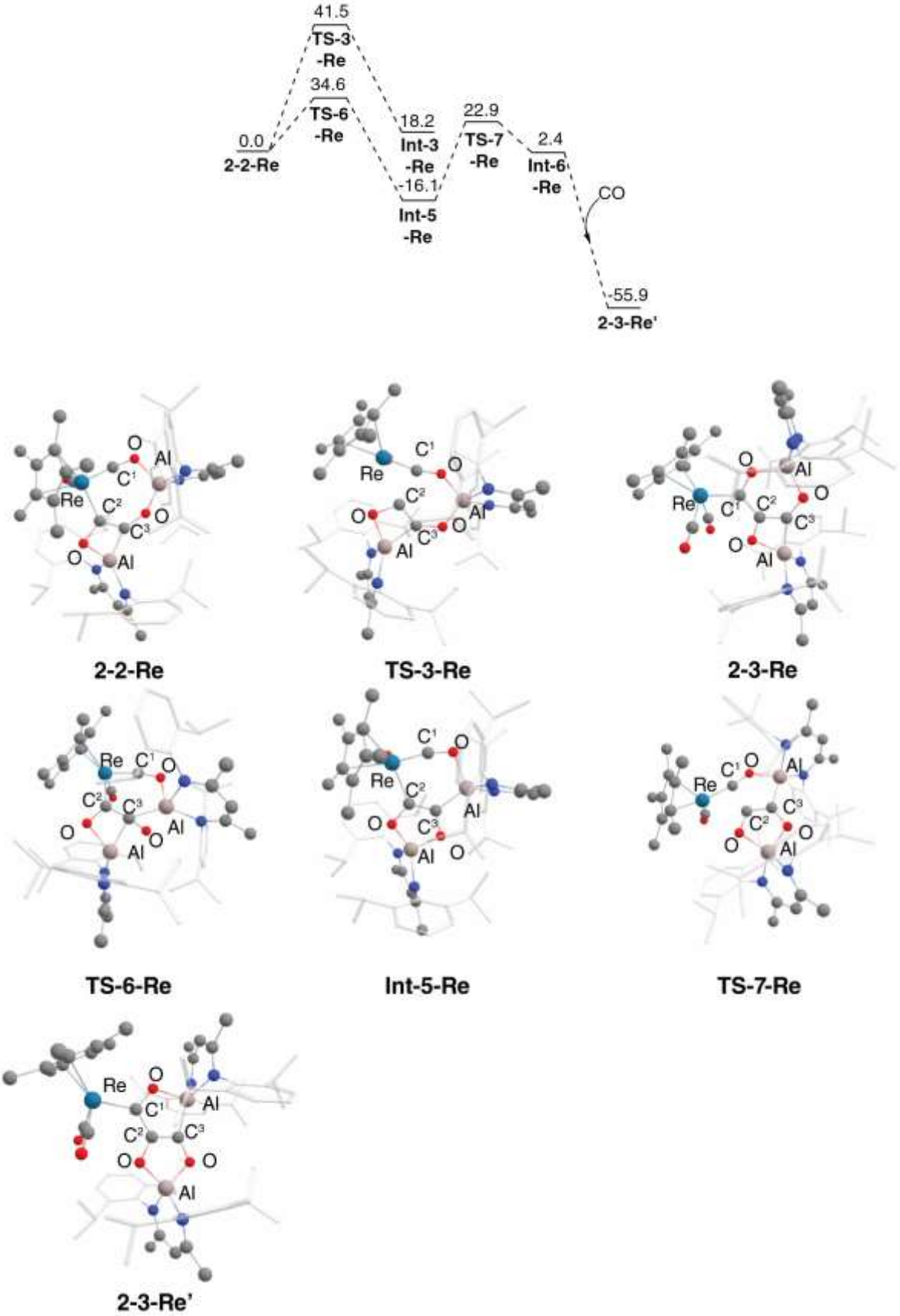


Figure 2.33: Calculated pathway towards **2-3-Re'**. **TS-3-Re** (on the pathway to **2-3-Re**) has been calculated as well to provide comparison. All energies in kcal mol^{-1}

2.6.5 – ETS-NOCV calculations

2-2-Mn

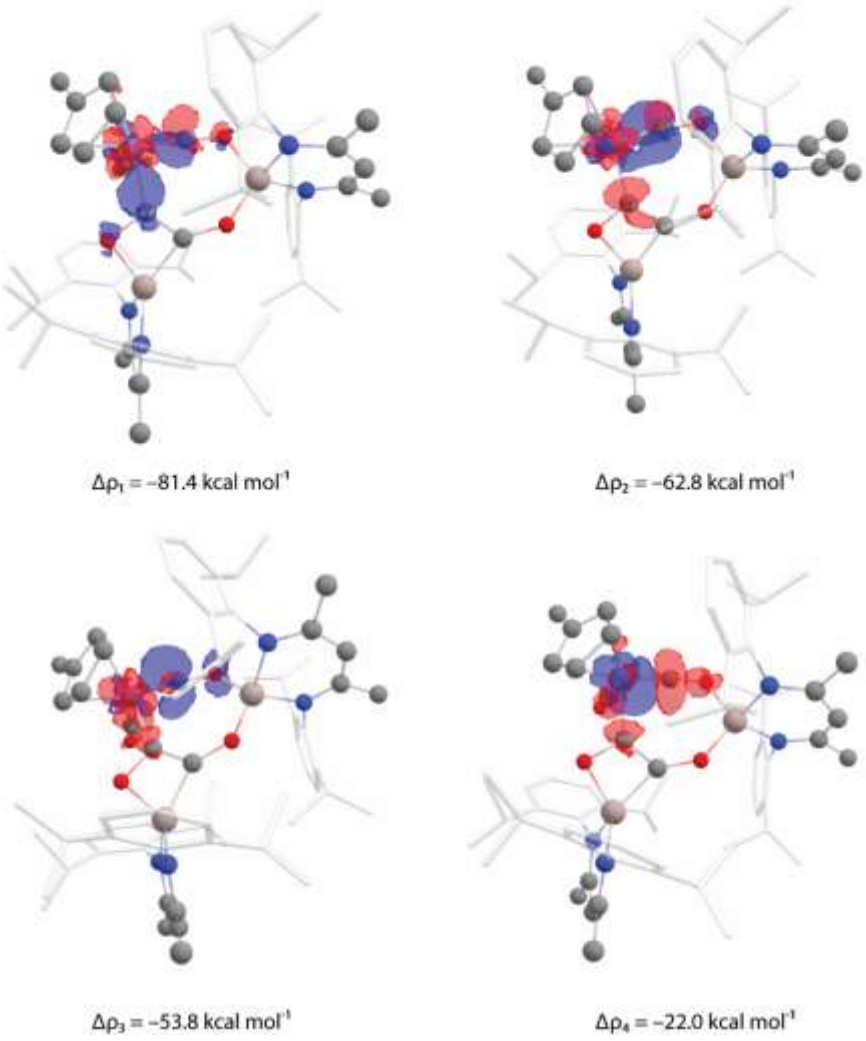
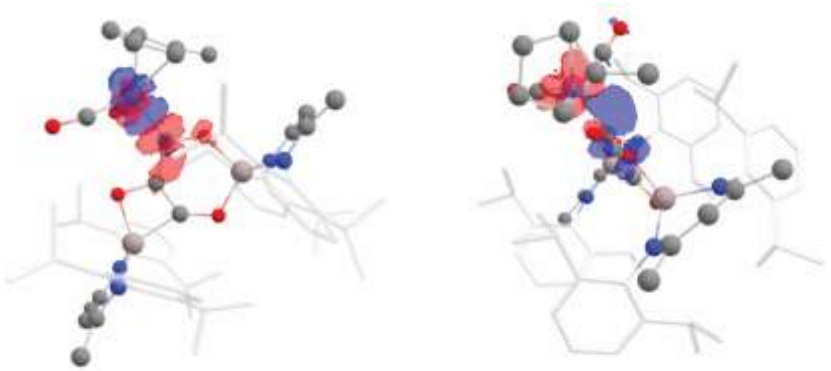


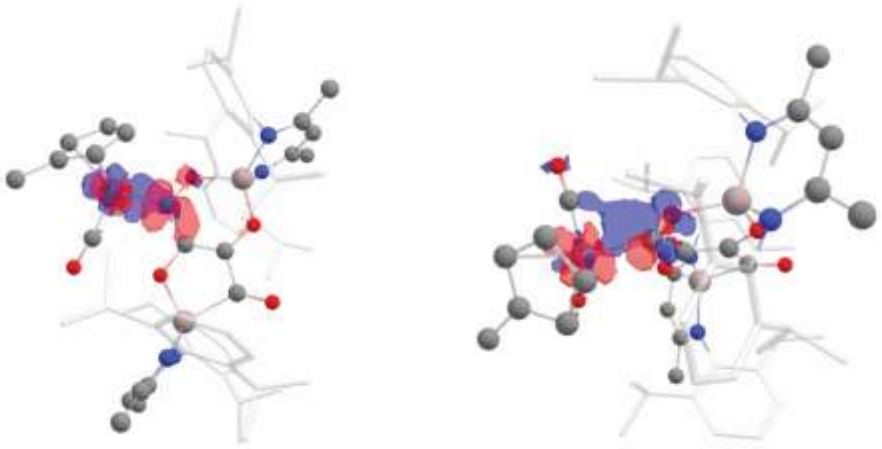
Figure 2.34: Deformation density plots for $\Delta\rho_{1\text{-}4}$ calculated for **2-2-Mn**. Charge flow from red to blue.

2-3-Mn



$\Delta\rho_1 = -41.7$ kcal mol^{-1} $\Delta\rho_2 = -25.2$ kcal mol^{-1}

2-4-Mn



$\Delta\rho_1 = -40.1$ kcal mol^{-1} $\Delta\rho_2 = -25.9$ kcal mol^{-1}

2.6.6 – NICS calculations on 2-3-Mn and 2-4-Mn

NICS(0) calculations were performed on the ring-systems involving the carbon chain in **2-3-Mn** and **2-4-Mn** respectively. The calculated values (Table 2.7) suggest that the ring systems are non-aromatic.

Ring Size	3-Mn	4-Mn
6	+1.95	+0.14
4	–6.20	–
5	–	+4.55

Table 2.7: Calculated NICS(0) values of the ring systems involving the carbon chain in **2-3-Mn** and **2-4-Mn**

2.6.7 – Functional testing on key stationary points

Single point calculations on the ωB97X optimised geometries of **2-2-Mn**, **TS-3**, and **TS-6** were performed using several functionals (B3PW91, M062X, ωB97X ,B3LYP, M06L). Dispersion (D3) and solvent (PCM, benzene) were applied for all functionals. In all cases, a higher activation barrier was calculated for **TS-6**. M06L was found to have the best agreement with the experimental results: observation of the formation of **2-3-Mn'** in a 91:9 ratio imply a ΔΔG = 1.4 kcal mol^{-1} for the two transition states.

	TS-3	**TS-6**	**$\Delta\Delta G_{TS6-TS3}$**
M06L	26.0	31.2	5.3
M062X	12.5	35.9	23.4
B3LYP	22.2	36.4	14.3
B3PW91	22.7	34.0	11.3
ωB97X	20.3	35.3	15.0

Table 2.8: Functional testing on key stationary points for the Mn pathway.

2.7 – References

1 C. Dohmeier, C. Robl, M. Tacke and H. Schnöckel, *Angew. Chem., Int. Ed.*, 1991, **30**, 564–565.
2 M. Tacke and H. Schnoeckel, *Inorg. Chem.*, 1989, **28**, 2895–2896.
3 J. Hicks, P. Vasko, J. M. Goicoechea and S. Aldridge, *Nature*, 2018, **557**, 92–95.
4 R. J. Schwamm, M. D. Anker, M. Lein and M. P. Coles, *Angew. Chem., Int. Ed.*, 2019, **58**, 1489–1493.
5 R. J. Schwamm, M. P. Coles, M. S. Hill, M. F. Mahon, C. L. McMullin, N. A. Rajabi and A. S. S. Wilson, *Angew. Chem., Int. Ed.*, 2020, **59**, 3928–3932.
6 S. Kurumada, S. Takamori and M. Yamashita, *Nat. Chem.*, 2020, **12**, 36–39.
7 K. Koshino and R. Kinjo, *J. Am. Chem. Soc.*, 2020, **142**, 9057–9062.
8 S. K. Mellerup, Y. Cui, F. Fantuzzi, P. Schmid, J. T. Goettel, G. Bélanger-Chabot, M. Arrowsmith, I. Krummenacher, Q. Ye, V. Engel, B. Engels and H. Braunschweig, *J. Am. Chem. Soc.*, 2019, **141**, 16954–16960.
9 R. J. Baker and C. Jones, *Coord. Chem. Rev.*, 2005, **249**, 1857–1869.
11 M. Zhong, S. Sinhababu and H. W. Roesky, *Dalton Trans.*, 2020, **49**, 1351–1364.
12 K. Hobson, C. J. Carmalt and C. Bakewell, *Chem. Sci.*, 2020, **11**, 6942–6956.
13 J. Hicks, P. Vasko, J. M. Goicoechea and S. Aldridge, *Angew. Chem., Int. Ed.*, 2021, **60**, 1702–1713.
14 C. Bakewell, A. J. P. White and M. R. Crimmin, *Angew. Chem., Int. Ed.*, 2018, **57**, 6638–6642.
1 R. Y. Kong and M. R. Crimmin, *Chem. Commun.*, 2019, **55**, 6181–6184.
15 C. Bakewell, M. Garçon, R. Y. Kong, L. O'Hare, A. J. P. White and M. R. Crimmin, *Inorg. Chem.*, 2020, **59**, 4608–4616.
16 C. Cui, H. W. Roesky, H.-G. Schmidt, M. Noltemeyer, H. Hao and F. Cimpoesu, *Angew. Chem., Int. Ed.*, 2000, **39**, 4274–4276.
17 T. Chu and G. I. Nikonov, *Chem. Rev.*, 2018, **118**, 3608–3680.
18 N. J. Hardman, B. E. Eichler and P. P. Power, *Chem. Commun.*, 2000, 1991–1992.
19 M. Driess, S. Yao, M. Brym, C. van Wüllen and D. Lentz, *J. Am. Chem. Soc.*, 2006, **128**, 9628–9629.
20 A. S. Frey, F. G. N. Cloke, P. B. Hitchcock, I. J. Day, J. C. Green and G. Aitken, *J. Am. Chem. Soc.*, 2008, **130**, 13816–13817.
21 T. N. Hooper, M. Garçon, A. J. P. White and M. R. Crimmin, *Chem. Sci.*, 2018, **9**, 5435–5440.
22 R. Y. Kong and M. R. Crimmin, *Dalton Trans.*, 2021, **50**, 7810–7817.
23 X. Li, C. Ni, H. Song and C. Cui, *Chem. Commun.*, 2006, 1763–1765.
24 A. Paparo, K. Yuvaraj, A. J. R. Matthews, I. Douair, L. Maron and C. Jones, *Angew. Chem., Int. Ed.*, 2021, **60**, 630–634.
25 R. Y. Kong and M. R. Crimmin, *J. Am. Chem. Soc.*, 2018, **140**, 13614–13617.
26 F. Agbossou, E. J. O'Connor, C. M. Garner, N. Q. Méndez, J. M. Fernández, A. T. Patton, J. A. Ramsden, J. A. Gladysz, J. M. O'Connor, T. Tajima and K. P. Gable, in *Inorganic Syntheses*, John Wiley & Sons, Ltd, 1992, pp. 211–225.
27 P. Pyykkö and M. Atsumi, *Chem. Eur. J.*, 2008, **15**, 186–197.
28 Frisch, M. J.; Trucks, G. W.; Schlegel, H. B.; Scuseria, G. E.; Robb, M. A.; Cheeseman, J. R.; Scalmani, G.; Barone, V.; Mennucci, B.; Petersson, G. A.; Nakatsuji, H.; Caricato, M.; Li, X.; Hratchian, H. P.; Izmaylov, A. F.; Bloino, J.; Zheng, G.; Sonnenberg, J. L.; Hada, M.; Ehara, M.; Toyota, K.; Fukuda, R.; Hasegawa, J.; Ishida, M.; Nakajima, T.; Honda, Y.; Kitao, O.; Nakai, H.; Vreven, T.; Montgomery, J. A., Jr.; Peralta, J. E.; Ogliaro, F.; Bearpark, M.; Heyd, J. J.; Brothers, E.; Kudin, K. N.; Staroverov, V. N.; Kobayashi, R.; Normand, J.; Raghavachari, K.; Rendell, A.; Burant, J. C.; Iyengar, S. S.; Tomasi, J.; Cossi, M.; Rega, N.; Millam, J. M.; Klene, M.; Knox, J. E.; Cross, J. B.; Bakken, V.; Adamo, C.; Jaramillo, J.; Gomperts, R.; Stratmann, R. E.; Yazyev, O.; Austin, A. J.; Cammi, R.; Pomelli, C.; Ochterski, J. W.; Martin, R. L.; Morokuma, K.; Zakrzewski, V. G.; Voth, G. A.; Salvador, P.; Dannenberg, J. J.; Dapprich, S.; Daniels, A. D.; Farkas, Ö.; Foresman, J. B.; Ortiz, J. V.; Cioslowski, J.; Fox, D. J. Gaussian~09 Revision E.01. Gaussian, Inc., Wallingford, CT 2009.

29 J.-D. Chai and M. Head-Gordon, *J. Chem. Phys.*, 2008, **128**, 084106.
30 S. Miertuš, E. Scrocco and J. Tomasi, *Chem. Phys.*, 1981, **55**, 117–129.
31 R. Cammi and J. Tomasi, *J. Comput. Chem.*, 1995, **16**, 1449–1458.
32 S. Grimme, J. Antony, S. Ehrlich and H. Krieg, *J. Chem. Phys.*, 2010, **132**, 154104.
33 P. J. Stephens, F. J. Devlin, C. F. Chabalowski and M. J. Frisch, *J. Phys. Chem.*, 1994, **98**, 11623–11627.
34 Y. Zhao and D. G. Truhlar, *Theor. Chem. Acc.*, 2008, **120**, 215–241.
35 A. D. Becke, *J. Chem. Phys.*, 1993, **98**, 5648–5652.
36 H. P. Hratchian and H. B. Schlegel, in *Theory and Applications of Computational Chemistry*, eds. C. E. Dykstra, G. Frenking, K. S. Kim and G. E. Scuseria, Elsevier, Amsterdam, 2005, pp. 195–249.
36 Gleadening, E. D.; Bakenhoop, J. K.; Reed, A. E.; Carpenter, J. E.; Bohmann, J. A.; Morales, C. M.; Landis, C. R.; Weinhold, F. NBO 6.0. Theoretical Chemistry Institute, University of Wisconsin, Madison 2013.
37 P. Bag, A. Porzelt, P. J. Altmann and S. Inoue, *J. Am. Chem. Soc.*, 2017, **139**, 14384–14387.
38 R. L. Falconer, K. M. Byrne, G. S. Nichol, T. Krämer and M. J. Cowley, *Angew. Chem., Int. Ed.* In press.

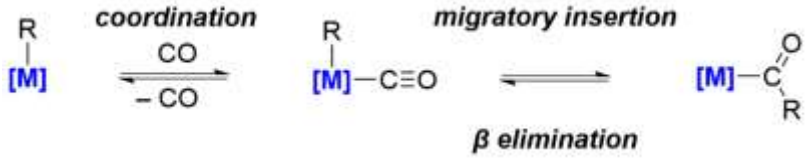
Chapter 3

Reversible insertion of CO into an Al–C bond

3.1 – Introduction to migratory insertion

3.1.1 – Migratory insertion and reverse elimination

Migratory insertion, and its microscopic reverse elimination, are fundamental transformations in transition metal chemistry. In a migratory insertion reaction, two ligands on the transition metal combine to form one with no changes in formal oxidation state. Perhaps the most widely studied and applied variant of this reactivity involves the 1,1-insertion of CO into metal–alkyl bonds (Scheme 3.1). This reaction requires a *cis*-relation of the ligands and can be thought of in terms of an intramolecular nucleophilic attack of the alkyl group on CO to generate a new acyl ligand.[1] Metal-acyl species are typically highly reactive and are only observed transiently. The coordination site vacated during the reaction may be trapped by an external ligand to isolate the metal acyl species.



Scheme 3.1: Coordination, migratory insertion and β elimination at a transition-metal centre.

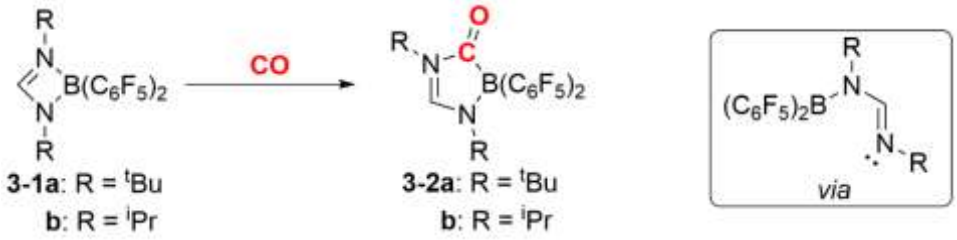
The reactivity underpins some of the most widely applied homogeneously catalysed industrial processes including the Cativa acetic acid synthesis[2] and hydroformylation. In 2008, it was estimated that hydroformylation accounted for the production of 10.4 million metric tonnes of carbonylated hydrocarbons.[3] The reverse reaction elimination has been applied in organic synthesis and used to decarbonylate carbonyl functional groups.[4]

3.1.2 – Migratory insertion at main-group centres

The migratory insertion of small molecules into main-group–element bonds has captured the attention of researchers in the last decade. These types of reactions are inferred in carbon chain growth processes documented in Chapter 2 and implicated as a key step in the reaction mechanism between main-group elements and small molecules (Chapter 1). The intermediates, however, are often too reactive to isolate and so only a handful of discrete examples of the migratory insertion of CO have been documented.

In 2010, Dureen and Stephan reported the insertion of CO into a boron amidinate complex **3-1** to form a resultant 5-membered boracycle **3-2**. The insertion of CO_2 was also achieved to furnish the analogous 6-membered boracycle. The reaction was proposed to proceed *via* an

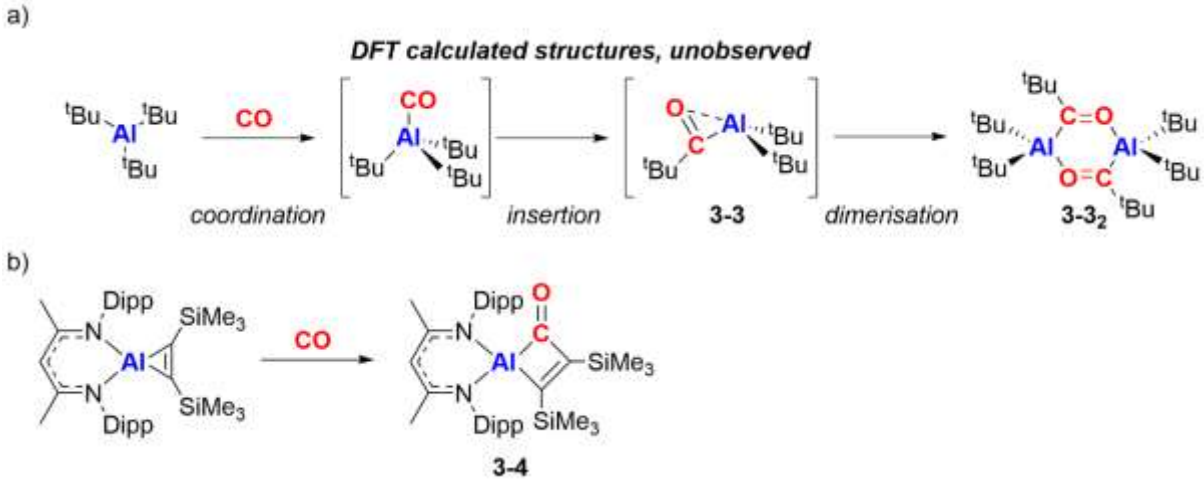
FLP-type mechanism, rather than a migratory insertion type mechanism, where the strained four-membered ring of **3-1** opens to form an "open-chain" species (Scheme 3.2, inset).



Scheme 3.2: Insertion of CO into a boron amidinate.

In 2004, Mason and co-workers reported the insertion of CO into tri-tert-butylaluminium (Scheme 3.3a).[5] The reaction is proposed to form an unobserved monomeric aluminium-acyl complex **3-3** which dimerises to form the crystallographically characterised complex **[3-3]$_2$**. This reactivity has been extended to gallium, to form the analogous gallium complex. DFT studies suggest both reactions proceed by stepwise coordination, and insertion events. Both reactions are irreversible due to the highly-stabilising M–O bonds formed in the dimer.[6]

In 2006, Cui and co-workers reported the insertion of CO into a strained aluminacyclopropene complex **3-4** (Scheme 3.3b).[7]



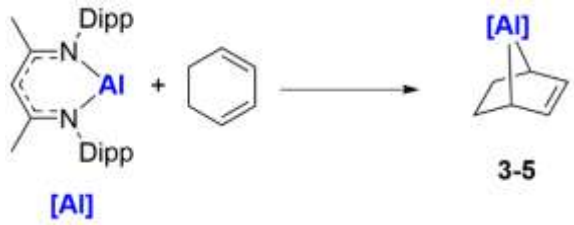
Scheme 3.3: Insertion of CO into a) a tri-alkylaluminium complex and b) a metallacyclopropene.

The study into chain-growth (Chapter 2) prompted us to study the insertion of CO into various other aluminacycles. In this chapter, the reversible insertion of CO into an aluminium–carbon bond is reported. To the best of our knowledge, our findings represent the first reversible insertion chemistry of CO at a main group metal and a new variant of migratory insertion reactivity. A combination of kinetics, DFT studies, and isotope labelling confirm that the reaction is reversible and proceeds through an asynchronous concerted transition state.

3.2 – Results and discussion

3.2.1 – Synthesis

The reaction of the low-valent aluminium complex **[Al]** with 1,3-cyclohexadiene furnishes **3-5**, a (4 + 1) cycloaddition product that contains a [2.2.1] metallabicycle (Scheme 3.4). The reaction is analogous to reports of the reaction of **[Al]** with acyclic 1,3-diene systems.[8] In this case, the formation of metallabicycle **3-5** is a non-reversible process as confirmed by cross-over experiments.



Scheme 3.4: Reaction of **[Al]** with 1,3-cyclohexadiene.

Compound **3-5** forms single crystals that contain a unit cell which possesses a C_2 symmetry axis bisecting the N–Al–N angle of the β-diketiminate ligand. The entirety of the cyclohexene ring fragment is disordered over the mirror plane precluding unequivocal measurement of carbon–carbon bond lengths within the fragment. The shortening of the Al–N bond distance to 1.9095(15) Å and expansion of the N–Al–N angle to 95.96° in **3-5** compared to the metrics reported for **[Al]** (Al–N: 1.957(2) Å, N–Al–N: 89.86(8)°)[9] are consistent with the formation of an Al(III) centre in **3-5**. The ^{1}H NMR spectrum of **3-5** in C_6D_6 shows a diagnostic alkene proton resonance at δ = 6.02 ppm along with the bridgehead methine positions at δ = 2.04 ppm. The latter protons are shielded due to the proximity of aluminium and so resonate further upfield relative to its hydrocarbyl homologue norbornene (δ = 2.74 ppm). The ^{1}H NMR spectroscopic data in combination with the structural constraints imposed by Bredt's rule on the location of the alkene moiety allow the unequivocal assignment of **3-5**.

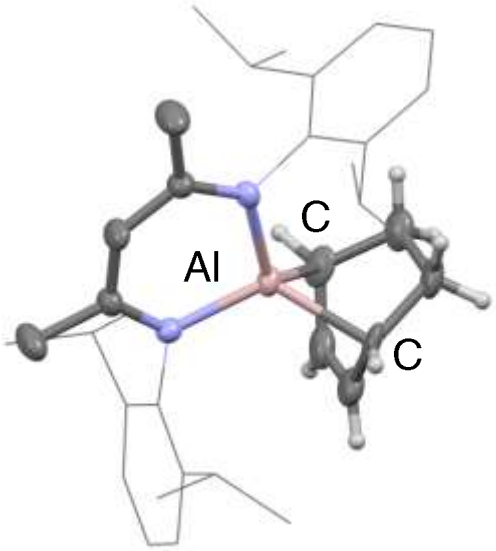
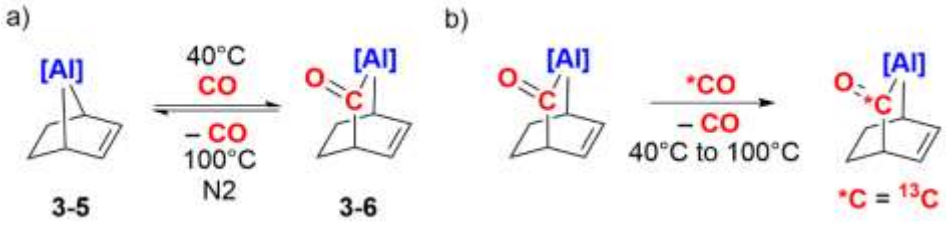


Figure 3.1: The X-ray crystal structure of **3-5**. The disordered fragment has been hidden for clarity.

Exposure of a C_6D_6 solution of **3-5** to 1 atm. of CO results in its slow conversion to **3-6** at 25°C (Scheme 3.5). **3-6** is the result of insertion of CO into the Al–C bond of **3-5**. The reaction converts an alkyl ligand into an acyl ligand and results in a ring-expansion to form a [2.2.2] metallabicycle. Despite multiple attempts at crystallisation, single crystals of **3-6** suitable for X-ray diffraction were unable able to be attained. Nevertheless, the structure of **3-6** can be determined through multinuclear NMR spectrometry. The desymmetrisation of the metallacycle is clear in the now two unique alkene environments which resonate at δ = 5.56 and 5.61 ppm along with δ = 121.7 and 139.4 ppm in the respective ^{1}H and ^{13}C NMR spectra. The newly incorporated acyl group is identifiable in the ^{13}C NMR spectrum as a broad singlet at δ = 255.3 ppm consistent with our previous reports of aluminium acyls.[10] A correlation between the acyl carbon and the bridgehead methine (δ = 2.77 ppm) is identifiable in the ^{1}H–^{13}C HMBC spectrum. The incorporation of an acyl group is further confirmed by assignment of the acyl stretch in the infrared spectrum at 1620 cm^{-1}. While prolonged heating at 40°C (>48 h) allows for the formation of **3-6** as the major product, at higher temperatures (100°C) equilibration to an approximate 1:1 mixture of **3-5**:**3-6** is observed. The data suggest that insertion of CO into the Al–C bond of **3-5** is reversible.



Scheme 3.5: a) Insertion of CO into **3-5** at 40°C under an atmosphere of CO, and de-insertion under an atmosphere of N_2 at 100°C. b) Isotopic substitution of ^{12}CO for ^{13}CO under thermal conditions.

Reversible CO insertion was confirmed in two separate experiments. Heating samples of **3-6** in C_6D_6 at 100°C under an atmosphere of N_2 results in quantitative reformation of **3-5**. Furthermore, heating a solution of **3-6** in C_6D_6 at 100°C for 3 h under 1 atm. of ^{13}CO results in the exchange of the ^{13}C isotopic label into the ^{12}C position of the acyl group. This degenerate exchange reaction is evident by the change in multiplicity of the bridgehead methine resonance in the ^1H NMR spectrum due to a $^2J_{13C-1H}$ coupling of 5.5 Hz as well as the signal intensity enhancement for the quaternary carbonyl resonance in the ^{13}C NMR spectrum (see Section 3.3.3).

Reports of the insertion of CO into Al–C bonds remain rare. In the absence of crystallographic characterization of **3-5**, the insertion of CO into a related heterocycle, **3-7**, was studied to improve the confidence of our structural assignment. Reaction of **3-7** with CO generates the insertion product **3-8** within five minutes at 25°C (Scheme 3.2a). Like **3-6**, **3-8** demonstrates a diagnostic ^{13}C NMR resonance for the carbonyl moiety δ_C = 292.3 ppm. In the solid state, **3-8** possesses a C_s symmetry plane bisecting the N–Al–N angle and passing through the atoms Al1 and C11 (Fig. 3.2b). Despite disorder of the norbornyl fragment over this plane of symmetry, the insertion of CO to the Al–C bond of **3-7** to form a metallacyclobutanone is clear. The sum of internal angles ($\Sigma\angle$ = 358.66°) of the metallacycle imply a near planar geometry of the four-membered ring. While the formation of **3-8** is supported by solid-state and solution-state characterisation (see ESI), **3-8** decomposes at 25 °C over 12 h to an intractable mixture of products.

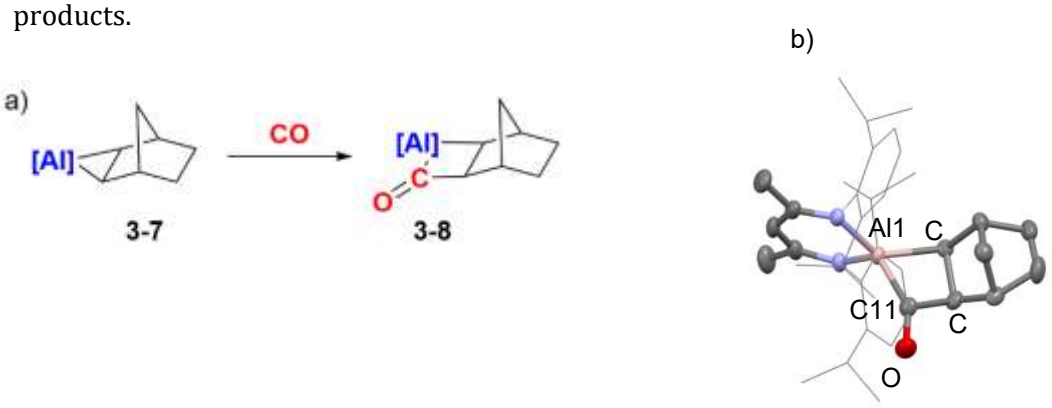


Figure 3.2: a) Synthesis of **3-8** from **3-7**. b) X-ray crystal structure of **3-8**.

3.2.2 – Kinetics

To quantify the reversible behaviour of **3-5** + CO ↔ **3-6,** kinetics measurements were made by ^1H NMR spectroscopy. Rates were measured using a low concentration of **3-6** (2 mM) in toluene-d_8 a J Youngs NMR tube[§] under a N_2 atmosphere; as such the liberated CO is at high-dilution and not expected to participate in the forward reaction. Under these conditions, the

[§] The headspace of an NMR tube is approx. 2 mL. Under ideal gas conditions, and 0.6 mL of solution, the concentration of CO gas in the reaction atmosphere is not expected to exceed 15 ppm.

elimination of CO was found to fit first order kinetics with respect to the concentration of **3-6**. Eyring analysis using this approach over a 90-105°C temperature range gave activation parameters for the back reaction of $\Delta H^{\ddagger}$ = 23.5 ±1.7 kcal mol^{-1} and $\Delta S^{\ddagger}$ = –10.3 ± 3.5 cal K^{-1} mol^{-1} (Fig. 1c). The negative entropy of activation is consistent with a highly ordered transition state. The associated Gibbs activation energy is $\Delta G^{\ddagger}_{298K}$ = 26.6 ±3.0 kcal mol^{-1}.

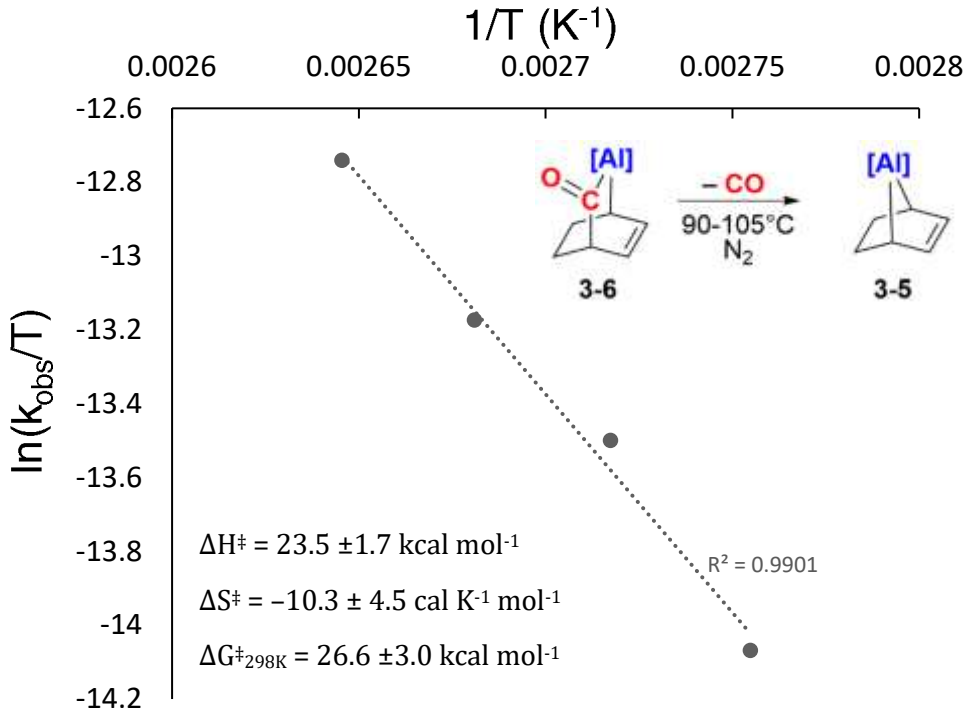


Figure 3.3: Eyring analysis on of the de-inesrtion of CO from **3-6** to form **3-5**.

3.2.3 –DFT study of mechanism

To provide further insight into the reactivity, density functional theory (DFT) calculations were performed (Figure 3.4). The formation of **3** by insertion of CO into the Al–C bond of **3-5** was found to proceed *via* **TS-1** corresponding to a calculated activation barrier of $\Delta G^{\ddagger}_{298K}$ = 20.0 kcal mol^{-1} for the forward-reaction, $\Delta G^{\ddagger}_{298K}$ = 28.7 kcal mol^{-1} for the back-reaction, within error of the experimentally determined activation parameters. The conversion of **3-7** to **3-8** proceeds through **TS-2**, calculated to have an activation barrier of $\Delta G^{\ddagger}_{298K}$ = 7.7 kcal mol^{-1}. The transformation of **3-7** to **3-8** is calculated to be more exergonic than **3-5** to **3-6**, ΔG°_{298K} = –18.7 kcal mol^{-1} but the low activation barrier means that the back reaction should also be feasible, $\Delta G^{\ddagger}_{298K}$ = 26.5 kcal mol^{-1}. Experimentally the decomposition of **3-8** occurs before the elimination of CO can be observed.

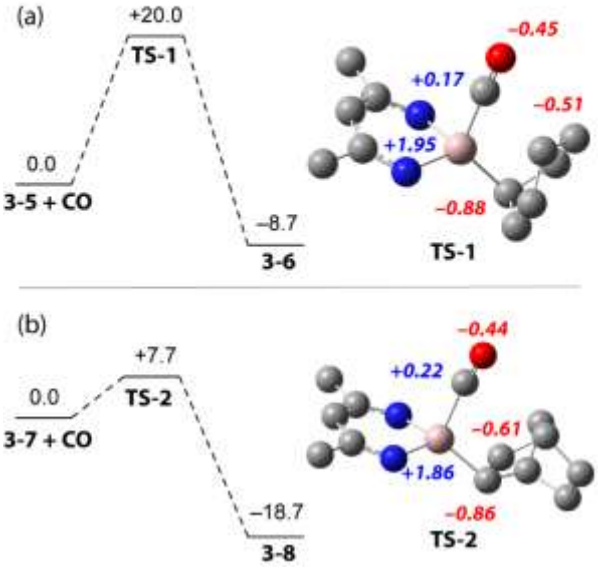


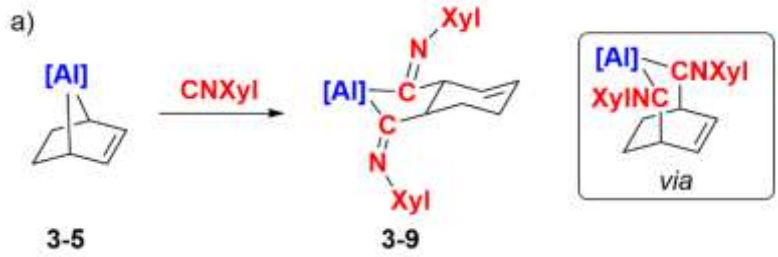
Figure 3.4: DFT calculations on the insertion of CO into the Al–C bond of a) **3-5** and b) **3-7**. All energies provided in kcal mol^{-1}. NPA charges provided in italicised bold for transition states **TS-1** and **TS-2**.

Both **TS-1** and **TS-2** directly connect reactants and products and involve an asynchronous concerted Al–C and C–C bond forming process. In contrast to more established migratory insertion reactions of transition metal complexes and a previously calculated pathway for CO insertion into a trialkylaluminium complex,[6] there is no intermediate in these pathways. Despite this, there is a clear parallel between the asynchronicity of these transition states and the stepwise coordination/insertion processes documented for transition metal mediated carbonylation. NBO analysis (Wiberg bond indices) allows the characterisation of a strong Al–CO interaction in the transition states relative the products (**TS-1**, 0.45; **3-6**, 0.48; **TS-2**, 0.50; **3-8**, 0.53). Incipient C---C bond formation is also clear from these data (**TS-1**, 0.46; **3-6**, 0.92; **TS-2**, 0.41; **3-8**, 0.95). The notable disparity in values between the transition-state and product suggest that C–C bond formation occurs *after* Al–C bond formation along the reaction coordinate and that CO binding to Al is an important consideration. Analysis of the NPA charges (Fig. 2) indicates that C–C bond formation occurs *via* a nucleophilic attack on the bound CO by the electronegative aluminium alkyl. The role of electrophilic aluminium centres as Lewis acids in migratory insertion reactions of transition metal carbonyls has been established before.[11,12]

3.3 – Conclusions and Future Work

In this chapter, the reversible insertion of CO into an Al–C bond for two different metallacycles is demonstrated. DFT calculations show that the reaction proceeds through a concerted but highly asynchronous transition state. The reaction parallels the well-established transition-metal migratory insertion reactivity.

The insertion of various other small molecules should be explored. Preliminary reactions of **3-5** with isocyanides (Scheme 3.6) showed that the double insertion of isocyanides is possible through the crystallographically characterised complex **3-9**. The mechanism may proceed through initial double-insertion to generate an intermediate (Scheme 3.6, inset). Several other uncharacterised side-products form alongside **3-9**, however. The insertion of other small molecules such as carbodiimides should also be explored.



Scheme 3.6: Reaction of **3-5** with 2,6-dimethylphenyl isocyanide.

Exploration of the reaction of CO with various other aluminium heterocycles can be considered. A diverse range of aluminium heterocycles have been synthesised by our group and others – exploring the factors that govern CO insertion into aluminium–carbon bonds will yield fundamental knowledge for further application.

Functionalisation of the aluminium-acyl complexes should be explored. Hydroformylation is a key catalytic technology which currently relies on transition-metal catalysts (Rh, Ir, Co) which are in increasingly short supply. While no catalytic methodologies have been developed within this chapter, the striking parallels between transition-metal reactivity and main-group reactivity warrant investigation into main-group catalysed hydroformylation reactions.

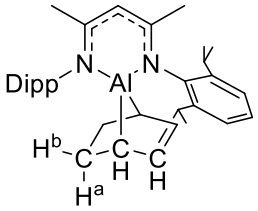
3.4 – Experimental

3.4.1 – General experimental

All manipulations were carried out using standard Schlenk-line and glovebox techniques under an inert atmosphere of argon or dinitrogen. A MBraun Labmaster glovebox was employed, operating at <0.1 ppm O_2 and <0.1 ppm H_2O. Solvents were dried over activated alumina from an SPS (solvent purification system) based upon the Grubbs design and degassed before use. Glassware was dried for 12 h at 120°C prior to use. Benzene-d_6 was dried over 3 Å molecular sieves and subjected to the freeze-pump-thaw degassed thrice before use. 1,3-cyclohexadiene was dried over molecular sieves and freeze-pump-thaw degassed thrice before use.

NMR Spectra were recorded on Bruker 400 MHz or 500 MHz at 298 K unless otherwise stated and values recorded in ppm. Data were processed in MestReNova software. Where needed, chemical shifts were assigned with the assistance of 2D NMR (HSQC, HMBC, COSY) spectra. **[Al]** and **3-7** were prepared according to literature procedure.[9,13] IR spectra were taken with a Cary Agilent 630 spectrometer.

3.4.2 – Preparation of Compounds



In a glovebox, **[Al]** (18 mg, 0.040 mmol) was dissolved in toluene (~ 3 mL). To this solution, 1,3-cyclohexadiene (5 µL, 0.052 mmol) was added *via* micropipette. An instantaneous colour change from the characteristic orange-red of **[Al]** to yellow was observed. The reaction was stirred for approximately 20 minutes before volatiles were removed *in vacuo*, to afford **3-5** as a pale yellow powder. The product thus obtained is sufficiently pure for use and characterisation, however **3-5** can be recrystallised from mixtures of toluene:hexane (1:3) as pale yellow blocks (Yield: 16 mg, 0.030 mmol, 75%).

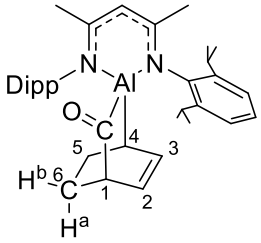
^{1}H NMR (400 MHz, C_6D_6, 298 K): δ 7.21-706 (m, 6H, Ar**H**), 6.02 (m, 2H, **H**C=C**H**), 4.84 (s, 1H, $(CH_3)C(CH)C(CH_3)$), 3.41 (hept, $^{3}J_{HH}$ = 6.8 Hz, 2H, $(CH_3)_2CH$), 3.21 (hept, $^{3}J_{HH}$ = 6.8 Hz, 2H, $(CH_3)_2CH$), 2.09 – 2.00 (m, 2H, AlC**H**), 1.56 (s, 3H, $(CH_3)C(CH)C(CH_3)$), 1.52 (s, 3H, $(CH_3)C(CH)C(CH_3)$), 1.44 (d, $^{3}J_{HH}$ = 6.8 Hz, 6H, $(CH_3)_2CH$)), 1.40 (d, $^{3}J_{HH}$ = 6.8 Hz, 6H, $(CH_3)_2CH$)), 1,40 (m, 2H, (CH)(CH_aH_b)(CH_aH_b)(CH), 1.29 (dd, $^{3}J_{HH}$ = 10.0, 3.8 Hz, 2H, (CH)(CH_aH_b)(CH_aH_b)(CH)), 1.04 (d, $^{3}J_{HH}$ = 6.8 Hz, 8H, $(CH_3)_2CH$)), 1.02 (d, ^{3}J = 6.8 Hz, 6H, $(CH_3)_2CH$)).**

$^{13}C\{^{1}H\}$ NMR (101 MHz, C_6D_6, 298K)

δ 171.6 (**C**N), 169.5 (**C**N), 144.1 (Ar**C**), 143.5 (Ar**C**), 142.3 (Ar**C**), 140.5 (Ar**C**), 131.3 (H**C**=**C**H), 127.6 (Ar**C**), 126.7 (Ar**C**), 124.3 (Ar**C**), 124.0 (Ar**C**), 96.0 ($(CH_3)C(CH)C(CH_3)$), 29.9 (br, Al**C**H), 28.5 ((CH)(CH_aH_b)(CH_aH_b)(CH)), 28.4 $(CH_3)_2CH$), 28.1 $(CH_3)_2CH$), 24.9 $(CH_3)_2CH$), 24.8 $(CH_3)_2CH$), 24.4 $(CH_3)C(CH)C(CH_3)$, 23.4 $(CH_3)_2CH$), 23.2 $(CH_3)_2CH$), 23.1 $(CH_3)C(CH)C(CH_3)$.

Anal. calc. for $C_{35}H_{49}AlN_2$: C 80.11, H 9.41, N 5.34. Found: C 80.04, H 9.50, N 5.39.

** Unequivocal assignment of the diastereotopic methylene protons is not possible due to the overlap between the multiplet at 1.40 ppm with the di-isopropyl methyl groups.



In a glovebox, **[Al]** (40.5 mg, 0.091 mmol) was dissolved in ~0.5 mL of C_6D_6 and transferred to a J-Young NMR tube. 1,3-cyclohexadiene (12.5 µL, 0.137 mmol) was added to the NMR tube *via* micropipette and the tube was shaken to allow the reagents to mix. An immediate colour change was observed from the characteristic orange-red colour of **[Al]** to the light yellow colour of **3-5**. The reaction was checked by ^{1}H NMR spectroscopy to ensure the complete conversion to **3-5**. The NMR tube was returned to the glovebox and all volatiles were removed *in vacuo*. The resultant yellow powder was redissolved in 0.6 mL of C_6D_6 and freeze-pump thaw degassed thrice before an atmosphere of CO (~1.1 bar) was introduced. The reaction was heated at 100°C for 1 h and then at 40°C for 7 days.†† ^{1}H NMR spectroscopy was used to monitor the reaction progress. Upon completion, the NMR tube was returned to the glovebox, the solution decanted into a 20 mL scintillation vial and all volatiles were removed *in vacuo*. The resultant powder was washed once with toluene (1 x 3 mL) and thrice with pentane (3 x 3 mL) affording **3-6** as a bright yellow powder (19 mg, 0.035 mmol, 38% yield).

^{1}H NMR (400 MHz, C_6D_6, 298 K) δ 7.03-7.16 (m, 6H, Ar**H**), 5.61 (m, 1H, C^3**H**), 5.56 (m, 1H, C^2-**H**), 4.78 (s, 1H, $(CH_3)C(C\mathbf{H})C(CH_3)$), 3.42 (hept, $^2J_{HH}$ = 6.6 Hz, 1H), $(CH_3)_2C\mathbf{H}$), 3.38 – 3.30 (hept, $^3J_{HH}$ = 6.6 Hz, 1H, $(CH_3)_2C\mathbf{H}$), 3.28 (hept, $^3J_{HH}$ = 6.7 Hz, 1H, $(CH_3)_2C\mathbf{H}$), 3.27 (hept, $^3J_{HH}$ = 6.7 Hz, 1H, $(CH_3)_2C\mathbf{H}$), 2.80-2.75 (m, C^1**H**, 1H), 1.73 – 1.62 (m, 1H, C^6-**H**^{a}H^b), 1.62 – 1.55 (m, 1H, C^4-**H**), 1.52 (s, 3H, $(C\mathbf{H_3})C(CH)C(CH_3)$), 1.51 (s, 3H, $(C\mathbf{H_3})C(CH)C(CH_3)$), 1.48 (m, 1H, C^6-H^a**H^b**), 1.41 (m, 1H, C^5-**H**^{a}H^b), 1.36 (d, $^3J_{HH}$ = 6.7 Hz, 2H, $(C\mathbf{H_3})CH(CH_3)$), 1.33 (d, $^3J_{HH}$ = 6.7 Hz, 3H, $(C\mathbf{H_3})CH(CH_3)$), 1.26 (d, $^3J_{HH}$ = 6.6 Hz, 3H, $(C\mathbf{H_3})CH(CH_3)$), 1.04 (d, $^3J_{HH}$ = 6.7 Hz, 2H, $(C\mathbf{H_3})CH(CH_3)$), 1.04 (d, $^3J_{HH}$ = 6.7 Hz, 2H, $(C\mathbf{H_3})CH(CH_3)$), 1.03 (d, $^3J_{HH}$ = 6.7 Hz, 2H, $(C\mathbf{H_3})CH(CH_3)$), 1.02 (d, $^3J_{HH}$ = 6.7 Hz, 2H, $(C\mathbf{H_3})CH(CH_3)$), 0.93 (s, 1H, C^5-H^a**H^b**).

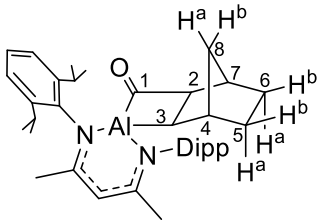
†† The reaction rate is concentration dependent and repeating this procedure with 9 mg of **[Al]** results in the reaction completion after approximately 48 h. The reaction is deemed complete upon >95% consumption of starting materials.

^{13}C NMR (101 MHz, C_6D_6) δ 254.1 (**C**O), 171.4 (**C**N), 171.1 (**C**N), 145.9 (Ar**C**), 145.7 (Ar**C**), 143.7 (Ar**C**), 143.1 (Ar**C**), 140.3 (Ar**C**), 139.6 (Ar**C**), 139.4 (**C**^{3}-H), 125.4 (Ar**C**), 125.2 (Ar**C**), 123.9 (Ar**C**), 123.7 (Ar**C**), 121.8 (**C**^{2}-H), 97.1 ($(CH_3)C(\mathbf{C}H)C(CH_3)$), 61.5 (**C**^{1}-H), 29.1 $(CH_3)_2\mathbf{C}H$), 28.9 $(CH_3)_2\mathbf{C}H$), 28.1 (br, **C**^{4}-H), 27.7 $(CH_3)_2\mathbf{C}H$), 25.9 (**C**^{6}-H_aH_b), 25.7 ($\mathbf{C}H_3)_2CH$), 25.6 ($\mathbf{C}H_3)_2CH$), 25.5 ($\mathbf{C}H_3)_2CH$), 25.1 (overlapping, $\mathbf{C}H_3)_2CH$), 25.1 (overlapping, $\mathbf{C}H_3)_2CH$), 24.9 ($\mathbf{C}H_3)_2CH$), 23.8 ($\mathbf{C}H_3)_2CH$), 23.6 ($\mathbf{C}H_3)_2CH$), 23.3 (overlapping, $(\mathbf{C}H_3)C(CH)C(CH_3)$), 23.3 (overlapping, $(\mathbf{C}H_3)C(CH)C(CH_3)$, 22.5 (**C**^{5}-$H_aH_b$).

IR (ATR), cm^{-1}: 1620 (CO).

Anal. calc. for $C_{36}H_{49}AlN_2O$: C 78.22, H 8.94, N 5.07. Found: C 72.57, H 9.32, N, 4.83.‡‡

‡‡ Thermal sensitivity of **3-6** prevented attainment of accurate elemental analysis.



In a glovebox, **[Al]** (9 mg, 0.020 mmol) and norbornene (5 mg, 0.050 mmol) were dissolved in C_6D_6 (0.600 mL) and transferred to a J-young NMR tube. The formation of **3-7** was monitored by NMR spectroscopy, and upon reaction completion, all volatiles were removed *in vacuo*. The residue was redissolved in C_6D_6 (0.6 mL) and freeze-pump-thaw degassed thrice before an atmosphere of CO was introduced to the sample. An instantaneous colour change from the characteristic dark-red of **3-7** to yellow was observed. An NMR taken after reaction completion shows the formation of **3-8** (95% yield, vs. internal ferrocene standard). Allowing **3-8** to stand under these conditions results in decomposition over the course of 12 h. X-ray quality were grown by rapidly transferring a solution of **5** in C_6D_6 to a vial, diluting with toluene and concentrating *in vacuo* and setting vapour diffusion of pentane into a concentrated toluene solution of **3-8** at -35°C. While **3-8** is amenable to X-ray diffraction analysis as single crystals, it decomposes as a solid under inert atmosphere, and vacuum, at ambient temperature thus precluding attainment of elemental analysis and meaningful isolated yields.

^{1}H NMR (400 MHz, C_6D_6, 298 K) δ 7.08-7.28 (m, Ar**H**), 5.00 (s, 1H, $(CH_3)C(C\mathbf{H})C(CH_3)$), 3.46 (hept, $^3J_{HH}$ = 6.7 Hz, 1H, $(CH_3)_2C\mathbf{H}$), 3.46 (hept, $^3J_{HH}$ = 6.7 Hz, 1H, $(CH_3)_2C\mathbf{H}$), 3.33 (hept, $^3J_{HH}$ = 6.7 Hz, 1H, 3.46 (hept, $^3J_{HH}$ = 6.7 Hz, 1H, $(CH_3)_2C\mathbf{H}$), 3.09 (hept, $^3J_{HH}$ = 6.6 Hz, 1H, 2.85 – 2.83 (m, 1H, C^7-**H**), 2.47 (m, 1H, C^6-**H**), 1.63 (d, $^3J_{HH}$ = 6.8 Hz, 6H, $(C\mathbf{H_3})_2CH$), 1.61 (s, H, $(C\mathbf{H_3})C(CH)C(CH_3)$), 1.60 (m, overlapping, 1H, C^2-**H**), 1.59 (s, 3H, $(C\mathbf{H_3})C(CH)C(CH_3)$), 1.55 (m, 1H, C^6-**H^a**) 1.47 (d, $^3J_{HH}$ = 6.7 Hz, 3H, $(C\mathbf{H_3})_2CH$)), 1.33 (d, $^3J_{HH}$ = 6.7 Hz, 3H, $(C\mathbf{H_3})_2CH$), 1.25 (m, overlapping, 1H, C^5-**H^b**), 1.22 (d, $^3J_{HH}$ = 6.9 Hz, 3H, $(C\mathbf{H_3})_2CH$), 1.19 (d, $^3J_{HH}$ = 6.8 Hz, 3H, $(C\mathbf{H_3})_2CH$), 1.15 (m, overlapping, 1H, C^3-**H**), 1.11 (d, $^3J_{HH}$ = 6.8 Hz, 3H, $(C\mathbf{H_3})_2CH$), 1.02 (d, $^3J_{HH}$ = 6.7 Hz, 3H, $(C\mathbf{H_3})_2CH$), 0.97 (m, 1H, C^5-**H^a**), 0.92 (m, 1H, C6-**H^b**), 0.66 (m, 1H, C^8-**H^a**), 0.30 (m, 1H, C^8-**H^b**).

^{13}C NMR (101 MHz, C_6D_6, 298 K) δ 292.3 (**C**O), 170.6 (**C**N), 170.0 (**C**N), 145.1 (Ar**C**), 144.6 (Ar**C**), 143.1 (Ar**C**), 142.7 (Ar**C**), 139.9 (Ar**C**), 139.3 (Ar**C**), 125.1 (Ar**C**), 124.8 (Ar**C**), 124.0 (Ar**C**), 123.9(Ar**C**), 97.8 ($(CH_3)C(\mathbf{C}H)C(CH_3)$), 69.1 (**C**2-H), 43.9 (**C**3-H), 40.1 (**C**6-H), 38.7 (**C**7-H_2), 34.5 (br, **C**8-H), 34.4 (**C**4-H_2), 29.4 $(CH_3)_2\mathbf{C}H$), 29.4 $(CH_3)_2\mathbf{C}H$), 29.0 (**C**5-H), 27.7 $(CH_3)_2\mathbf{C}H$), 27.4 $(CH_3)_2\mathbf{C}H$), 25.0 $(\mathbf{C}H_3)_2CH$), 24.8 $(\mathbf{C}H_3)_2CH$), 24.8 $(\mathbf{C}H_3)_2CH$), 24.7 $(\mathbf{C}H_3)_2CH$), 24.6 $(\mathbf{C}H_3)_2CH$), 24.1 $(\mathbf{C}H_3)_2CH$), 23.9 $(\mathbf{C}H_3)_2CH$), 23.9 $(\mathbf{C}H_3)_2CH$), 23.1 $(\mathbf{C}H_3)C(CH)C(CH_3)$, 22.9 $(CH_3)C(CH)C(\mathbf{C}H_3)$.

Anal. calc. for $C_{37}H_{51}AlN_2O$: C 78.40, H 9.07, N 4.94. Found: C 76.11, H 9.59, N 4.79.[§§]

IR (ATR), cm^{-1}: 1652 (CO).

[§§] Thermal sensitivity of **3-8** prevented attainment of accurate elemental analysis.

3.4.3 – Labelling Experiments

Exchange of ^{13}CO into **3-6**

In a glovebox, **3-6** (5 mg, 0.009 mmol) was dissolved in 0.600 mL C_6D_6 and transferred to a J-Young NMR tube. An initial time point (t1) ^1H (16 scans) and ^{13}C NMR spectrum was taken (Figure 3.5, 3.6). The tube was degassed *via* the freeze-pump-thaw procedure thrice before the introduction of ^{13}CO gas (~1 bar). The solution was heated at 100 °C for 3 hours before a second timepoint ^1H NMR spectrum was taken (t2) (Figure 3.7). The $^2J_{C-H}$ coupling of the α-carbonyl methine resonance (δ = 2.78 ppm) to ^{13}CO was observed, signalling the completion of the degenerate isotope exchange. The sample was heated at 40°C until **^{13}C-3-6** was the predominant species at which point a third taken (Figure 3.8, 3.9).

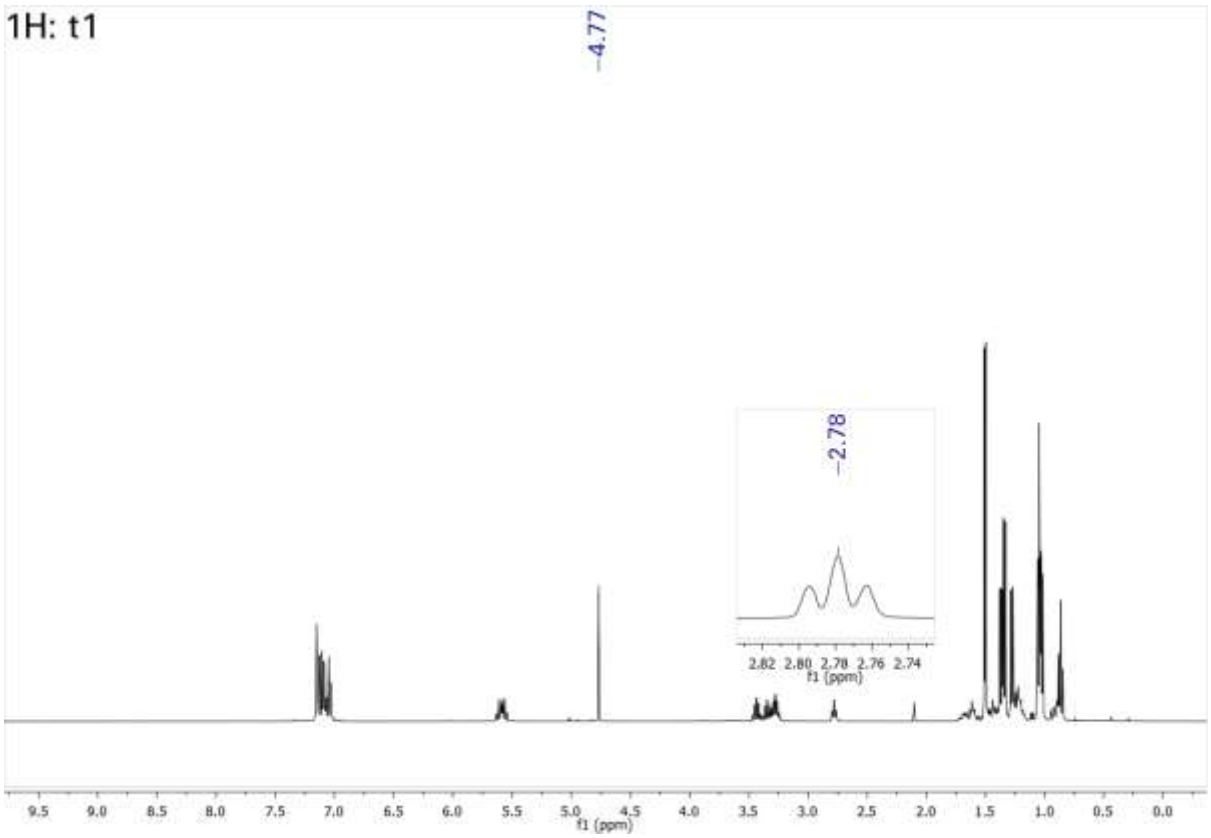


Figure 3.5: ^1H spectrum at initial timepoint of exchange experiment.

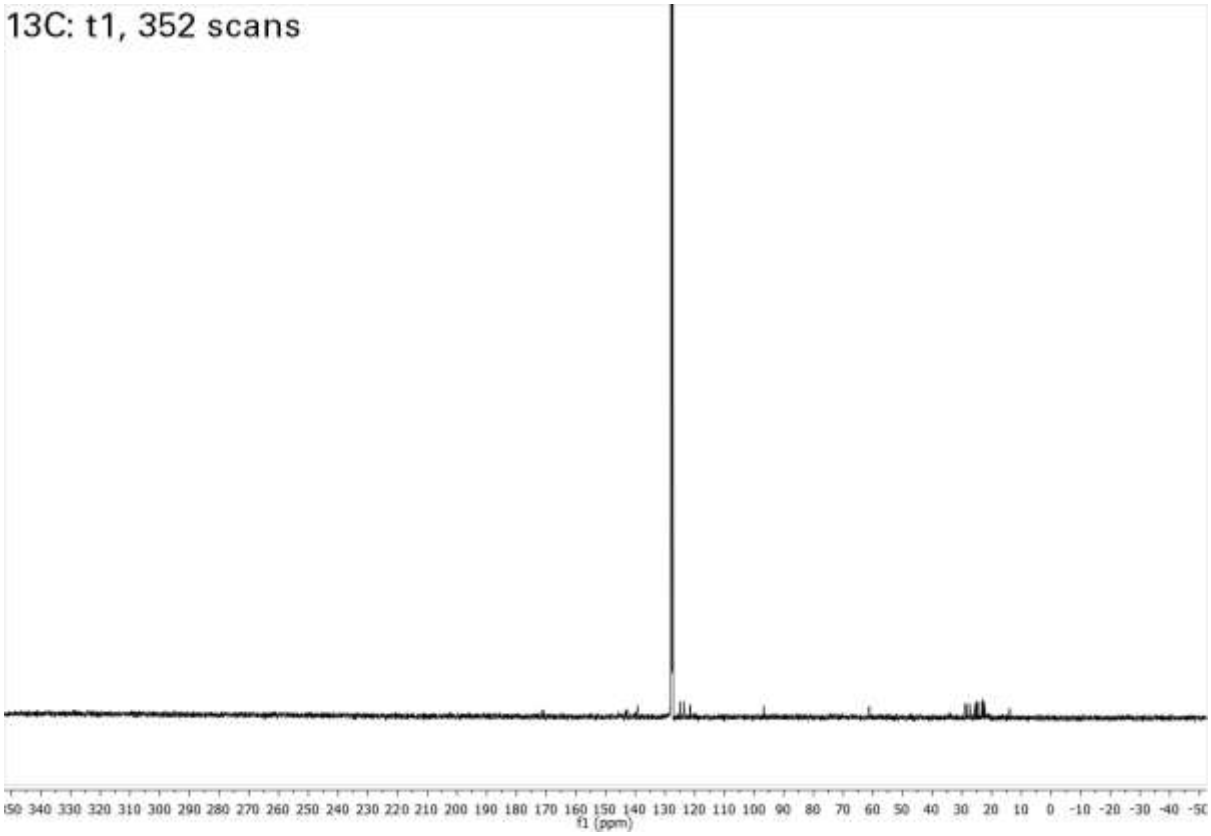


Figure 3.6: ^{13}C spectrum at initial timepoint of exchange experiment.

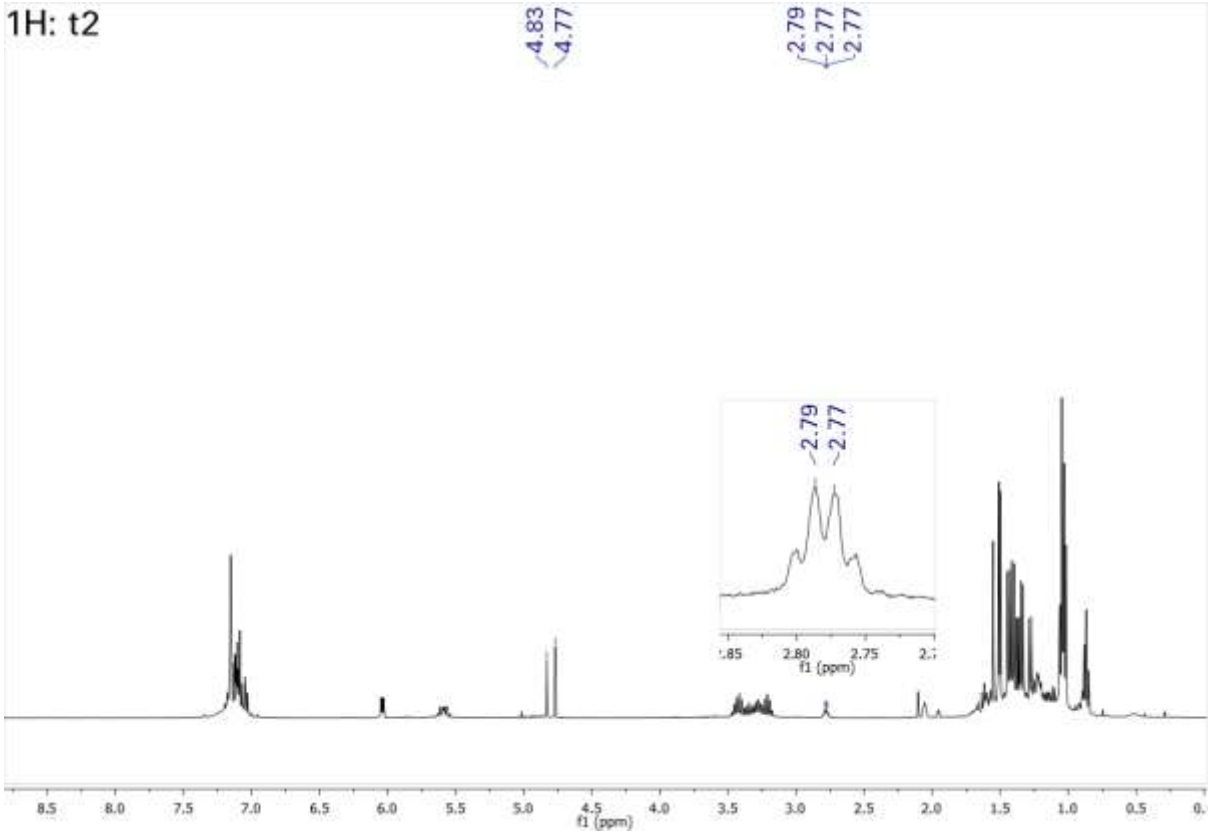


Figure 3.7: ^{1}H spectrum at 2nd timepoint in exchange experiment showing completion of exchange.

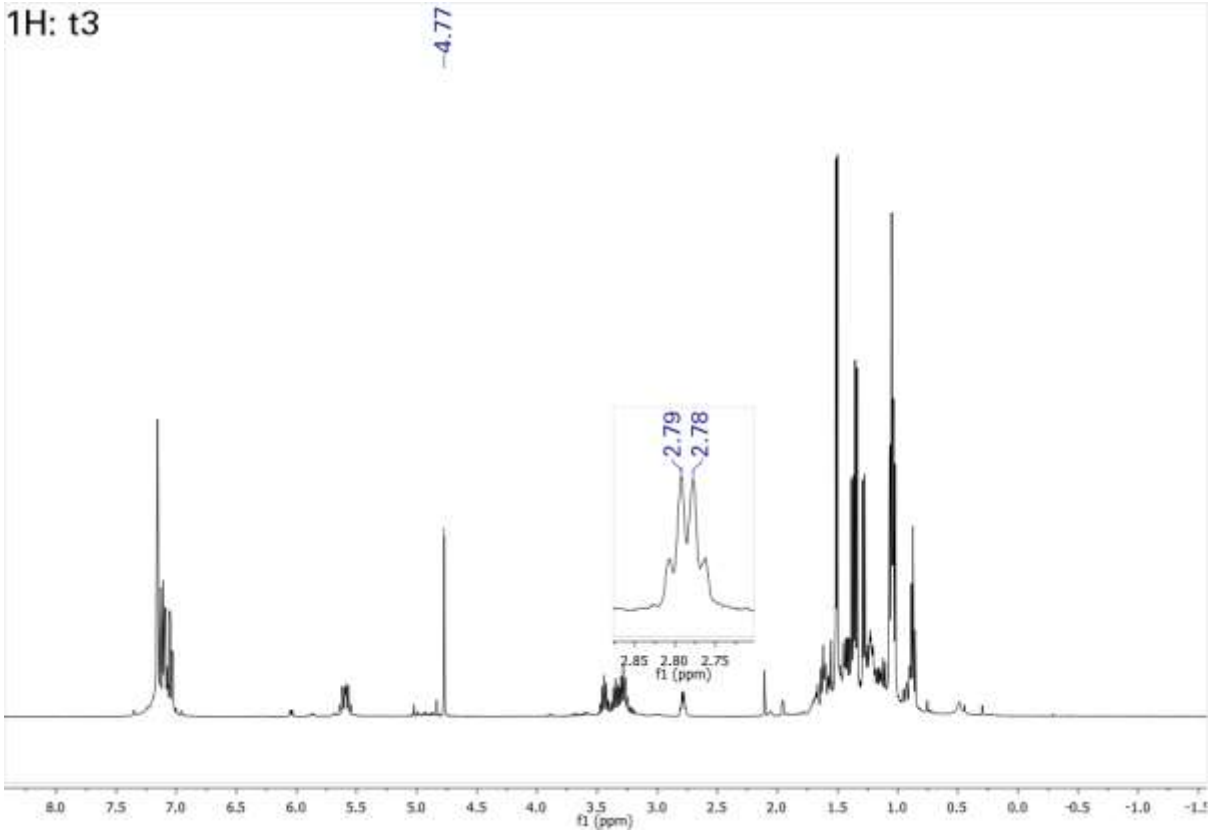


Figure 3.8: ^{1}H spectrum of **^{13}C-3-6**

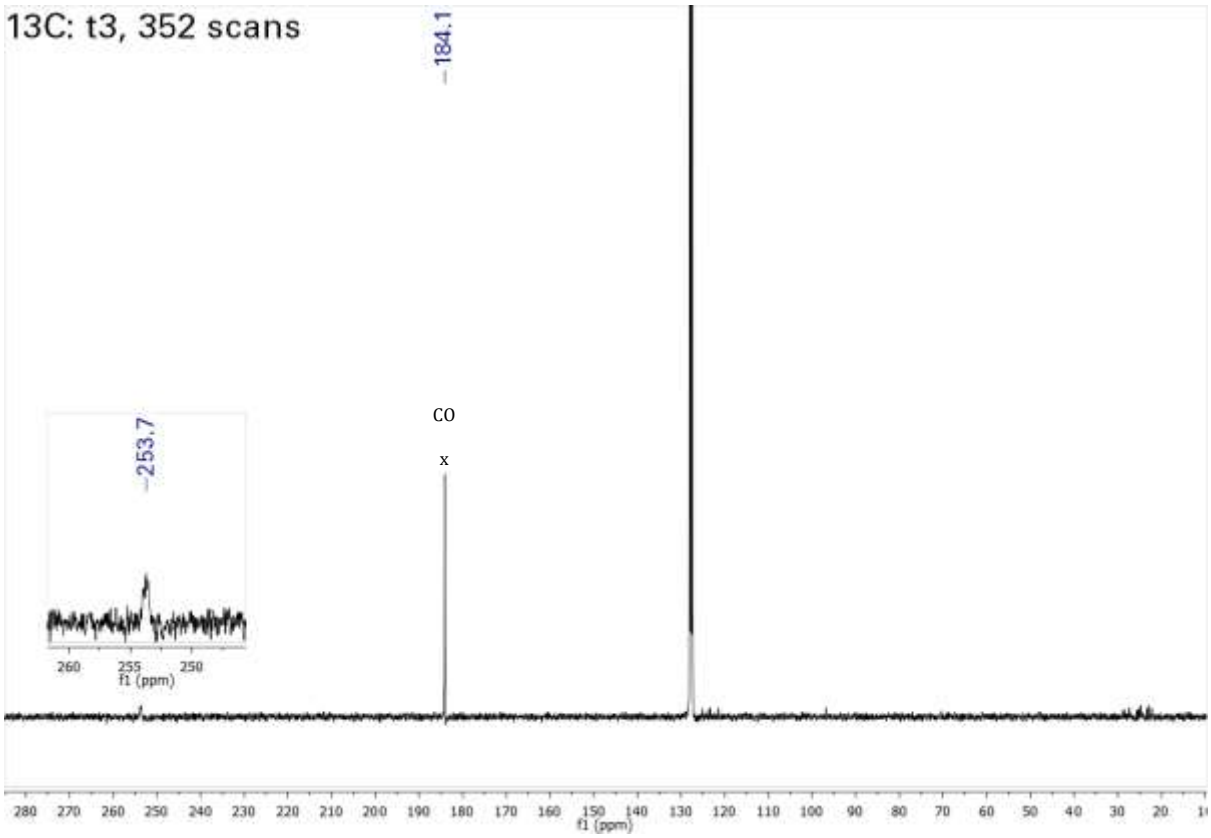


Figure 3.9: ^{13}C spectrum of ^{13}CO enriched ^{13}C-3-6.

3.4.4 – Kinetic experiments on the elimination of CO from 3-6 to form 3-5

In a glovebox, complex **3-6** (3 mg, 0.005 mmol) was dissolved in d_8-toluene (2.5 mL) and a small amount of ferrocene (1 mg) was added to be used as an internal standard. The solution of **3-6** (2 mM, 2.5 mL) was portioned into 4 x 0.550 mL aliquots and transferred into four separate J-Young NMR tubes and kept at –35°C in the glovebox.*** The NMR tubes were removed from the glovebox and inserted into a pre-heated NMR spectrometer probe. ^{1}H NMR spectra were recorded at 2 minute intervals.

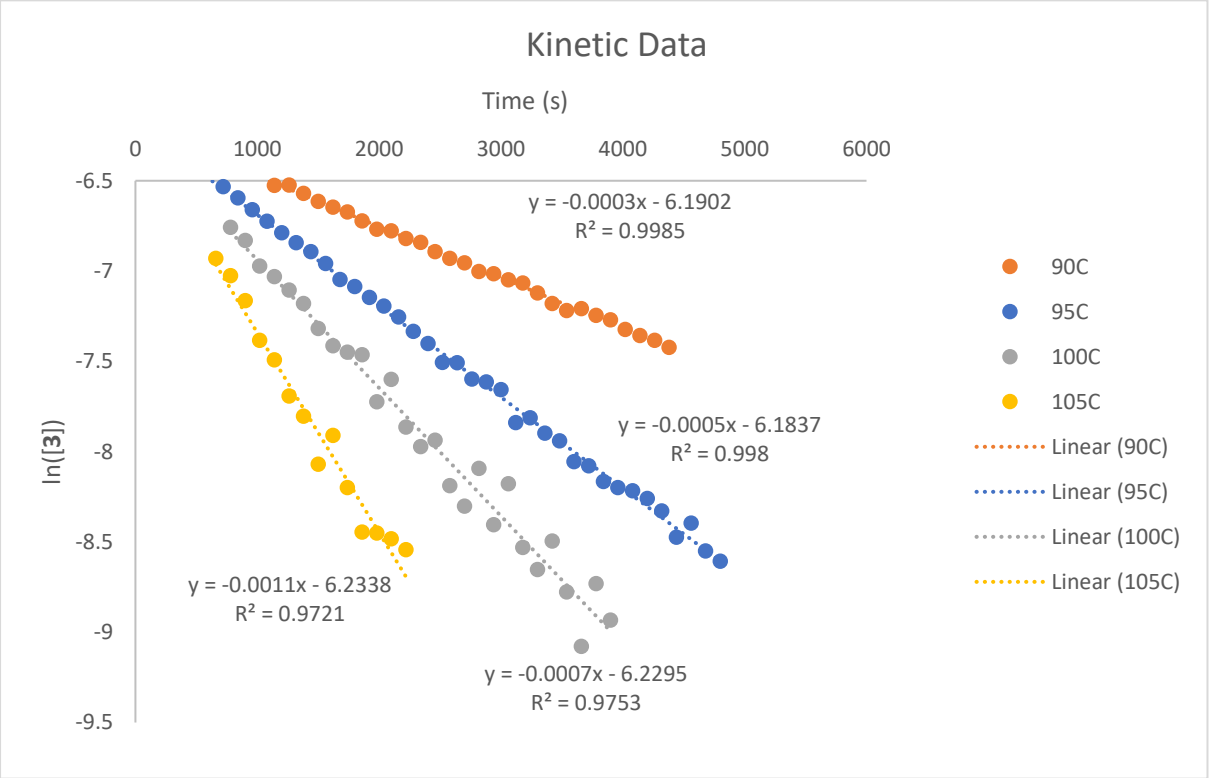


Figure 3.10: Kinetic data for the transformation from **3-6** to **3-5** at varying temperatures. Concentrations derived from integration of the methine resonances of the β-diketiminate backbone versus an internal standard.

Plotting ln[**3-6**] (concentration determined by the integration of the internal ferrocene standard) against time showed a linear relationship indicating that the reaction is first order in [**3-6**] (Figure 3.10). Four rate constants were determined in the temperature range of 90 °C to 105°C at 5°C intervals and a plot of $\ln(k_{obs})$ against 1/T allowed calculation of the thermodynamic parameters using the Eyring equation. Standard errors were calculated using regression analysis in the Microsoft Excel program. The activation parameters for the reverse reaction were found to be: $\Delta H^{\ddagger}$ = 23.5 ±1.7 kcal mol^{-1}, $\Delta S^{\ddagger}$ = –10.3 ± 4.5 cal K^{-1} mol^{-1} and an associated $\Delta G^{\ddagger}_{298K}$ = 26.5 ±3.0 kcal mol^{-1} (Figure 3.11).

*** Assuming a standard 7-inch J-Young NMR tube with usable volume of approx. 2.4 mL, the maximum concentration of CO in the headspace (1.85 mL) should not exceed 15 ppm.

T (K)	K_{obs} (s^{-1})	1/T (K^{-1})	ln(k/T)
363	0.000282	0.002755	-14.0679
368	0.000505	0.002717	-13.4993
373	0.000709	0.002681	-13.1732
378	0.001107	0.002646	-12.7406

Table 3.1: Rate constants extracted from kinetic experiments.

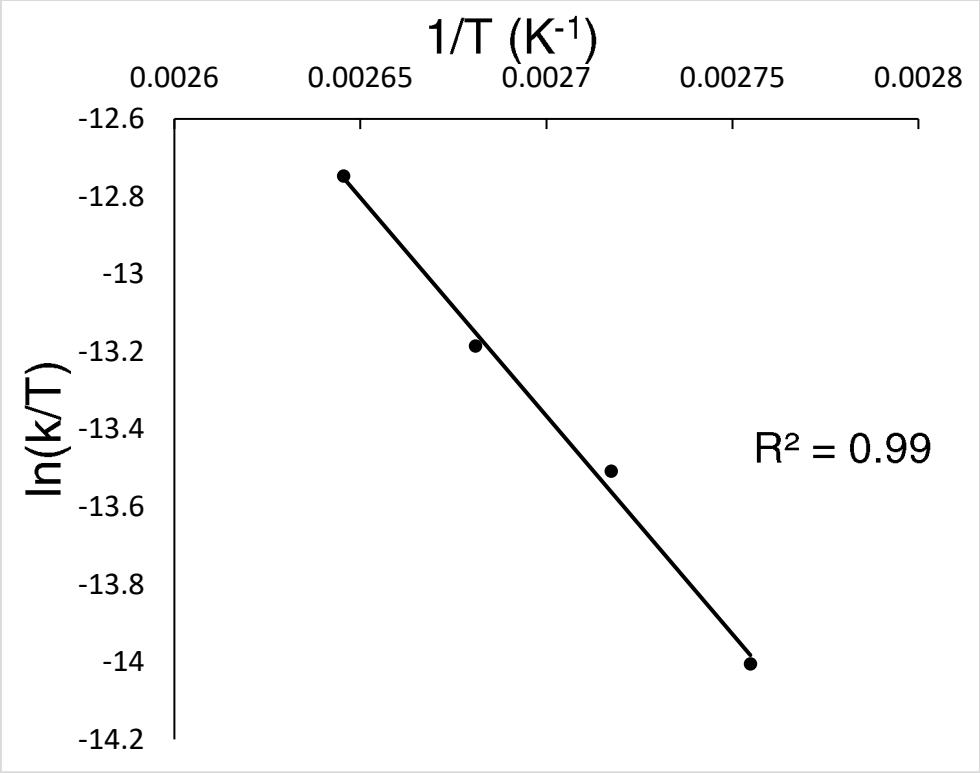


Figure 3.11: Eyring plot of data from Table 4.1.

3.5 – X-ray Structures

*The X-ray crystal structure of **3-5***

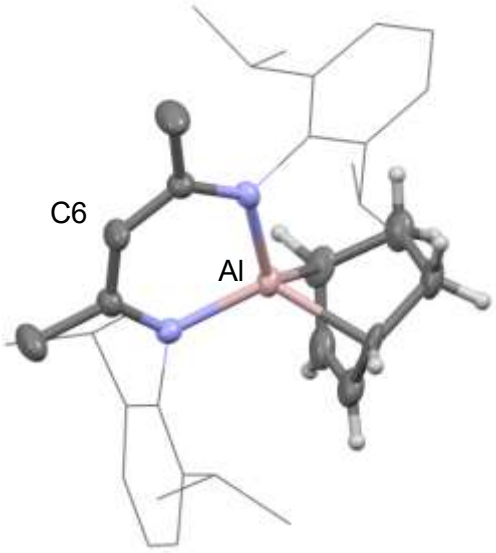


Figure 3.12: The X-ray crystal structure of **3-5.**

The structure of **3-5** was found to have C_{2v} symmetry which passes through the Al1-C6 axis. The entirety of the cyclohexene fragment was found to be disordered over C_{2v} symmetry and was modelled using one complete 50% occupancy orientation (with the mirror symmetry generating a second 50% orientation). Distance restraints between the C2–C3 and C5–C6 bonds were used to model the double and single bonds respectively. The geometries of both orientations were optimised and the thermal parameters of the entirety of the disordered fragment were restrained to be similar.

The carbon atoms (C14, C15) in the C13 isopropyl group were found to be disordered and two orientations were identified to *ca.* 75% and 25% occupancy. The geometries of both orientations were optimised and the thermal parameters of adjacent atoms were restrained to be similar, and only the non-hydrogen atoms of the major occupancy orientation were refined anisotropically (those of the minor occupancy orientation were refined isotropically).

Crystal Data for $C_{35}H_{51}AlN_2$, M =526.75, monoclinic, space group P2/n (no. 13), a = 12.7484(13) Å, b = 9.4906(9) Å, c = 13.5651(15) Å, β = 105.015(11)°, V = 1585.2(3) Å^3, Z = 2, ρ_{calc}g/cm^3 = 1.104, μ(MoKα) = 0.089 mm^{-1}, T = 173.00(10), yellow plates, F^2 refinement, R_1(obs) = 0.0567, wR_2(all) = 0.1604, 3191 independent observed reflections (R_{int} = 0.0259), 2414 independent measured reflections [$|F_o| > 4\sigma(|F_o|)$, $2\theta_{full}$ = 56.576], 189 parameters. CCDC 1905522.

The X-ray crystal structure of ***3-8***

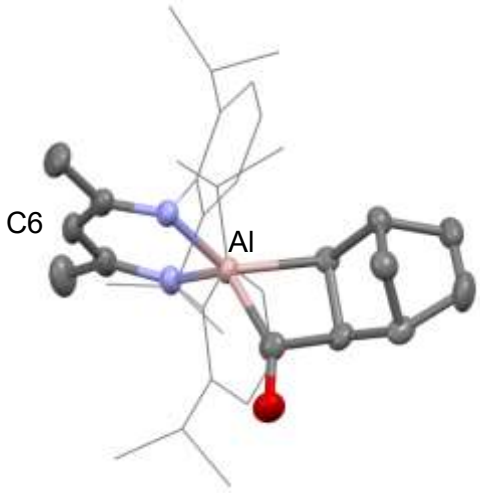


Figure 3.13: The X-ray structure of **3-8.**

The structure of **3-8** was found to have C_s symmetry which passes through the Al1, C6 axis. The whole of the acyl-norbornane fragment was found to be disordered over the mirror plane and was modelled using one complete 50% occupancy orientation (with the mirror symmetry generating a second 50% occupancy orientation).

Crystal Data for $C_{44}H_{59}AlN_2O$, M =658.91, orthorhombic, space group Pnma (no. 62), a = 24.3410(10) Å, b = 14.7167(6) Å, c = 10.9529(5) Å, V = 3923.5(3) Å^3, Z = 4, ρ_{calc}g/cm^3 = 1.115, μ(MoKα) = 0.086 mm^{-1}, T = 173.00(10), yellow plates, F^2 refinement, R_1(obs) = 0.0644, wR_2(all) = 0.1703, 4102 independent observed reflections (R_{int} = 0.0393), 2954 independent measured reflections [$|F_o| > 4\sigma(|F_o|)$, $2\theta_{full}$ = 56.402], 274 parameters. CCDC 1905523.

3.6 – Computational details

DFT calculations were run using Gaussian 09 (Revision D.01)[14] using the M06l Minnesota functional.[15] Other functionals investigated were Al centres were described with Stuttgart SDDAll and associated basis sets and the 6-31G** basis sets were used for all other atoms.

Geometry optimisation calculations were performed without symmetry constraints. Frequency analyses for all stationary points were performed using the enhanced criteria to confirm the nature of the structures as either minima (no imaginary frequency) or transition states (only one imaginary frequency). Single point solvent corrections (benzene, $\varepsilon = 2.2706$) were applied using the polarizable continuum model (PCM)[16] to free energies reported in the main text. Single point dispersion corrections were applied to the free energies; to the ωB97X energies using the ωB97X-D functional, to the B3PW91 energies using Grimme's D3 correction with Becke-Johnson damping, and to the Minnesota functional (M06L, M062X) energies, using Grimme's D3 correction.[17]

Intrinsic reaction coordinate (IRC) calculations were used to connect transition states and minima located on the potential energy surface allowing a full energy profile (calculated at 298.15 K, 1 atm) of the reaction to be constructed.[18,19] Natural Bond Orbital analysis was carried out using NBO 6.0.[20]

3.7 – References

1 J. F. Hartwig, *Organotransition metal chemistry: from bonding to catalysis*, University Science Books, 2010.
2 J. H. Jones, *Platin. Met. Rev.*, 2000, **44**, 94–105.
3 R. Franke, D. Selent and A. Börner, *Chem. Rev.*, 2012, **112**, 5675–5732.
4 K. Ohno and J. Tsuji, *J. Am. Chem. Soc.*, 1968, **90**, 99–107.
5 M. R. Mason, B. Song and K. Kirschbaum, *J. Am. Chem. Soc.*, 2004, **126**, 11812–11813.
6 M. R. Mason, B. Song, Y. Han and X. Hu, *Inorg. Chim. Act.*, 2008, **361**, 3332–3337.
7 X. Li, C. Ni, H. Song and C. Cui, *Chem. Commun.*, 2006, 1763–1765.
8 C. Bakewell, M. Garçon, R. Y. Kong, L. O'Hare, A. J. P. White and M. R. Crimmin, *Inorg. Chem.*, 2020, **59**, 4608–4616.
9 C. Cui, H. W. Roesky, H.-G. Schmidt, M. Noltemeyer, H. Hao and F. Cimpoesu, *Angew. Chem., Int. Ed.*, 2000, **39**, 4274–4276.
10 R. Y. Kong and M. R. Crimmin, *J. Am. Chem. Soc.*, 2018, **140**, 13614–13617.
11 S. B. Butts, S. H. Strauss, E. M. Holt, R. E. Stimson, N. W. Alcock and D. F. Shriver, *J. Am. Chem. Soc.*, 1980, **102**, 5093–5100.
12 T. G. Richmond, Fred. Basolo and D. F. Shriver, *Inorg. Chem.*, 1982, **21**, 1272–1273.
13 C. Bakewell, A. J. P. White and M. R. Crimmin, *Angew. Chem., Int. Ed.*, 2018, **57**, 6638–6642.
14 Frisch, M. J.; Trucks, G. W.; Schlegel, H. B.; Scuseria, G. E.; Robb, M. A.; Cheeseman, J. R.; Scalmani, G.; Barone, V.; Mennucci, B.; Petersson, G. A.; Nakatsuji, H.; Caricato, M.; Li, X.; Hratchian, H. P.; Izmaylov, A. F.; Bloino, J.; Zheng, G.; Sonnenberg, J. L.; Hada, M.; Ehara, M.; Toyota, K.; Fukuda, R.; Hasegawa, J.; Ishida, M.; Nakajima, T.; Honda, Y.; Kitao, O.; Nakai, H.; Vreven, T.; Montgomery, J. A., Jr.; Peralta, J. E.; Ogliaro, F.; Bearpark, M.; Heyd, J. J.; Brothers, E.; Kudin, K. N.; Staroverov, V. N.; Kobayashi, R.; Normand, J.; Raghavachari, K.; Rendell, A.; Burant, J. C.; Iyengar, S. S.; Tomasi, J.; Cossi, M.; Rega, N.; Millam, J. M.; Klene, M.; Knox, J. E.; Cross, J. B.; Bakken, V.; Adamo, C.; Jaramillo, J.; Gomperts, R.; Stratmann, R. E.; Yazyev, O.; Austin, A. J.; Cammi, R.; Pomelli, C.; Ochterski, J. W.; Martin, R. L.; Morokuma, K.; Zakrzewski, V. G.; Voth, G. A.; Salvador, P.; Dannenberg, J. J.; Dapprich, S.; Daniels, A. D.; Farkas, Ö.; Foresman, J. B.; Ortiz, J. V.; Cioslowski, J.; Fox, D. J. Gaussian~09 Revision E.01. Gaussian, Inc., Wallingford, CT 2009.
15 Y. Zhao and D. G. Truhlar, *Theor. Chem. Acc.*, 2008, **120**, 215–241.
16 J. Tomasi, B. Mennucci and R. Cammi, *Chem. Rev.*, 2005, **105**, 2999–3094.
17 S. Grimme, J. Antony, S. Ehrlich and H. Krieg, *J. Chem. Phys.*, 2010, **132**, 154104.
18 K. Fukui, *Acc. Chem. Res.*, 1981, **14**, 363–368.
19 H. P. Hratchian and H. B. Schlegel, in *Theory and Applications of Computational Chemistry*, eds. C. E. Dykstra, G. Frenking, K. S. Kim and G. E. Scuseria, Elsevier, Amsterdam, 2005, pp. 195–249.
20 Gleadening, E. D.; Bakenhoop, J. K.; Reed, A. E.; Carpenter, J. E.; Bohmann, J. A.; Morales, C. M.; Landis, C. R.; Weinhold, F. NBO 6.0. Theoretical Chemistry Institute, University of Wisconsin, Madison 2013.

Chapter 4

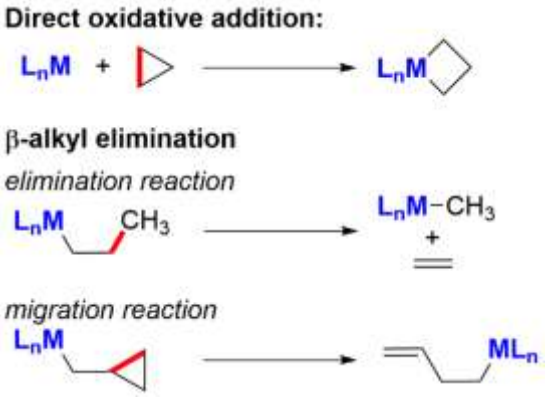
Activation and Functionalization of C–C σ-Bonds of Alkylidene Cyclopropanes at Main Group Centres

4.1 – Introduction to C–C activation

4.1.1 – Background

The activation of a C–C bond is a powerful method for editing the hydrocarbon scaffold of a molecule. It is a key technology in the upgrading of hydrocarbon feedstocks such as crude oil, where catalytic cracking is used to convert high-molecular weight alkanes to more valuable alkenes, and medium chain-length hydrocarbons (C_7 to C_9 alkanes). The reaction has further found utility in organic synthesis, where C–C activation affords a powerful method for rearranging the hydrocarbon skeleton of organic compounds allowing for novel synthetic routes to complex organic molecules.[1,2] Despite the usefulness of this transformation, the field of C–C activation has lagged behind the development of other inert-bond functionalisations due to the challenging nature of the reaction. C–C σ-bonds are strong, sterically congested, and often surrounded by C–H bonds which are typically the first site to react.

Transition metals have typically been used to effect C–C bond activation. Two broad classes of mechanism are employed by transition metals to accomplish this transformation: 1) the direct oxidative addition of the transition metal to the C–C bond,[3] and 2) β-carbon elimination at a transition-metal centre.[4] In Scheme 4.1, elimination reactions have been distinguished from migration reactions. In the case of the former reaction, the hydrocarbon substrate is fragmented following C–C cleavage, and while in the latter reaction, the substrate remains intact on the transition metal. These reactions often rely on a strong enthalpic driving force, such as the relief of ring-strain, or an entropic driving force, through the elimination of a small volatile molecule.

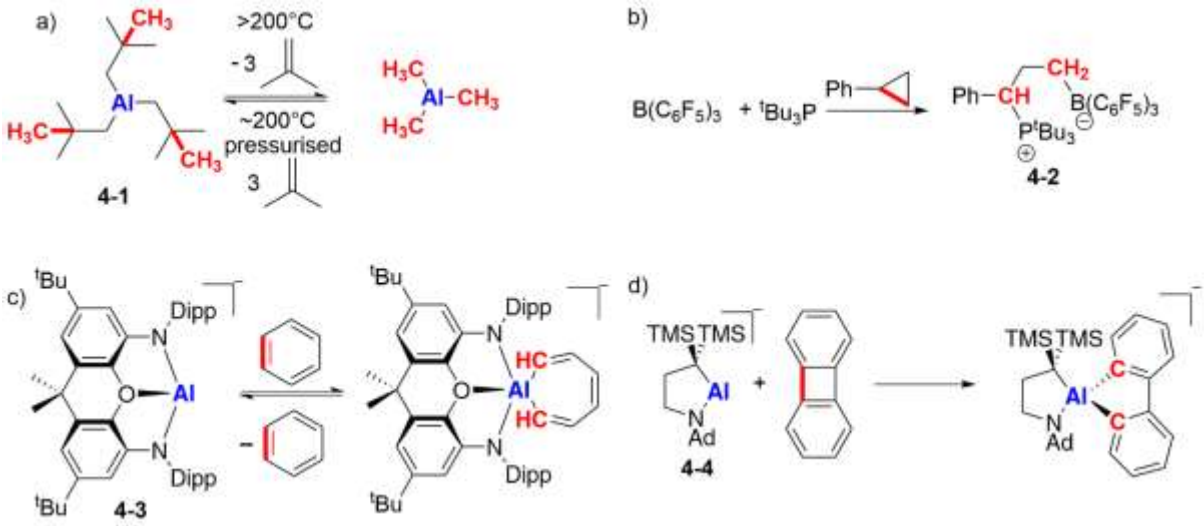


Scheme 4.1: Mechanisms for C–C cleavage at transition metal centres.

4.1.2 – Main-group C–C activation

Compared to their transition-metal counterparts, main-group elements such as magnesium and aluminium are a more abundant resource, and less chemically toxic. Hence, significant efforts have been made to access transformations traditionally accomplished using heavy-metals using light non-toxic main-group metals.[5] The lack of available d-orbitals which participate in chemical bonding on main-group elements presents a significant challenge to emulating transition metal chemistry. As a result, reports of C–C activation by main-group elements are limited in comparison to those involving transition metals.

The first reported β-carbon elimination reaction at any metal centre was demonstrated for aluminium in 1960 by Pfohl. Heating tris-neopentyl aluminium (**4-1**) at 200°C in an autoclave resulted in the clean formation of isobutene gas and trimethylaluminium (Scheme 4.2a). Remarkably the reaction is reversible: heating trimethylaluminium under a pressure of isobutene gas reformed tris-neopentyl aluminium. The elimination of isobutene gas is likely a significant entropic driving force for this reaction.



Scheme 4.2: a) β-carbon elimination from tris-neopentylaluminium. b) Frustrated Lewis pair activation of benzenecyclopropane. c) Reversible activation of benzene by a monomeric aluminyl anion. d) Oxidative addition of a C–C bond in biphenylene to an cyclic-alkyl-alumniyl anion.

In 2009, Stephan and co-workers reported the use of a frustrated Lewis pair strategy to cleave a strained C–C bond in cyclopropylbenzene to form a zwitterionic phosphonium borate (**4-2**, Scheme 4.2 b).[6] The phosphine attacks the most electrophilic benzylic carbon, while the borane reacts at the cyclopropyl methylene. This FLP strategy was developed into a catalytic protocol by Wang and co-workers in 2017: using a catalytic quantity of $B(C_6F_5)_3$ in tandem with stoichiometric 2,6-dichloropyridine and triphenylsilane, olefins were generated from cyclopropanes.[7]

In 2019, Aldridge and co-workers reported the formal oxidative insertion of a monomeric aluminyl anion (**4-3**) into benzene (Scheme 4.2c). Remarkably, the reaction is reversible and heating the insertion product results in reformation of the anion and an equivalent of benzene. Kinetics and DFT studies suggest that the reaction proceeds as a heavy-atom analogue of the Buchner ring expansion: the (2 + 1) cycloaddition of **4-3** to benzene forms a norcaradiene-type intermediate which undergoes a 6π-electrocyclic ring-opening to form the observed product. While this is the first report of an intermolecular C–C activation process at a main-group metal centre, similar reports for the cleavage of intramolecular C–C bonds have been reported at low oxidation state Si(II),[8–10] and P(I) centres.[11]

Most recently, the oxidative addition of the central C–C σ-bond in biphenylene to a cyclic alkyl aluminyl anion (**4-4**) has been reported by Koshino and Kinjo (Scheme 4.2 d).[12] The anti-aromaticity and ring-strain of the 4-membered ring in biphenylene render the central C–C bond exceptionally weak (see Section 5.1.3 for further details).[13]

This chapter explores the reactivity of an aluminium(I) complex and magnesium(I) complexes with alkylidene cyclopropanes. C–C bond activation is achieved in both instances. Isolation of an intermediate in the case of aluminium showed that the alkene functionality is critical to this reactivity. The main-group reagents reacted first with the alkene to form an intermediate, where a main-group metal is in proximity to the strained cyclopropane ring, from which C–C cleavage evolved. The stoichiometric reactions were used to develop a catalytic methodology using a magnesium hydride catalyst.

4.2 – Results and Discussion

4.2.1 – Activation of alkylidene cyclopropanes with an aluminium (I) reagent

Reaction of the aluminium(I) complex **[Al]** with the unsaturated cyclopropane **4-5a** at 25°C in C_6D_6 resulted in the formation of **4-6a** over the course of 4 hours (Figure 4.1). This product is the result of a (4 + 1) cycloaddition and is related to a previous report of the reaction of **[Al]** with 1,1-diphenylethene.[14] The formation of the product could be observed in the ^{1}H NMR spectrum where characteristic strongly coupled alkene signals (Figure 4.1) are measured (δ_H = 5.74, 5.95, 6.34, 6.54 ppm) and are consistent with a (*E,E*)–1,3-diene. A broad singlet corresponding to the aluminium bound methine resonance is observed at δ_H = 3.17 ppm. The cyclopropyl resonances are further desymmetrised and form a series of multiplets in the aliphatic region (δ_H = –0.15, +0.22, 0.54, 0.62 ppm), indicating that the symmetry elements of the C_{2v} point group present in **4-5a** are not preserved in **4-6a** and that the proton environments on the cyclopropane methylene carbon atoms are diastereotopic. A highly desymmeterised β-

diketiminate ligand environment is also observed suggesting an unsymmetric aluminium centre.

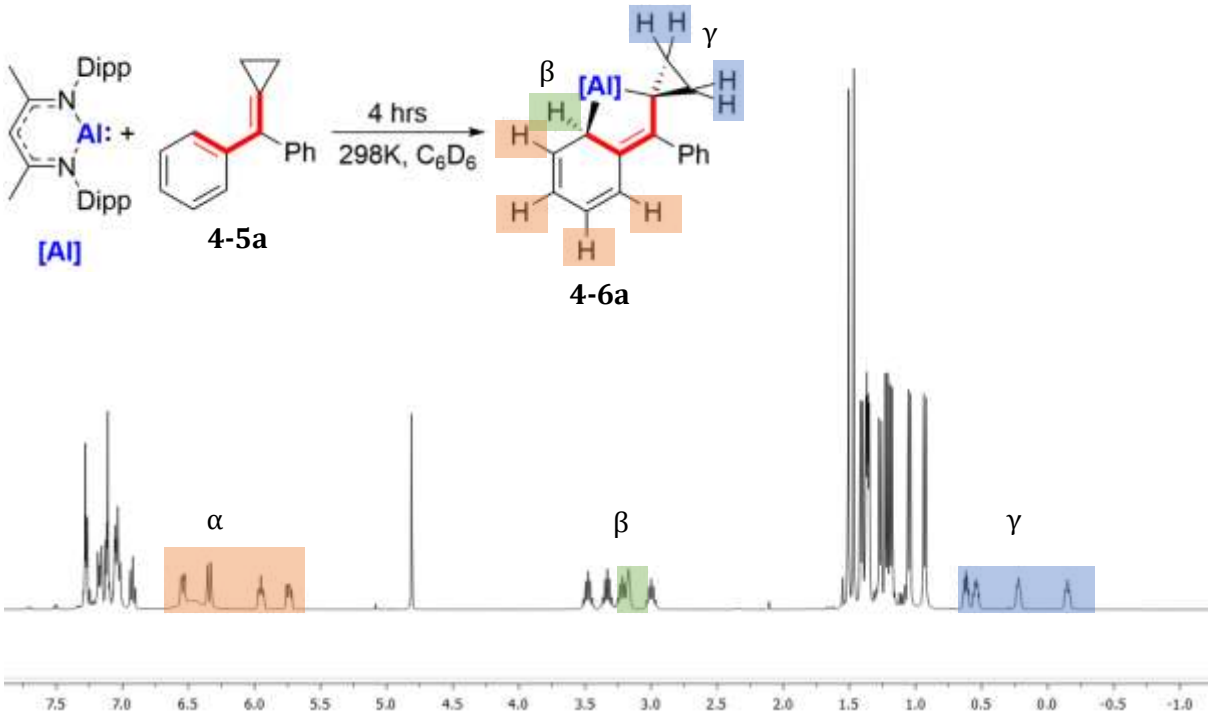
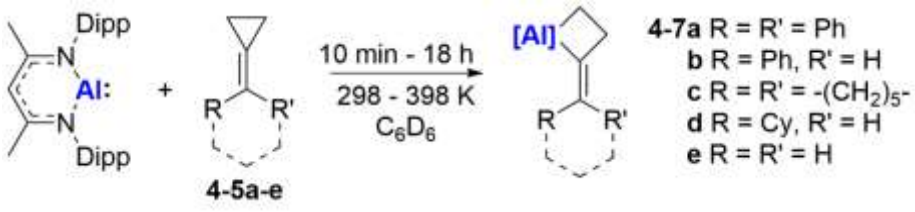


Figure 4.1: ^{1}H NMR spectrum of **4-6a**. Inset: synthesis of **4-6a** from **[Al]** and **4-5a**. The α (alkene), β (methine), and γ (methylene) proton environments are coloured and labelled on the spectrum.

Heating either crude or isolated samples of **4-6a** at 100°C in C_6D_6 for 15 minutes results in the formation of **4-7a**, a metallacyclobutane derived from C–C σ-bond activation (Scheme 4.3). A concomitant change in colour from the deep orange-red of **4-6a** to colourless for **4-7a** is also observed. The reaction also proceeds slowly to completion at 25°C over the course of several days. The relief of the ring strain and rearomatisation of the aromatic ring provide significant thermodynamic driving forces for this reaction. A characteristic upfield two proton multiplet at δ_H = 0.61 ppm in the ^{1}H NMR spectrum can be assigned as the methylene protons adjacent to the aluminium centre.

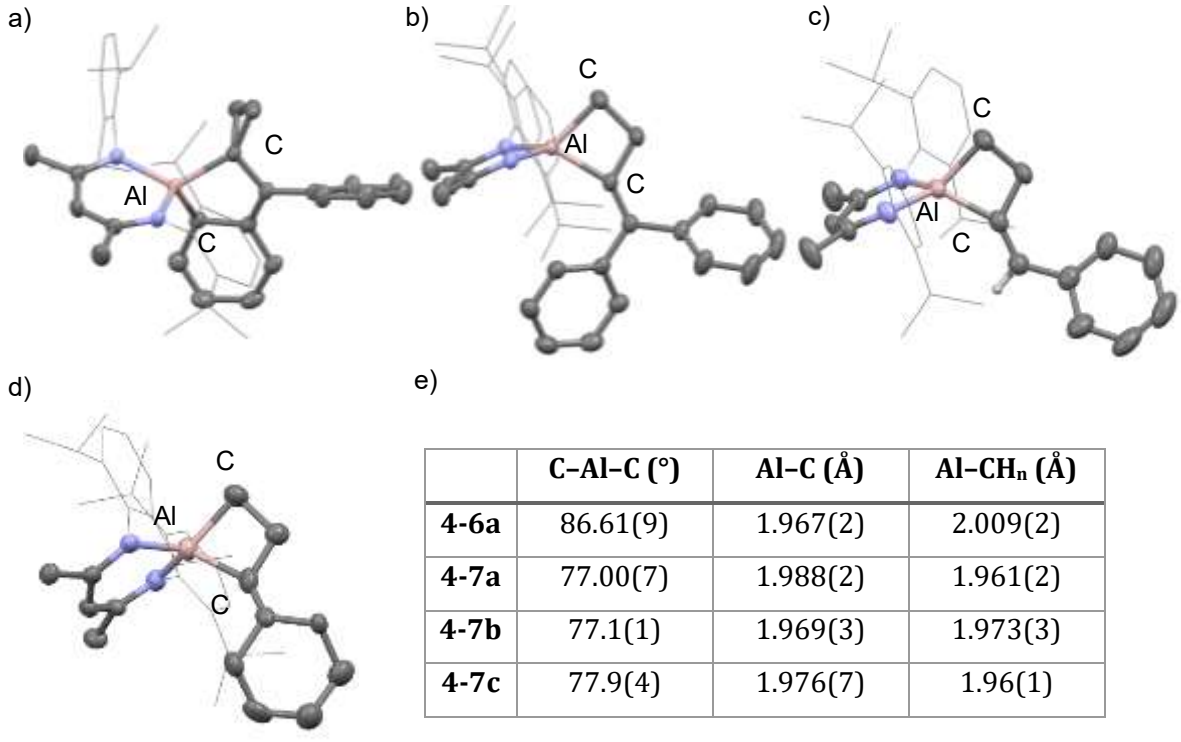


Scheme 4.3: Reaction of alkylidene cyclopropanes with **[Al]**.

The reaction scope can be expanded to **4-5b-e** (Scheme 4.3). For **4-5b**, key alkene proton environments of an analogue of **4-6a** can be observed in the ^{1}H NMR spectrum during the reaction, however the increased rate of ring-opening precludes isolation of the intermediate. In

the case of **4-5c-e**, no intermediates are observed and the reaction proceeded directly to the ring-opened metallacyclobutanes **4-7c-e**. Harsher conditions were required for more sterically encumbered alkenes. Hence, the tetrasubstituted alkene **4-7c** required prolonged heating to effect C–C cleavage. Under these conditions competitive allylic C–H activation was observed (see Section 4.4.3 for further details).[15] The least sterically demanding substrate **4-5e** was observed to react essentially instantaneously with **[Al]**. For trisubstituted alkenes **4-5b,d** a single *E* stereoisomer of the product was observed to form in the ^{1}H NMR spectrum of both crude and purified reaction mixtures.

Products **4-6a** and **4-7a-c** have been characterised in the solid state by single crystal x-ray diffraction (Figure 4.2). In the X-ray crystal structure of **4-6a**, the aluminium centre forms part of a metallacyclopentene ring. The C–C bond lengths for the hydrocarbon fragment are consistent with the double-bond assignments as made by ^{1}H NMR spectroscopy. The solid state structures of **4-7a-c** clearly show metallacyclobutane connectivity and little variation in geometry is observed across the series. In all three examples, the C–Al–C angle (77°) is more acute than the idealised cyclobutane angle (90°). The Al–C bond lengths to the quaternary carbon and methylene carbon are largely identical in each structure.



	C–Al–C (°)	Al–C (Å)	Al–CH$_n$ (Å)
4-6a	86.61(9)	1.967(2)	2.009(2)
4-7a	77.00(7)	1.988(2)	1.961(2)
4-7b	77.1(1)	1.969(3)	1.973(3)
4-7c	77.9(4)	1.976(7)	1.96(1)

Figure 4.2: X-ray crystal structures of a) **4-6a**, b) **4-7a**, c) **4-7b**, d) **4-7c**. e) Key structural metrics from X-ray data.

4.2.2 – Kinetics and DFT investigation into mechanism

In order to better understand the mechanism for cyclopropane ring-opening, kinetic measurements were undertaken. The transformation of **4-6a** → **4-7a** was found to be first-

order with respect to **4-6a** and Eyring analysis over a 45-70°C range gave activation parameters: $\Delta H^{\ddagger}$ = 22.3 ± 0.4 kcal mol^{-1} and $\Delta S^{\ddagger}$ = –6.9 ± 1.3 cal K^{-1} mol^{-1}. The negative entropy of activation is consistent with an ordered transition state. The Gibbs activation energy is $\Delta G^{\ddagger}_{298K}$ = 24.4 ± 0.8 kcal mol^{-1} and is consistent with the observed reaction at 25°C.

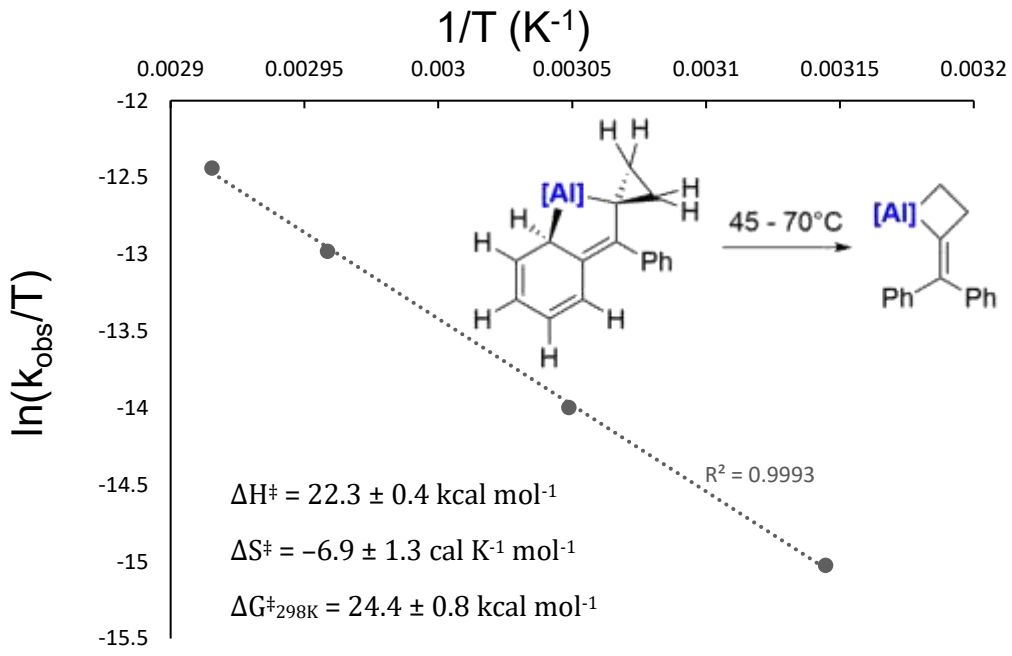


Figure 4.3: a) Kinetic data on transformation of **4-6a** to **4-7a**. b) Eyring plot from kinetic data.

DFT was used to elucidate the mechanism for cyclopropane ring-opening. The initial formation of the (4 + 1) cycloaddition intermediate **4-6a** was calculated to occur *via* a concerted pericyclic transition state, **TS-1**.[14] The modest energy barrier of **TS-1**, $\Delta G^{\ddagger}_{298K}$ = 14.1 kcal mol^{-1}, is consistent with the observation that formation of **4-6a** occurs at 25°C and is not the rate-determining step of the C–C σ-bond activation sequence. From the (4 + 1) cycloaddition intermediate **4-6a**, **TS-2** was located ($\Delta G^{\ddagger}_{298K}$ = 25.8 kcal mol^{-1}) and connects directly to the product **4-7a**. The calculated activation barrier is in excellent agreement with the experimentally determined activation barrier. This key step breaks the C–C σ-bond and involves an α-migration mechanism (Figure 4.4a).

Analysis of the geometry of the key transition state, **TS-2** shows that the rearomatisation of the phenyl ring and cleavage of the cyclopropane C–C bond is concerted but asynchronous. Both are significant enthalpic driving forces in the reaction. The C–C bond lengths of the phenyl ring suggest that it has completed rearomatisation at the transition state geometry. The aluminium centre is positioned centrally between the breaking cyclopropane C–C σ-bond and the alkylidene C=C bond and is reminiscent of a transition-metal η^3-allyl complex.

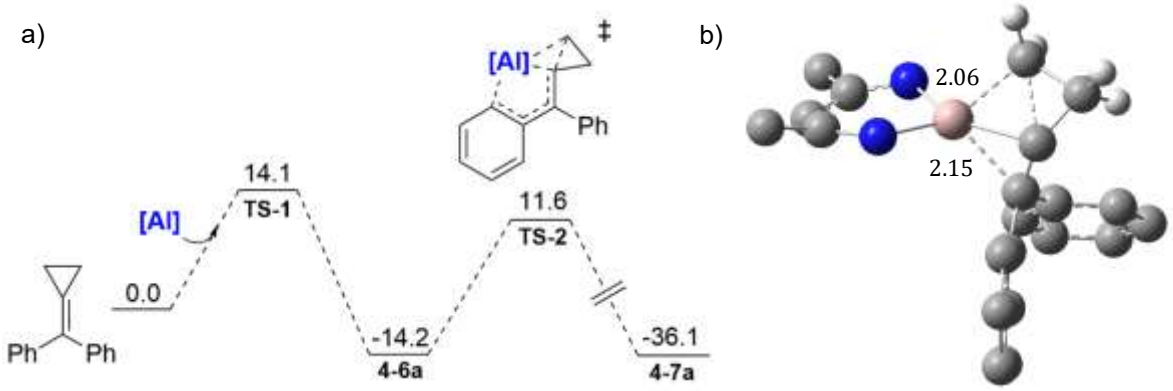


Figure 4.4: a) Calculated pathway for the ring-opening of **4-5a**. b) Geometry of key transition state **TS-2**. Gibbs free energies in kcal mol^{-1} and bond lengths measured in Å.

An alternative mechanism in which the cleavage of the cyclopropane for **4-5a** proceeds from a metallacyclopropane (**4-6a'**, Figure 4.5) was also considered. While the formation of the metallacyclopropane was found to be mildly exergonic (ΔG_{298K} = –3.0 kcal mol^{-1}), the barrier towards C–C cleavage was found to be higher than the corresponding pathway from **4-6a** ($\Delta G^{‡}_{298K}$ = 33.9 kcal mol^{-1}). Considering the activation barrier determined by Eyring analysis, the cleavage of the cyclopropane is likely to proceed from the isolable (4 + 1) **4-6a** rather than the metallacyclopropane intermediate **4-6a'**.

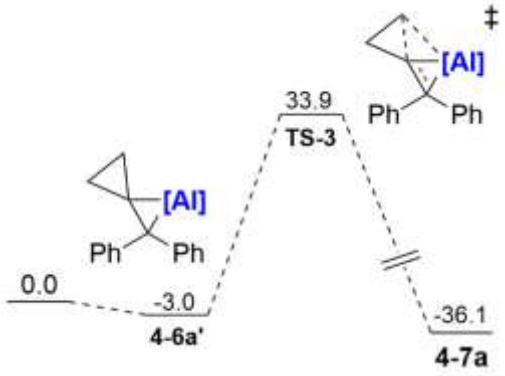


Figure 4.5: C–C cleavage pathway proceeding from a metallacyclopropane intermediate **4-6a'**. Gibbs free energies in kcal mol^{-1}.

While substrates **4-5a-b** may both proceed through an intermediate derived from a (4 + 1) cycloaddition, this pathway is inaccessible for alkylidene cyclopropane substrates without an aromatic ring (**4-5c-e**). Further calculations on the reaction of **[Al]** with **4-5e** support the notation that a closely related reaction sequence involving a (2+1) cycloaddition and α-migration becomes accessible (**TS-5**). The low activation barrier for the reaction of **4-5e** and **[Al]** ($\Delta G^{‡}_{298K}$ = 19.8 kcal mol^{-1}) is consistent with the observation that the reaction is complete upon mixing the substrates. **4-6e'** was not observed experimentally.

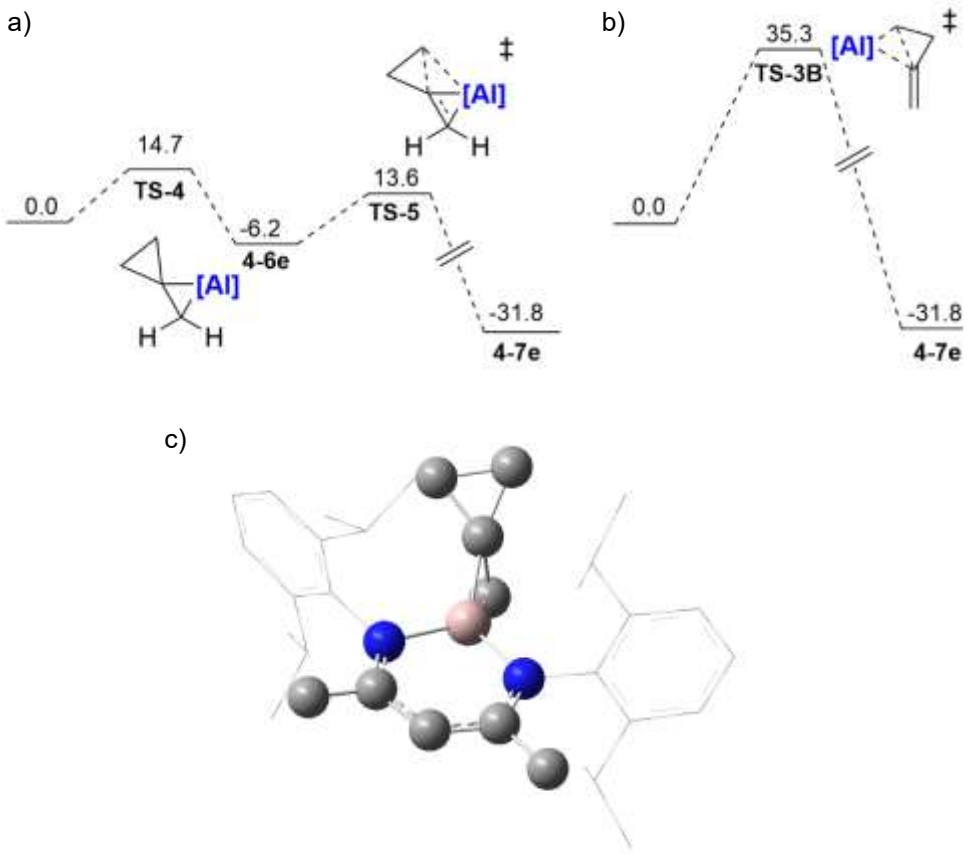


Figure 4.6: a) Ring-opening of the cyclopropane from a metallacyclopropane intermediate **4-6e**. b) Direct oxidative addition of **[Al]** to **4-5e**. Gibbs free energies in kcal mol^{-1}. c) View along an Al–C bond of **4-6e.**

The direct oxidative addition of a C–C σ-bonds of strained three-membered rings to **1** was also considered (Figure 4.6b).[16] A transition state that directly connects **[Al]** and **4-5e** with **4-7e,** corresponding to an oxidative addition pathway, was found to be significantly higher in energy than the corresponding α-migration pathway ($\Delta G^{\ddagger}_{298K}$ = 35.3 kcal mol^{-1}). Experimentally, **1** does not react with cyclopropylbenzene to form metallacyclobutane products even when heated at 100°C for one week in C_6D_6. Hence, the C–C activation mechanism for substrates **4-5a-e** proceeds from a strained metallacyclic intermediate **4-6a-e** which proceed to ring-open the cyclopropane *via* an α-migration mechanism. The key redox event involves the installation of the aluminium centre *via* a cycloaddition reaction, as opposed to the cleavage of the C–C σ-bond.

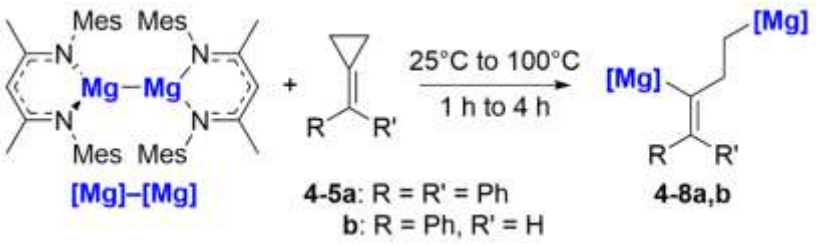
The reaction of **4-5b** and **4-5d** with **[Al]** result in one stereoisomer. The formation of **4-6b** can be observed in the ^{1}H NMR during the reaction of **4-5b** with **[Al]**. Hence, formation of **4-7b** and **4-7d** from aluminacyclopentane and aluminacyclopropane intermediates both result in the formation of the *E* stereoisomer. While the pathways for these compounds have not been calculated, inspection of calculated intermediate **4-6e** show that the two carbon atoms in the cyclopropane ring are within proximity of the aluminium centre (Figure 4.6c). In the case of the

reaction of [Al] and **4-5b** and **4-5d** stereospecific α-migration of aluminium to form the least sterically encumbered product is likely.

4.2.3 – Ring opening of alkylidene cyclopropanes with a magnesium(I) reagent

The strategic installation of an aluminium centre near a strained ring was a key insight from the reactivity explored with an aluminium(I) reagent. The alkene functionality provided a route to installing aluminium within a strained substrate leading to subsequent C–C bond-activation chemistry, and the key C–C bond cleavage event did not involve formal oxidation state changes at the main-group centre. Considering the recent reports of the reaction of a magnesium(I) dimer, **[Mg]–[Mg]**, with alkenes we were curious to explore the reaction of this magnesium(I) dimer with alkylidene cyclopropanes.

Upon mixing a solution magnesium dimer **[Mg]–[Mg]** with **4-5a**, a bright purple solution formed immediately. ^{1}H NMR spectroscopy of this solution showed predominantly the starting materials in solution. Upon heating the reaction mixture at 100°C, however, a new upfield 2 proton resonance was observed, consistent with the formation of a magnesium alkyl group (Scheme 4.4). Reaction of **[Mg]–[Mg]** with **4-5b** resulted in no observable colour change, however the reaction was complete after 1 h at room temperature as monitored by ^{1}H NMR spectroscopy. In this case, formation of a single stereoisomer was observed.



Scheme 4.4: Reaction of a magnesium (I) dimer with alkylidene cyclopropanes **4-5a** and **4-5b.**

While efforts to isolate **4-8a,b** resulted in a viscous yellow oil, both have both been characterised using single crystal X-ray diffraction as their base-stabilised DMAP adduct (Figure 4.7). The X-ray crystal structure of **4-8a** shows a 1,3-dimagnesiated hydrocarbon in both **4-8a** and **4-8b**. The rupture of the cyclopropane ring is evident in both crystal structures. A single *Z* stereoisomer of **4-8b** is observed in the single crystal X-ray structure. Each magnesium centre in the structures of **4-8a** and **4-8b** are four-coordinate.

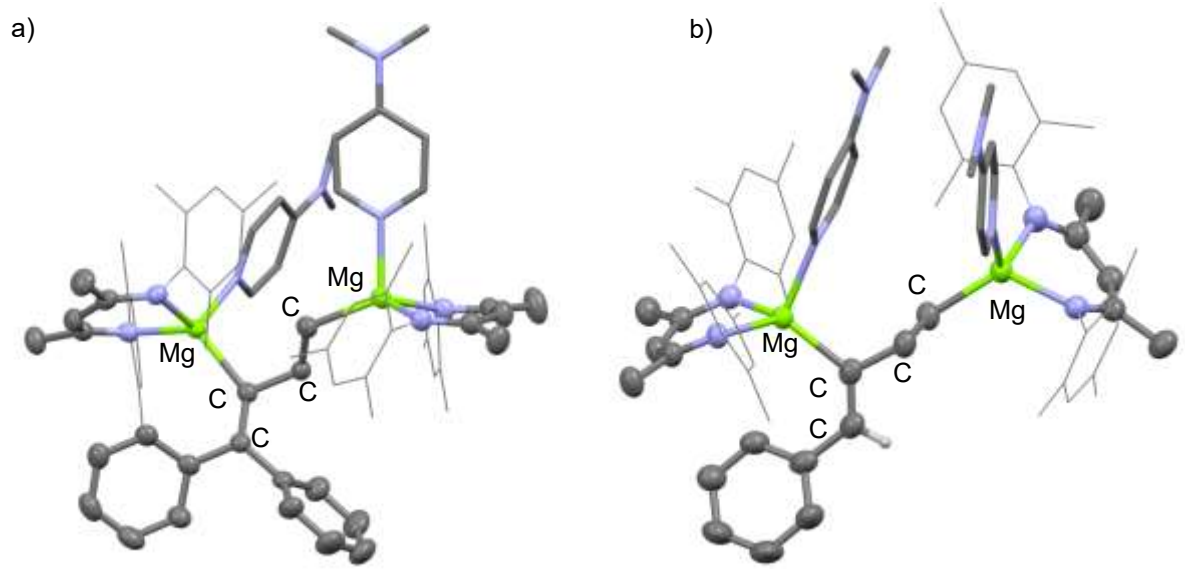


Figure 4.7: X-ray crystal structures of a) **4-8a.DMAP**$_2$ and b) **4-8b.DMAP**$_2$.

The reaction is more limited in scope than those of alkylidene cyclopropanes with **[Al]**. **[Mg]–[Mg]** did not react with alkyl substituted alkylidene cyclopropanes **4-5c,d** nor with the parent methylene cyclopropane **4-5e**. Using a more sterically encumbered magnesium(I) dimer (with 2,6-di-isopropylphenyl groups instead of mesityl groups on the β-diketiminate ligand) also resulted in no reactivity. Furthermore, no intermediates were observed in the ^{1}H NMR spectrum towards the formation of the ring-opened products.

DFT calculations were employed to gather further insight into the mechanism. Based on literature precedent and by analogy to the aluminum reagent **[Al]**, it is highly likely that this reaction is initiated by the 1,2-addition of the Mg–Mg bond of **[Mg]–[Mg]** across the alkene to form a 1,2-dimagnesioethane intermediate.[17,18] While a transition state could not be identified, **Int-1** was calculated as a potential intermediate ($\Delta G°_{298K}$ = –12.7 kcal mol^{-1}). From **Int-1**, C–C σ-bond activation occurs by β-alkyl migration *via* **TS-7** to form **4-8a** ($\Delta G^{‡}_{298K}$ = 12.7 kcal mol^{-1}, Figure 3c). As with the reactions with **[Al]** no formal change in oxidation state of the metal accompanies ring-opening.

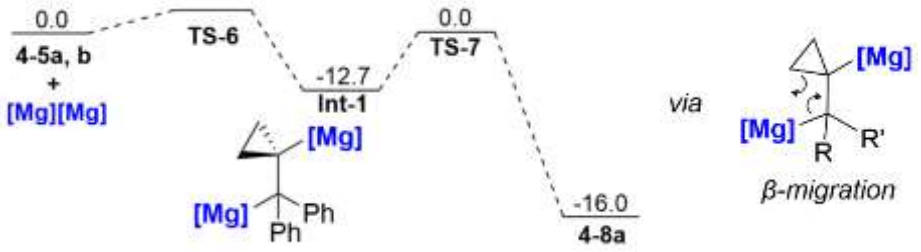


Figure 4.8: DFT calculated pathway for the formation **4-8a**. Gibbs free energies provided in kcal mol^{-1}.

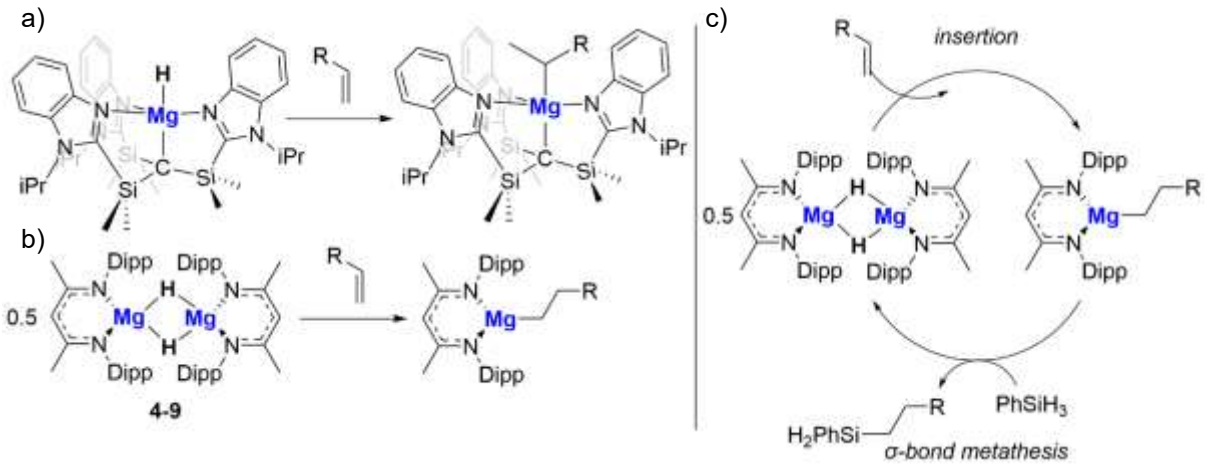
The discrepancy between experimentally observed reaction conditions (4 h at 100°C) and calculated barriers ($\Delta G^{\ddagger}_{298K}$ = 12.7 kcal mol^{-1}) suggest that in this case, breaking of the C–C bond is not rate limiting. While a transition state towards the formation of the 1,2-dimagnesioethane intermediate could not be located, the reaction proved sensitive to the steric demands of the magnesium reagent and did not proceed with bulkier analogues of **[Mg]–[Mg]**. The limitations in scope for this reaction mirror the limitations reported by Jones and co-workers for the 1,2-dimagnesiation of alkenes. Hence, C–C cleavage is likely to be facile upon strategic incorporation of magnesium into the β-position of a cyclopropane ring.

4.2.4 – Catalytic hydrosilylation of a C–C σ-bond in alkylidene cyclopropanes

In the previous sections, reaction of a low-oxidation state main-group compound with an alkylidene cyclopropane resulted in the cleavage of the cyclopropane C–C σ-bond. In both cases, the formal oxidation of the main-group centre (Al(I) to Al(III) and Mg(I) to Mg(II) respectively) occurs through reaction with either the alkene or 1,3-diene in the substrate to generate a metalated intermediate. C–C cleavage proceeds from this intermediate with no formal oxidation state change at the main-group centre.

As an alternative to reductive metalation of the substrate, hydromagnesiation was considered as a route to install main-group fragments. The hydromagnesiation of alkenes has been reported for a terminal magnesium hydride (Scheme 4.5a) by Parkin and co-workers,[19] and a dimeric β-diketiminate magnesium hydride (Scheme 4.5b) by Hill and co-workers.[20] Interestingly, the two different magnesium hydride species show different selectivities: Markovnikov addition is solely observed in the former, while both Markovnikov and anti-Markovnikov products were observed in the latter.††† In both cases, σ-bond metathesis of phenylsilane with the resultant magnesium alkyl species regenerates the magnesium hydride reagent along with the silylated hydrocarbon fragment. This is subsequently incorporated into a catalytic protocol for the hydrosilylation of alkenes (Scheme 4.5c).

††† Hill and co-workers showed that the selectivity depended on the substituents of the terminal alkene. Alkyl substituents resulted in formation of the anti-Markovnikov product, while both anti-Markovnikov and Markovnikov products were observed with aryl substituents.



Scheme 4.5: a) Markovnikov addition of Parkin and co-workers' magnesium hydride to an alkene. b) Anti-Markovnikov addition of Hill and co-workers. c) Catlaytic anti-Markovnikov hydrosilylation of alkenes reported by Hill and co-workers. A related Markovnikov hydrosilylation is possible using Parkin and co-workers' catalyst.

Reaction of dimeric magnesium hydride **4-9** with an excess of **4-5e** furnished the magnesium complex **4-10e** (Figure 4.9a). In the ^{1}H NMR spectrum, the presence of mutually coupled alkene resonances (δ_H = 4.66, 4.78, 5.67 ppm) and absence of any cyclopropane signals suggests that product **4-10e** is the ring-opened product. The direct anti-Markovnikov hydromagensiation product is not observed during the formation of **4-9**. This suggests that C–C cleavage is not rate-limiting in this reaction. The structural assignment is confirmed by X-ray diffraction (Figure 4.9c).

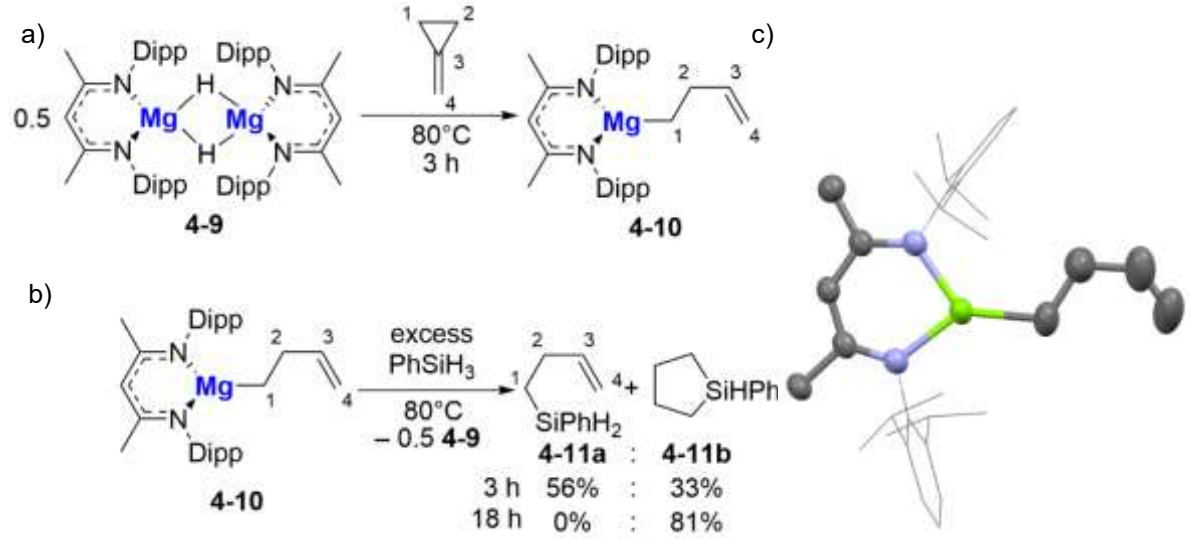
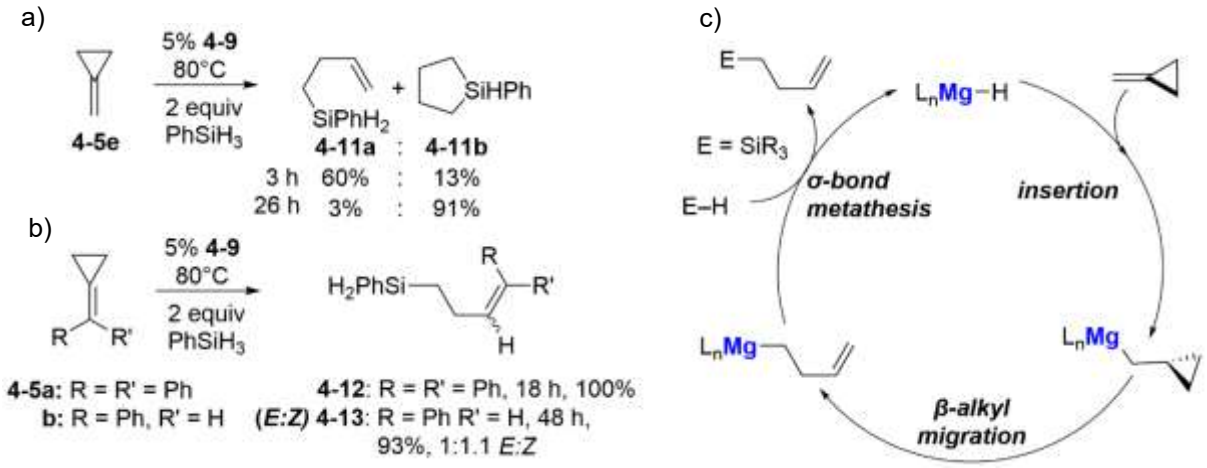


Figure 4.9: a) Reaction of **4-8** with **4-5e**. b) Reaction of **4-9** with $PhSiH_3$. c) X-ray structure of **4-10**.

Reaction of **4-10** with phenylsilane at 80°C for 3 h yielded products **4-11a** and **4-11b** (Figure 4.9b). **4-10a** corresponds to the product of σ-bond metathesis between the Mg–C bond in **4-10** with an Si–H bond. **4-11b** results from the hydromagnesiation of **4-11a** followed by an

intramolecular σ-bond metathesis to form the silolane. After heating for 18 h, complete conversion to the **4-11b** can be observed.

The knowledge of stoichiometric reactivity of **4-9** was developed into a catalytic protocol. Hence, reaction of **4-5e** with 2 equiv. of phenylsilane and a 5 mol% catalyst loading of **4-9** (10 mol% Mg–H) at 80°C for 3 h resulted in formation of **4-11a** and **4-11b** in 60% and 13% yields respectively. Heating for a further 23 h resulted in almost complete conversion to **4-11b** (91%). Under these conditions, the substrates **4-5a** and **4-5b** also reacted to form silylated products. In these cases, no intramolecular hydrosilylation product was observed, likely due to the increased sterics of the alkene. In the case of **4-5b** a 1:1.1 mixture of *E:Z*-stereoisomers of the product was obtained (Figure 5.9). Monitoring the ratio of *E:Z* stereoisomeric products along the course of the reaction (See Section 4.4.5 for further details) suggests that the *Z* isomer forms preferentially to the *E* isomer initially, however the former is slowly isomerised under the reaction conditions. The *E*/*Z* distribution of the reaction is unclear due to the competing subsequent isomerisation . The reactions did not proceed in the absence of **4-9** at 80 °C. The reaction did not work with alkyl-substituted alkylidene cyclopropanes **4-5c** and **4-5d**. These limitations likely reflect the scope of the hydromagnesiation reaction rather than the generality of C–C cleavage.

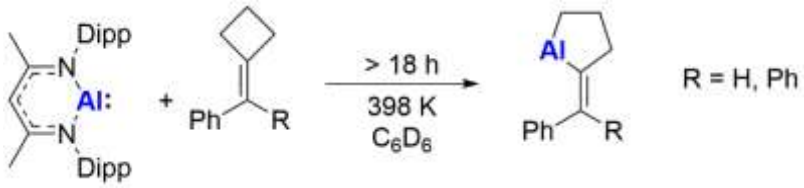


Scheme 4.6: a) Catalytic hydrosilylation of a C–C σ-bond in **4-5e**. b) Catalytic hydrosilylation of a C–C σ-bond in **4-5a** and **4-5b**. c) Proposed catalytic cycle

4.3 Conclusion and future work

In summary, the C–C σ-bond activation of strained alkylidene cyclopropanes by main group reagents is reported. Analysis of the mechanism through isolation of intermediates, kinetics and DFT studies shows that C–C σ-bond activation at main group centres is possible by either α- or β-migration mechanisms. This understanding was used to develop a magnesium catalysed hydrosilylation of C–C bonds.

Preliminary experiments of the reaction between **[Al]** and a diphenylmethylenecyclobutane show that ring-opening is possible based on ^{1}H NMR data. An upfield 2H multiplet is observed in a similar region to the **4-7a-e**. Reaction with the parent methylenecyclobutane yields primarily the allylic C–H activation product with trace amounts of the C–C activated product. Interestingly, the analogous reaction of the magnesium(I) dimer does not occur and heating the materials together only results in the gradual decomposition of the starting materials. Understanding the substrate limitations, and limits of the C–C activation chemistry will be possible through a more detailed study. Attempts should be made to expand the scope to 4-membered ring systems.



Scheme 4.7: Activation of alkylidenecyclobutanes with [Al].

The functionalisation of the metallacyclic products is also a topic of interest. The products aluminacyclobutane **4-7a-e** possess two Al–C bonds which are primed to react as nucleophiles. Metathesis of one Al–C bond was successful with the electrophile $SnMe_2Cl_2$, however ring closure to form the stannacycle was not observed. An exploration of these reagents with transition-metal chlorides is also warranted. Products **4-7a-e** are notably structurally reminiscent of intermediates in transition-metal mediated alkene metathesis. While the compounds **4-7a-e** are not competent for alkene metathesis, their use in the direct synthesis of transition-metal metallacyclobutanes may be rewarding.

4.4 – Experimental

4.4.1 – General experimental

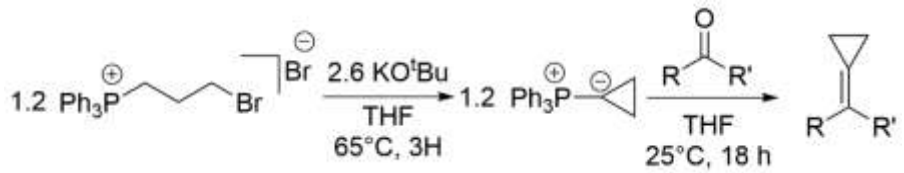
All manipulations were carried out using standard Schlenk-line and glovebox techniques under an inert atmosphere of argon or dinitrogen. A MBraun Labmaster glovebox was employed, operating at <0.1 ppm O_2 and <0.1 ppm H_2O. Solvents were dried over activated alumina from an SPS (solvent purification system) based upon the Grubbs design and degassed before use. Glassware was dried for 12 h at 120°C prior to use. C_6D_6 was dried over 3 Å molecular sieves and subjected to the freeze-pump-thaw degassed thrice before use. Column chromatography was performed with silica (SiO_2, 60 Å, 230-400 mesh, Sigma Aldrich).

NMR Spectra were recorded on Bruker 400 MHz or 500 MHz at 298 K unless otherwise stated and values recorded in ppm. Data were processed in MestReNova software. Where needed, chemical shifts were assigned with the assistance of 2D NMR (HSQC, HMBC, COSY) spectra. **[Al]**,[21] **[Mg]–[Mg]**,[22] and **4-9**[22] were synthesized according to literature procedures. Chemicals

were purchased from Sigma Aldrich, Fluorochem, Alfa Aesar and VWR. Elemental analyses were performed by Medac Ltd. Primary data (NMR, XYZ coordinates) may be downloaded from dx.doi.org/10.14469/hpc/7252.

4.4.2 – Substrate synthesis

General synthesis of alkylidenecyclopropanes



Scheme 4.8: Synthesis of alkylidenecyclopropanes **4-5a-d**

Compounds **4-5a-d** were prepared through a modified literature procedure.[23–25] In a glovebox, the triphenylphosphonium salt $[Ph_3P(CH_2)_3Br]Br$ (5 g, 0.011 mol, 1.2 eq.) and KO^{t}Bu (2.7 g, 0.024 mol, 2.2 eq.) were dissolved in THF (~20 mL) and transferred to a Schlenk flask. The Schlenk flask was sealed and removed from the glovebox. The reaction mixture was stirred and heated to 65°C for 3 hours. At this point, the carbonyl (0.009 mol) was added dropwise *via* syringe (or quickly as a solid for **2a**). Following addition, the reaction mixture was cooled to 25°C and allowed to stir for 18 h. Pentane (~30 mL) was added to the tan-orange suspension, and the reaction mixture was filtered through a short pad of silica, which was washed pentane (3x 30 mL). The combined organic filtrates were concentrated under reduced pressure to yield a yellow oil. The yellow oil was transferred to a 5mL round bottom flask, and all volatiles were transferred *via* trap-to-trap distillation under vacuum to afford the product as colourless oils (**4-5d**) or recrystallisation from pentane (–35°C) to yield a colourless solid (**4-5a**). Compounds **4-5a-d** were characterised by ^{1}H and ^{13}C NMR spectroscopy. These are known compounds and data match the literature values (**4-5b**,[23] **4-5d c**,[24], **4-5d**[25]). All compounds were stored in the glovebox for further use. *Note: **4-5b** should be stored in the glovebox freezer to prevent decomposition.*

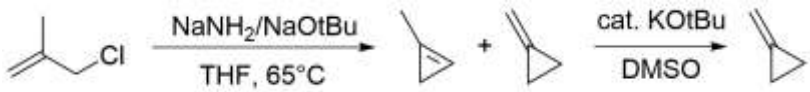
4-5a: ^{1}H NMR (400 MHz, C_6D_6, 298 K) δ 1.07 (s, 4H, 2x C***H*₂***), 7.09 – 7.24 (m, 6H, Ar-***H***), 7.47 – 7.52 (m, 4H, Ar-***H***).

4-5b: ^{1}H NMR (400 MHz, C_6D_6, 298 K) δ 0.91 (m, 2H, CH_2), 1.04 – 1.10 (m, 2H, C***H*₂***), 6.75 (apparent p, $^4J_{HH}$ = 2.1 Hz, 1H, C=C***H***Ph), 7.04 – 7.12 (m, 1H, Ar-***H***), 7.17 – 7.24 (m, 2H, Ar-***H***), 7.45 – 7.54 (m, 2H, Ar-***H***).

4-5c: ^{1}H NMR (400 MHz, C_6D_6, 298 K) δ 0.96 (p, $^5J_{HH}$ = 1.3 Hz, 4H, cyclopropyl-CH_2C***H*₂***), 1.43 – 1.60 (m, 6H, Cy-***H***), 2.33 (m, 4H, Cy-***H***).

4-5d: ^{1}H NMR (400 MHz, C_6D_6, 298 K) δ 0.87 – 1.02 (m, 4H, C***H*₂**C***H*₂***C), 1.09 – 1.33 (m, 5H, Cy-***H***), 1.56 – 1.66 (m, 1H, Cy-***H***), 1.70 (m, 2H, Cy-***H***), 1.85 (m, 2H, Cy-***H***), 2.16 – 2.30 (m, 1H, Cy-***H***), 5.83 (dp, $^3J_{HH}$ = 6.3 Hz, $^4J_{HH}$ = 2.0 Hz, 1H, C=C(***H***)(Cy)).

*Synthesis of methylenecyclopropane (**4-5e**)*



Scheme 4.9: Synthesis of methylenecyclopropane **4-5e**.

Preparation of a mixture of methylenecyclopropane and 1-methylcycloprop-1-ene:

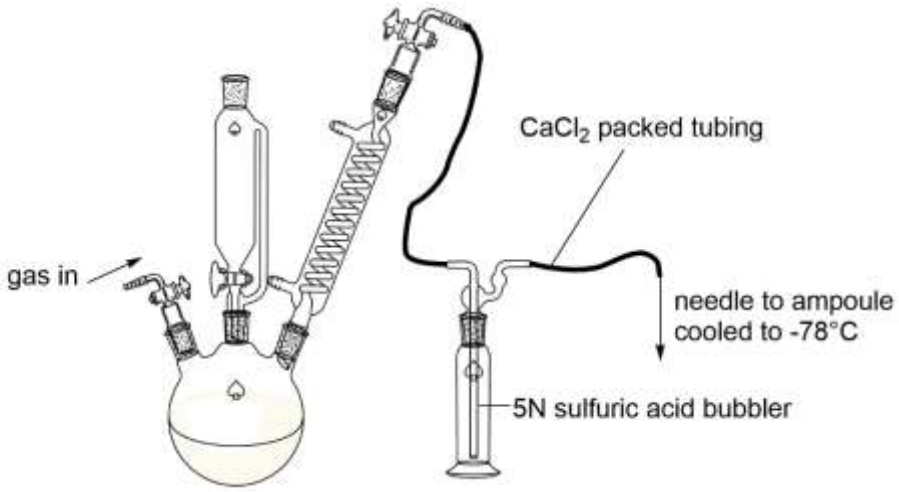


Figure 4.10: Reaction set-up for the synthesis of methylenecyclopropane and 1-methylcycloprop-1-ene.

A modified literature procedure was used.[26] A three necked 1L round-bottom flask with a heavy stirrer-bar was equipped with a gas adaptor to a Schlenk line, a pressure-equalized dropping funnel, and an efficient condenser. The flask was charged with sodium amide (50 g, 1.28 mol) and sodium tert-butoxide (62 g, 0.64 mol). The outlet of the condenser was connected *via* a gas adaptor and hose to the inlet of bubbler filled with a 5 N sulfuric acid. The outlet of the bubbler, in turn, was joined to a length of hose plugged on both ends with cotton wool and filled calcium chloride, with a well-secured needle placed on the outlet of the hose. The needle was fixed into a receiving ampoule cooled to -78°C in a dry-ice/acetone bath using a rubber septum and bleed needle. The entire apparatus up to the gas outlet at the condenser was evacuated and refilled three times with argon. THF (500 mL) was added to the solids in the flask. The reaction mixture was heated to 65°C while being stirred vigorously. A solution of dry, freshly distilled methylallyl chloride (41 mL, 0.42 mol) in THF (100 mL) was added dropwise *via* the pressure-equalized dropping over the course of 3 hours. A light stream of argon was used to bubble the product into the ampoule. Following the addition of methylallyl chloride, the reaction mixture was heated for a further 6 hours under these conditions to ensure complete conversion of reagents to product. The needle was then removed from the receiving ampoule and this ampoule was sealed. The products were then distilled under reduced pressure by trap-to-trap distillation into a second

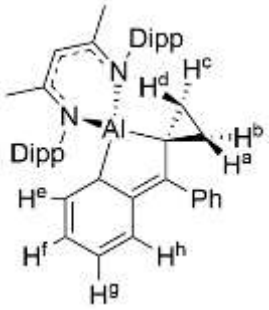
ampoule (equipped with a stirrer bar) and cooled to -78°C as a colourless liquid. The product obtained here was immediately used in the next step.

Isomerisation of 1-methylcycloprop-1-ene to methylenecyclopropane: Dry DMSO (~2.5 mL) was added to the product mixture obtained in the previous step, and potassium tert-butoxide (1 g, 0.009 mol) was added as a solid to the ampoule. The ampoule was sealed and warmed to 25°C. The mixture was stirred for 18 h to allow full conversion to methylenecyclopropane. After 18 h, the product was isolated by trap-to-trap distillation under reduced pressure by warming the distillation flask to 40°C, cooling the receiving flask to –78°C. **4-5e** was isolated as a colourless liquid. Yield:~ 10 mL, 0.23 mol, 56%. ^{1}H NMR spectroscopic data are in agreement with literature values.[26]

4-5e: ^{1}H NMR (400 MHz, C_6D_6, 298 K) δ 0.88 (t, $^{4}J_{HH}$ = 2.1 Hz, 4H), 5.47 (p, $^{4}J_{HH}$ = 2.1 Hz, 2H).

Note: Depending on the efficiency of the condenser and flow-rate of argon used to carry the product to the cold trap, THF may or may not carry over and so the subsequent distillation steps are not needed. The calcium chloride drying tube is capable of removing the bulk of the moisture from the argon stream, however some solid water still forms within the cold receiving flask and is largely removed with a preliminary distillation. While the original preparation formed the product directly from the starting materials, without need for a subsequent isomerization catalysed by potassium tert-butoxide, under the conditions described here we observed both isomers form: we attribute this to not using a sealed stirrer.

4.4.3 – Synthesis of compounds

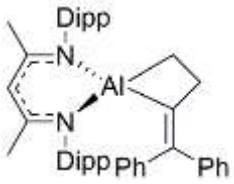


***Synthesis of 4-6a*:** In a glovebox, to a solution of **[Al]** (10 mg, 0.022 mmol) in toluene (~0.2 mL) in a scintillation vial was added a solution **4-6a** (5 mg, 0.024 mmol) in toluene (~0.2 mL). The reaction mixture solution was allowed to stand at 25°C for 3 hours. The mixture was then concentrated *in vacuo* to ~0.1 mL of toluene. **4-6a** was isolated as red-orange blocks by crystallization by vapour diffusion of pentane into this concentrated toluene solution in the glovebox freezer at –35°C. Crystals of **4-6a** were isolated by decanting the mother liquor. The crystals were washed with cold pentane (3x 0.5 mL) and dried *in vacuo.* Yield: 13.6 mg, 0.021 mmol, 93%.

^{1}H NMR (400 MHz, C_6D_6, 298 K) δ -0.15 (ddd, $^{2}J_{HH}$ = 2.1 Hz, $^{3}J_{HH}$ = 8.2, 5.2 Hz, 1H, C(***H*^{a}**H^{b})C(H^{c}H^{d})C), 0.22 (ddd, $^{2}J_{HH}$ = 2.1 Hz, $^{3}J_{HH}$ 7.2, 4.4 Hz, 1H, C(H^{a}***H*^{b}**)C(H^{c}H^{d})C), 0.54 (ddd, $^{2}J_{HH}$ = 3.7 Hz, $^{3}J_{HH}$ = 7.7, 5.3 Hz, 1H, C(H^{a}H^{b})C(***H*^{c}**H^{d})C), 0.62 (ddd, $^{2}J_{HH}$ = 3.7 Hz, $^{3}J_{HH}$ = 8.4, 4.4 Hz, 1H, C(H^{a}H^{b})C(H^{c}***H*^{d}**)C), 0.93 (d, $^{3}J_{HH}$ = 6.7 Hz, 3H, (C***H*$_3$**)CH(CH$_3$)), 1.05 (d, $^{3}J_{HH}$ = 6.7 Hz, 3H, (C***H*$_3$**)CH(CH$_3$)), 1.19 (d, $^{3}J_{HH}$ = 6.7 Hz, 3H, (C***H*$_3$**)CH(CH$_3$)),1.22 (d, $^{3}J_{HH}$ = 6.7 Hz, 3H, (C***H*$_3$**)CH(CH$_3$)), 1.27 (d, $^{3}J_{HH}$ = 6.7 Hz, 3H, (C***H*$_3$**)CH(CH$_3$)), 1.36 (d, $^{3}J_{HH}$ = 6.8 Hz, 3H, (C***H*$_3$**)CH(CH$_3$)), 1.37 (d, $^{3}J_{HH}$ = 6.7 Hz, 3H, (C***H*$_3$**)CH(CH$_3$)), 1.41 (d, $^{3}J_{HH}$ = 6.7 Hz, 3H, (C***H*$_3$**)CH(CH$_3$)), 1.47 (s, 3H, (CH$_3$)C(CH)C(C***H*$_3$**)), 1.51 (s, 3H, (C***H*$_3$**)C(CH)C(CH$_3$)), 3.00 (hept, $^{3}J_{HH}$ = 6.8 Hz, 1H, (CH$_3$)C***H***(CH$_3$)), 3.17 (s, 1H, AlC***H***), 3.23 (hept, $^{3}J_{HH}$ = 6.9 Hz, 1H, (CH$_3$)C***H***(CH$_3$)), 3.33 (hept, $^{3}J_{HH}$ = 6.7 Hz, 1H, (CH$_3$)C***H***(CH$_3$)), 3.48 (hept, $^{3}J_{HH}$ = 6.7 Hz, 1H, (CH$_3$)C***H***(CH$_3$)), 4.81 (s, 1H, (CH$_3$)C(C***H***)C(CH$_3$)), 5.74 (dddd,$^{3}J_{HH}$ = 9.6, 5.5, 2.0, 1.1 Hz, 1H, ***H*^{g}**), 5.95 (ddd, J = 9.3, 5.5, 3.0 Hz, 1H, H^{f}), 6.34 (d, $^{3}J_{HH}$ = 9.6 Hz, 1H, ***H*^{h}**), 6.47 (2H, Ar-***H*** (ortho -Ph)), 6.54 (dd, J = 9.1, 3.7 Hz, 1H, ***H*^{e}**), 6.90 – 7.30 (m, 9H, Ar-*H*). N.B. cyclopropyl proton resonances cannot be distinguished and so have been given arbitrary designation.

^{13}C NMR (101 MHz, C_6D_6, 298K) δ 9.0 (**C**(H^aH^b)C(H^cH^d)C), 10.5 (C(H^aH^b)***C***(H^cH^d)C), 23.5 (***C***H_3)C(CH)C(CH_3), 23.7 (CH_3)C(CH)C(***C***H_3), 24.4 (***C***H_3)CH(CH_3), 24.8 (***C***H_3)CH(CH_3), 25.1 (***C***H_3)CH(CH_3), 25.1 (***C***H_3)CH(CH_3), 25.2 (***C***H_3)CH(CH_3), 25.3 (***C***H_3)CH(CH_3), 25.9 (***C***H_3)CH(CH_3), 26.9 (***C***H_3)CH(CH_3), 28.0 (CH_3)***C***H(CH_3), 29.2 (2x (CH_3)***C***H(CH_3), 29.5 (CH_3)***C***H(CH_3), 37.1 (Al***C***H), 98.7 (CH_3)C(***C***H)C(CH_3), 118.7 (***C***H^f), 123.0 (***C***H^g), 123.9 (Ar***C***), 124.3 (Ar***C***), 125.1 (Ar***C***), 125.2 (Ar***C***), 125.5 (Ar***C***), 126.6 (***C***H^h), 127.5 (Ar***C***), 130.6 (2x Ar***C***), 135.6 (2C, ***C***H^e), 136.0 (Ar***C***), 138.0 (Ar***C***), 140.6 (Ar***C***), 141.0 (Ar***C***), 142.6 (Ar***C***), 143.1 (Ar***C***), 143.3 (Ar***C***), 143.4 (Ar***C***), 145.1 (Ar***C***), 145.2 (Ar***C***), 171.3 (CH_3)***C***(CH)C(CH_3), 172.3 (CH_3)C(CH)***C***(CH_3). Note: **4-6a** converts to **4-7a** at an appreciable rate during ^{13}C NMR data acquisition hampering high quality ^{13}C data. Some quaternary carbon resonances could not be observed due to quadrupolar broadening (Al***C***) and low intensities. The quaternary carbon resonances adjacent to ***C***H^h and Al***C*** has been assigned as "Ar*C*".

Due to the instability of this compound accurate CHN analysis could not be obtained. Anal. Calc. ($C_{45}H_{55}AlN_2$): C, 83.03; H, 8.52; N, 4.30. Found: C, 80.31; H, 8.58; N, 4.07.



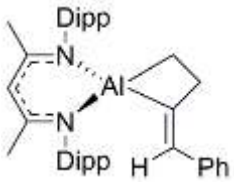
***Synthesis of 4-7a*:** In a glovebox, to a solution of **1** (10 mg, 0.022 mmol) in toluene (~0.3 mL) was added a solution of **4-5a** (5 mg, 0.024 mmol) in toluene (~0.3 mL). The reaction mixture was transferred to a J-Young NMR tube which was sealed and removed from the glovebox. The reaction was monitored by ^{1}H NMR spectroscopy. The J-Young NMR tube was heated at 100°C for approximately 15 minutes during which the colour changed from yellow/orange to light yellow/colourless. The J-Young NMR tube was returned to the glovebox, the reaction mixture was decanted into a scintillation vial and concentrated *in vacuo* to ~0.1 mL of toluene. **4-7a** was isolated as colourless blocks by crystallization by vapour diffusion of pentane into this concentrated toluene solution in the freezer at –35°C. Crystals of **4-7a** were isolated by decanting the mother liquor. The crystals were washed with cold pentane (3x 0.5 mL) and dried *in vacuo.* Yield: 12.3 mg, 0.019 mmol, 84%.

^{1}H NMR (400 MHz, C_6D_6, 298 K) δ 0.53 – 0.69 (m, 2H, AlC***H₂***CH_2C), 0.93 (d, $^{3}J_{HH}$ = 6.8 Hz, 6H, (C***H₃***)$_2$CH), 1.11 (d, $^{3}J_{HH}$ = 6.9 Hz, 6H, (C***H₃***)$_2$CH), 1.17 (d, $^{3}J_{HH}$ = 6.6 Hz, 6H, (C***H₃***)$_2$CH), 1.30 (d, $^{3}J_{HH}$ = 6.8 Hz, 6H, (C***H₃***)$_2$CH), 1.55 (s, 6H, {(C***H₃***)C}$_2$CH), 2.30 – 2.38 (m, 2H, AlCH$_2$C***H₂***C), 3.24 (hept, $^{3}J_{HH}$ = 6.7 Hz, 2H, (CH$_3$)$_2$C***H***), 3.37 (hept, $^{3}J_{HH}$ = 6.8 Hz, 2H, (CH$_3$)$_2$C***H***), 5.08 (s, 1H, {(CH$_3$)C}$_2$C***H***), 7.03-7.14 (m, 8H, Ar-***H***), 7.19-7.26 (m, 4H, Ar-***H***), 7.31-7.36 (m, 2H, Ar-***H***), 7.68-7.73 (m, 2H, Ar-***H***).

^{13}C NMR (101 MHz, C_6D_6, 298K) δ 10.6 (Al***C***H$_2$), 23.6 ({***C***H$_3$)C}$_2$CH), 24.5 ((***C***H$_3$)$_2$CH), 24.5 ((***C***H$_3$)$_2$CH), 24.6 ((***C***H$_3$)$_2$CH), 25.8 ((***C***H$_3$)$_2$CH), 28.2 ((CH$_3$)$_2$***C***H), 29.2 ((CH$_3$)$_2$***C***H), 31.8 (AlCH$_2$***C***H$_2$C), 98.1 ({CH$_3$)C}$_2$***C***H), 124.1 (Ar-***C***), 125.0 (Ar-***C***), 125.7 (Ar-***C***), 125.9 (Ar-***C***), 126.9 (Ar-***C***), 127.7 (Ar-***C***), 127.9 (Ar-***C***), 128.5 (Ar-***C***), 129.9 (Ar-***C***), 140.2 (Ar-***C***), 142.3 (***C***Ph$_2$), 143.6 (2x Ar-***C***), 143.8 (Ar-***C***), 144.9 (Ar-***C***), 145.6(2x Ar-***C***), 170.9 {(CH$_3$)***C***}$_2$CH), 173.8 (AlCH$_2$CH$_2$***C***).

Some Ar-*C* resonances overlap and cannot be identified.

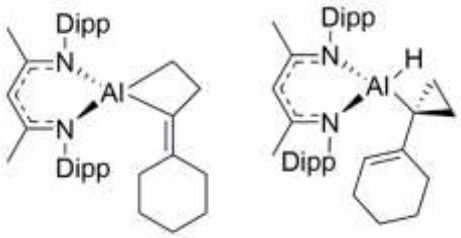
Due to the instability of this compound a satisfactory CHN analysis could not be obtained. Anal. Calc. ($C_{45}H_{55}AlN_2$): C, 83.03, H, 8.52; N, 4.30. Found: C, 53.44; H, 5.60; N, 2.88.



***Synthesis of 4-7b*:** In a glovebox, to a solution of **[Al]** (10 mg, 0.022 mmol) in toluene (~0.6 mL) was added **4-5b** (5 µL, ~0.041 mmol) *via* micropipette. The reaction mixture was transferred to a J-Young NMR tube which was sealed and removed from the glovebox. The reaction was monitored by ^{1}H NMR spectroscopy. The J-Young NMR tube was heated at 100°C for approximately 5 minutes at 100°C during which time the reaction mixture colour changed from yellow/orange to light yellow/colourless. The J-Young NMR tube was returned to the glovebox, the reaction mixture was decanted into a scintillation vial and concentrated *in vacuo* to ~0.1 mL of toluene. The product **4-7b** was recrystallized from a concentrated pentane solution -35°C as fluffy white needles. Yield: 15 mg, 0.014 mmol, 62 %.

^{1}H NMR (400 MHz, C_6D_6, 298 K) δ 0.60 – 0.71 (dd, 2H, AlC***H₂***CH_2), 1.11 (d, $^{3}J_{HH}$ = 6.9 Hz, 6H, (C***H₃***)$_2$CH), 1.16 (d, $^{3}J_{HH}$ = 6.8 Hz, 6H, (C***H₃***)$_2$CH), 1.24 (d, $^{3}J_{HH}$ = 6.6 Hz, 6H, (C***H₃***)$_2$CH), 1.34 (d, $^{3}J_{HH}$ = 6.8 Hz, 6H, (C***H₃***)$_2$CH), 1.57 (s, 6H, {(C***H₃***)C}$_2$CH), 2.58 (m, 2H, AlCH$_2$C***H₂***C), 3.34 (hept, $^{3}J_{HH}$ = 6.8 Hz, 2H, (CH$_3$)$_2$C***H***), 3.56 (hept, $^{3}J_{HH}$ = 6.7 Hz, 2H, (CH$_3$)$_2$C***H***), 4.89 (s, 1H), 6.87 (dd, $^{4}J_{HH}$ = 2.9, 2.9 Hz, 1H, CPh(***H***)), 6.97 – 7.22 (m, 9H, Ar***H***), 7.41 – 7.46 (m, 2H, Ar***H***).

^{13}C NMR (101 MHz, C_6D_6, 298 K) δ 13.7 (Al***C***H$_2$CH$_2$), 23.4 ({***C***H$_3$)C}$_2$CH), 24.3 ((***C***H$_3$)$_2$CH), 24.8 ((***C***H$_3$)$_2$CH), 25.2 ((***C***H$_3$)$_2$CH), 26.2 ((***C***H$_3$)$_2$CH), 28.6 ((CH$_3$)$_2$***C***H), 29.2 ((CH$_3$)$_2$***C***H), 32.3 (AlCH$_2$***C***H$_2$C), 97.7 ({CH$_3$C}$_2$***C***H), 124.2 (Ar-***C***), 125.0 (Ar-***C***), 125.4 (Ar-***C***), 129.0 (Ar-***C***), 133.8 (***C***(Ph)H), 139.9 (Ar-***C***), 141.5 (Ar-***C***), 143.8 (Ar-***C***), 145.2 (Ar-***C***), 170.3 ({CH$_3$)***C***}$_2$CH), 175.1 (Al(CH$_2$)(CH$_2$)***C***).



4-7c **4-7c'**

Synthesis of 4-7c and 4-7c': In a glovebox, to a solution of **[Al]** (10 mg, 0.022 mmol) in C_6D_6 (~0.3 mL) was added **4-5c** (5 mg, 0.041 mmol) *via* micropipette. The reaction mixture was transferred to a J-Young NMR tube with an internal capillary standard (ferrocene in C_6D_6) and removed from the glovebox. The reaction was monitored by ^{1}H NMR spectroscopy. The J-Young NMR tube was heated at 100°C for approximately 18 h during which the colour changed from orange/red to light yellow/colourless. ^{1}H NMR spectroscopy shows complete consumption of **[Al]** and formation of **4-7c** and **4-7c'** (**4c**:**5c**=1.8:1, 99% NMR yield, vs ferrocene standard). The J-Young NMR tube was returned to the glovebox, the reaction mixture was decanted into a scintillation vial and the solvent was removed *in vacuo* to yield an oily off-white solid. A minimal amount of pentane was added to dissolve the crude solid (~0.1 mL). **4-7c** was isolated as colourless needles by recrystallization in the glovebox freezer at –35°C. The supernatant was decanted, and the crystals were washed with cold n-pentane (–35°C) before the crystals were dried *in vacuo*. Yield: 6 mg, 0.011 mmol, 47%. *Note:* A second recrystallisation may be required to remove any residual **4-7c'**.

Data for 4-7c

^{1}H NMR (400 MHz, C_6D_6, 298 K) δ 0.52 – 0.61 (m, 2H, AlC***H₂***), 1.11 (d, *J* = 6.9 Hz, 6H, (C***H₃***)$_2$CH), 1.28 (d, $^3J_{HH}$ = 6.8 Hz, 6H, (C***H₃***)$_2$CH), 1.29 (d, $^3J_{HH}$ = 6.8 Hz, 6H, (C***H₃***)$_2$CH), 1.30 (d, $^3J_{HH}$ = 7.6 Hz, 6H, (C***H₃***)$_2$CH), 1.51 (s, 6H, {(C***H₃***)$_2$C}$_2$CH), 1.56 – 1.69 (m, 4H, 2xCy-C***H₂***), 1.72-1.79 (m, 2H, CyC***H₂***), 2.20-2.26 (m, 2H, Cy-C***H₂***), 2.38 (m, overlapping, 2H, AlCH$_2$C***H₂***), 2.38 (m, overlapping, 2H, Cy-C***H₂***), 3.33 (hept, $^3J_{HH}$ = 6.9 Hz, 2H, (CH$_3$)$_2$C***H***), 3.50 (hept, $^3J_{HH}$ = 6.7 Hz, 2H, (CH$_3$)$_2$C***H***), 4.83 (s, 1H, {(CH$_3$)C}C***H***), 7.05 – 7.21 (m, 6H, Ar-***H***).

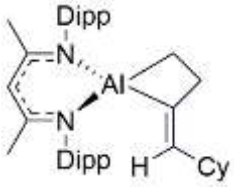
^{13}C NMR (101 MHz, C_6D_6, 298 K) δ 8.5 (Al***C***H$_2$), 23.4 {(***C***H$_3$)C}$_2$CH, 24.5 ((***C***H$_3$)$_2$CH), 24.8 ((***C***H$_3$)$_2$CH), 24.9 ((***C***H$_3$)$_2$CH), 26.5 ((***C***H$_3$)$_2$CH), 27.4 (Cy-***C***H$_2$), 27.6 (Cy-***C***H$_2$), 28.2 ((CH$_3$)$_2$***C***H), 28.2 (Cy-***C***H$_2$), 28.5 (Cy-***C***H$_2$), 29.1 ((CH$_3$)$_2$***C***H), 31.1 (Cy-***C***H$_2$), 41.0 (AlCH$_2$***C***H$_2$), 97.8 {(CH$_3$)C}$_2$***C***H, 124.2 (Ar-***C***), 125.1 (Ar-***C***), 127.5 (Ar-***C***), 140.1 (Ar-***C***), 140.4 (Cy-***C***), 143.6 (Ar-***C***), 145.3 (Ar-***C***), 169.8 ({(CH$_3$)***C***}$_2$CH). Al*C*=C is not observed in both 1D and 2D spectra.

Due to the instability of this compound a satisfactory CHN analysis could not be obtained. Anal. Calc. ($C_{38}H_{55}AlN_2$): C, 80.52, H, 9.78; N, 4.94. Found: C, 74.43; H, 9.12; N, 5.29.

Data for 4-7c'

4-7c' could not be isolated due to its high solubility and formation as minor product. Limited ^{1}H NMR data from the crude reaction mixture is provided; some resonances are overlapping with **4-7c**.

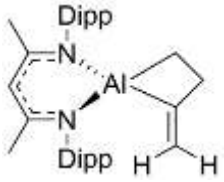
^{1}H NMR (400 MHz, C_6D_6, 298 K) δ 0.19 (d, J = 1.8 Hz, 2H), 0.33 – 0.39 (m, 2H, $CH_2C\boldsymbol{H_2}CAl$), 1.13 (m, 2H, $C\boldsymbol{H_2}CH_2CAl$), 1.17 (d, $^3J_{HH}$ = 6.9 Hz, 6H, $(C\boldsymbol{H_3})_2CH$), 1.37 (d, $^3J_{HH}$ = 6.7 Hz, 6H, $(C\boldsymbol{H_3})_2CH$), 1.45 (d, $^3J_{HH}$ = 6.8 Hz, 6H, $(C\boldsymbol{H_3})_2CH$), 1.54 (s, 6H, $\{(C\boldsymbol{H_3})_2C\}_2CH$), 3.43 (hept, $^3J_{HH}$ = 7.1 Hz, 2H, $(CH_3)_2C\boldsymbol{H}$), 4.08 (br s, 1H, $Al\boldsymbol{H}$), 4.92 (s, 1H, $\{(CH_3)C\}C\boldsymbol{H}$), 5.15 (br s, 1H, $C{=}C\boldsymbol{H}$).



***Synthesis of 4-7d*:** In a glovebox, to a solution of **[Al]** (10 mg, 0.022 mmol) in toluene (~0.5 mL) was added **4-7d** (5 µL, 0.036 mmol) *via* micropipette. The reaction was allowed to stand at 25 ºC for 4 hours during which the gradual decolourisation of the solution from the characteristic orange-red of **[Al]** to colourless was observed. The toluene was removed *in vacuo,* the crude product was redissolved in the minimum amount of pentane (~0.2 mL), and **4-7d** recrystallized as colourless blocks at –35°C. The supernatant was decanted, and the crystals were washed with cold n-pentane (–35°C) before the crystals were dried *in vacuo*. Yield: 8 mg, 0.014 mmol, 61%.

^{1}H NMR (400 MHz, C_6D_6, 298 K) δ 0.55 – 0.63 (m, 2H, AlC***H₂***), 1.09 (d, $^{3}J_{HH}$ = 6.8 Hz, 6H, (C***H₃***)$_2$CH), 1.16 (d, $^{3}J_{HH}$ = 6.8 Hz, 6H, (C***H₃***)$_2$CH), 1.16– 1.25 (m, 6H, 6xCy-***H***), 1.35 (d, $^{3}J_{HH}$ = 6.8 Hz, 6H, (C***H₃***)$_2$CH), 1.40 (d, $^{3}J_{HH}$ = 6.7 Hz, 6H, (C***H₃***)$_2$CH), 1.54 (s, 6H, {(C***H₃***)C}$_2$CH), 1.60 (m, 1H, Cy-***H***), 1.69 (m, 1H, Cy-***H***), 1.81 (m, 2H, 2x Cy-***H***), 2.23 (m, overlapping, 1H, Cy-C***H***), 2.26 (m, 2H, AlCH$_2$C***H₂***), 3.39 (hept, $^{3}J_{HH}$ = 6.8 Hz, 2H, (CH$_3$)$_2$C***H***), 3.50 (hept, $^{3}J_{HH}$ = 6.8 Hz, 2H, (CH$_3$)$_2$C***H***) 4.88 (s, 1H, {(CH$_3$)C}$_2$C***H***), 5.63 (dt, $^{3}J_{HH}$ = 7.9, 2.9 Hz, 1H, C***H***(Cy)), 7.08-7.17 (m, 6H, Ar-***H***).

^{13}C NMR (101 MHz, C_6D_6, 298 K) δ 11.9 (Al***C***H$_2$), 23.5 ({(***C***H$_3$)C}$_2$CH), 24.3 ((***C***H$_3$)$_2$CH), 24.9 ((***C***H$_3$)$_2$CH), 25.0 ((***C***H$_3$)$_2$CH), 26.6 ((***C***H$_3$)$_2$CH), 26.8 (Cy-***C***), 26.9 (Cy-***C***), 28.2 ((CH$_3$)$_2$***C***H), 28.8 (AlCH$_2$***C***H$_2$), 29.1 ((CH$_3$)$_2$***C***H), 33.8 (Cy-***C***), 40.2 (***C***H of Cy), 97.7 ({(CH$_3$)C}$_2$***C***H), 124.2 (Ar-***C***), 124.8 (Ar-***C***), 127.6 (Ar-***C***), 140.3 (Ar-***C***), 141.1 (***C***HCy), 143.9 (Ar-***C***), 145.0 (Ar-***C***), 164.5 (AlCH$_2$CH$_2$***C***), 170.1 ({(CH$_3$)***C***}$_2$CH).



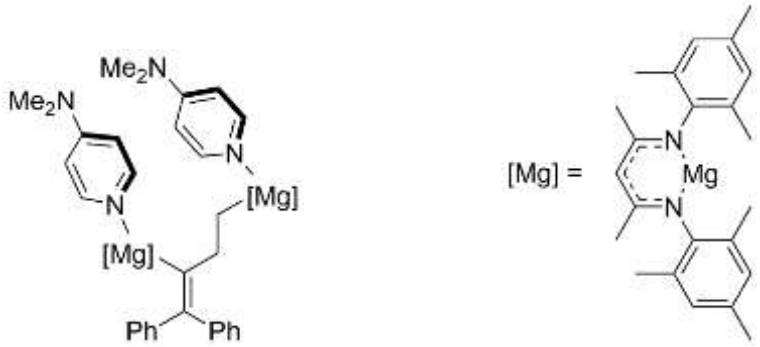
***Synthesis of 4-7e*:** A solution of **[Al]** (10 mg, 0.022 mmol) in C_6D_6 (0.600 mL) was transferred to a J-Young NMR tube which was sealed and placed within the glovebox freezer (–35°C). Once the solution was frozen, the NMR tube was removed from the glovebox freezer, unsealed and cold (–35°C) methylenecyclopropane **4-7e** (5 µL, 0.12 mmol) was added *via* micropipette. The NMR tube was quickly resealed and the solution allowed to thaw. An instant colour change from the characteristic orange-red of **[Al]** to colourless was observed. Monitoring the reaction by ^{1}H NMR spectroscopy showed complete conversion of **[Al]** to **4-7e**. The J-Young NMR tube was returned to the glovebox and the volatiles were removed *in vacuo* affording **4-7e** as an analytically pure white solid in quantitative yield. **4-7e** can be recrystallized from pentane as colourless blocks. Yield: 11 mg, 0.022, 98%.

^{1}H NMR (400 MHz, C_6D_6) δ 0.58 (t, $^3J_{HH}$ = 8.8 Hz, 2H, AlC***H*₂**), 1.10 (d, $^3J_{HH}$ = 6.9 Hz, 6H, (C***H*₃**)$_2$CH), 1.15 (d, $^3J_{HH}$ = 6.8 Hz, 6H, (C***H*₃**)$_2$CH), 1.33 (d, $^3J_{HH}$ = 6.8 Hz, 6H, (C***H*₃**)$_2$CH), 1.40 (d, $^3J_{HH}$ = 6.6 Hz, 6H, (C***H*₃**)$_2$CH), 1.54 (s, 6H, {(C***H*₃**)C}$_2$CH), 2.31 (t, $^3J_{HH}$ = 8.8 Hz, 2H, AlCH$_2$C***H*₂**), 3.34 (hept, $^3J_{HH}$ = 6.9 Hz, 2H, (CH$_3$)$_2$C***H***), 3.52 (hept, $^3J_{HH}$ = 6.9 Hz, 2H, (CH$_3$)$_2$C***H***), 4.87 (s, 1H, ({CH$_3$C}$_2$C***H***), 5.49 (br s, 1H, C=C(***H***)(H)), 5.93 (s, 1H, C=C(H)(***H***)), 7.07-7.17 (m, 6H, Ar***H***).

^{13}C NMR (101 MHz, C_6D_6) δ 11.4 (Al***C***H$_2$), 23.5 ({(***C***H$_3$)C}$_2$CH), 24.4 ((***C***H$_3$)$_2$CH), 24.8 ((***C***H$_3$)$_2$CH), 25.1 ((***C***H$_3$)$_2$CH), 25.9 ((***C***H$_3$)$_2$CH), 28.1 ((CH$_3$)$_2$***C***H), 29.0 ((***C***H$_3$)$_2$*C*H), 35.1 (AlCH$_2$***C***H$_2$), 97.7 ({(CH$_3$)C}$_2$***C***H), 119.0 (C=***C***H$_2$), 124.3 (Ar***C***), 124.9 (Ar***C***), 139.9 (Ar***C***), 143.9 (Ar***C***), 145.0 (Ar***C***), 170.3 ({(CH$_3$)***C***}$_2$CH), 177.6 (***C***=CH$_2$).

Some Ar-*C* resonances overlap and cannot be identified.

Anal. Calc. ($C_{33}H_{47}AlN_2$): C, 79.47, H, 9.50; N, 5.62. Found: C, 77.88; H, 10.45; N, 5.72.

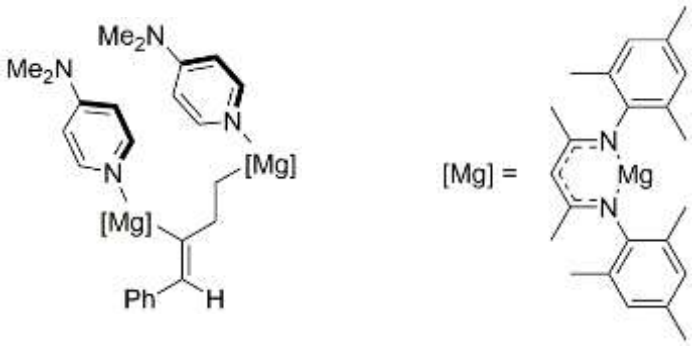


Synthesis of 4-8a.DMAP$_2$: In a glovebox, to a solution of **[Mg]–[Mg]** (15 mg, 0.02 mmol) in C_6D_6 (0.600 mL), alkylidenecyclopropane **4-5a** (10 mg 0.048 mmol) was added as a solid. An instant colour change from the characteristic light yellow of **[Mg]–[Mg]** to deep purple was observed. The solution was transferred to a J-Young NMR tube. The tube sealed and removed from the glovebox. The reaction mixture was monitored by ^{1}H NMR spectroscopy. The mixture was heated at 100°C for 4 h at which point the complete consumption of **[Mg]–[Mg]** was observed by ^{1}H NMR spectroscopy. The J-Young NMR tube was returned to the glovebox and 4-dimethylaminopyridine (5 mg, 0.041 mmol) in toluene (0.100 mL) was added to the reaction mixture. The reaction mixture was then decanted into a scintillation vial and the solvent was removed *in vacuo* to yield a brown oil. Toluene (~0.3 mL) was added to dissolve this brown oil, and removed *in vacuo*. This process was repeated until colourless crystals of **4-8a.DMAP$_2$** formed upon *in vacuo* removal of toluene. Toluene was added to these crystals (~0.2 mL) and the solid suspension was left in the glovebox freezer (–35°C) overnight. The supernatant was decanted, the crystals washed three times with pentane (3 x 0.3 mL) and dried *in vacuo*. Yield: 17 mg, 0.015 mmol, 70%.

^{1}H NMR (400 MHz, C_6D_6, 298 K) δ -0.41 (br s, 2H, Mg-C***H$_2$***), 1.76 (s, 6H, {C***H$_3$***C}$_2$CH), 1.79 (s, 6H, {C***H$_3$***C}$_2$CH), 1.80 (s, 6H, 2x ArC***H$_3$***), 2.03 (br s, 12H, 2x N(C***H$_3$***)$_2$), 2.10 (s, 2H, MgCH$_2$C***H$_2$***), 2.24 (s, 6H, 2x ArC***H$_3$***), 2.28 (s, 6H, 2x ArC***H$_3$***), 2.29 – 2.34 (br m, 18H, 6x ArC***H$_3$***), 4.97 (s, 1H, {CH$_3$C}$_2$C***H***), 5.05 (s, 1H, {CH$_3$C}$_2$C***H***), 5.66 (br s, 2H, 2x DMAP C***H***), 5.85 (br s, 2H, 2x DMAP C***H***), 6.73-7.51 (m, 18H, Ar-***H***), 7.61 (br s overlapping, 2H, DMAP C***H***), 7.84 (br s, 2H, DMAP C***H***).

^{13}C NMR (101 MHz, C_6D_6, 298 K) δ 9.5 (Mg***C***H$_2$), 18.7 (2x Ar***C***H$_3$), 19.4 (2x Ar***C***H$_3$), 19.6 (4x Ar***C***H$_3$), 21.1 (2x Ar***C***H$_3$), 21.2 (2x Ar***C***H$_3$), 21.4 (MgCH$_2$***C***H$_2$), 23.4 ({***C***H$_3$C}$_2$CH), 23.8 ({***C***H$_3$C}$_2$CH), 38.1 (2x N(***C***H$_3$)$_2$), 93.7 ({CH$_3$C}$_2$***C***H), 95.7 ({***C***H$_3$C}$_2$*C*H), 106.1 (4x DMAP ***C***H), 123.3 (Ar***C***), 123.6 (Ar***C***), 125.7 (Ar***C***), 127.4 (Ar***C***), 127.4 (Ar***C***), 128.4 (Ar***C***), 128.6 (Ar***C***), 128.6 (Ar***C***), 128.9 (Ar***C***), 129.1 (Ar***C***), 129.1 (Ar***C***), 129.3 (Mg***C***), 129.6 (Ar***C***), 131.0 (Ar***C***), 131.8 (Ar***C***), 131.9 (Ar***C***), 132.1 (Ar***C***), 132.4 (Ar***C***), 132.9 (Ar***C***), 137.9 (MgC***C***Ph$_2$), 140.9 (Ar***C***), 146.8 (2x Ar***C***), 147.7 (Ar***C***), 148.2 (Ar***C***), 148.9 (Ar***C***, 4x DMAP-*C*), 151.6 (Ar***C***), 166.6 ({CH$_3$***C***}$_2$CH), 166.9 ({CH$_3$***C***}$_2$CH), 193.9 (2x Me$_2$N***C***).

Anal. Calc. ($C_{76}H_{92}Mg_2N_8$): C, 78.27, H, 7.95; N, 9.60. Found: C, 79.34; H, 8.53; N, 8.60.



Synthesis of 4-8b.DMAP$_2$: In a glovebox, to a solution of **[Mg]–[Mg]** (15 mg, 0.021 mmol) in C_6D_6 (0.600 mL), alkylidenecyclopropane **4-5b** (5 µL, 0.036 mmol) was added *via* micropipette. No colour change was observed. The solution was transferred to a J-Young NMR tube. The tube sealed and removed from the glovebox. The reaction mixture was monitored by ^{1}H NMR spectroscopy. The mixture was allowed to stand at 25°C for 1 h. at which point the complete consumption of **6** was observed by ^{1}H NMR spectroscopy. The J-Young NMR tube was returned to the glovebox and 4-dimethylaminopyridine (5 mg, 0.041 mmol) in toluene (0.100 mL) was added to the reaction mixture. The reaction mixture was decanted into a scintillation vial and the solvent was removed *in vacuo* to yield an off-white solid. Toluene (~0.3 mL) was added to the crude product and the sample was left in the glovebox freezer (–35°C) overnight to yield **4-8b.DMAP$_2$** as a colourless solid. The supernatant was decanted, the white solid was washed three times with pentane (3x 0.3 mL) and dried *in vacuo*. Yield: 13 mg, 0.012 mmol, 57%.

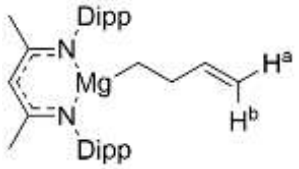
1H NMR (400 MHz, C_6D_6, 298 K) δ -0.51 (t, $^3J_{HH}$ = 7.6 Hz, 2H, MgC***H$_2$***), 1.78 (s, 6H, 2x C***H$_3$***), 1.79 (s, 6H), 1.93 (s, 6H), 1.96 (s, 6H), 2.03 (s, 6H), 2.11 (s, 1H), 2.13 – 2.20 (m, 2H, MgCH$_2$C***H$_2$***), 2.23 (s, 6H), 2.24 (s, 6H), 2.40 (s, 6H), 2.47 (s, 6H), 4.99 (s, 1H, {CH$_3$C}$_2$C***H***), 5.18 (s, 1H, {CH$_3$C}$_2$C***H***), 5.66 (s, 4H, DMAP C***H***), 6.77 (s, 1H, C***H***Ph), 6.82 – 7.14 (m, 9H, Ar-***H***), 7.30 (apparent t, $^3J_{HH}$ = 7.5 Hz, 2H, Ar***H***), 7.54 (apparent d, $^3J_{HH}$ = 7.6 Hz, 2H, Ar***H***) 7.85 (s, 2H, DMAP C***H***), 8.05 (s, 2H, DMAP C***H***). **7b.DMAP$_2$** is not soluble enough to acquire meaningful ^{13}C NMR data in C_6D_6.

1H NMR (400 MHz, THF-d_8, 298 K) δ -1.28 – -1.09 (m, 2H, MgC***H$_2$)***, 1.51 (s, 6H, {C***H$_3$***C}$_2$CH), 1.54 (s, 6H, {C***H$_3$***C}$_2$CH), 1.75 (m, MgCH$_2$C***H$_2$***, 2H), 1.92 (s, 6H, 2x ArC***H$_3$***), 1.94 (s, 18H, 6x ArC***H$_3$***), 2.17 (s, 6H, 2x ArC***H$_3$***), 2.19 (s, 6H, 2x ArC***H$_3$***), 2.95 (s, 12H, 2x N(C***H$_3$***)$_2$, 4.69 (s, 1H, {CH$_3$C}$_2$C***H***), 4.95 (s, 1H, {CH$_3$C}$_2$C***H***), 6.43 (s, 4H, 4x DMAP C***H***), 6.50 (s, 1H, C***H***Ph), 6.67 (s, 4H, MesAr***H***), 6.74 (s, 4H, MesAr***H***) 6.99 (m, 2H, PhAr***H***), 7.12 – 7.22 (m, 3H, PhAr***H***), 7.91 (s, 4H, 4x DMAP C***H***).

^{13}C NMR (101 MHz, THF-d_8, 298 K) δ 18.9 (4x Ar***C***H$_3$), 19.0 (4x Ar***C***H$_3$), 20.8(2x Ar***C***H$_3$), 20.9 (2x Ar***C***H$_3$), 23.0 ({***C***H$_3$C}$_2$CH), 23.3 ({***C***H$_3$C}$_2$CH), 38.8 (4x N(***C***H$_3$)$_2$), 47.5 (MgCH$_2$***C***H$_2$), 93.6 ({CH$_3$C}$_2$***C***H), 95.0 ({CH$_3$C}$_2$***C***H), 106.8 (4x DMAP ***C***H), 122.5 (Ar***C***), 125.8 (Mg***C***CHPh)126.7 (Ar***C***),

127.9 (Ar***C***), 128.7 (Ar***C***), 129.1 (Ar***C***), 129.2 (Ar***C***), 129.5 (Ar***C***), 132.2 (Ar***C***), 132.4 (Ar***C***), 132.5 (Ar***C***), 133.9 (***C***HPh), 147.0 (Ar***C***), 147.6 (Ar***C***), 148.1 (Ar***C***), 149.9 (4x DMAP ***C***H), 155.3 (Ar***C***), 166.7 ({CH_3C}$_2$***C***H), 167.1 ({CH_3C}$_2$***C***H). *Some Ar*C* resonances overlap. *Note: The $MgCH_2$ carbon resonance was unobservable in either 1D or 2D spectra, due to line-broadening assumed to arise from a fluxional process.*

Due to the instability of this compound a satisfactory CHN analysis could not be obtained. Anal. Calc. ($C_{70}H_{88}Mg_2N_8$): C, 77.13, H, 8.14; N, 10.27. Found: C, 64.02; H, 6.38; N, 11.27.



Synthesis of 4-10: A solution of **4-9** (20 mg, 0.045 mmol) in C_6D_6 (0.600 mL) in a J-Young NMR tube was sealed and placed within the glovebox freezer (–35°C). Once the solution was frozen, the NMR tube was removed from the glovebox freezer, unsealed and cold (–35°C) methylenecyclopropane **4-5e** (10 µL, 12.5 mg, 0.24 mmol) was added *via* micropipette. The J-Young NMR tube was removed from the glovebox and the solution was heated at 80°C for 3 hours, or until the complete conversion of **4-9** to **4-10** was observed *via* ^{1}H NMR spectroscopy. The J-Young NMR tube was returned to the glovebox and the solution was diluted with toluene (~0.5 mL) and decanted into a scintillation vial. The volatiles were removed *in vacuo* yielding **4-10** as an analytically pure colourless solid in quantitative yield. **4-10** may be recrystallized from a concentrated toluene solution as a white microcrystalline powder. Yield: 12 mg, 0.024 mmol, 53%.

^{1}H NMR (400 MHz, C_6D_6, 298 K) δ -0.37 – -0.05 (m, 2H, MgC***H₂***), 1.15 (d, $^3J_{HH}$ = 6.9 Hz, 12H, 2x (C***H₃***)$_2$CH), 1.24 (d, $^3J_{HH}$ = 6.9 Hz, 12H, 2x (C***H₃***)$_2$CH), 1.66 (s, 6H, ({(C***H₃***)C}$_2$CH)), 2.01 – 2.08 (m, 2H, MgCH$_2$C***H₂***), 3.14 (hept, $^3J_{HH}$ = 6.9 Hz, 4H, 4x (CH$_3$)$_2$C***H***), 4.66 (ddt, $^3J_{HH}$ = 9.9, $^2J_{HH}$ = 2.5, 1.2 Hz, 1H, ***H^a***), 4.78 (ddt, $^3J_{HH}$ = 16.9, 3.0, 1.6 Hz, 1H, ***H^b***), 4.91 (s, 1H, ({(CH$_3$)C}$_2$C***H***)), 5.67 (ddt, $^3J_{HH}$ = 16.4, 9.9, 6.4 Hz, 1H, ***H***C=C(H^a)(H^b)), 7.10 (m, 6H, Ar-***H***).

^{13}C NMR (101 MHz, C_6D_6, 298 K) δ 4.4 (Mg***C***H$_2$), 23.2 ({(***C***H$_3$)C}$_2$CH), 23.2 ((***C***H$_3$)$_2$CH), 24.3 ((***C***H$_3$)$_2$CH), 28.3 ((CH$_3$)$_2$***C***H), 32.4 (MgCH$_2$***C***H$_2$), 94.9 ({(CH$_3$)C}$_2$***C***H), 109.4 (HC=***C***(H^a)(H^b)), 123.7 (Ar-***C***), 125.6 (Ar-***C***), 141.5 (Ar-***C***), 143.6 (Ar-***C***), 146.9 (H***C***=C(H^a)(H^b)), 168.9 ({(CH$_3$)***C***}$_2$CH).

Due to the instability of this compound a satisfactory CHN analysis could not be obtained. Anal. Calc. ($C_{33}H_{48}MgN_2$): C, 79.74, H, 9.73; N, 5.64. Found: C, 73.51; H, 9.85; N, 6.40.

4.4.4 – Kinetic experiments on the conversion of 4-6a to 4-7a

Run 1

4-6a.(0.5C_7H_8) (22 mg, 0.0317 mmol) was dissolved in C_6D_6 (3 mL) and a small amount of ferrocene (~ 3 mg) was added as an internal standard. The solution of **4-6a** (10.5 mmol) was apportioned into 4 NMR tubes in 0.600 mL aliquots and stored in the glovebox freezer at –35°C. The NMR tubes were removed from the glovebox and inserted into a pre-heated NMR spectrometer probe. ^{1}H NMR spectra were recorded at 1 min intervals.

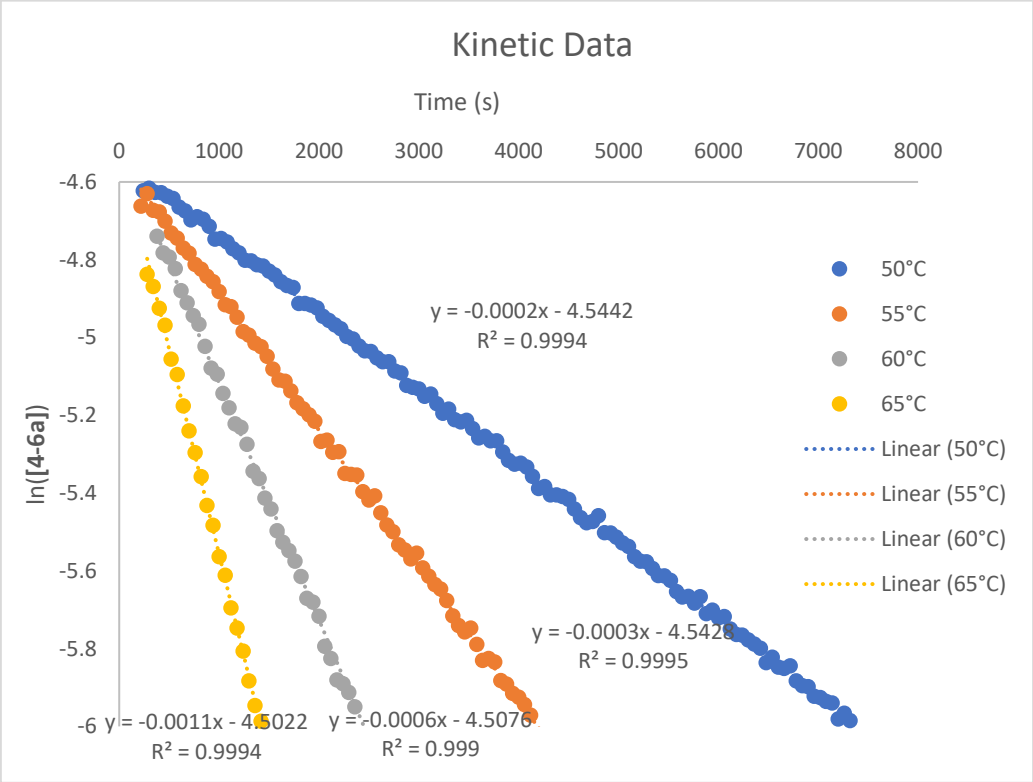


Figure 4.11: Kinetic data for the transformation of **4-6a** to **4-7a** at temperatures 50-65°C (5°C intervals). Concentration was determined through integration of the diagnostic β-diketiminate methine resonance versus an internal standard

Plotting ln[**4-6a**] (concentration determined by the integration of the internal ferrocene standard) against time showed a linear relationship indicating that the reaction is first order in [**4-6a**]. Four rate constants were determined in the temperature range of 50°C to 65°C at 5°C intervals and a plot of ln(k_{obs}) against 1/T allowed calculation of the thermodynamic parameters using the Eyring equation. Standard errors were calculated using regression analysis in the Microsoft Excel program. The activation parameters for the reaction were found to be: $\Delta H^{\ddagger}$ = 23.6 ±0.08 kcal mol^{-1}, $\Delta S^{\ddagger}$ = –2.5 ± 0.2 cal K^{-1} mol^{-1} and an associated $\Delta G^{\ddagger}_{298K}$ = 24.4 ±0.2 kcal mol^{-1}.

T (K)	1/T	k (s^{-1})	ln(k/T)
323	0.003095975	0.00019654	-14.3122972
328	0.00304878	0.000347809	-13.7568712
333	0.003003003	0.000609033	-13.2117804
338	0.00295858	0.001054862	-12.6773915

Table 4.1: Table of rate constants derived from kinetic experiments.

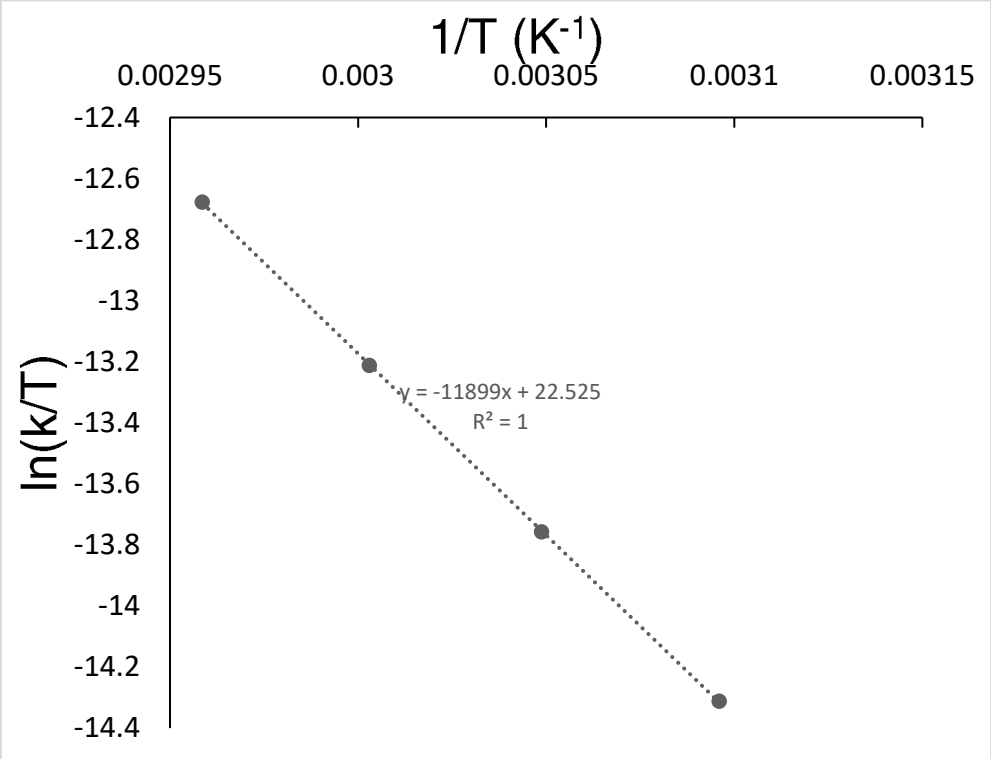


Figure 4.12: Eyring plot of data from Table 4.1.

Run 2

4-6a.(0.5C_7H_8) (20 mg, 0.0287 mmol) was dissolved in C_6D_6 (3 mL) and a small amount of ferrocene (~ 3 mg) was added as an internal standard. The solution of **4-6a** (9.56 mmol) was apportioned into 4 NMR tubes in 0.600 mL aliquots and stored in the glovebox freezer at –35°C. The NMR tubes were removed from the glovebox and inserted into a pre-heated NMR spectrometer probe. ^{1}H NMR spectra were recorded at 1 min intervals.

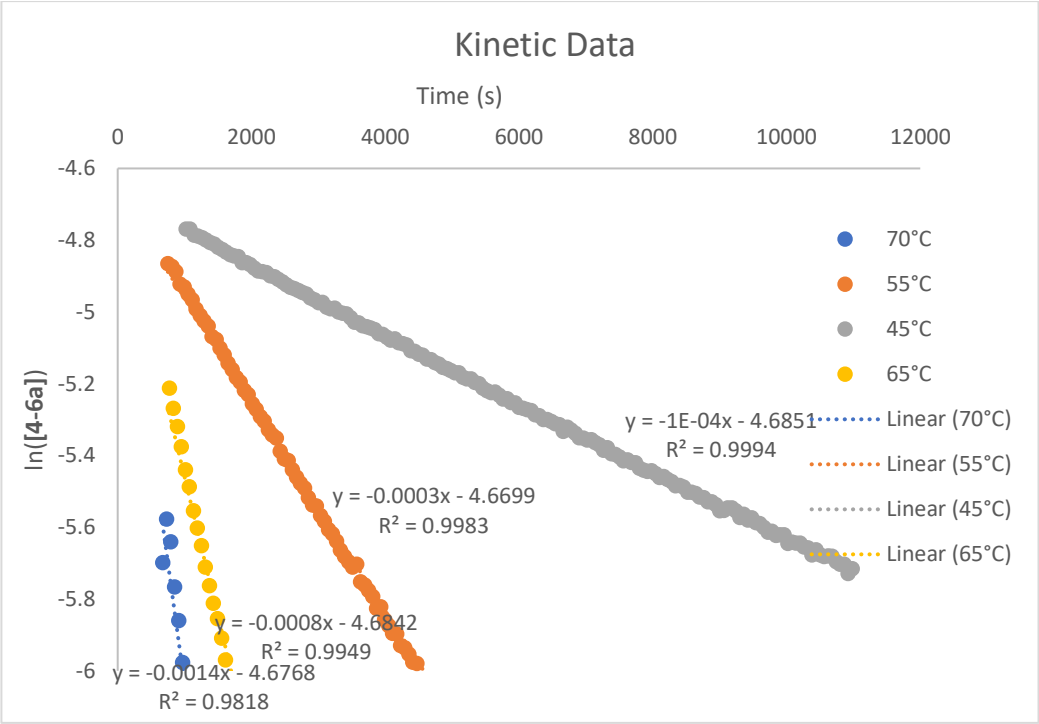


Figure 4.13: Kinetic data for the transformation of **4-6a** to **4-7a** at temperatures 45°C, 55°C, 65°C, and 70°C. Concentration was determined through integration of the diagnostic β-diketiminate methine resonance versus an internal standard

Plotting ln[**4-6a**] (concentration determined by the integration of the internal ferrocene standard) against time showed a linear relationship indicating that the reaction is first order in [**4-6a**]. Four rate constants were determined in the temperature range of 45°C to 70°C and a plot of ln(k_{obs}) against 1/T allowed calculation of the thermodynamic parameters using the Eyring equation. Standard errors were calculated using regression analysis in the Microsoft Excel program. The activation parameters for the reaction were found to be: $\Delta H^{\ddagger}$ = 22.3 ±0.4 kcal mol^{-1}, $\Delta S^{\ddagger}$ = –6.9 ± 1.3 cal K^{-1} mol^{-1} and an associated $\Delta G^{\ddagger}_{298K}$ = 24.4 ±0.8 kcal mol^{-1}.

T (K)	1/T	k (s^{-1})	ln(k/T)
318	0.003144654	0.0000950994	-15.0226392
328	0.00304878	0.000273852	-13.9959369
338	0.00295858	0.000780753	-12.9782979
343	0.002915452	0.001361268	-12.4370692

Table 4.2: Table of rate constants derived from kinetic experiments.

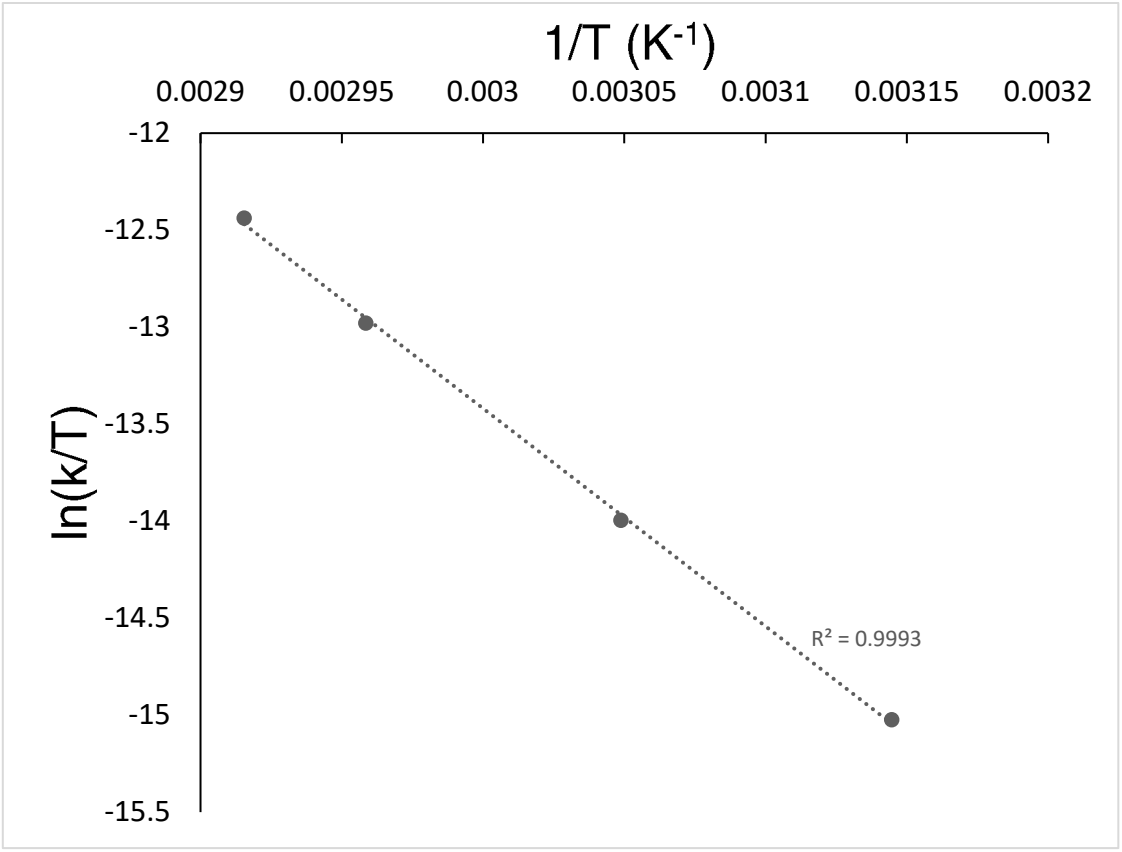
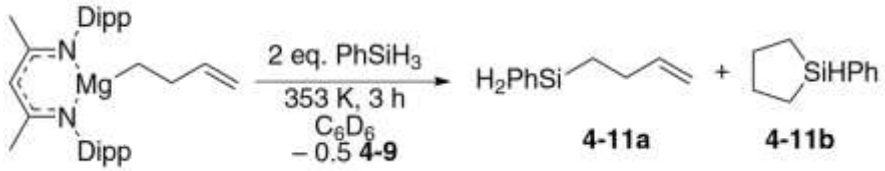


Figure 4.14: Eyring plot of data from Table 4.2.

4.4.5 – Magnesium hydride catalysis

Stoichiometric reaction of 9 with $PhSiH_3$

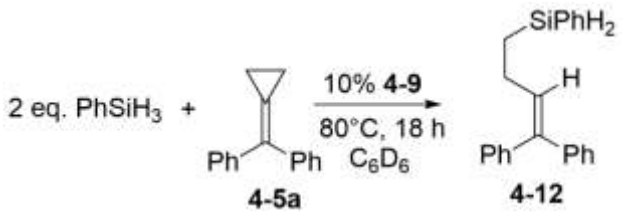


In a glovebox, **4-10** (20 mg, 0.045 mmol) was dissolved C_6D_6 (0.600 mL) and transferred to a J-Young NMR tube fitted with an internal capillary standard (pyridine in C_6D_6). This NMR was not sealed and was placed in the glovebox freezer (–35°C) and allowed to cool for 5 minutes. At this time, cold (–35°C) methylenecyclopropane (34 μL) was added to the cold NMR tube *via* micropipette and the J-Young NMR tube was sealed quickly. The J-Young NMR tube containing the reaction mixture was removed from the glovebox. A ^{1}H NMR spectrum was taken at this timepoint. The reaction mixture was heated in an oil bath at 80°C. The consumption of **4-10** and concomitant formation of **4-9** was monitored by ^{1}H NMR spectroscopy. Upon completion of the reaction, the NMR tube was returned to the glovebox. The volatiles were removed *in vacuo* from the J-Young NMR tube to afford the product **4-10** as a white solid. C_6D_6 (0.600 mL) and $PhSiH_3$ (6 μL, 0.049 mmol) were added to the J-Young NMR tube and the reaction was heated at 80°C and monitored by ^{1}H NMR spectroscopy. The complete consumption of **4-10** is observed with the concomitant formation of **4-9**, **4-11a**, and **4-11b**. The reaction is complete once all of **4-11a** is converted to **4-11b**.

^{1}H NMR data for **4-11b** is in agreement with reported values.[27]

4-11b:

^{1}H NMR (400 MHz, C_6D_6, 298 K) δ 0.72 – 0.82 (m, 2H, $CH_2C(\boldsymbol{H})(H')C(\boldsymbol{H})(H')CH_2$), 0.88 – 0.95 (m, 2H, $CH_2C(H)(\boldsymbol{H'})C(H)(\boldsymbol{H'})CH_2$), 1.58 (m, 4H, $Si(C\boldsymbol{H_2})_2$), 4.71 (p, $^3J_{HH}$ = 3.2 Hz, 1H, Si***H***Ph), 7.14 – 7.18 (m, 3H, Ar***H***), 7.44 – 7.54 (m, 2H, Ar***H***).



***Catalytic hydrosilylation of 4-5a*:** In a glovebox, **4-9** (20 mg, 0.045 mmol), **4-5a** (93 mg, 0.45 mmol) and $PhSiH_3$ (111 µL, 0.90 mmol) were dissolved in C_6D_6 (0.600 mL) and transferred to a J-Young NMR tube with an internal capillary standard (pyridine in C_6D_6). The tube was sealed and removed from the glovebox. An initial ^1H NMR (8 scans, 20s delay) spectrum was taken at this timepoint. The solution was heated at 80°C in an oil bath and monitored at regular intervals for conversion. Upon completion of the reaction, the NMR tube was returned to the glovebox, diluted with toluene (~ 1 mL) and decanted into a scintillation vial. The volatiles were removed *in vacuo*, to afford a viscous colourless oil. **4-12** was redissolved in pentane and filtered. The pentane was removed under reduced pressure to afford **4-12**. Yield 138 mg, 0.44 mmol, 98%.

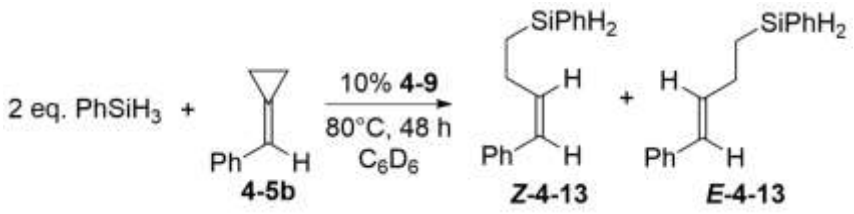
Time (h)	4-5a	4-12
1	84%	18%
2	70%	33%
3	57%	43%
18	0%	100%

Table 4.3: Catalytic conversion of **4-5a** to **4-12** at measured timepoints.

4-12:

^1H NMR (400 MHz, C_6D_6) δ 0.91 (tt, $^3J_{HH}$ = 8.0, 3.6 Hz, 2H, SiCH_2), 2.26 (dt, $^3J_{HH}$ = 8.0, 7.4 Hz, 2H, SiCH$_2$CH_2), 4.42 (t, $^3J_{HH}$ = 3.6 Hz, 2H, SiH_2), 6.02 (t, $^3J_{HH}$ = 7.4 Hz, 1H, C=C*H*), 7.03-7.06 (m, 11H, Ar*H*), 7.22 – 7.29 (m, 2H, Ar*H*), 7.38 (m, 2H, Ar*H*).

^{13}C NMR (101 MHz, C_6D_6) δ 11.0 (Si*C*H$_2$), 25.5 (SiCH$_2$*C*H$_2$), 127.3 (Ar*C*), 127.8 (2x Ar*C*), 128.3 (2x Ar*C*), 128.5 (2x Ar*C*), 128.5 (2x Ar*C*), 129.8 (Ar*C*), 130.3 (3x Ar*C*), 131.4 (C=*C*H), 132.4 (Ar*C*), 135.6 (2x Ar*C*), 140.5 (Ar*C*), 141.8 (*C*=CH), 143.2 (Ar*C*).



Catalytic hydrosilylation of 4-5b: In a glovebox, **4-9** (20 mg, 0.045 mmol), **4-5b** (59 µL, 0.45 mmol) and $PhSiH_3$ (111 µL, 0.90 mmol) were dissolved in C_6D_6 (0.600 mL) and transferred to a J-Young NMR tube with an internal capillary standard (pyridine in C_6D_6). The tube was sealed and removed from the glovebox. An initial ^1H NMR (8 scans, 20 s delay) spectrum was taken at this timepoint. The reaction mixture was heated at 80°C in an oil bath and the reaction monitored at regular intervals by ^1H NMR spectroscopy. Upon completion of the reaction, the NMR tube was returned to the glovebox, diluted with toluene (~ 1 mL) and decanted into a scintillation vial. The volatiles were removed *in vacuo* and the products were redissolved in pentane. The white suspension was filtered. The pentane was removed under reduced pressure to afford a mixture of ***Z*-4-13** and ***E*-4-13** as an oily solid. Yield 100 mg (both isomers), 0.42 mmol, 86%.

Time (h)	4-5b	*Z*-4-13	*E*-4-13	*E*:*Z*
1	87%	6%	5%	1:1.08
2	76%	10%	9%	1:1.21
3	71%	14%	12%	1:1.19
18	17%	43%	37%	1:1.17
24	9%	46%	40%	1:1.15
30	5%	49%	43%	1:1.14
48	0%	49%	44%	1:1.11

Table 4.4: Catalytic conversion of **4-5b** to ***E*-4-13** and ***Z*-4-13** at measured timepoints. Isomerisation of ***Z*-4-13** to ***E*-4-13** appears to be occurring slowly under the reaction conditions.

Z*-4-13:** ^{1}H NMR (400 MHz, C_6D_6, 298 K) δ 0.84-0.96 (m, overlapping, 2H, SiCH*₂**), 2.39 (dddd, $^{3}J_{HH}$ = 9.7, 7.9, 6.2 Hz, $^{4}J_{HH}$ = 1.8 Hz, 2H, $SiCH_2C$***H*₂**), 4.42 (t, $^{3}J_{HH}$ = 3.7 Hz, 2H, Si***H*₂**Ph), 5.58 (dt, $^{3}J_{HH}$ = 11.5, 7.3 Hz, 1H, $(CH_2)C$***H***), 6.36 (dt, $^{3}J_{HH}$ = 11.5 Hz, $^{4}J_{HH}$ = 1.9 Hz, 1H, PhC***H***).

^{13}C NMR (101 MHz, C_6D_6, 298 K) δ 10.9 ($H_2PhSiCH_2$), 24.2 ($HCCH_2$), 129.0, (Ph***C***H) 134.4 (H***C***CH_2).

E*-4-13**: ^{1}H NMR (400 MHz, C_6D_6, 298 K) δ 0.85-0.96 (m, overlapping, 2H, SiCH*₂**), 2.19 (dtd, $^{3}J_{HH}$ = 9.8, 6.5 Hz, $^{4}J_{HH}$ = 1.5 Hz, 2H, (***H*₂**C)CH), 4.48 (t, $^{3}J_{HH}$ = 3.6 Hz, 2H, Si***H*₂**Ph), 6.06 (dt, $^{3}J_{HH}$ = 15.7, 6.7 Hz, 1H, $(H_2C)C$***H***), 6.25 (dt, $^{3}J_{HH}$ = 15.7 Hz, $^{4}J_{HH}$ = 1.5 Hz, 1H, PhC***H***), 7.02-7.50 (m, overlapping, 10H, Ar***H***).

^{13}C NMR (101 MHz, C_6D_6, 298 K) δ 10.2 ($H_2PhSiCH_2$), 28.7 ($HCCH_2$), 129.9 (Ph***C***H), 137.9 (H***C***CH_2).

Note: aromatic resonances (^{1}H and ^{13}C) for the two isomers cannot be resolved due to overlap.

4.5 – Single crystal X-ray data

The X-ray crystal structure of ***4-6a***

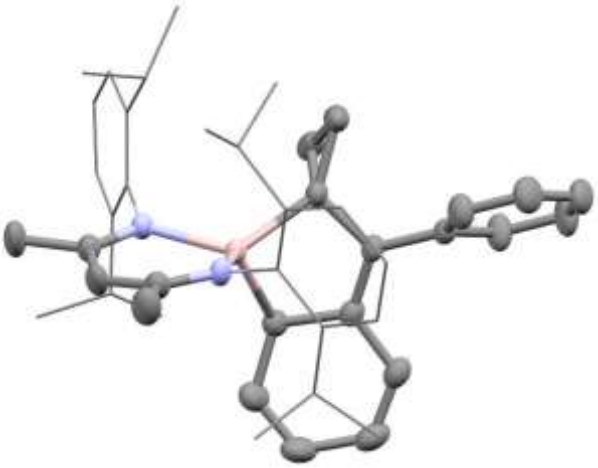


Figure 4.15: The X-ray crystal structure of **4-6a**. Hydrogen atoms and included solvent omitted for clarity.

4-6a was found to crystallise in the space group $P2_1/n$. The included toluene molecule was found to be disordered across two sites in *ca.* 66:34 ratio, and further across a mirror plane (co-planar to the toluene arene ring). The major and minor components were modelled at *ca.* 33% and 17% occupancies respectively (summing to 50.0% occupancy, with the mirror symmetry generating a second pair of ca. 33% and 17% occupancy orientations). The bond-lengths and angles of both orientations were restrained to a sensible model of toluene, their thermal parameters restrained to be similar, and their geometries optimized.

Crystal Data for $C_{48.5}H_{59}AlN_2$: M =696.95, monoclinic, space group $P2_1/n$ (no. 14), a = 11.8493(7) Å, b = 28.2974(14) Å, c = 13.3388(8) Å, β = 114.700(7)°, V = 4063.4(4) Å^3, Z = 4, ρ_{calc}g/cm^3 = 1.139, μ(MoKα) = 0.085 mm^{-1}, T = 173.00(14), orange prisms, F^2 refinement, R_1(obs) = 0.0543, wR_2(all) = 0.1338, 8100 independent observed reflections (R_{int} = 0.0256), 5776 independent measured reflections [$|F_o| > 4\sigma(|F_o|)$, $2\theta_{full}$ = 56.322], 478 parameters. CCDC 1984848.

The X-ray crystal structure of ***4-7a***

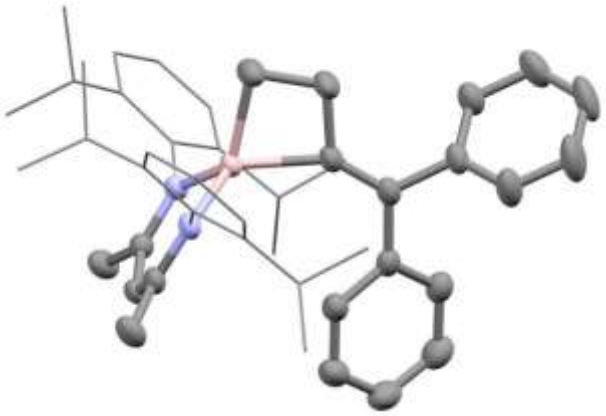


Figure 4.16: The X-ray crystal structure of **4-7a**. One of two independent molecules. Hydrogen atoms omitted for clarity.

4-7a was found to crystallise in the space group $P2_1/c$. Two independent molecules were located within the asymmetric unit (for a total of 8 molecules in the unit cell), suffixed A and B respectively.

Crystal Data for $C_{45}H_{55}AlN_2$: M =650.89, monoclinic, space group $P2_1/c$ (no. 14), a = 16.4712(4) Å, b = 13.2307(3) Å, c = 35.8219(9) Å, β = 97.951(2)°, V = 7731.5(3) Å^3, Z = 8, ρ_{calc}g/cm^3 = 1.118, μ(CuKα) = 0.688 mm^{-1}, T = 172.9(6), light yellow plates, F^2 refinement, R_1(obs) = 0.0451, wR_2(all) = 0.1248, 14875 independent observed reflections (R_{int} = 0.0313), 11852 independent measured reflections [$|F_o| > 4\sigma(|F_o|)$, $2\theta_{full}$ = 147.122], 885 parameters. CCDC 1984849.

The X-ray crystal structure of ***4-7b***

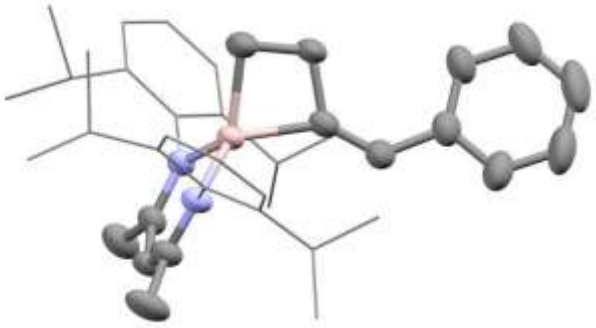


Figure 4.17: The X-ray crystal structure of **4-7b**. Hydrogen atoms, disorder, and included solvent omitted for clarity.

4-7b was found to crystallise in the space group $P2_12_12_1$. The iso-propyl group (C34-C35-C36) was modelled as disordered over two sites in *ca.* 70:30 occupancies for the major and minor orientations respectively. The iso-propyl group (C25-C26-C27) was modelled as disordered over two sites in *ca.* 80:20 occupancies for the major and minor orientations respectively. In both cases, the thermal parameters of major and minor components were restrained to be similar, and only the non-hydrogen atoms in the major orientation were refined anisotropically (those in the minor orientation were refined isotropically).

4-7b crystallises with one toluene molecule in the asymmetric unit. The included toluene molecule was modelled as disordered over two sites in *ca.* 71:29 occupancies for the major and minor orientations respectively. The thermal parameters of adjacent atoms in the major and minor components were restrained to be similar, their geometries optimised, and only the non-hydrogen atoms in the major orientation were refined anisotropically (those in the minor orientation were refined isotropically).

Crystal Data for $C_{46}H_{59}AlN_2$, M =666.93, orthorhombic, space group $P2_12_12_1$ (no. 19), a = 9.67292(16) Å, b = 18.0057(4) Å, c = 23.3938(4) Å, V = 4074.44(13) Å^3, Z = 4, ρ_{calc}g/cm^3 = 1.087, μ(CuKα) = 0.662 mm^{-1}, T = 173.00(10), colourless needles, F^2 refinement, R_1(obs) = 0.0477, wR_2(all) = 0.1343, 6401 independent observed reflections (R_{int} = 0.0384), 5384 independent measured reflections [$|F_o| > 4\sigma(|F_o|)$, $2\theta_{full}$ = 146.974], 489 parameters. CCDC 1984850.

The X-ray crystal structure of ***4-7c***

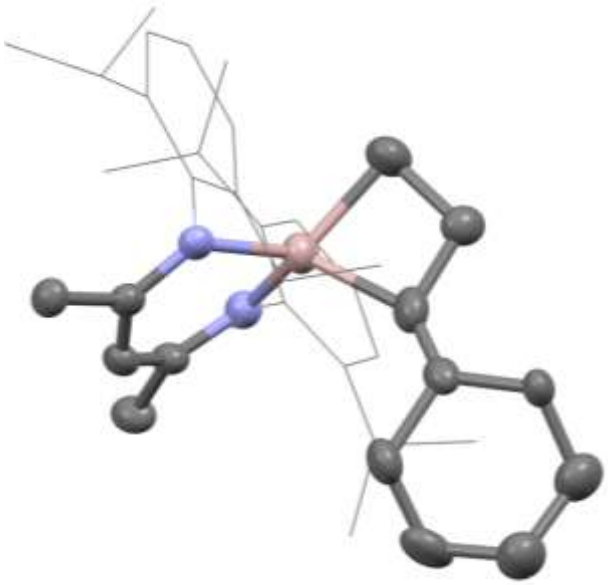


Figure 4.18: The X-ray crystal structure of **4-7c**. One of two independent molecules. Hydrogen and disorder omitted for clarity.

4-7c was found to crystallise in the $Pca2_1$ space group. Two independent molecules were located in the asymmetric unit (for a total of eight in the unit cell), suffixed A and B respectively.

The hydrocarbyl fragment (C2A, C4A>C9A) in molecule A was modelled as disordered over two sites in *ca.* 80:20 occupancies for the major and minor orientations respectively. The two orientations are related by ring-flip isomerisation of the cyclohexyl group (C4A>C9A), and corresponding shift in position for the β-carbon (C2A). The carbon atoms C1A and C3A occupy the same position in both ring conformations and so were not included in the disorder model. The thermal parameters of adjacent atoms in the major and minor components were restrained to be similar, their geometries optimized, and only the non-hydrogen atoms in the major orientation were refined anisotropically (those in the minor orientation were refined isotropically).

The hydrocarbyl fragment (C2B, C4B>C9B) in molecule B was modelled as disordered over two sites in *ca.* 62:38 occupancies for the major and minor orientations respectively. The two orientations are related by ring-flip isomerisation of the cyclohexyl group (C4B>C9B), and corresponding shift in position for the β-carbon (C2B). The carbon atoms C1B and C3B occupy the same position in both ring conformations and so were not included in the disorder model.

The thermal parameters of major and minor components were restrained to be similar, their geometries optimized, and only the non-hydrogen atoms in the major orientation were refined anisotropically (those in the minor orientation were refined isotropically). The di-iso-propylphenyl groups on the β-diketiminate ligand of molecule B were also found to be disordered over two sites in *ca.* 52:48 occupancies for the major and minor orientations respectively. The thermal parameters of adjacent atoms in the major and minor components were restrained to be similar, their geometries optimized, and only the non-hydrogen atoms in the major orientation were refined anisotropically (those in the minor orientation were refined isotropically).

Crystal Data for $C_{38}H_{56}AlN_2$, M =567.82, orthorhombic, space group $Pca2_1$ (no. 29), a = 21.9930(9) Å, b = 19.4948(6) Å, c = 16.2136(4) Å, V = 6951.6(4) Å^3, Z = 8, ρ_{calc}g/cm^3 = 1.085, μ(CuKα) = 0.693 mm^{-1}, T = 174(3), colourless needles, F^2 refinement, R_1(obs) = 0.0894, wR_2(all) = 0.2692, 8818 independent observed reflections (R_{int} = 0.0470), 6350 independent measured reflections [$|F_o| > 4\sigma(|F_o|)$, $2\theta_{full}$ = 146.542], 898 parameters. CCDC 1984851.

The X-ray crystal structure of ***4-8a.DMAP$_2$***

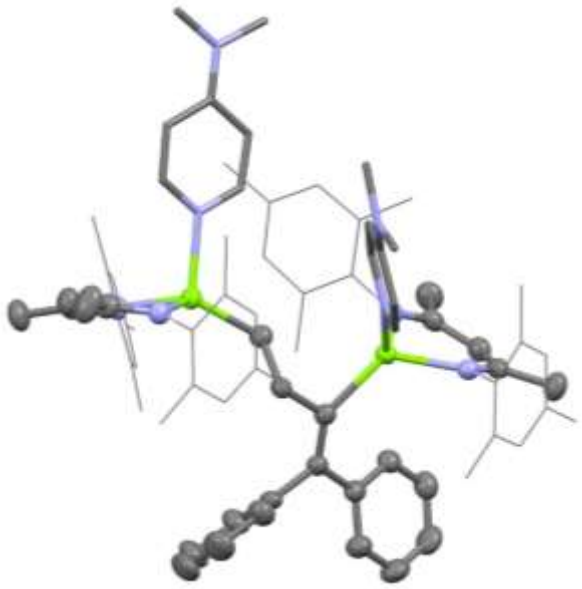


Figure 4.19: The X-ray crystal structure of **4-7.DMAP$_2$**. Hydrogen atoms and included solvent omitted for clarity.

4-8a.DMAP$_2$ was found to crystallise in the P2$_1$/c space group. The included toluene molecule (C77>C83) was modelled as disordered over two sites in *ca.* 51:49 ratio for the major and minor components respectively. The thermal parameters of adjacent atoms in the major and minor components were restrained to be similar, their geometries optimized, and only the non-hydrogen atoms in the major orientation were refined anisotropically (those in the minor orientation were refined isotropically).

The included toluene molecule (C84>C90) was modelled as disordered over two sites in *ca.* 61:39 ratio for the major and minor components respectively. The thermal parameters of adjacent atoms in the major and minor components were restrained to be similar, their geometries optimized, and only the non-hydrogen atoms in the major orientation were refined anisotropically (those in the minor orientation were refined isotropically).

Crystal Data for $C_{90}H_{108}Mg_2N_8$, M =1350.46, monoclinic, space group P2$_1$/c (no. 14), a = 14.4468(6) Å, b = 23.9140(8) Å, c = 23.7719(10) Å, β = 99.507(4)°, V = 8099.9(6) Å^3, Z = 4, ρ_{calc}g/cm^3 = 1.107, μ(MoKα) = 0.078 mm^{-1}, T = 173.00(10), colourless blocks, F^2 refinement, R_1(obs) = 0.0581, wR_2(all) = 0.1645, 16098 independent observed reflections (R_{int} = 0.0234), 10633 independent measured reflections [$|F_o| > 4\sigma(|F_o|)$, $2\theta_{full}$ = 56.642], 943 parameters. CCDC 1984852.

The X-ray crystal structure of ***4-8b.DMAP$_2$***

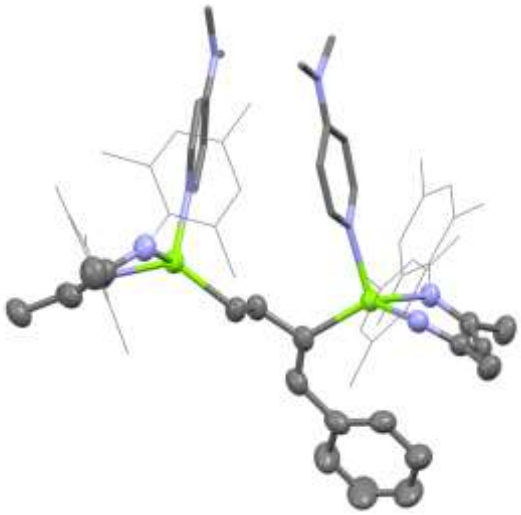


Figure 4.20: The X-ray crystal structure of **4-8b.DMAP$_2$**. Hydrogen atoms, disorder, and included solvent omitted for clarity.

4-8b.DMAP$_2$ was found to crystallise in the P-1 space group. The phenyl group (C5>C10) was modelled as disordered over two sites in *ca*. 62:38 ratio for the major and minor orientations respectively. The thermal parameters of adjacent atoms in the major and minor components were restrained to be similar, their geometries optimized, and only the non-hydrogen atoms in the major orientation were refined anisotropically (those in the minor orientation were refined isotropically).

The included toluene molecule (C71>C77) was modelled as disordered over two sites in *ca.* 66:34 ratio for the major and minor orientations respectively. The thermal parameters of adjacent atoms in the major and minor components were restrained to be similar, their geometries optimized, and only the non-hydrogen atoms in the major orientation were refined anisotropically (those in the minor orientation were refined isotropically).

Crystal Data for $C_{77}H_{96}Mg_2N_8$, M =1182.23, triclinic, space group P-1 (no. 2), a = 12.4127(6) Å, b = 15.6604(7) Å, c = 18.5977(9) Å, α = 83.253(4)°, β = 86.587(4)°, γ = 80.686(4)°, V = 3539.8(3) Å^3, Z = 2, ρ_{calc}g/cm^3 = 1.109, μ(CuKα) = 0.655 mm^{-1}, T = 173.1(2), colourless blocks, F^2 refinement, R_1(obs) = 0.0521, wR_2(all) = 0.1597, 13492 independent observed reflections (R_{int} = 0.0449), 9161 independent measured reflections [$|F_o| > 4\sigma(|F_o|)$, $2\theta_{full}$ = 147.15], 810 parameters. CCDC 1984853.

The X-ray crystal structure of ***4-10***

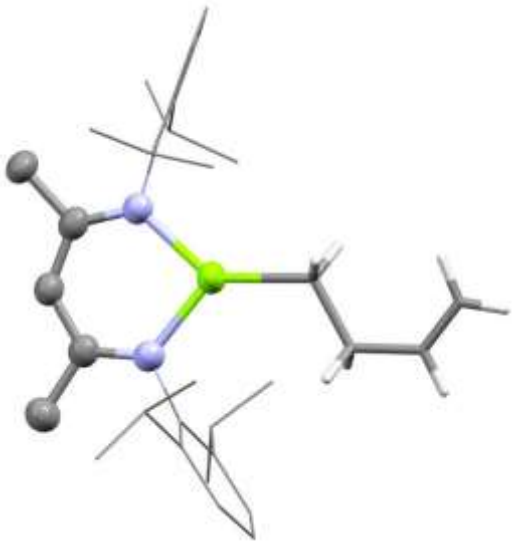


Figure 4.21: The X-ray crystal structure of **4-10**. One of two independent molecules. Hydrogen atoms and disorder omitted for clarity.

4-10 was found the crystallise in the P-1 space group with two independent molecules in the asymmetric unit (for a total of 4 within the unit cell). An isopropyl group (C31A>C33A) in the independent molecule suffixed A was modelled as disordered over two positions in *ca.* 69:31 ratio for the major and minor orientations respectively. The thermal parameters of adjacent atoms in the major and minor components were restrained to be similar, their geometries optimized, and only the non-hydrogen atoms in the major orientation were refined anisotropically (those in the minor orientation were refined isotropically). Attempts were made to model residual electron density around the allyl group (C1A>C3A) as a disordered fragment, however no convincing model could be constructed .

The allyl group (C1B>C3B) in the independent molecule suffixed B was modelled as disordered over two positions in *ca.* 57:43 ratio for the major and minor orientations respectively. An isopropyl group (C28B>C30B) in the independent molecule suffixed A was modelled as disordered over two positions in *ca.* 67:32 ratio for the major and minor orientations respectively. In both cases, the thermal parameters of adjacent atoms in the major and minor components were restrained to be similar, their geometries optimized, and only the non-hydrogen atoms in the major orientation were refined anisotropically (those in the minor orientation were refined isotropically).

Crystal Data for $C_{33}H_{48}MgN_2$, M =497.04, triclinic, space group P-1 (no. 2), a = 8.7189(4) Å, b = 17.8282(6) Å, c = 21.2753(11) Å, α = 74.100(4)°, β = 85.527(4)°, γ = 88.960(4)°, V = 3170.8(3) Å^3, Z = 4, ρ_{calc}g/cm^3 = 1.041, μ(CuKα) = 0.625 mm^{-1}, T = 173.00(14), colourless blocks,

F^2 refinement, R_1(obs) = 0.0671, wR_2(all) = 0.2176, 12099 independent observed reflections (R_{int} = 0.0417), 8173 independent measured reflections [$|F_o| > 4\sigma(|F_o|)$, $2\theta_{full}$ = 147.108], 716 parameters. CCDC 1984854.

Al–N bond Metrics

Metric	4-7a	4-7b	4-7c	4-6a
Al–N (Å)	1.9038(13)	1.891(2)	1.915(6)	1.9139(17)
	1.9124(13)	1.902(3)	1.931(6)	1.9134(16)
	1.9066(14)		1.880(8)*	
	1.9082(13)		1.882(6)*	
N–Al–N (°)	96.96(6)	96.72(11)	97.6(3)	97.43(7)
	96.77(6)		96.3(3)*	

Table 5.5: Comparison of Al–N bond metrics in compounds **4-7a**-**4-7c** and **4-6a.** Data taken from highly disordered fragment.

4.6 – Computational details

DFT calculations were run using Gaussian 09 (Revision D.01)[28] using the M06l Minnesota functional.[29] Al and Mg centres were described with Stuttgart SDDAll pseudopotential and associated basis sets and the 6-31G** basis sets were used for all other atoms. M06l has been previously benchmarked against other functionals (ωB97x, B3PW91, M062x) to provide the best agreement with experimental data.[30,31]

Geometry optimisation calculations were performed without symmetry constraints. Frequency analyses for all stationary points were performed using the enhanced criteria to confirm the nature of the structures as either minima (no imaginary frequency) or transition states (only one imaginary frequency). Single point solvent corrections (benzene, $\varepsilon = 2.2706$) were applied using the polarizable continuum model (PCM) to free energies reported in the main text. Single point dispersion corrections were applied to the free energies to the Minnesota functional (m06l) energies using Grimme's D3 correction.[32]

Intrinsic reaction coordinate (IRC) calculations were used to connect transition states and minima located on the potential energy surface allowing a full energy profile (calculated at 298.15 K, 1 atm) of the reaction to be constructed.[33] Natural Bond Orbital analysis was carried out using NBO 6.0.[34]

4.7 – References

1 M. Murakami and N. Ishida, *J. Am. Chem. Soc.*, 2016, **138**, 13759–13769.
2 B. Wang, M. A. Perea and R. Sarpong, *Angew. Chem., Int. Ed.*, 2020, **59**, 18898–18919.
3 L. Souillart and N. Cramer, *Chem. Rev.*, 2015, **115**, 9410–9464.
4 M. E. O'Reilly, S. Dutta and A. S. Veige, *Chem. Rev.*, 2016, **116**, 8105–8145.
5 P. P. Power, *Nature*, 2010, **463**, 171–177.
6 J. G. M. Morton, M. A. Dureen and D. W. Stephan, *Chem. Commun.*, 2010, **46**, 8947–8949.
7 Z.-Y. Zhang, Z.-Y. Liu, R.-T. Guo, Y.-Q. Zhao, X. Li and X.-C. Wang, *Angew. Chem., Int. Ed.*, 2017, **56**, 4028–4032.
8 H. Suzuki, N. Tokitoh and R. Okazaki, *J. Am. Chem. Soc.*, 1994, **116**, 11572–11573.
9 D. Wendel, A. Porzelt, F. A. D. Herz, D. Sarkar, C. Jandl, S. Inoue and B. Rieger, *J. Am. Chem. Soc.*, 2017, **139**, 8134–8137.
10 L. Zhu, J. Zhang and C. Cui, *Inorg. Chem.*, 2019, **58**, 12007–12010.
11 L. L. Liu, J. Zhou, L. L. Cao, R. Andrews, R. L. Falconer, C. A. Russell and D. W. Stephan, *J. Am. Chem. Soc.*, 2018, **140**, 147–150.
12 K. Koshino and R. Kinjo, *J. Am. Chem. Soc.*, 2020, **142**, 9057–9062.
13 W. D. Jones, in *C-C Bond Activation*, ed. G. Dong, Springer Berlin Heidelberg, Berlin, Heidelberg, 2013, vol. 346, pp. 1–31.
14 C. Bakewell, M. Garçon, R. Y. Kong, L. O'Hare, A. J. P. White and M. R. Crimmin, *Inorg. Chem.*, 2020, **59**, 4608–4616.
15 C. Bakewell, A. J. P. White and M. R. Crimmin, *Chem. Sci.*, 2019, **10**, 2452–2458.
16 S. Jain and K. Vanka, *Chem. Eur. J.*, 2017, **23**, 13957–13963.
17 A. J. Boutland, A. Carroll, C. Alvarez Lamsfus, A. Stasch, L. Maron and C. Jones, *J. Am. Chem. Soc.*, 2017, **139**, 18190–18193.
18 D. Dange, A. R. Gair, D. D. L. Jones, M. Juckel, S. Aldridge and C. Jones, *Chem. Sci.*, 2019, **10**, 3208–3216.
19 M. Rauch, S. Ruccolo and G. Parkin, *J. Am. Chem. Soc.*, 2017, **139**, 13264–13267.
20 L. Garcia, C. Dinoi, M. F. Mahon, L. Maron and M. S. Hill, *Chem. Sci.*, 2019, **10**, 8108–8118.
21 C. Cui, H. W. Roesky, H.-G. Schmidt, M. Noltemeyer, H. Hao and F. Cimpoesu, *Angew. Chem., Int. Ed.*, 2000, **39**, 4274–4276.
22 S. J. Bonyhady, C. Jones, S. Nembenna, A. Stasch, A. J. Edwards and G. J. McIntyre, *Chem. Eur. J.*, 2010, **16**, 938–955.
23 C. Liu, Y.-J. Yang, J.-Y. Dong, M.-D. Zhou, L. Li and H. Wang, *J. Org. Chem.*, 2019, **84**, 9937–9945.
24 I. R. Ramazanov, R. N. Kadikova, T. P. Zosim, U. M. Dzhemilev and A. de Meijere, *Eur. J. Org. Chem.*, 2017, **2017**, 7060–7067.
25 H. Xie and B. Xu, *Eur. J. Org. Chem.*, 2016, **2016**, 2594–2598.
26 J. R. Salaun, J. Champion and J. M. Conia, *Org. Synth.*, 1977, **57**, 36.
27 J. Seliger, X. Dong and M. Oestreich, *Angew. Chem., Int. Ed.*, 2019, **58**, 1970–1974.
28 Frisch, M. J.; Trucks, G. W.; Schlegel, H. B.; Scuseria, G. E.; Robb, M. A.; Cheeseman, J. R.; Scalmani, G.; Barone, V.; Mennucci, B.; Petersson, G. A.; Nakatsuji, H.; Caricato, M.; Li, X.; Hratchian, H. P.; Izmaylov, A. F.; Bloino, J.; Zheng, G.; Sonnenberg, J. L.; Hada, M.; Ehara, M.; Toyota, K.; Fukuda, R.; Hasegawa, J.; Ishida, M.; Nakajima, T.; Honda, Y.; Kitao, O.; Nakai, H.; Vreven, T.; Montgomery, J. A., Jr.; Peralta, J. E.; Ogliaro, F.; Bearpark, M.; Heyd, J. J.; Brothers, E.; Kudin, K. N.; Staroverov, V. N.; Kobayashi, R.; Normand, J.; Raghavachari, K.; Rendell, A.; Burant, J. C.; Iyengar, S. S.; Tomasi, J.; Cossi, M.; Rega, N.; Millam, J. M.; Klene, M.; Knox, J. E.; Cross, J. B.; Bakken, V.; Adamo, C.; Jaramillo, J.; Gomperts, R.; Stratmann, R. E.; Yazyev, O.; Austin, A. J.; Cammi, R.; Pomelli, C.; Ochterski, J. W.; Martin, R. L.; Morokuma, K.; Zakrzewski, V. G.; Voth, G. A.; Salvador, P.; Dannenberg, J. J.; Dapprich, S.; Daniels, A. D.; Farkas, Ö.; Foresman, J. B.; Ortiz, J. V.; Cioslowski, J.; Fox, D. J. Gaussian~09 Revision E.01. Gaussian, Inc., Wallingford, CT 2009.
29 Y. Zhao and D. G. Truhlar, *Theor. Chem. Acc.*, 2008, **120**, 215–241.

30 T. N. Hooper, M. Garçon, A. J. P. White and M. R. Crimmin, *Chem. Sci.*, 2018, **9**, 5435–5440.
31 R. Y. Kong and M. R. Crimmin, *Chem. Commun.*, 2019, **55**, 6181–6184.
32 S. Grimme, J. Antony, S. Ehrlich and H. Krieg, *J. Chem. Phys.*, 2010, **132**, 154104.
33 H. P. Hratchian and H. B. Schlegel, in *Theory and Applications of Computational Chemistry*, eds. C. E. Dykstra, G. Frenking, K. S. Kim and G. E. Scuseria, Elsevier, Amsterdam, 2005, pp. 195–249.
34 Gleadening, E. D.; Bakenhoop, J. K.; Reed, A. E.; Carpenter, J. E.; Bohmann, J. A.; Morales, C. M.; Landis, C. R.; Weinhold, F. NBO 6.0. Theoretical Chemistry Institute, University of Wisconsin, Madison 2013.

Chapter 5

Chemoselective C–C σ-Bond Activation of the Most Stable Ring in Biphenylene

5.1 – Introduction to Arene Activation

5.1.1 – Aromaticity and anti-aromaticity

Aromaticity is a key concept within chemistry. Several criteria exist to establish aromaticity: i) all atoms must be coplanar, ii) the atoms must have a conjugated π-system, iii) an even number of π-electrons that is even but not a multiple of 4 (commonly known as the 4n+2 rule or Huckel's rule). Delocalisation of electrons into the π-manifold of an aromatic ring is highly stabilising. For example, it is estimated that benzene rings are stabilised by 36 kcal mol^{-1} due to aromaticity.‡‡‡

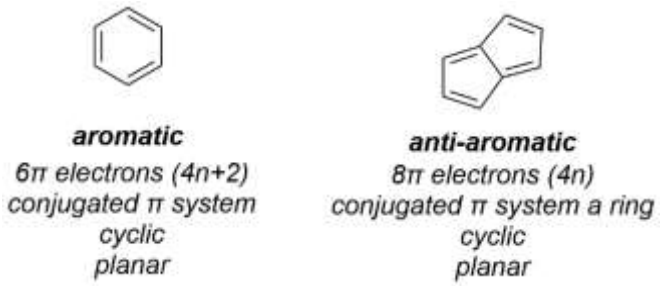


Figure 5.1: Examples of typical aromatic and anti-aromatic compounds.

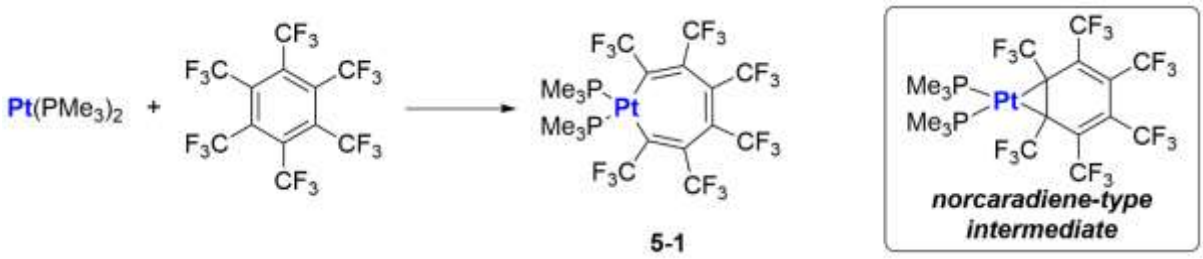
Conversely, for systems which satisfy the first two criteria (coplanarity and π-conjugation) but have a number of π-electrons that is a multiple of 4 (i.e. 4n), the resultant ring system is said to be 'anti-aromatic'. Anti-aromaticity is a destabilising effect. Consequently, anti-aromatic cyclic ring systems will distort to disrupt the anti-aromaticity. For example, the ground state structure of cyclobutadiene has been calculated to be rectangular (as opposed to square) with minimal π-delocalisation.[1] Anti-aromatic structures are typically highly reactive and react to disrupt their anti-aromaticity, either through $2e^-$ oxidation/reduction to attain aromaticity or through reaction at the ring-system to disrupt their π-delocalisation.

5.1.2 – Arene activation

The difficulties associated with the activation of C–C bonds (see Chapter 5.1.2) are compounded by the stability afforded to arene rings through aromaticity in the context of arene cleavage. The C–C activation of 6-membered aromatic rings is highly challenging. Nevertheless, the ability to convert aromatic rings into acyclic alkenes would greatly ameliorate processing of crude chemical feedstocks. Furthermore, the selective cleavage of arene rings would provide access to highly novel disconnections in the retrosynthesis of complex organic molecules. Several stoichiometric strategies have been developed to functionalise 6-membered arene rings.

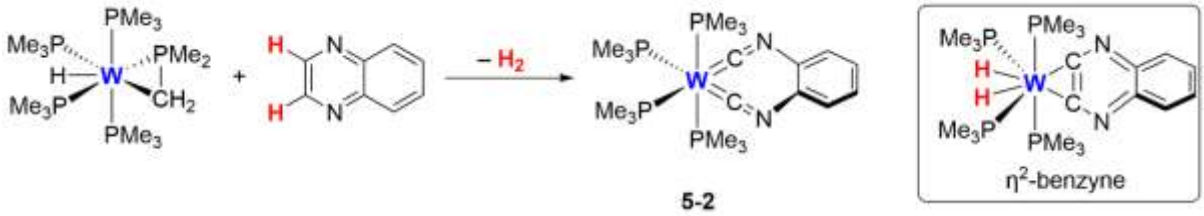
‡‡‡ Estimated by comparing the change in enthalpy upon hydrogenating one molecule of benzene to cyclohexane to hydrogenating three molecules of cyclohexene to cyclohexane.

The first example of insertion of a metal centre into an arene ring was reported by Stone and co-workers in 1975. In this reaction, a platinum(0) complex [$Pt(PMe_3)_2$] inserted into the highly electron deficient arene $C_6(CF_3)_6$ to form the metallacycloheptatriene **5-1** (Scheme 5.1).[2] The reaction is proposed to proceed through a norcaradiene-type intermediate (Scheme 5.1 inset). Similar reactivity to [$Pt(PMe_3)_2$] may be achieved through reaction of the trinuclear [$Pt_3(CN^tBu)_6$] cluster with $C_6(CF_3)_6$, however insertion into the arene was not observed with [$Pt(PEt_3)_2$]. The reaction is related to subsequent reports of silylene and aluminyl insertion into arene rings (See Chapter 5.1.2).



Scheme 5.1: Insertion of Pt (0) into an electron-deficient arene. Inset: structure of the proposed norcaradiene intermediate.

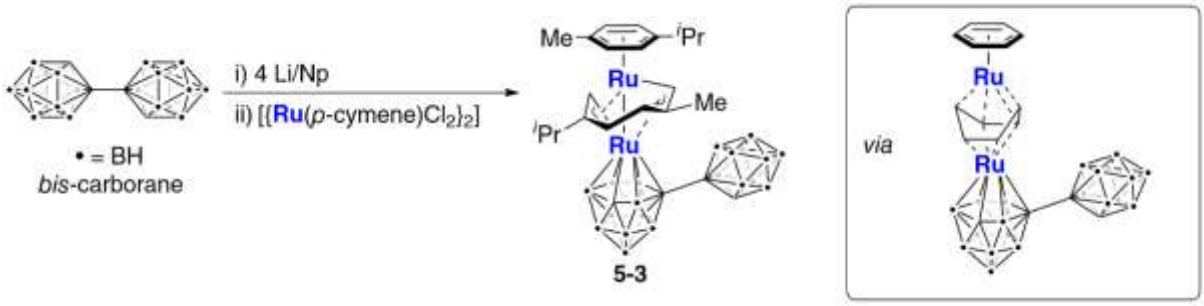
In 2010 Sattler and Parkin reported the cleavage of quinoxaline with a tungsten complex to form a bis-alkylidene complex **5-2** (Scheme 5.2). The bis-alkylidene ligand is derived from the dehydrogenation and C–C cleavage of the quinoxaline ring. The reaction does not occur with an analogous molybdenum complex; an η^6-arene complex is formed instead. The reaction was proposed to proceed through two successive C–H activation steps of quinoxaline to form a η^2-benzyne intermediate (Scheme 5.2 inset). Reductive elimination of dihydrogen, and a ring-opening reaction resulted in the product **5-2**.



Scheme 5.2: C–C activation of quinoxaline by a tungsten complex. Insert: proposed η^2-benzyne intermediate.

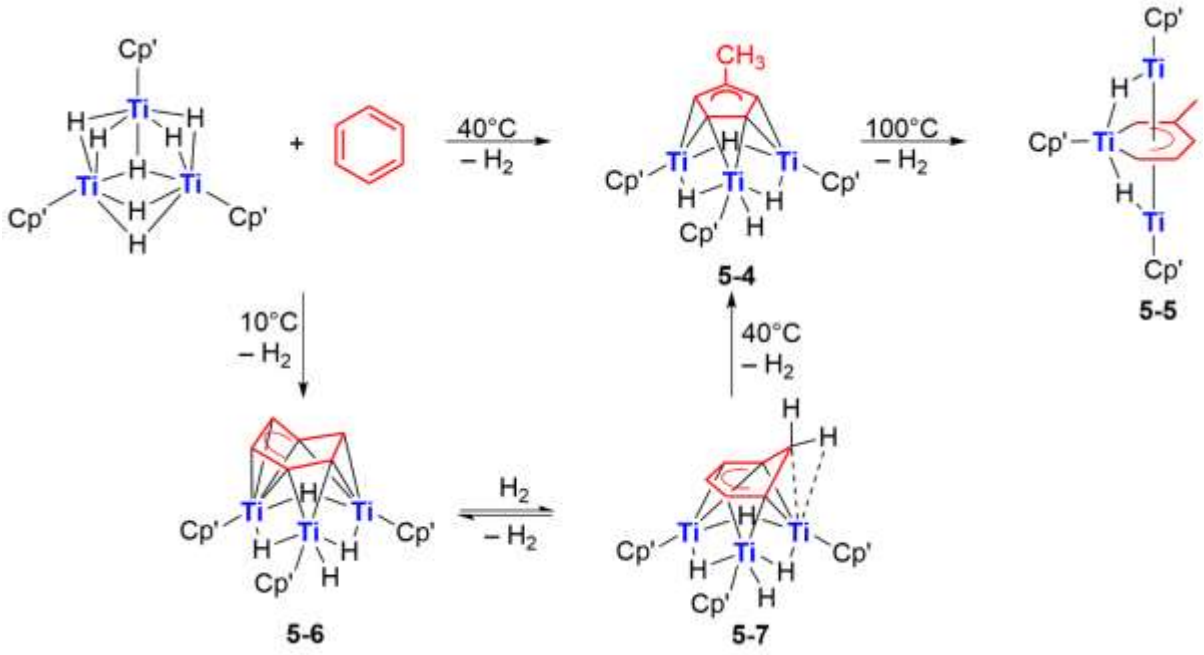
In the same year, Macgregor, Welch, and co-workers reported the room-temperature cleavage of an arene with a metallacarborane (Scheme 5.3).[3] Reduction of a *bis*-carborane precursor with lithium, followed by addition of [Ru(*p*-cymene)Cl(μ-Cl)]$_2$ resulted in formation of **5-3**. In this complex, the *p*-cymene derived ligand bridges two ruthenium centres and is bound at each centre as an η^1-alkyl:η^3-allyl complex. The two ruthenium centres share a metal–metal bond. DFT calculations on a simplified benzene system suggest that the C–C cleavage step proceeded

from a key intermediate in which the reduced arene bridges two ruthenium centres in η^2:η^2 and η^4 fashion (Scheme 5.3, inset) and is in a boat conformation. The intermediate has been drawn as represented in the manuscript, and there is some ambiguity in assigning single and double bonds to the arene. Regardless, C–C bond scission was calculated to evolve from this intermediate to form a benzene analogue of the observed product.



Scheme 5.3: C–C activation of *p*-cymene at ruthenium centres.

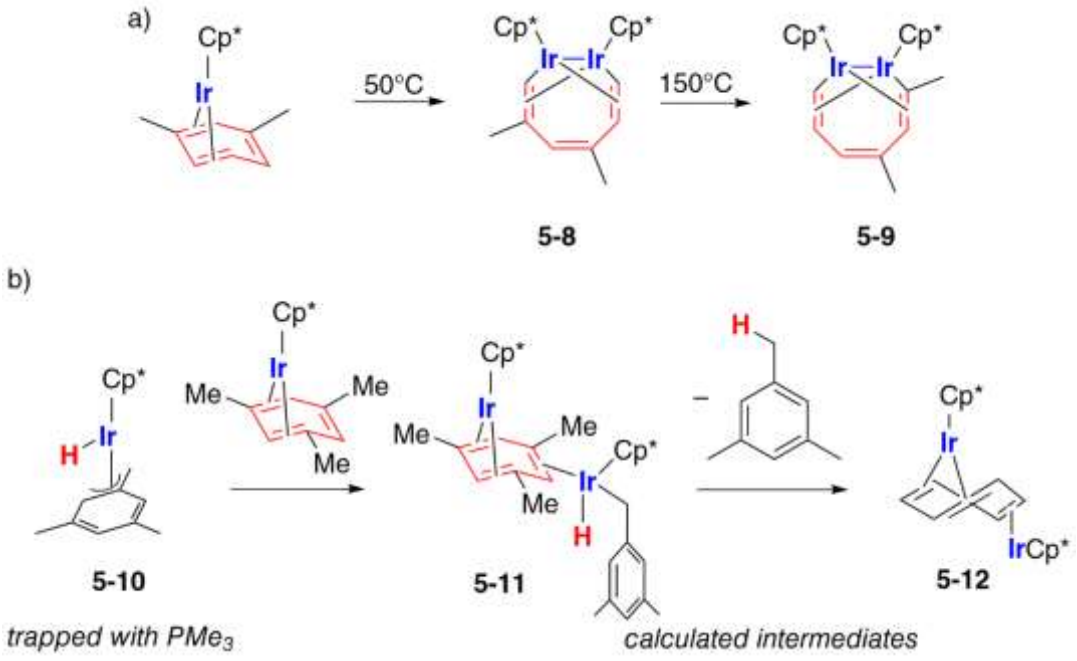
In 2014, Hou and co-workers reported the cleavage of benzene using a tri-titanium heptahydride cluster [$Ti_3H_7Cp'_3$] (Cp' = $C_5Me_4SiMe_3$).[4] Remarkably, intermediates *en route* to arene C–C cleavage were observed and spectroscopically characterised. Hence, reaction of the titanium heptahydride cluster with benzene at 40°C results in the formation of **5-4**. **5-4** features a methylcyclopentene moiety bridging three titanium centres. ^{13}C labelling experiments showed that the methycyclopentene moiety is derived from the successive C–C activation and ring-contraction of benzene. Further thermolysis of **5-4** at 100°C results in a second C–C activation reaction to form **5-5** which contains a methylpentenyl ligand bridging three titanium centres.



Scheme 5.4: Cleavage of benzene with a trinuclear titanium heptahydride complex. Cp' = $C_5Me_4SiMe_3$.

Reaction of the tri-titanium heptahydride cluster with benzene at low temperature (10°C) resulted in isolable crystals of **5-6** along with concomitant formation of **5-4**. The benzene ligand in **5-6** takes the form of a $\{C_6H_6\}^{4-}$ ligand and bridges three titanium centres. While heating solutions of **5-6** did not result in the formation of **5-4** directly, reaction of **5-6** with an atmosphere of dihydrogen resulted in the clean formation of **5-7** which is observable by ^{1}H NMR spectroscopy. **5-7** is observed to convert to **5-4** and is proposed to form *in situ*.

Over a series of reports between 2017 and 2021, Sergeev and co-workers reported the insertion of an Ir(I) pentamethylcyclopentadienyl complex into the C–C bond of arenes to form bimetallacyclooctatrienes (Scheme 5.5) .[5–7] The substrate scope was limited to substituted arene rings with a minimum of one methyl group: the activation of benzene was not observed. The kinetic product of the insertion of iridium into the arene ring was shown to be reversible in the case of *m*-xylene: heating at 50°C resulted in formation of **5-8**, while prolonged heating of **5-8** resulted in formation of the isomeric **5-9**.



Scheme 5.5: Arene C–C cleavage by an Ir(I) complex.

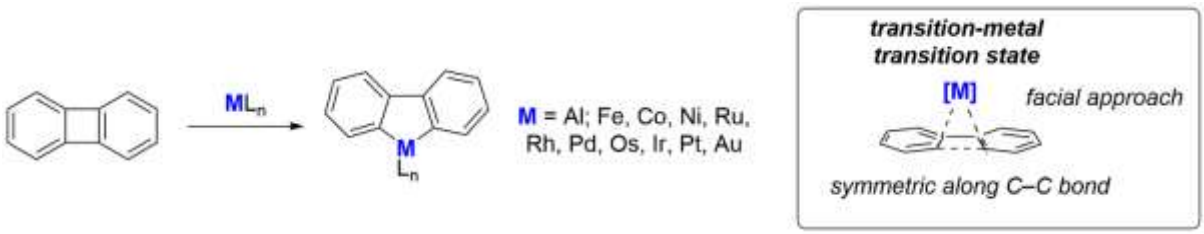
The mechanism for this transformation was uncovered using a combination of DFT, kinetics, trapping experiments, and isotope labelling. The reaction was found to proceed *via* a key-benzylic C–H activation step to form an Ir(III) intermediate. This pathway explains the strict requirement for at least one methyl group in the arene. When the reaction was performed with 1,3,5-trimethylbenzene the formation of **5-10** is observed, this intermediate could be trapped by addition of PMe_3. **5-10** was proposed to combine with a second equivalent of the Ir(I) fragment to form a bimetallic arene bridged complex, **5-11**. **5-11** proceeded to lose an

equivalent of 1,3,5-trimethylbenzene to form **5-12** in which the arene adopts a twist-boat conformation and bridges two iridium centres. The C–C cleavage step proceeded from this intermediate and following a series of skeletal rearrangements resulted in the observed products.

The reports detailed herein largely summarise efforts to functionalise arene rings. While there are examples of ring contraction and expansion, the direct insertion of metals into arene rings is a difficult transformation.[8,9] Several themes emerge from the strategies explored: i) aromaticity is disrupted early in the reaction pathway *via* reduction of the arene by a metal-based reductant, ii) use of more than one metal can stabilise the resultant reduced arene ring through multiple chelation, and iii) bimetallic strategies typically chelate the arene ring on both faces.

5.1.3 – Biphenylene

Biphenylene is a tricyclic hydrocarbon in which two arene rings flank a central 4-membered ring in 1,2-fashion. While aromaticity contributes to the stability of the two arene rings, the central ring is conformationally locked and is anti-aromatic. Both the ring-strain and anti-aromaticity of the 4-membered ring destabilise it. As a result, the central C–C bond is weakened. The bond formation enthalpy of biphenylene is lower ($\Delta H_f°$ = 65.4 kcal mol^{-1}) than that of biphenyl ($\Delta H_f°$ = 114.4 kcal mol^{-1}).



Scheme 5.6: Reactivity of biphenylene with a range of metal centres.

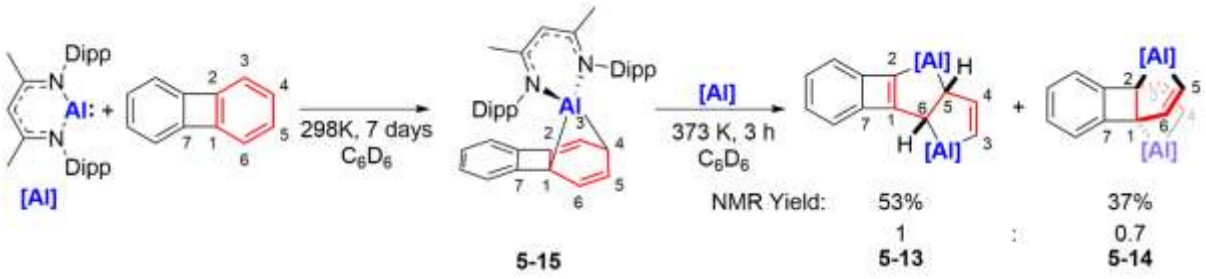
The central 4-membered ring renders biphenylene a biased substrate towards C–C activation. The first conclusive demonstration of the oxidative addition of a transition-metal to biphenylene was reported in 1985 by Eisch and co-workers.[10] In this report, reaction of [Ni(cod)$_2$] with biphenylene in the presence of PEt$_3$ resulted in C–C activation of biphenylene. The oxidative addition of a range of transition metal complexes to the central ring of biphenylene has since been studied in great detail (Scheme 5.6) and reviewed recently.[10–15]

Computational studies on the C–C activation of biphenylene reveal that the reaction proceeds through a single transition state (Scheme 5.6, inset). Both iridium and nickel have been calculated to approach the biphenylene from one face of the planar biphenylene substrate, and the geometry of the transition state exhibits essentially equidistant M–C distances, suggesting a concerted, synchronous event (Scheme 5.6, inset).[16,17]

5.2 – Results and Discussion

5.2.1 – Reaction of [Al] with biphenylene

The reaction of 2 equiv. of **[Al]** with biphenylene at 100°C for 3 h yields a mixture of **5-13** and **5-14** in a 1:0.7 ratio (Scheme 2). **5-13** and **5-14** are derived from the cleavage of the C^2–C^3 and C^4–C^5 bonds in biphenylene respectively. Both products incorporate metallacycles in which aluminium(III) centres are in 5-membered rings. **5-13** crystallised readily from a concentrated toluene or THF solution of the reaction mixture at –35°C. **5-14** can be separated from **5-13** by extraction with THF and purified by recrystallising from toluene. Heating isolated samples of either **5-13** or **5-14** resulted in their decomposition and no interconversion was observed between these two compounds in either purified or crude mixtures.



Scheme 5.7: Reaction of **[Al]** with biphenylene. Dipp = 2,6-di-iso-propylphenyl.

Repeating the reaction of **[Al]** with biphenylene at lower temperatures allowed the isolation of a reaction intermediate. After 7 days at 25°C addition of **[Al]** to biphenylene yields **5-15** as a major product (Scheme 5.7). **5-15** is derived from a (4 + 1) cycloaddition of **[Al]** to the C^1 and C^4 positions of an arene ring of biphenylene. Based on cross-over experiments, the formation of **5-15** is, at least, partially reversible (See Section 5.4.3 for further details). The formation of **5-15** can be explained by a pericyclic reaction, specifically a (4 + 1) cycloaddition.[18–21] Formation of **5-15** generates a highly strained and dearomatised hydrocarbon framework that is primed for further reactivity. Addition of a further equiv. of **[Al]** to **5-15** and heating to 100°C generates the **5-13** and **5-14** with similar yields and selectivity to that observed directly from **[Al]** and biphenylene.

5.2.2 – Spectroscopic data and solid state structures

Compounds **5-13**, **5-14**, and **5-15** have all been characterised by solution NMR and by X-ray crystallography. The X-ray crystal structure of **5-13** is disordered across two special positions (See Section 5.5.4 for detailed discussion). Nevertheless, the connectivity for **5-13** can be extracted from the X-ray data. The solid-state structure supports the assignment of the C^5–C^6 fragment of **5-13** as a *cis*-fused ring junction. This has been confirmed by 1D NOE experiments.

Characteristic alkene signals are observed for the protons attached to C^3 and C^4 resonate at δ = 5.32 and 7.44 ppm respectively in the ^{1}H NMR spectrum of **5-13**.

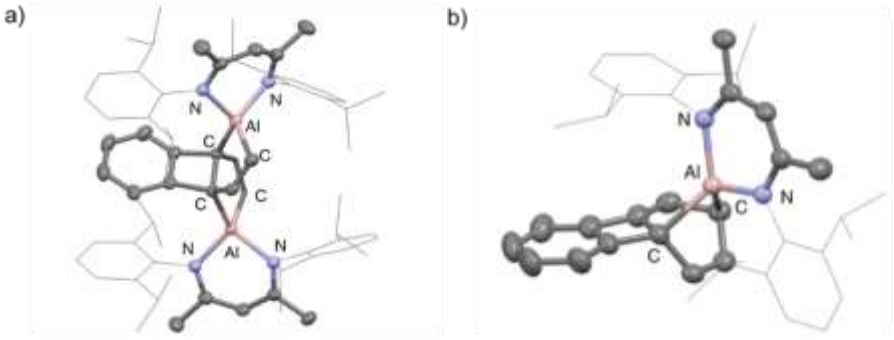


Figure 5.2: X-ray structures of a) **5-14** and b) **5-15**.

The X-ray structure of **5-14** clearly shows the rupture of the aromatic ring. The aluminium centres of **5-14** are related by C_2-rotation around the perpendicular bisector of the C^1–C^2 bond. This compound again contained two contiguous stereocentres, now at the C^1 and C^2 positions, which impose a *trans*-fused ring junction and C_2-symmetry (Figure 5.2). Characteristic alkene signals for the protons attached to C^5 and C^6 (and their symmetry related counterparts C^3 and C^4) in **5-14** resonate at δ = 5.87 and 7.41 ppm respectively in the ^{1}H NMR spectrum.

The X-Ray crystal structure of **5-15** shows the aluminium centre bound to biphenylene at the apical position of a metallanorbornadiene ring. C–C bond lengths of the ring identify that the coordinated arene has been reduced to a 1,4-diene.

5.2.3 – DFT study of the mechanism

DFT calculations were used to explore the mechanism of C–C σ-bond activation (Figure 5.3).[22,23] The (4 + 1) cycloaddition of **[Al]** to biphenylene was found to proceed *via* a single transition-state **TS-1** ($\Delta G^{\ddagger}_{298K}$ = 28.5 kcal mol^{-1}) and forms **5-15** directly. Disruption of the anti-aromaticity of the central ring of biphenylene likely determines the selectivity of the (4 + 1) addition. NICS calculations show that this ring has less anti-aromatic character in **5-15** (NICS(0) = 5.3) than in biphenylene itself (NICS(0) = 18.3) (Figure 5.3, Figure 5.4).

Intermediate **5-15** has two chemically distinct alkene systems. **[Al]** has previously been shown to perform (2 + 1) cycloadditions with alkenes.[24–27] Addition of **[Al]** to the more substituted alkene (C^2=C^3) of **5-15** was found to proceed *via* a low energy transition state **TS-2** to form **Int-1**.[27,28] **Int-1** is the product of an overall 4e$^-$ reduction of the arene ring of biphenylene with two equiv. of **[Al]**. **Int-1** incorporates two aluminium centres at the bridgehead positions of a norbornane (Al^A) and norcarane (Al^B) skeleton on opposite faces of the reduced arene ring.

Subsequent isomerisation of **Int-1** to **Int-2** occurs *via* transition state **TS-3**. This reaction involves a concerted rearrangement of the ring framework of **Int-1** with two four-membered metallacycles forming from one three-membered and one five-membered metallacycle (Figure 5.5a). The relief of strain from the ring-expansion of the aluminacyclopropane is the likely thermodynamic driving force of this reaction.

The calculated energies reported at this level of theory suggest (see Section 5.6 for details) that **Int-2** should be the isolable species. The trend of calculated energies reported is consistent across several different functionals (see Section 5.6.1 for further details). Regardless, the formation of **5-15** is consistently observed experimentally with no other isolable products other than **5-13** and **5-14**. The calculated energies will have some degree of error – especially in a step where two molecular fragments combine and accurate consideration of both entropy and dispersion contributions is required. The discrepancy between the isolable intermediate and computationally suggested intermediate likely arises from this error.

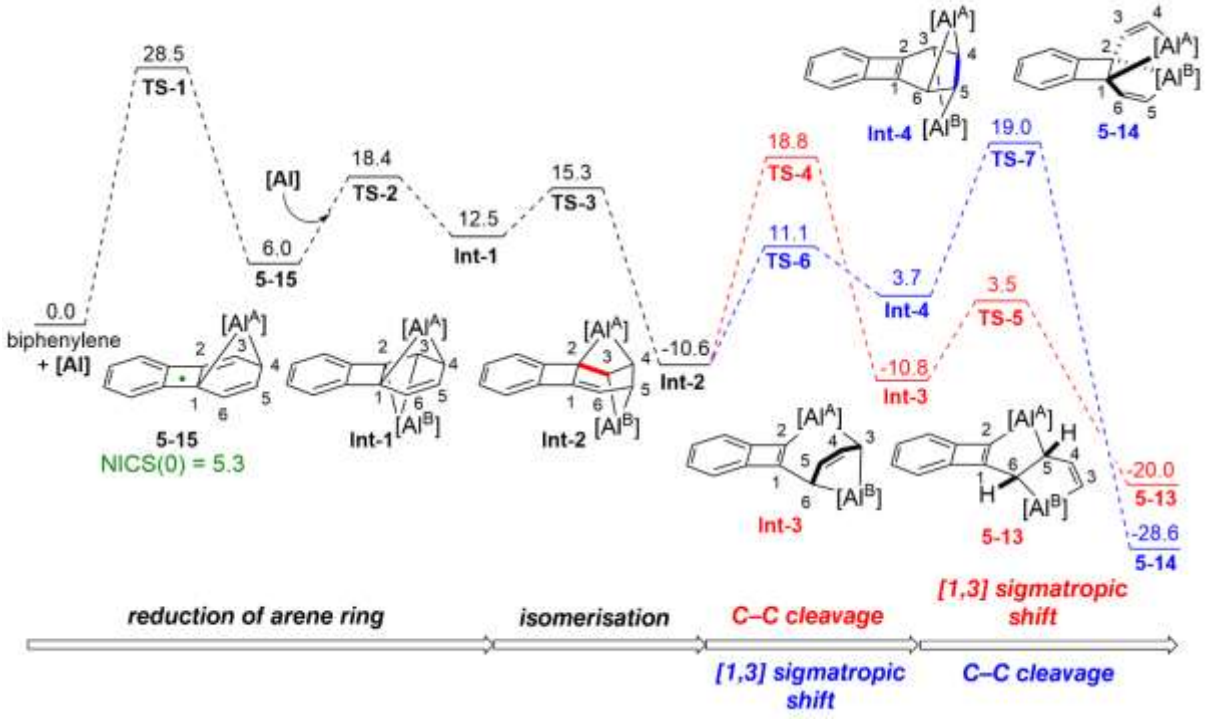


Figure 5.3: DFT calculated pathway towards the formation of **5-13** and **5-14**. Energies in kcal mol^{-1}.

From **Int-2** C–C σ-bond activation can occur by two different pathways. These pathways both involve a [1,3]-sigmatropic shift and a step that breaks the C–C σ-bond, however the order of these processes differs between the two. C^2–C^3 σ-bond activation is possible directly from **Int-2** *via* **TS-4** to form **Int-3**. **TS-4** is an early transition state in which a key bond cleavage step triggers a series of bond migrations to form **Int-3**. A subsequent [1,3]-sigmatropic shift of [Al^A] along the C^3---C^5 allyl system *via* **TS-5** results in formation of the observed product **5-13**.

Alternatively, [Al^A] can perform a [1,3]-sigmatropic shift along the C^2---C^6 allyl system in **Int-2** *via* **TS-6** to form **Int-4**. The aluminium centres in **Int-4** are related by C_2-rotation around the perpendicular bisector of the C^4–C^5 bond and this symmetry is preserved into the product. Activation of the C^4–C^5 σ-bond from **Int-4** occurs *via* **TS-7** and resulted in formation of **5-14**.

NBO analysis was used to explore the mechanism more deeply. The nucleophilicity of **[Al]** and reduction of the arene ring are the key driving force to the installation of aluminium centres. Both **TS-1** and **TS-2** show electron transfer from **[Al]** to the substrate (NPA charges for the Al centre: 1.85 in **TS-1**, and 1.57 in **TS-2** vs 0.78 in **1** Figure 5.4b).

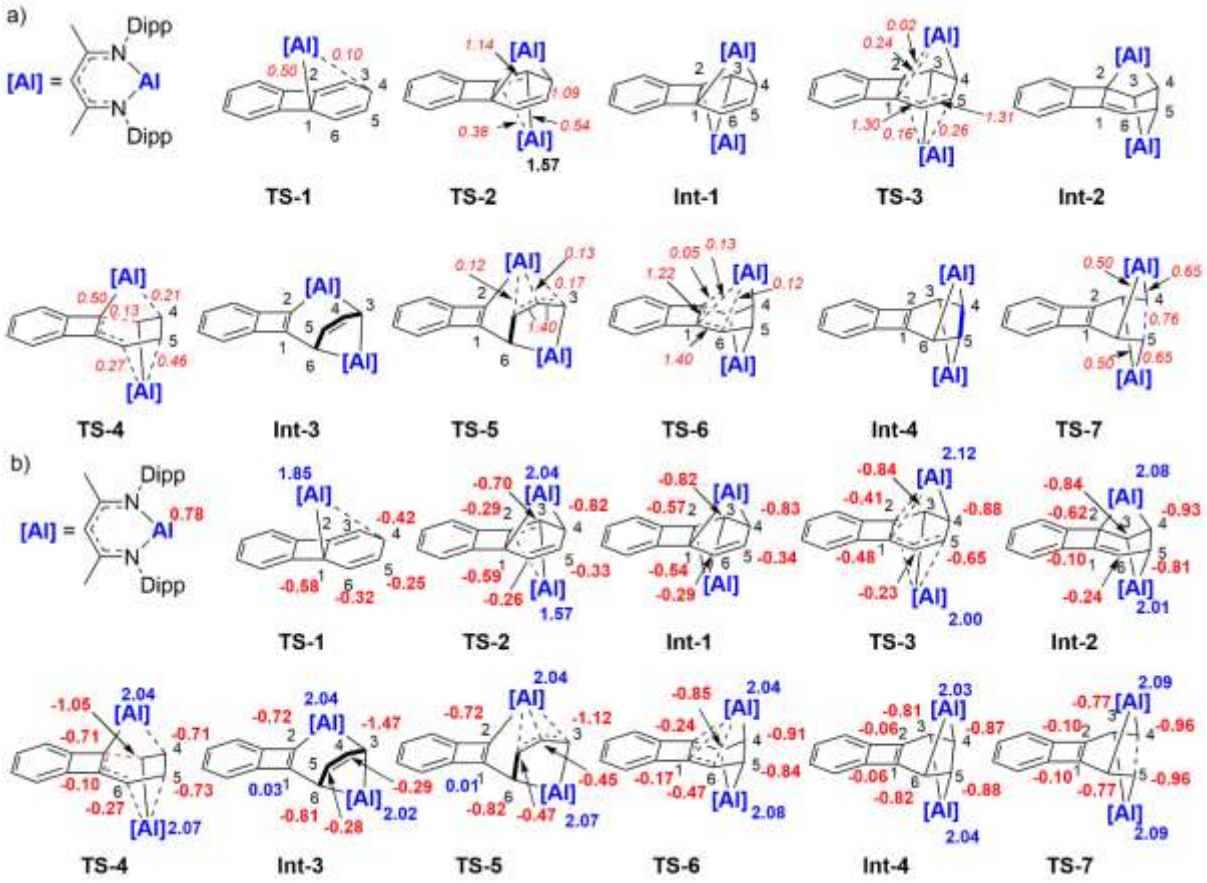


Figure 5.4: NBO data of all transition states, intermediates, and **[Al]**. Some intermediates provided for reference. a) Wiberg bond indices provided in *italics*, and b) natural charges provided in **bold**.

The 1,3-sigmatropic shift of the aluminium centres along an allyl system (**TS-5**, **TS-6**) is highly reminiscent of the analogous transition metal reactivity. Analysis of the Wiberg bond indices (WBI) of both **TS-5** and **TS-6** show that the Al(III) centres have significant bonding interactions with the central carbon of the allyl system at the transition state geometry. This is particularly notable as there is no bond between the migrating aluminium centre and the central allyl carbon in the stationary points associated with the transition states. The transition state geometries are reminiscent of transition-metal π-allyl complexes. However, the reaction

demonstrated here is concerted and proceeds *via* a η^3-π-allyl transition state, rather than through a defined π-allyl complex intermediate.

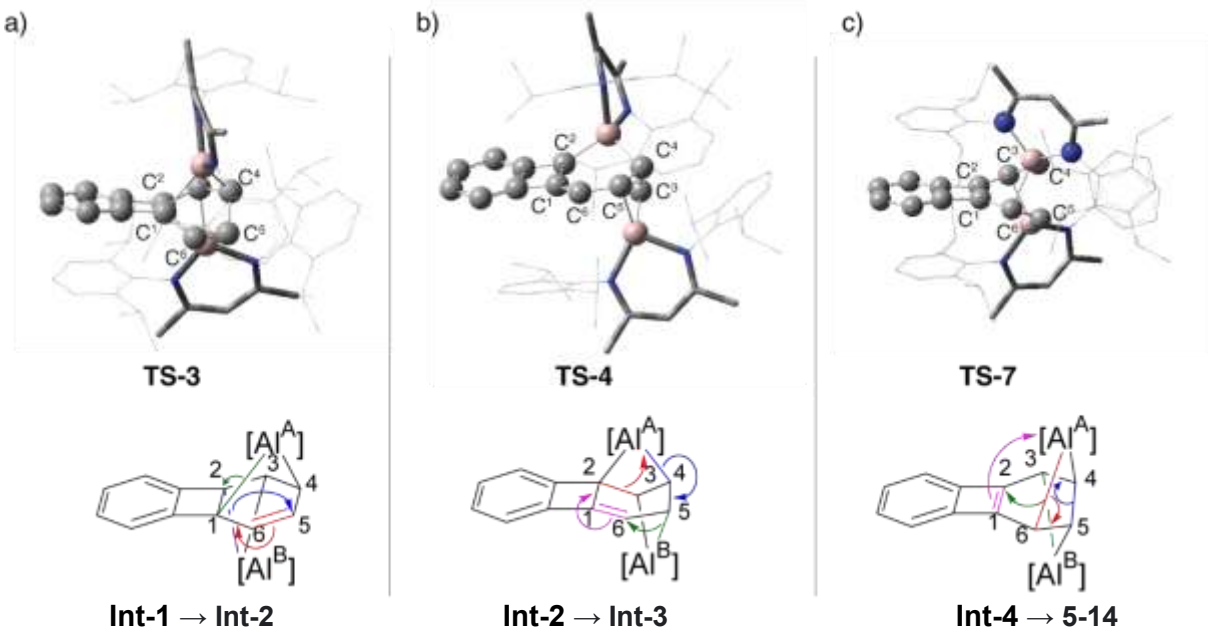


Figure 5.5: Structures of key transition states **TS-3** (a), **TS-4** (b), and **TS-7** (c) alongside the arrow-pushing formalism.

The C–C activation step (**TS-4**, **TS-7**) proceeded from intermediates (**Int-3**, **Int-5**) where both aluminium(III) centres occupy positions in metallacyclobutane rings (Figure 5.5b,c). The C–C bonds which are cleaved in the reaction are also constituents of the metallacyclobutane rings. As a result, the relief of ring strain from these highly strained rings is a thermodynamic driving force for the C–C cleavage reaction and subsequent isomerisations. This is reflected in the early transition-state. In both **TS-4** and **TS-7** aluminium centres occupy similar positions on the hydrocarbon manifold as the preceding intermediates (**Int-3** and **Int-5** respectively). Analysis of the WBI reflects this as the bonding is substantively similar with the exception of the broken C–C bond. Taken together, the transition states evolve from an initial C–C activation event followed by subsequent bond migrations to form the observed products.

5.2.4 – DFT study of alternate pathways

Several alternate mechanisms were considered. The (4 + 1) cycloaddition of **[Al]** to the C^3 and C^6 positions of biphenylene was also explored computationally to form **5-15'**, a regioisomer of **5-15** (Figure 5.5a). Both the transition state and product were found to be higher in energy than the pathway toward the formation of **5-15**. The 4-membered ring in the intermediate **5-15'** (NICS(0) = 21.5) was further shown to be more anti-aromatic than either **5-15** (NICS(0) = 5.3)

and biphenylene (NICS(0) = 18.3). Hence, it is unlikely that the reaction proceeds *via* cycloaddition of **[Al]** to the diene spanning C^3 to C^6.

The (2 + 1) cycloaddition of **[Al]** to the C^5–C^6 alkene of **5-15** was also considered, to form **Int-1'**, a regioisomer of **Int-1** (Figure 5.5b). While **Int-1'** ($\Delta G°_{298K}$ = 8.6 kcal mol^{-1}) is marginally more stable than **Int-1** ($\Delta G°_{298K}$ = 12.5 kcal mol^{-1}) the activation barrier to form **Int-1'** (**TS-9**: $\Delta G^{‡}_{298K}$ = 24.6 kcal mol^{-1}) is higher than the corresponding barrier to form **Int-1** (**TS-2**: $\Delta G^{‡}_{298K}$ = 18.4 kcal mol^{-1}). It is possible for **Int-1'** to form under the reaction conditions, and participate in similar skeletal rearrangements to **Int-1**, however it is more likely that the pathway proceeds through the pathway with the lower activation barrier.

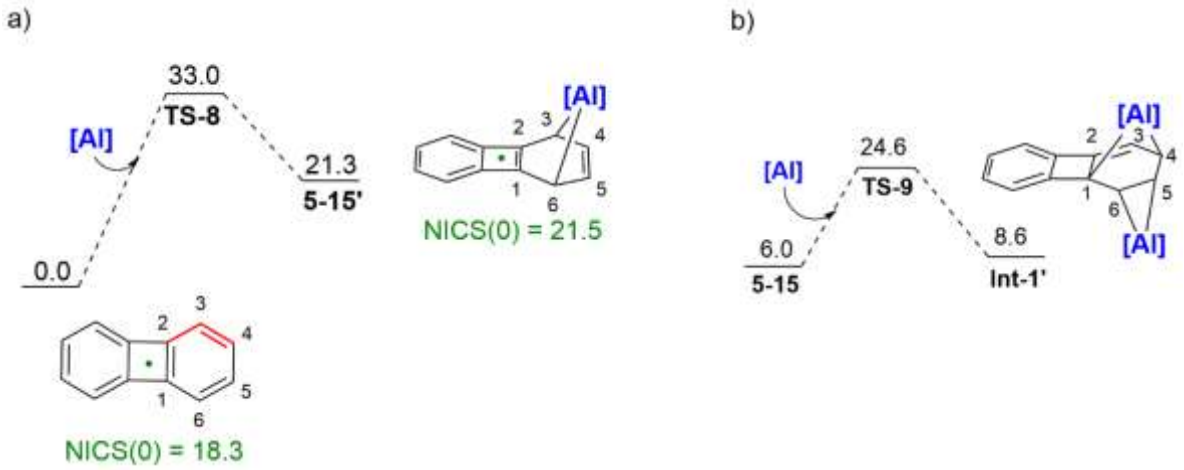


Figure 5.6: Cycloaddition of **[Al]** to the a) C^3---C^6 diene system in biphenylene and b) C^5–C^6 alkene in **5-15.**

The oxidative addition of **[Al]** to the central C^1–C^7 σ-bond of biphenylene was also explored computationally (Figure 5.6). While the overall reaction is highly exergonic (ΔG_{298K} = –64.9 kcal mol^{-1}), the transition state is high in energy (**TS-10**, $\Delta G^{‡}_{298K}$ = 42.0 kcal mol^{-1}) and unlikely to be accessible under the reaction conditions. The reaction of a recently reported anionic aluminium (I) fragment, **[Al]-K**,[29] with biphenylene was also explored as a parallel to the observed reactivity of biphenylene with a cyclic-alkylaluminyl anion.[15] While the activation barrier (**TS-11**, $\Delta G^{‡}_{298K}$ = 27.7 kcal mol^{-1}) is lower than the barrier for the neutral complex, it is still inaccessible under the reaction conditions.

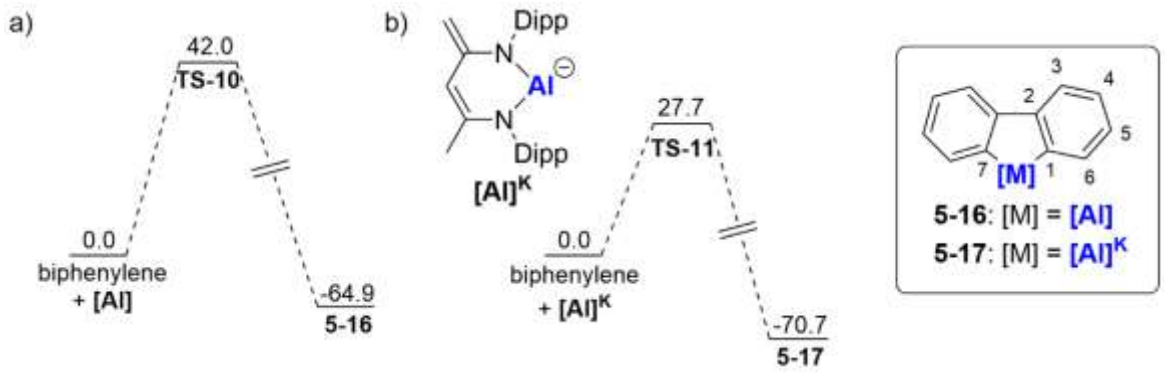


Figure 5.7: Oxidative addition of **[Al]** and a related anionic aluminium (I) reagent **[Al]^{K}** to biphenylene.

The divergent reactivity between **[Al]** and transition-metals with biphenylene can be understood through a deeper consideration of the transition states and frontier orbitals involved in the reaction. Transition states for oxidative addition are typically destabilised by steric repulsion due to the requirement for a close – and side-on – approach of the C–X bond to the metal to achieve orbital overlap (e.g. X = C, H, Halogen). The oxidative addition of biphenylene to transition metal complexes has been calculated to involve a side-on approach and the synchronous breaking of the C–C σ-bond and formation of both M–C bonds along the reaction coordinate.[16,17]

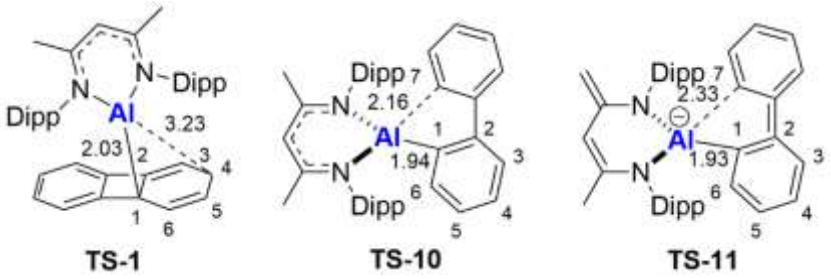


Figure 5.8: Geometries for **TS-1**, **TS-10**, and **TS-11**. Key Al–C bond lengths provided in Å.

[Al] differs from common transition metal fragments in terms of both the symmetry and energy of the frontier molecular orbitals. The HOMO and the LUMO of **[Al]** are orthogonal to one another and the 3p orbitals which contribute to them have a smaller radial extension than the 4d and 5d orbitals of 2nd and 3rd row transition metals. In line with these differences, **TS-10** is unusual and is not consistent with a symmetric approach of the C–C bond to the metal (Figure 5.7). **TS-10** has an asymmetric geometry and involves close approach of the metal to only one carbon atom of the breaking C–C σ-bond. Similar asymmetry is observed in the transition states associated with the oxidative addition of the aluminyl anion **[Al]^{K}** to biphenylene as well as the cycloaddition of **[Al]** to the arene ring in biphenylene (Figure 5.4). This reflects the highly nucleophilic nature of the aluminium(I) species and suggests that nucleophilic attack of the

substrate *via* donation of aluminium based lone pair into a π* (**TS-1**) or σ* (**TS-10**, **TS-11**) orbital is an early driving force for the reaction.

5.2.5 – Activation strain analysis

Activation strain analysis (ASA) was used to interrogate this phenomenon further. The activation strain model decomposes the electronic energy of structures along the reaction coordinate into the stabilising interaction energy between fragments (E_{int}) and the energy required to distort the fragments from their equilibrium electronic and geometric structures (E_{dist}). The reaction coordinate is projected onto a bond metric (e.g. bond length or angle). The method allows a detailed interrogation of the reaction pathway, and insight into which factors govern calculated energy barriers.[30,31] The model has been used to explore the factors controlling C–H and C–C bond oxidative addition at an aluminyl anion.[32]

The ASA profile derived from **TS-10** was generated (Figure 5.8a). In this profile, E_{Int} decreases modestly along the reaction coordinate and a high degree of distortion in biphenylene is required before a favourable interaction between the two fragments is observed. This is further supported by the complex curvature of the reaction coordinate as a function of the Al–C bond distance.

For comparison, the profile associated with **TS-1**, and the (4 + 1) cycloaddition is provided.[§§§] While both **TS-1** and **TS-10** proceed *via* an initial nucleophilic attack of **[Al]** onto biphenylene, the ASA profile **TS-1** shows a steady increase in E_{dist}(Biph) that is offset by a steady decrease in E_{int} (Figure 5.8b). Contrasting **TS-10**, the E_{int} curve of the ASA profile of **TS-1** is monotonically decreasing implying that only moderate distortion of the arene is required for favourable orbital overlap with the aluminium fragment. The extreme distortion required for the overlap of the C–C σ-bonding orbital with the Al p-orbital in **TS-10** is a consequence of the orthogonality of the HOMO and LUMO of **[Al]**. These data allow us to conclude that the oxidative addition of the weak C–C σ-bond of biphenylene to **[Al]** is unfavourable due to the high degree of biphenylene reorganisation that is required for effective orbital overlap.

[§§§] As two bonds are forming over the course of both reactions, these values have been plotted against the lengths of the weaker Al–C bond at the transition state (See Section 5.6.2 for further discussion).

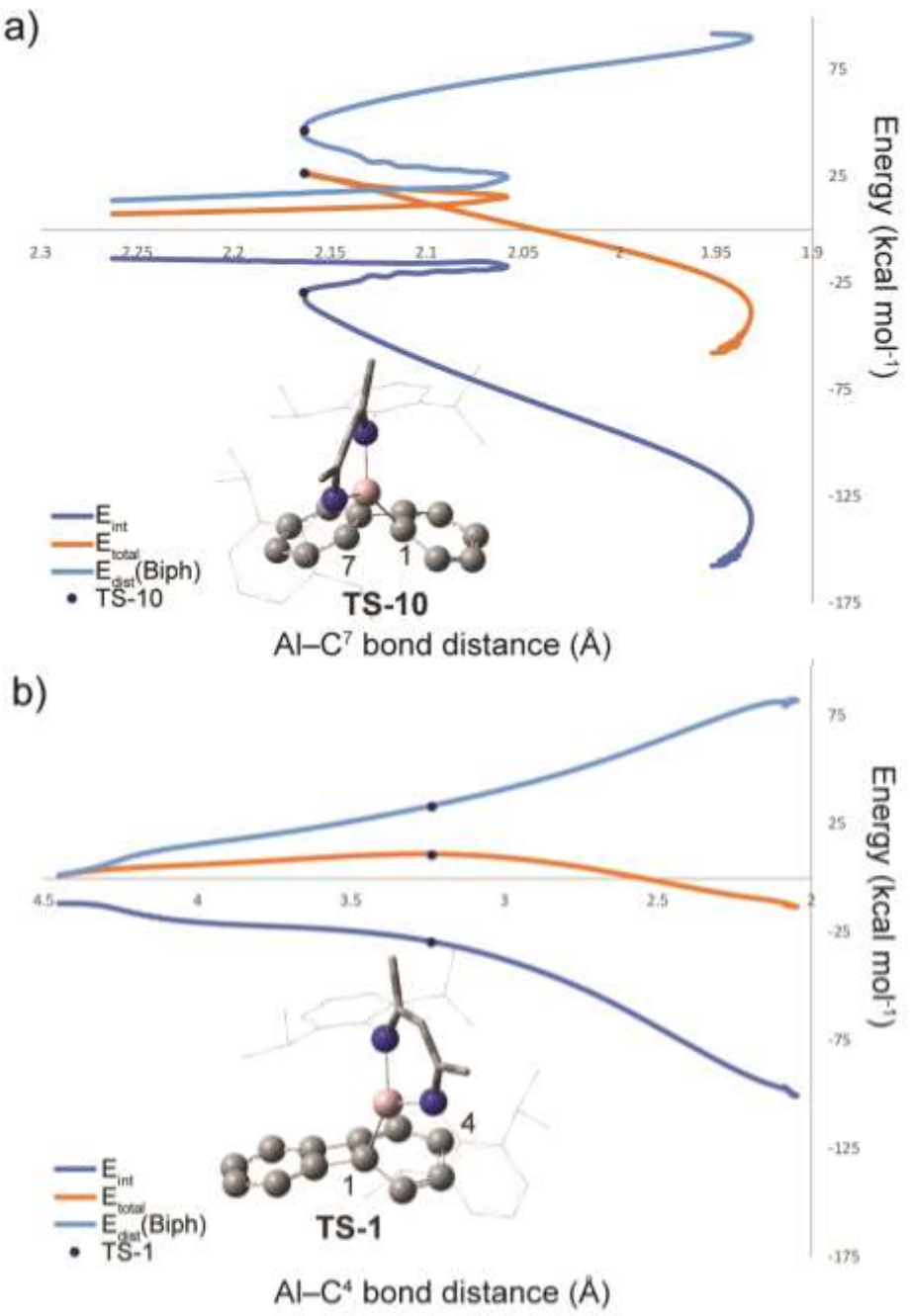


Figure 5.9: Activation strain analysis plots generated for **TS-10** and **TS-1**.

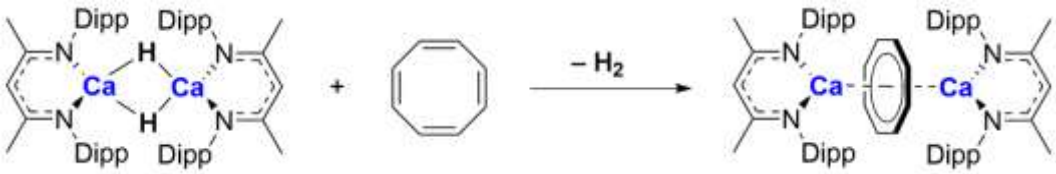
5.3 Conclusion and future work

In this chapter, the remarkable chemoselective C–C σ-bond activation reaction involving the stable six-membered ring of biphenylene is reported. This selectivity is unprecedented. Transition metal complexes react exclusively with the weakest C–C σ-bond of the four-membered ring of biphenylene, typically by an oxidative addition step. The divergent reactivity of **[Al]** from transition-metal systems is a direct consequence of the orthogonality and limited radial extension of the frontier molecular orbitals of the aluminium reagent. This reagent cannot

easily reach a stable transition state for oxidative addition of a σ-C–C bond – due to the strain required to achieve orbital overlap – instead it reacts preferentially with the flat and accessible π-system of the substrate opening an alternative pathway for σ-C–C bond activation.

Investigation of substitution patterns on biphenylene should be explored as a point of future work. Substitution may direct reactivity towards one of the two observed products or stabilise some reactive intermediates for further study, and allow selective functionalisation of one of the 6-membered rings of biphenylene. The selective functionalisation of one of the 6-membered rings of biphenylene may also be achieved through judicious substitution of the substrate. Biphenylene substrates with directing groups in particular have been shown to direct the oxidative addition of transition-metals to the central carbon–carbon bond.[14]

The strategy to cleave arene rings involves reduction of the arene ring to form metallacycles, followed by cleavage from a strained intermediate. As reported in the last chapter, installation of the metal centre can be approached using a hydroelementation strategy. Specifically, calcium hydride has been shown to react with cyclic conjugated alkene systems to form inverse sandwich complexes which are structurally reminiscent to intermediates proposed in the arene cleavage of biphenylene (Scheme 5.8).[33,34] Further exploration of the reactivity with calcium hydrides with strained polycyclic aromatic hydrocarbons may allow for the development of catalytic arene functionalisations.



Scheme 5.8: Reaction of a calcium hydride complex with 1,3,5,7-cyclooctatetraene. Dipp = 2,6-di-iso-propylphenyl.

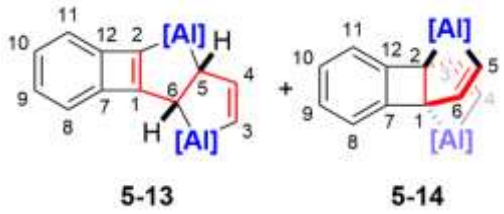
5.4 – Experimental

5.4.1 – General experimental

All manipulations were carried out using standard Schlenk-line and glovebox techniques under an inert atmosphere of argon or dinitrogen. A MBraun Labmaster glovebox was employed, operating at <0.1 ppm O_2 and <0.1 ppm H_2O. Solvents were dried over activated alumina from an SPS (solvent purification system) based upon the Grubbs design and degassed before use. Glassware was dried for 12 h at 120°C prior to use. C_6D_6 was dried over 3 Å molecular sieves and subjected to the freeze-pump-thaw degassed thrice before use.

NMR Spectra were recorded on Bruker 400 MHz or 500 MHz at 298 K unless otherwise stated and values recorded in ppm. Data were processed in MestReNova software. Where needed, chemical shifts were assigned with the assistance of 2D NMR (HSQC, HMBC, COSY) spectra. **[Al]**,[35] and biphenylene[36] were synthesised according to literature procedures. Chemicals were purchased from Sigma Aldrich, Fluorochem, Alfa Aesar and VWR. Elemental analyses were performed by Elemental Lab. Primary data can be downloaded from dx.doi.org/10.14469/hpc/7325.

5.4.2 – Synthesis of compounds



5-13 **5-14**

***Synthesis of 5-13 and 5-14*:** In a glovebox, **[Al]** (45 mg, 0.10 mmol) was transferred as a solid into a J-Young NMR tube and a solution of biphenylene (15 mg, 0.10 mmol) in C_6D_6 (0.600 mL) was added. The reaction mixture was heated at 100°C for 3 h upon which the solution changed colour from a dark red-orange to a yellow-orange. The reaction was monitored by ^1H NMR spectroscopy and was complete upon observation of total consumption of **[Al]**. The NMR tube was returned to the glovebox and diluted with toluene (~ 0.5 mL) before all volatiles were removed *in vacuo*. The residue was redissolved in the minimum amount of THF, filtered, and recrystallised at –35°C to afford **5-13** as dark orange-red crystals. The crystals were washed with cold THF (1 x 0.2 mL) and thrice with n-pentane (3 x 0.2 mL) to afford **5-13** as orange-red crystals. Yield: 18 mg, 0.017 mmol, 34%.

The THF and pentane washings were combined with the mother liquor and transferred to a separate vial. The volatiles were removed *in vacuo*. The residue was redissolved in the minimum amount of toluene and allowed to recrystallise at –35°C to afford **5-14** as pale yellow crystals. The supernatant was decanted, and the residue was washed once with toluene (~ 0.2 mL), to remove any cocrystallised **5-14**. Yield: 17 mg, 0.016 mmol, 32%.

NB: Both **5-13** and **5-14** decompose under thermal (100°C) conditions. As a result, NMR yields and ratios vary slightly however repeated experiments show that the ratio between **5-13**:**5-14** fall between 1:0.6 and 1:0.8.

Compound 5-13

^{1}H NMR (400 MHz, C_6D_6, 298 K) δ 0.57 (d, $^{3}J_{HH}$ = 6.7 Hz, 3H, (C***H₃***)CH(CH₃)), 0.76 (d, $^{3}J_{HH}$ = 6.8 Hz, 3H, (C***H₃***)CH(CH₃)), 0.78 (d, $^{3}J_{HH}$ = 6.7 Hz, 3H, (C***H₃***)CH(CH₃)), 0.84 (d, $^{3}J_{HH}$ = 6.6 Hz, 3H, (C***H₃***)CH(CH₃)), 1.02-1.08 (m overlapping, 15H, 5x (C***H₃***)CH(CH₃)), 1.12 (d, $^{3}J_{HH}$ = 7.1 Hz, 3H, (C***H₃***)CH(CH₃)), 1.14 (d, $^{3}J_{HH}$ = 7.4 Hz, 3H, (C***H₃***)CH(CH₃), 1.16 (d, $^{3}J_{HH}$ = 7.2 Hz, 3H, (C***H₃***)CH(CH₃)), 1.31 (d, $^{3}J_{HH}$ = 6.1 Hz, 1H, C^{6}-***H***), 1.38 (d overlapping, $^{3}J_{HH}$ = 6.6 Hz, 6H, 2x (C***H₃***)CH(CH₃)), 1.39 (d, $^{3}J_{HH}$ = 6.6 Hz, 3H, (C***H₃***)CH(CH₃)), 1.41 (s, 3H, (C***H₃***)C(CH)C(CH₃)) 1.43 (s, (CH₃)C(CH)C(C***H₃***)), 1.48 (d, $^{3}J_{HH}$ = 6.6 Hz, 3H, (C***H₃***)CH(CH₃)), 1.48 (s, 3H, (CH₃)C(CH)C(C***H₃***)), 1.52 (s, 3H, (C***H₃***)C(CH)C(CH₃)), 1.55 (dd overlapping, $^{3}J_{HH}$ = 6.1, 3.0 Hz, 1H, C^{5}-***H***), 2.93 (hept, $^{3}J_{HH}$ = 6.6 Hz, 1H, (CH₃)C***H***(CH₃)), 3.02 (hept, $^{3}J_{HH}$ = 6.7 Hz, 1H, (CH₃)C***H***(CH₃)), 3.17 (hept, $^{3}J_{HH}$ = 6.7 Hz, 1H, (CH₃)C***H***(CH₃)), 3.24 (hept, $^{3}J_{HH}$ = 6.7 Hz, 1H), 3.39 (hept, $^{3}J_{HH}$ = 6.9 Hz, (CH₃)C***H***(CH₃)), 3.40 (hept, $^{3}J_{HH}$ = 6.9 Hz, (CH₃)C***H***(CH₃)), 3.44 (hept, $^{3}J_{HH}$ = 6.7 Hz, 1H, (CH₃)C***H***(CH₃)), 3.57 (hept, $^{3}J_{HH}$ = 6.7 Hz, 1H, (CH₃)C***H***(CH₃)), 4.75 (s, 1H, (CH₃)C(C***H***)C(CH₃)), 4.76 (s, 1H, (CH₃)C(C***H***)C(CH₃)), 5.32 (dd, $^{3}J_{HH}$ = 12.0 Hz, $^{4}J_{HH}$ = 2.9 Hz, 1H, C^{3}-***H***), 5.78 (d, $^{3}J_{HH}$ = 6.0 Hz, 1H, C$^{8/11}$-***H***), 5.96 (d, $^{3}J_{HH}$ = 6.3 Hz, 1H, C$^{8/11}$-***H***), 6.31 (dd, ^{3}J = 8.6, 6.1 Hz, 1H, C$^{9/10}$-***H***), 6.50 (dd, $^{3}J_{HH}$ = 8.6, 6.3 Hz, 1H, C$^{9/10}$-***H***), 6.97 – 7.23 (m, 12H, Ar-H), 7.44 (dd, $^{3}J_{HH}$ = 11.9, 2.8 Hz, 1H, C^{4}-***H***).

^{13}C NMR (101 MHz, C_6D_6, 298 K) δ 23.6 ((C***H₃***)C(CH)C(CH₃)), 23.9 ((C***H₃***)C(CH)C(CH₃)), 24.0 ((CH₃)C(CH)C(C***H₃***)), 24.1 ((CH₃)C(CH)C(C***H₃***)), 24.5 ((***C***H₃)CH(CH₃)), 24.5 ((***C***H₃)CH(CH₃)), 24.6 ((***C***H₃)CH(CH₃)), 24.8 ((***C***H₃)CH(CH₃)), 24.9 ((***C***H₃)CH(CH₃)), 24.9 ((CH₃)CH(***C***H₃)), 24.9 ((***C***H₃)CH(CH₃)), 25.0 (2x (***C***H₃)CH(CH₃)), 25.0 ((CH₃)CH(***C***H₃)), 25.1 ((CH₃)CH(***C***H₃)), 25.2 ((CH₃)CH(***C***H₃)), 25.5 ((CH₃)CH(***C***H₃)), 25.6 (2x (CH₃)CH(***C***H₃)), 25.6 ((CH₃)CH(***C***H₃)), 27.9 ((CH₃)***C***H(CH₃)), 28.5 ((CH₃)***C***H(CH₃)), 28.6 ((CH₃)***C***H(CH₃)), 28.7 ((CH₃)***C***H(CH₃)), 28.8 ((CH₃)***C***H(CH₃)), 29.1 ((CH₃)***C***H(CH₃)), 29.2 ((CH₃)***C***H(CH₃)), 29.7 ((CH₃)***C***H(CH₃)), 33.6 (Al***C***^{6}H), 39.0 (Al***C***^{5}H), 97.1 ((CH₃)C(***C***H)C(CH₃)), 97.2 ((CH₃)C(***C***H)C(CH₃)), 106.9 (***C***$^{8/11}$), 110.1 (***C***$^{8/11}$), 122.1 (***C***$^{9/11}$), 123.9 (Ar***C***), 124.1 (Ar***C***), 124.3 (Ar***C***), 124.5 (Ar***C***), 124.5 (Ar***C***), 124.8 (Ar***C***), 124.9 (Ar***C***), 125.1 (***C***^{4}), 127.0 (Ar***C***), 127.1 (Ar***C***), 127.3 (***C***$^{9/11}$), 140.9 (Ar***C***), 141.4 (Ar***C***), 142.2 (Ar***C***), 142.3 (Ar***C***), 143.9 (Ar***C***), 144.0 (Ar***C***), 144.0 (Ar***C***), 144.2 (Ar***C***), 144.3 (Ar***C***), 144.4 (Ar***C***), 144.5 (Ar***C***), 145.5 (Ar***C***), 153.6 (***C***$^{7/12}$), 155.0 (***C***^{2}) 158.6 (***C***$^{7/12}$), 162.0 (***C***^{3}), 170.0 ((CH₃)***C***(CH)C(CH₃)), 170.2 ((CH₃)***C***(CH)C(CH₃)), 170.3 ((CH₃)C(CH)***C***(CH₃)), 170.6 ((CH₃)C(CH)***C***(CH₃)), 195.0 (***C***^{1}). Some Ar***C*** resonances overlap and are not observed.

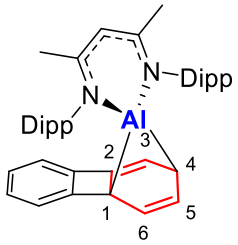
Anal. Calc. ($C_{70}H_{90}Al_2N_4$): C, 80.73, H, 8.71, N, 5.38. Found: C, 78.58; H, 8.81; N, 5.16.

Compound 5-14

^{1}H NMR (400 MHz, C_6D_6, 298 K) δ 0.68 (d, $^{3}J_{HH}$ = 6.7 Hz, 6H, 2x (C***H₃***)CH(CH_3)), 0.96 (d, $^{3}J_{HH}$ = 6.8 Hz, 6H, 2x (C***H₃***)CH(CH_3)), 1.04 (d, $^{3}J_{HH}$ = 6.7 Hz, 6H, 2x (C***H₃***)CH(CH_3)), 1.05 (d, $^{3}J_{HH}$ = 6.7 Hz, 6H, 2x (C***H₃***)CH(CH_3)), 1.07 (d, $^{3}J_{HH}$ = 6.8 Hz, 6H, 2x (CH_3)CH(C***H₃***)), 1.20 (d, $^{3}J_{HH}$ = 6.8 Hz, 6H, 2x (CH_3)CH(C***H₃***)), 1.27 (s, 6H, 2x (C***H₃***)C(CH)C(CH_3)), 1.37 (s, 6H, 2x (CH_3)C(CH)C(C***H₃***)), 1.61 (d, $^{3}J_{HH}$ = 6.7 Hz, 12H, 4x (CH_3)CH(C***H₃***)), 2.95 (hept, $^{3}J_{HH}$ = 6.8 Hz, 2H, 2x (CH_3)C***H***(CH_3)), 2.99 (hept, $^{3}J_{HH}$ = 6.7 Hz, 2H, 2x (CH_3)C***H***(CH_3)), 3.15 (hept, $^{3}J_{HH}$ = 6.8 Hz, 2H, 2x (CH_3)C***H***(CH_3)), 3.73 (hept, $^{3}J_{HH}$ = 6.8 Hz, 2H, 2x (CH_3)C***H***(CH_3)), 4.83 (s, 2H, 2x (CH_3)C(C***H***)C(CH_3)), 5.87 (d, $^{3}J_{HH}$ = 11.9 Hz, 2H, $C^{4,5}$-***H***), 5.92 (m, 2H, $C^{9,10}$-***H***), 6.10 (m, 2H, $C^{8,11}$-***H***), 6.74 (m, 2H, Ar-***H***), 6.91 – 7.19 (m, 10H, Ar-***H***), 7.41 (d, $^{3}J_{HH}$ = 11.9 Hz, 2H, $C^{3,6}$-***H***).

^{13}C NMR (101 MHz, C_6D_6, 298 K) δ 22.8 (2x (***C***H_3)CH(CH_3)), 24.0 (2x (***C***H_3)C(CH)C(CH_3)), 24.3 (2x (CH_3)CH(***C***H_3)), 24.8 ((6x (***C***H_3)CH(CH_3)), 24.9 (2x (CH_3)CH(***C***H_3)), 25.1 (2x (CH_3)CH(***C***H_3)), 25.2 (2x (CH_3)C(CH)C(***C***H_3)), 27.4 ((2x (CH_3)***C***H(CH_3)), 27.6 (2x (CH_3)***C***H(CH_3)), 28.4 (2x (CH_3)CH(***C***H_3)), 29.0 (2x (CH_3)***C***H(CH_3)), 30.2 (2x (CH_3)***C***H(CH_3)), 60.6 (***C^{1,2}***), 98.4 (CH_3)C(***C***H)C(CH_3)), 120.7 (***C^{8,11}***), 122.4 (***C^{9,10}***), 123.3 (2x Ar***C***), 123.8(2x Ar***C***), 125.1(2x Ar***C***), 125.7(2x Ar***C***), 126.7(2x Ar***C***), 127.1(2x Ar***C***), 134.6 (***C^{4,5}***), 142.5(2x Ar***C***), 142.6(2x Ar***C***), 142.6(2x Ar***C***), 143.8(2x Ar***C***), 143.8(2x Ar***C***), 145.0(2x Ar***C***), 150.7 (***C^{7,12}***), 158.3 (***C^{3,6}***), 170.3 (2x (CH_3)***C***(CH)C(CH_3)), 171.0 (2x (CH_3)C(CH)***C***(CH_3)).

Anal. Calc. ($C_{70}H_{90}Al_2N_4$): C, 80.73, H, 8.71, N, 5.38. Found: C, 78.84; H, 8.52; N, 5.10.



***Synthesis of 5-15*:** In a glovebox, **[Al]** (45 mg, 0.10 mmol) was transferred as a solid into a J-Young NMR tube and a solution of biphenylene (30 mg, 0.20 mmol) in C_6D_6 (0.600 mL) was added. The suspension was sonicated for 10 minutes before being allowed to stand for one week at 25 °C. **[Al]** dissolved as the reaction progressed. The reaction was monitored by ^{1}H NMR spectroscopy and was complete upon observation of total consumption of **[Al]**. The NMR tube was returned to the glovebox and diluted with toluene (~ 0.5 mL) before all volatiles were removed *in vacuo*. The residue was redissolved in the minimum amount of toluene (~ 0.2 mL) and the product was recrystallised at–35 °C. The mother liquor was decanted and the crystals were washed twice with toluene (2 x 0.2 mL) and three times with n-pentane (3 x 0.2 mL) and dried *in vacuo*, affording **5-15** as bright yellow crystals. Yield: 16 mg, 0.027 mmol, 27%.

A second crop of **5-15** may be isolated by concentrating the supernatant and toluene/pentane washings in the previous steps, recrystallizing at –35°C, and isolating as above. The second crop has small amounts of **5-13** and **5-14** as an impurity. Yield: 22 mg, 0.037 mmol, 37%.

NB: It is important to use two equivalents of biphenylene in the synthesis of **5-15** otherwise significant amounts of **5-13** and **5-14** form competitively, lowering yield and impeding isolation.

^{1}H NMR (400 MHz, C_6D_6, 298 K) δ 0.78 (d, $^3J_{HH}$ = 6.7 Hz, 3H, (C***H*₃**)CH(CH₃)), 0.90 (d, $^3J_{HH}$ = 6.8 Hz, 3H, (C***H*₃**)CH(CH₃)), 1.01 (d, $^3J_{HH}$ = 7.1 Hz, 3H, (C***H*₃**)CH(CH₃)), 1.03 (d, $^3J_{HH}$ = 7.2 Hz, 3H, (C***H*₃**)CH(CH₃)), 1.07 (d, $^3J_{HH}$ = 6.8 Hz, 3H, (CH₃)CH(C***H*₃**)), 1.38 (d, $^3J_{HH}$ = 6.8 Hz, 3H, (CH₃)CH(C***H*₃**)), 1.42 (d, $^3J_{HH}$ = 6.7 Hz, 3H, (CH₃)CH(C***H*₃**)), 1.46 (s, 3H, (C***H*₃**)C(CH)C(CH₃)), 1.50 (s, 3H, (CH₃)C(CH)C(C***H*₃**)), 1.62 (d, $^3J_{HH}$ = 6.8 Hz, 3H, (CH₃)CH(C***H*₃**)), 3.01 (ddd, $^3J_{HH}$ = 6.5, 5.5, $^4J_{HH}$ = 1.7 Hz, 1H, C^4-***H***), 3.09 (hept, $^3J_{HH}$ = 6.8 Hz, 1H, (CH₃)C***H***(CH₃)), 3.16 (hept, $^3J_{HH}$ = 6.8 Hz, 1H, (CH₃)C***H***(CH₃)), 3.27 (hept, $^3J_{HH}$ = 6.8 Hz, 1H, (CH₃)C***H***(CH₃)), 3.38 (hept, $^3J_{HH}$ = 6.8 Hz, 1H, (CH₃)C***H***(CH₃)), 4.86 (s, 1H, (CH₃)C(C***H***)C(CH₃)), 5.73 – 5.79 (m overlapping, 2H, C^{5,6}-***H***), 5.98 (dd,

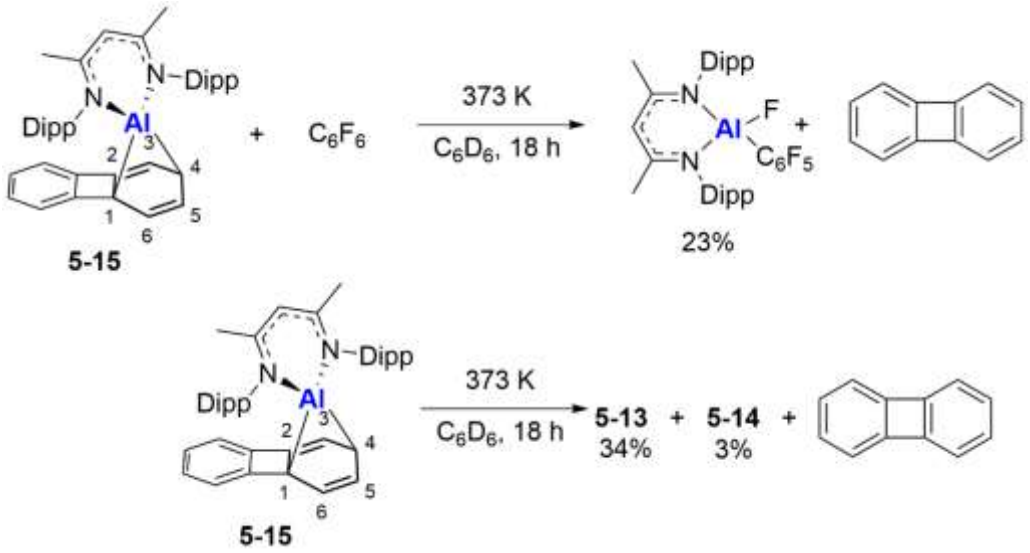
$^{3}J_{HH}$ = 6.5, $^{4}J_{HH}$ = 6.5 Hz, 1H, C^{3}-***H***), 6.61 (d, $^{3}J_{HH}$ = 7.2 Hz, 1H, Ar_{Biph}-***H***), 6.90 (ddd, $^{3}J_{HH}$ = 7.9, 7.1, $^{4}J_{HH}$ = 0.9 Hz, 1H, Ar_{Biph}***H***), 6.99 – 7.20 (m, 8H, 2x Ar_{Biph}-***H***, 6x Ar-***H***).

^{13}C NMR (101 MHz, C_6D_6, 298 K) δ 23.2 (($\boldsymbol{C}H_3$)CH(CH_3)), 23.6 ((CH_3)C(CH)C($\boldsymbol{C}H_3$)), 24.2 (($\boldsymbol{C}H_3$)C(CH)C(CH_3)), 24.4 (($\boldsymbol{C}H_3$)CH(CH_3)), 24.4 (($\boldsymbol{C}H_3$)CH(CH_3)), 24.6 (($\boldsymbol{C}H_3$)CH(CH_3)), 24.7 ((CH_3)CH($\boldsymbol{C}H_3$)), 24.9 ((CH_3)CH($\boldsymbol{C}H_3$)), 25.2 ((CH_3)CH($\boldsymbol{C}H_3$)), 25.3 ((CH_3)CH($\boldsymbol{C}H_3$)), 28.5 ((CH_3)$\boldsymbol{C}$H(CH_3)), 28.6 ((CH_3)$\boldsymbol{C}$H(CH_3)), 28.6 ((CH_3)$\boldsymbol{C}$H(CH_3)), 29.7 ((CH_3)$\boldsymbol{C}$H(CH_3)), 42.4 (***C^{4}***), 67.0 (***C^{1}***) 97.5 ((CH_3)C($\boldsymbol{C}$H)C(CH_3)), 118.4 (($Ar_{Biph}\boldsymbol{C}$)), 120.6 (***C$^{5/6}$***), 120.7 ($Ar_{Biph}\boldsymbol{C}$), 124.5 (Ar***C***), 124.6 (Ar***C***), 124.7 (3x Ar***C***), 126.9($Ar_{Biph}\boldsymbol{C}$), 127.3 (Ar***C***), 129.3 (***C$^{5/6}$***), 130.3 (***C^{3}***), 140.7 ($Ar_{Biph}\boldsymbol{C}$), 142.4 (Ar***C***), 142.6 (Ar***C***), 142.7 (Ar***C***), 143.1 (Ar***C***), 143.3 (Ar***C***), 143.4 (Ar***C***), 144.1 ($Ar_{Biph}\boldsymbol{C}$), 151.4 ($Ar_{Biph}\boldsymbol{C}$), 171.4 ((CH_3)$\boldsymbol{C}$(CH)C(CH_3)), 171.5 ((CH_3)C(CH)$\boldsymbol{C}$(CH_3)).

Some biphenylene resonances overlap with Ar***C*** resonances and cannot be observed.

Anal. Calc. ($C_{41}H_{49}AlN_2$): C, 82.51, H, 8.28, N, 4.69. Found: C, 82.37; H, 8.37; N,4.63.

5.4.3 – Reversibility experiments with 5-15



Scheme 5.9: Experiments confirming the partially reversible formation of **5-15**.

In both experiments outlined in Scheme S1, the partial reversibility of **5-15** to form **[Al]** and biphenylene is demonstrated. The formation of biphenylene is evident in the ^{1}H NMR spectrum, and **[Al]** can be trapped out either through onwards reactivity with **5-15** to form **5-13** and **5-14** or through reaction with C_6F_6 to form the known C–F aluminated product.[37] An unidentified decomposition product likely originating from **5-15** is also observed to form in both cases.

Reaction with C_6F_6

In a glovebox, **5-15** (5 mg, 0.008 mmol) was dissolved in C_6D_6 (0.600 mL) and transferred to a J-Young NMR tube with a ferrocene capillary, and an initial timepoint ^{1}H NMR spectrum was taken. The J-Young NMR tube was returned to the glovebox, and C_6F_6 (5 µL, 0.04 mmol) was added *via* micropipette. The J-Young NMR tube was placed in a 100°C bath for 18 h. The complete consumption of **5-15** was evident in the ^{1}H NMR spectrum at this timepoint.

Thermolysis

In a glovebox, **5-15** (5 mg, 0.008 mmol) was dissolved in C_6D_6 (0.600 mL) and transferred to a J-Young NMR tube with a ferrocene capillary, and an initial timepoint ^{1}H NMR spectrum was taken. The J-Young NMR tube was placed in a 100°C bath for 18 h. The complete consumption of **5-15** was evident in the ^{1}H NMR spectrum at this timepoint.

5.5 – X-ray data

*The X-ray structure of **5-13***

5-13 was found to crystallise in the space group I2/m. The unit cell of the crystal contains two full molecules of **5-13**, two molecules of pentane, two molecules of benzene, and eight asymmetric units. Accordingly, the asymmetric unit of the unit cell contains ¼ of the full molecule of **5-13**. A full molecule of **5-13**, disordered over two positions, can be built from the asymmetric unit through two symmetry operations: 1) a mirror plane passing through Al1 and C15 and perpendicular to the β-diketiminate plane, and 2) a C_2 rotation along the (010) axis.

As a result, the hydrocarbon fragment C1>C12 was found to be disordered over four sites. C1>C12 were modelled at 25% occupancy in Part -1, with the two symmetry operations generating a quartet of 25% occupancy atoms (summing to 100%) for a complete molecule. The two central metallabicycle rings are essentially unchanged in position along the disordered fragment, with the key difference being the position of the arene ring on either the "left" (50% total occupancy) of the metallabicycle or the "right" (50% total occupancy). Due to the disorder across multiple positions, the thermal parameters of C1>C12 were restrained to be similar over a wide distance (4 Å) and the fragment was refined isotropically.

Benzene was found to be included in the asymmetric unit as well and in proximity to the molecule. The benzene molecule was found to be disordered over four positions in a similar fashion to the ring-opened biphenylene unit. As a result, the included benzene molecule unit was found to be disordered over four sites. C33>C38 were modelled at 25% occupancy in Part -2, with the two symmetry operations generating a quartet of 25% occupancy atoms (summing to 100%) for a complete molecule. The benzene molecule was found to be in the complementary position to the arene ring of the molecule: in the cases where the arene ring is on the "left" of the metallabicycle, the benzene molecule occupies the void on the "right", and vice versa. Consequently, in the asymmetric unit, the benzene intersects the arene ring of the C1>C12 fragment. The thermal parameters of the benzene ring and C4/C5 (the point of intersection) were restrained to be similar, and the fragment was refined isotropically.

The iso-propyl group (C22>C24) was modelled as disordered over two sites in *ca.* 80:20 occupancies for the major and minor orientations respectively. Only the non-hydrogen atoms in the major orientation were refined anisotropically (those in the minor orientation were refined isotropically).

The included n-pentane molecule was found to be disordered over four positions in a similar fashion to the ring-opened biphenylene unit. Accordingly, it has been modelled at 25% occupancy in the asymmetric unit in Part -1 with the two symmetry operations generating a quartet of 25% occupancy molecules (summing to 100%). The thermal parameters of adjacent atoms were restrained to be similar, and the fragment was refined isotropically.

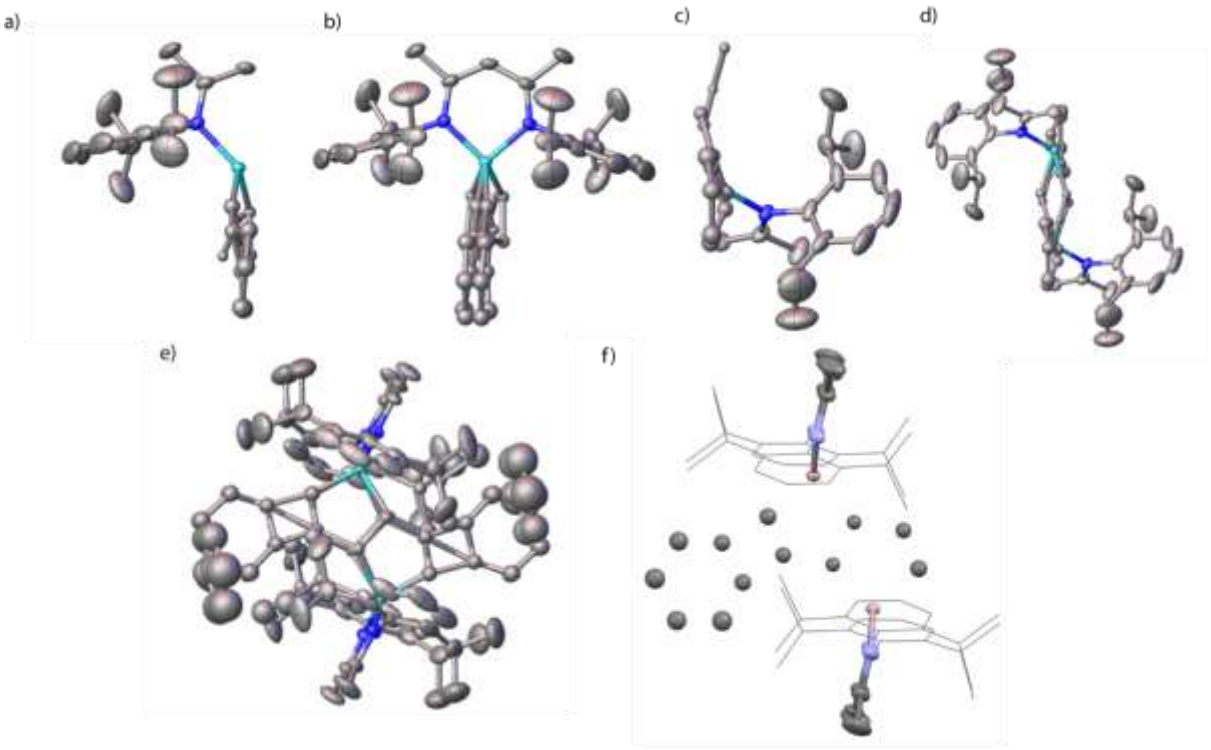


Figure 5.10: Representations of the X-ray crystal structure of **5-13**. a) The asymmetric unit with the mirror plane perpendicular to the page. b) Two asymmetric units generated by application of mirror plane symmetry to the asymmetric unit. c) The asymmetric unit along the 010 axis. d) The Two asymmetric units generated by application of C_2 rotation around the 100 axis. e) The entire disordered fragment. f) A single molecule of **5-13**, extracted from the disordered fragment.

Crystal Data for $C_{81}H_{106}Al_2N_4$, M =1189.65, monoclinic, space group I2/m (no. 12), a = 12.1877(5) Å, b = 18.1554(6) Å, c = 16.3722(6) Å, β = 99.134(4)°, V = 3576.8(2) Å^3, Z = 2, ρ_{calc}g/cm^3 = 1.105, μ(MoKα) = 0.086 mm^{-1}, T = 172.95(10), red blocks, F^2 refinement, R_1(obs) = 0.0614, wR_2(all) = 0.1840, 3712 independent observed reflections (R_{int} = 0.0162), 3048 independent measured reflections [$|F_o| > 4\sigma(|F_o|)$, $2\theta_{full}$ = 56.44], 250 parameters. CCDC 2023760.

Comment on relative stereochemical assignment of C9 and C10

The solid-state structure implies a *cis* arrangement of hydrogen atoms at C9 and C10. In the asymmetric unit, the C9–C10 bond length is 1.562(8) Å. An interpretation of a *trans* junction would require C9 and C10 to bond with their symmetry generated counterparts, which give C–C

bond distances of approximately 1.9 Å in both cases. As a result, a *cis* geometry is the most likely interpretation of the ring junction.

The X-ray structure of ***5-14***

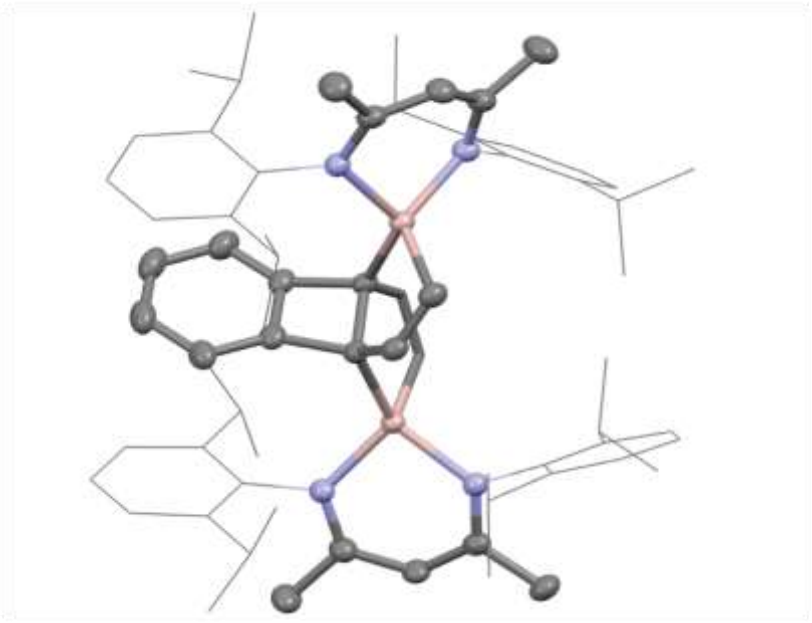


Figure 5.11: The solid-state structure of **5-14**.

5-14 was found to crystallise in the Pbca space group with two molecules of toluene in the asymmetric unit, for a total of 16 in the unit cell.

The included toluene molecules (C71>C77 and C78>C84) were modelled as disordered over two sites in *ca.* 63:37 and *ca.* 70:30 ratio respectively for the major and minor orientations. The thermal parameters of adjacent atoms in the major and minor components were restrained to be similar, their geometries optimised, and only the non-hydrogen atoms in the major orientation were refined anisotropically (those in the minor orientation were refined isotropically).

Crystal Data for $C_{84}H_{106}Al_2N_4$, M =1225.68, orthorhombic, space group Pbca (no. 61), a = 15.48357(18) Å, b = 30.2740(3) Å, c = 30.9141(3) Å, V = 14491.0(3) Å^3, Z = 8, ρ_{calc}g/cm^3 = 1.124, μ(CuKα) = 0.704 mm^{-1}, T = 173.1(3), light yellow plates, F^2 refinement, R_1(obs) = 0.0581, wR_2(all) = 0.1773, 14055 independent observed reflections (R_{int} = 0.0358), 10629 independent measured reflections [$|F_o| > 4\sigma(|F_o|)$, $2\theta_{full}$ = 147.398], 840 parameters. CCDC 2023761.

The X-ray structure of ***5-15***

5-15 was found to crystallise in the $P2_1/n$ space group.



Figure 5.12: The solid-state structure of **5-15**.

Crystal Data for $C_{41}H_{49}AlN_2$, M =596.80, monoclinic, space group $P2_1/n$ (no. 14), a = 12.8984(2) Å, b = 17.1692(3) Å, c = 16.9756(3) Å, β = 110.561(2)°, V = 3519.86(13) Å^3, Z = 4, ρ_{calc}g/cm^3 = 1.126, μ(CuKα) = 0.714 mm^{-1}, T = 172.95(10), yellow plates, F^2 refinement, R_1(obs) = 0.0486, wR_2(all) = 0.1354, 6728 independent observed reflections (R_{int} = 0.0406), 4730 independent measured reflections [$|F_o| > 4\sigma(|F_o|)$, $2\theta_{full}$ = 147.036], 422 parameters. CCDC 2023762.

5.6 – Computational details

DFT calculations were run using Gaussian 09 (Revision D.01)[38] using the M06l Minnesota functional.[39] Al and Mg centres were described with Stuttgart SDDAll RECPs and associated basis sets and the 6-31G** basis sets were used for all other atoms. Several functionals (M06l, B3PW91, ωB97X) were benchmarked against the experimentally observed product formations.[40,41]

Geometry optimisation calculations were performed without symmetry constraints. Frequency analyses for all stationary points were performed using the enhanced criteria to confirm the nature of the structures as either minima (no imaginary frequency) or transition states (only one imaginary frequency). Single point solvent corrections (benzene, $\varepsilon = 2.2706$) were applied using the polarizable continuum model (PCM) to free energies reported in the main text. Single point dispersion corrections were applied to the free energies to the Minnesota functional (m06l) energies using Grimme's D3 correction.[42]

Intrinsic reaction coordinate (IRC) calculations were used to connect transition states and minima located on the potential energy surface allowing a full energy profile (calculated at 298.15 K, 1 atm) of the reaction to be constructed.[43] Natural Bond Orbital analysis was carried out using NBO 6.0.[44]

Activation strain analysis was performed using the AutoDIAS software package.[45]

5.6.1 – Functional testing

Structure	M06l	M06l (corr)	ωB97x	ωB97x (corr)	B3PW91	B3PW91 (corr)
TS-1	32.0	28.5	46.6	35.1	46.0	28.0
5-15	8.6	6.0	12.9	5.3	29.4	5.6
Int-2	-1.5	-10.6	17.9	-6.2	55.1	-4.8
TS-4	27.8	18.8	62.1	34.2	89.9	30.0
TS-7	27.0	19.0	59.9	30.8	92.9	26.4

Table 6.1: Functional testing on key transition states with associated preceeding minima.

Key transition states were tested using the B3PW91 and ωB97x functionals in addition to the M06l functional used for the complete pathway. Only the M06l functional correctly predicts the selectivity for **5-13** (TS-4) over **5-14** (TS-7).

Of particular note, is the role of dispersion in these systems. Uncorrected energies differ greatly (up to 66.5 kcal mol^{-1}) from corrected energies in the ωB97x and B3PW91 functionals. In the case of the M06l functional, the correct selectivity is only observed upon applying dispersion corrections, suggesting that dispersion plays a key role in determining the selectivity of C–C cleavage. Dispersion controlled selectivity has been previously observed in the reactivity of **[Al]**, and is well-documented for main-group systems.[40,46]

5.6.2 – Activation strain analysis

ASA plots against the Al–C¹ bond at the transition state

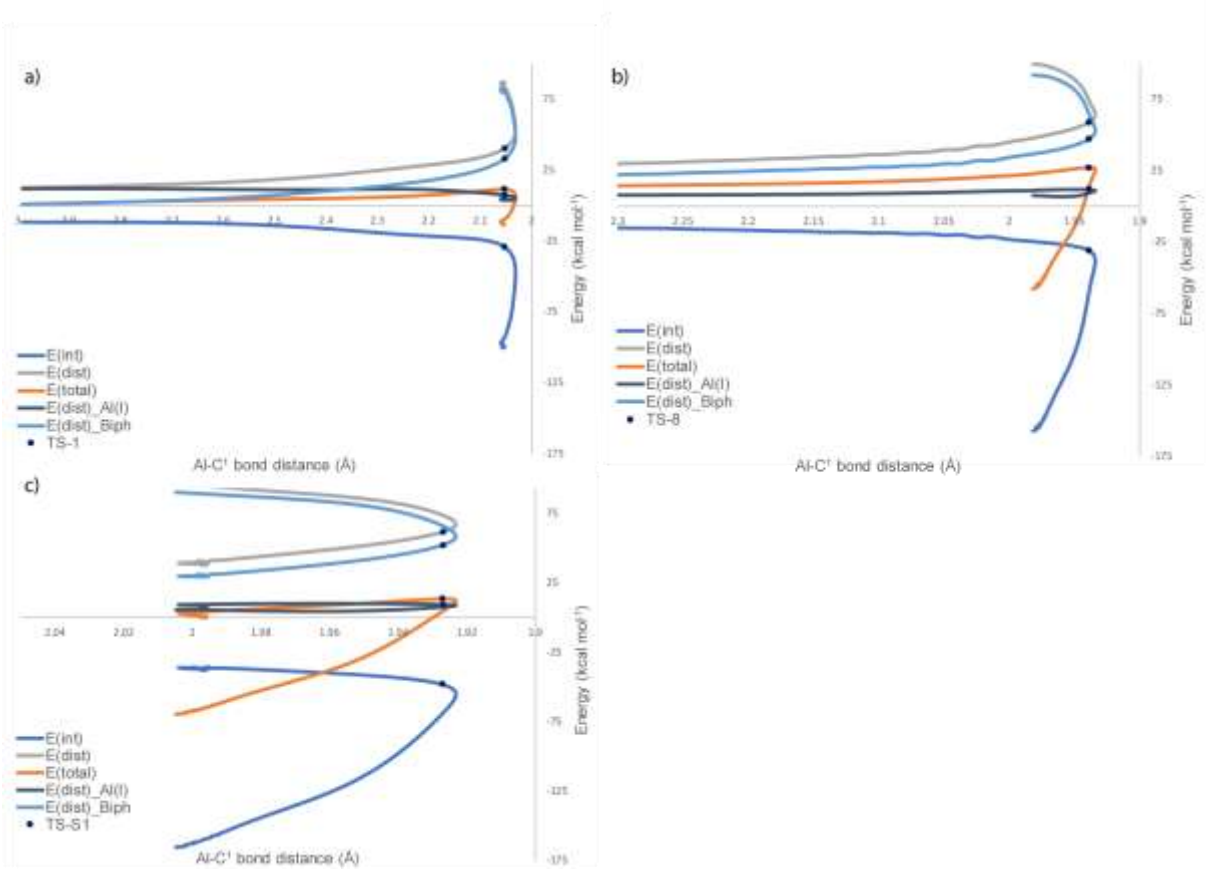


Figure 5.13: ASA plots for **TS-1** (a), **TS-10** (b), and **TS-11** (c) plotted against the shorter Al–C bond of the transition state.

In all three cases, E_{int} is essentially unchanged relative to the Al–C bond distance, up until the transition state geometry. This reflects the overlap between the σ-lone pair of **1** with an anti-bonding orbital in the substrate. The highly nucleophilic nature of **1** makes this an energetically favourable interaction and the data suggest that this is a large contributor to the stability of the transition state.

The raised HOMO of **[Al]^K** results in a greater contribution of E_{int} to the overall energy. Notably, E_{int} for the oxidative addition pathway involving **[Al]^K** is approximately 15 kcal mol^{-1} greater in magnitude than for the analogous pathway involving **1**. This is reflected in the overall activation energy with for **TS-11** being lower in energy than **TS-10** ($\Delta\Delta G^{\ddagger}_{298K}$ = –14.3 kcal mol^{-1}).

ASA plots against Al–C⁴ (TS-1) and Al–C⁷(TS-10, TS-11) bond at the transition state

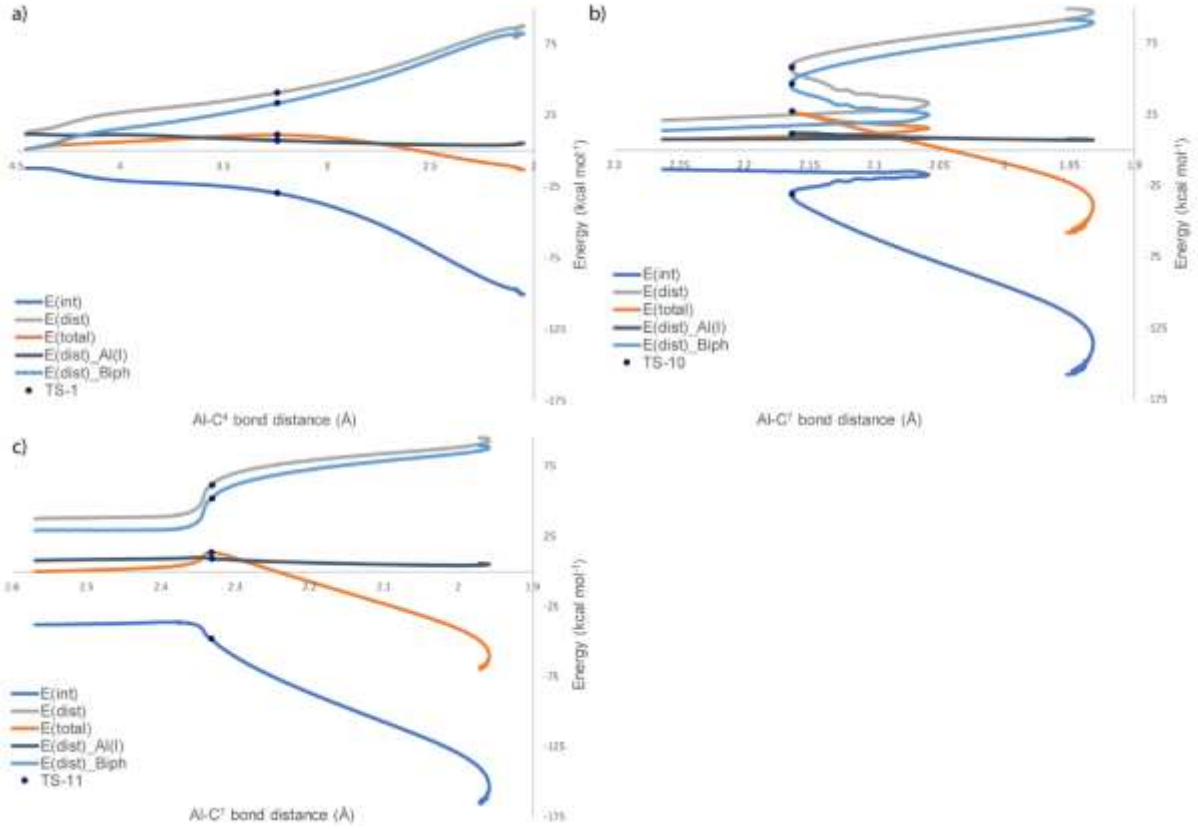


Figure 5.14: ASA plots for **TS-1** (a), **TS-10** (b), and **TS-11** (c) plotted against the change in bond length of the longer Al–C bond of the transition state.

The ASA profile shapes diverge significantly when plotted against the longer Al–C bond length. Interestingly, when comparing the oxidative addition of **[Al]** and **[Al]ᴷ**, the Al–C bond length smoothly decreases towards formation of the product in the case of latter, whereas the Al–C bond length sequentially decreases, increases, and decreases towards formation of the product. This likely reflects the high degree of reorganisation required of biphenylene to allow for effective overlap with the vacant 3p orbital of **[Al]**.

In the case of **[Al]ᴷ** the earlier transition state is evident in the longer Al–C bond (~2.33 Å in TS-S1 vs 2.16 Å in TS-8), and there is no complex reorganization of biphenylene required in order to achieve effective orbital overlap. This is likely a consequence for the greater radial extension of the frontier molecular orbitals in **[Al]ᴷ** relative to **[Al]**, allowing for better overlap.

5.7 – References

1 A. Balková and R. J. Bartlett, *J. Chem. Phys.*, 1994, **101**, 8972–8987.
2 J. Browning, M. Green, A. Laguna, L. E. Smart, J. L. Spencer and F. G. A. Stone, *J. Chem. Soc., Chem. Commun.*, 1975, 723–724.
3 D. Ellis, D. McKay, S. A. Macgregor, G. M. Rosair and A. J. Welch, *Angew. Chem., Int. Ed.*, 2010, **49**, 4943–4945.
4 S. Hu, T. Shima and Z. Hou, *Nature*, 2014, **512**, 413–415.
5 M. Jakoobi, N. Halcovitch, G. F. S. Whitehead and A. G. Sergeev, *Angew. Chem., Int. Ed.*, 2017, **56**, 3266–3269.
6 M. Jakoobi, Y. Tian, R. Boulatov and A. G. Sergeev, *J. Am. Chem. Soc.*, 2019, **141**, 6048–6053.
7 Y. Tian, M. Jakoobi, R. Boulatov and A. G. Sergeev, *Chem. Sci.*, 2021, **12**, 3568–3579.
8 M. Jakoobi and A. G. Sergeev, *Chem.: Asian J.*, 2019, **14**, 2181–2192.
9 A. P. Y. Chan and A. G. Sergeev, *Coord. Chem. Rev.*, 2020, **413**, 213213.
10 J. J. Eisch, A. M. Piotrowski, K. I. Han, Carl. Kruger and Y. H. Tsay, *Organometallics*, 1985, **4**, 224–231.
11 C. Perthuisot and W. D. Jones, *J. Am. Chem. Soc.*, 1994, **116**, 3647–3648.
12 C. Perthuisot, B. L. Edelbach, D. L. Zubris and W. D. Jones, *Organometallics*, 1997, **16**, 2016–2023.
13 A. B. Chaplin, R. Tonner and A. S. Weller, *Organometallics*, 2010, **29**, 2710–2714.
14 H. Takano, T. Ito, K. S. Kanyiva and T. Shibata, *Eur. J. Org. Chem.*, 2019, **2019**, 2871–2883.
15 K. Koshino and R. Kinjo, *J. Am. Chem. Soc.*, 2020, **142**, 9057–9062.
16 Z. Gu, G. B. Boursalian, V. Gandon, R. Padilla, H. Shen, T. V. Timofeeva, P. Tongwa, K. P. C. Vollhardt and A. A. Yakovenko, *Angew. Chem., Int. Ed.*, 2011, **50**, 9413–9417.
17 H. Takano, N. Sugimura, K. S. Kanyiva and T. Shibata, *ACS Omega*, 2017, **2**, 5228–5234.
18 S. Brand, H. Elsen, J. Langer, W. A. Donaubauer, F. Hampel and S. Harder, *Angew. Chem., Int. Ed.*, 2018, **57**, 14169–14173.
19 R. J. Schwamm, M. D. Anker, M. Lein and M. P. Coles, *Angew. Chem., Int. Ed.*, 2019, **58**, 1489–1493.
20 K. Sugita, R. Nakano and M. Yamashita, *Chem. Eur. J.*, 2020, **26**, 2174–2177.
21 C. Bakewell, M. Garçon, R. Y. Kong, L. O'Hare, A. J. P. White and M. R. Crimmin, *Inorg. Chem.*, 2020, **59**, 4608–4616.
22 X. Kang, G. Luo, L. Luo, S. Hu, Y. Luo and Z. Hou, *J. Am. Chem. Soc.*, 2016, **138**, 11550–11559.
23 B. Zhu, W. Guan, L.-K. Yan and Z.-M. Su, *J. Am. Chem. Soc.*, 2016, **138**, 11069–11072.
24 J. Hicks, P. Vasko, J. M. Goicoechea and S. Aldridge, *J. Am. Chem. Soc.*, 2019, **141**, 11000–11003.
25 H. Zhu, J. Chai, H. Fan, H. W. Roesky, C. He, V. Jancik, H.-G. Schmidt, M. Noltemeyer, W. A. Merrill and P. P. Power, *Angew. Chem., Int. Ed.*, 2005, **44**, 5090–5093.
26 H. Zhu, R. B. Oswald, H. Fan, H. W. Roesky, Q. Ma, Z. Yang, H.-G. Schmidt, M. Noltemeyer, K. Starke and N. S. Hosmane, *J. Am. Chem. Soc.*, 2006, **128**, 5100–5108.
27 C. Bakewell, A. J. P. White and M. R. Crimmin, *Chem. Sci.*, 2019, **10**, 2452–2458.
28 R. Y. Kong and M. R. Crimmin, *J. Am. Chem. Soc.*, 2020, **142**, 11967–11971.
29 S. Grams, J. Eyselein, J. Langer, C. Färber and S. Harder, *Angew. Chem., Int. Ed.*, 2020, **59**, 15982–15986.
30 F. M. Bickelhaupt and K. N. Houk, *Angew. Chem., Int. Ed.*, 2017, **56**, 10070–10086.
31 I. Fernández and F. M. Bickelhaupt, *Chem. Soc. Rev.*, 2014, **43**, 4953–4967.
32 J. J. Cabrera-Trujillo and I. Fernández, *Chem. Eur. J.*, 2020, **26**, 11806–11813.
33 M. S. Hill, M. F. Mahon, A. S. S. Wilson, C. Dinoi, L. Maron and E. Richards, *Chem. Commun.*, 2019, **55**, 5732–5735.
34 A. S. S. Wilson, C. Dinoi, M. S. Hill, M. F. Mahon, L. Maron and E. Richards, *Angew. Chem., Int. Ed.*, 2020, **59**, 1232–1237.
35 C. Cui, H. W. Roesky, H.-G. Schmidt, M. Noltemeyer, H. Hao and F. Cimpoesu, *Angew. Chem., Int. Ed.*, 2000, **39**, 4274–4276.

36 J. M. Darmon, S. C. E. Stieber, K. T. Sylvester, I. Fernández, E. Lobkovsky, S. P. Semproni, E. Bill, K. Wieghardt, S. DeBeer and P. J. Chirik, *J. Am. Chem. Soc.*, 2012, **134**, 17125–17137.
37 M. R. Crimmin, M. J. Butler and A. J. P. White, *Chem. Commun.*, 2015, **51**, 15994–15996.
38 Frisch, M. J.; Trucks, G. W.; Schlegel, H. B.; Scuseria, G. E.; Robb, M. A.; Cheeseman, J. R.; Scalmani, G.; Barone, V.; Mennucci, B.; Petersson, G. A.; Nakatsuji, H.; Caricato, M.; Li, X.; Hratchian, H. P.; Izmaylov, A. F.; Bloino, J.; Zheng, G.; Sonnenberg, J. L.; Hada, M.; Ehara, M.; Toyota, K.; Fukuda, R.; Hasegawa, J.; Ishida, M.; Nakajima, T.; Honda, Y.; Kitao, O.; Nakai, H.; Vreven, T.; Montgomery, J. A., Jr.; Peralta, J. E.; Ogliaro, F.; Bearpark, M.; Heyd, J. J.; Brothers, E.; Kudin, K. N.; Staroverov, V. N.; Kobayashi, R.; Normand, J.; Raghavachari, K.; Rendell, A.; Burant, J. C.; Iyengar, S. S.; Tomasi, J.; Cossi, M.; Rega, N.; Millam, J. M.; Klene, M.; Knox, J. E.; Cross, J. B.; Bakken, V.; Adamo, C.; Jaramillo, J.; Gomperts, R.; Stratmann, R. E.; Yazyev, O.; Austin, A. J.; Cammi, R.; Pomelli, C.; Ochterski, J. W.; Martin, R. L.; Morokuma, K.; Zakrzewski, V. G.; Voth, G. A.; Salvador, P.; Dannenberg, J. J.; Dapprich, S.; Daniels, A. D.; Farkas, Ö.; Foresman, J. B.; Ortiz, J. V.; Cioslowski, J.; Fox, D. J. Gaussian~09 Revision E.01. Gaussian, Inc., Wallingford, CT 2009.
39 Y. Zhao and D. G. Truhlar, *Theor. Chem. Acc.*, 2008, **120**, 215–241.
40 T. N. Hooper, M. Garçon, A. J. P. White and M. R. Crimmin, *Chem. Sci.*, 2018, **9**, 5435–5440.
41 R. Y. Kong and M. R. Crimmin, *Chem. Commun.*, 2019, **55**, 6181–6184.
42 S. Grimme, J. Antony, S. Ehrlich and H. Krieg, *J. Chem. Phys.*, 2010, **132**, 154104.
43 H. P. Hratchian and H. B. Schlegel, in *Theory and Applications of Computational Chemistry*, eds. C. E. Dykstra, G. Frenking, K. S. Kim and G. E. Scuseria, Elsevier, Amsterdam, 2005, pp. 195–249.
44 Gleadening, E. D.; Bakenhoop, J. K.; Reed, A. E.; Carpenter, J. E.; Bohmann, J. A.; Morales, C. M.; Landis, C. R.; Weinhold, F. NBO 6.0. Theoretical Chemistry Institute, University of Wisconsin, Madison 2013.
45 D. Svatunek and K. N. Houk, *J. Comput. Chem.*, 2019, **40**, 2509–2515.
46 D. J. Liptrot and P. P. Power, *Nat. Rev. Chem.*, 2017, **1**, 1–12.

Concluding Remarks

This thesis has described the construction and deconstruction of carbon–carbon bonds using main-group reagents.

The use of main group reagents as selective reductants has enabled a detailed investigation into CO homologation chemistry. The aluminium (I) reagent employed allowed for the reduction and carbon chain growth of CO from a transition metal centre. CO insertion into aluminium–carbon bonds was further found to be reversible. While it is unlikely for the systems to explored to achieve catalytic turnover in the main-group reagent, the synergistic effect of reacting an aluminium reductant and transition metal fragment was demonstrated and a wealth of mechanistic insight was available through study of such systems. The transformations explored in this thesis involved the conversion of aluminium (I) to aluminium (III) species – it may be possible to extend this chemistry through the reaction of other main-group reagents such as hydrides or alkyl species.

The cleavage of strained C–C bonds was demonstrated using both aluminium and magnesium. The key bond cleavage transformation was shown to be redox neutral, whereas the formal reduction of the substrate occurs upon installation of the main-group fragment. The results suggest that the chemistry of main-group metals is capable of effecting bond transformations traditionally reserved for transition metals, once installed within the framework of the substrate.

In the final chapter, the chemoselective cleavage of an arene ring was demonstrated with an aluminium (I) reagent. This transformation is essentially unknown in both transition metal and main-group chemistry. The unique reactivity of aluminium is ascribed to the symmetry and radial extension of the frontier orbitals. Hence, while there remains continued interest in mimicking transition metal chemistry with main-group reagents, the chapter indicates that unique transformations are available to main-group metals and that these unique transformations warrant investigation.

More broadly, main-group reagents have the potential to access exciting new reactions in their own right. While turnover persists as an impediment to broader application, alternative strategies for the installation of main-group metals into small-molecule may be fruitful. Alternatively, electrochemistry may provide another entry point into main-group mediated catalysis. Regardless of the approach taken, fundamental studies into main-group reactivity will guide efforts for sustainable main-group catalysis.